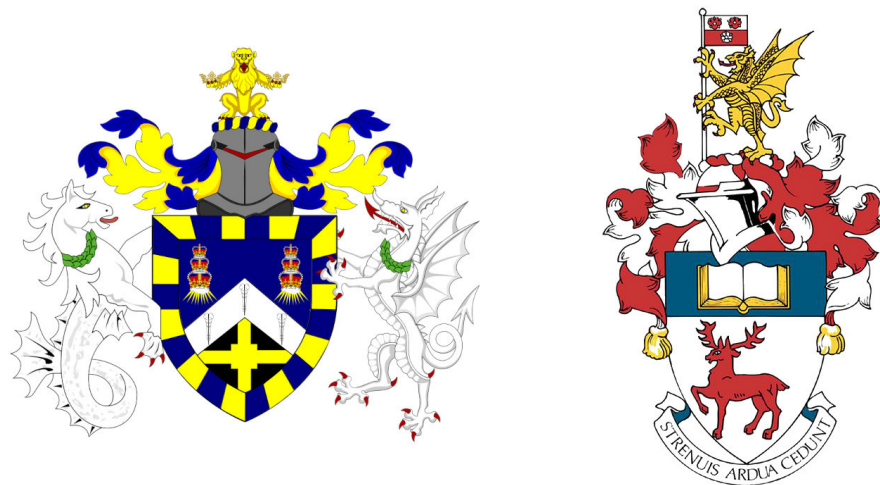


¹ ADVANCING NEUTRINO
² DETECTION AND TRIGGERING IN
³ DUNE



⁵ Francisco Martínez López

⁶ Submitted in partial fulfillment of the requirements
⁷ of the Degree of Doctor of Philosophy

⁸ School of Physical and Chemical Sciences
⁹ Queen Mary University of London

¹⁰ School of Physics and Astronomy
¹¹ University of Southampton

¹² December 2024

¹³ Statement of originality

- ¹⁴ I, Francisco Martínez López, confirm that the research included within this thesis is my
¹⁵ own work or that where it has been carried out in collaboration with, or supported by
¹⁶ others, that this is duly acknowledged below and my contribution indicated. Previously
¹⁷ published material is also acknowledged below.
- ¹⁸ I attest that I have exercised reasonable care to ensure that the work is original, and
¹⁹ does not to the best of my knowledge break any UK law, infringe any third party's
²⁰ copyright or other Intellectual Property Right, or contain any confidential material.
- ²¹ I accept that the University has the right to use plagiarism detection software to check
²² the electronic version of the thesis.
- ²³ I confirm that this thesis has not been previously submitted for the award of a degree
²⁴ by this or any other university.
- ²⁵ The copyright of this thesis rests with the author and no quotation from it or information
²⁶ derived from it may be published without the prior written consent of the author.
- ²⁷ Signature: [can be digital signature]
- ²⁸ Date:
- ²⁹ Details of collaboration and publications:
³⁰ [insert details here if applicable]

³¹ Abstract

³² Work in progress . . .

¡Oh memoria, enemiga mortal de mi descanso!

El ingenioso hidalgo don Quijote de la Mancha

MIGUEL DE CERVANTES SAAVEDRA

³³ Acknowledgements

³⁴ Work in progress . . .

³⁵ Contents

³⁶	Statement of originality	3
³⁷	Abstract	5
³⁸	Acknowledgements	9
³⁹	List of Figures	15
⁴⁰	List of Tables	31
⁴¹	List of Abbreviations	33
⁴²	1 Introduction	35
⁴³	2 Neutrino physics	37
⁴⁴	2.1 Historical remarks	38
⁴⁵	2.2 Neutrinos in the SM	38
⁴⁶	2.3 Massive neutrinos	41
⁴⁷	2.4 Neutrino oscillations	44
⁴⁸	2.4.1 Oscillations in vacuum	45
⁴⁹	2.4.2 Oscillations in matter	46
⁵⁰	2.4.3 Current status of neutrino oscillations	46
⁵¹	2.5 Open questions in the neutrino sector	47
⁵²	2.6 Neutrino interactions	49
⁵³	3 The Deep Underground Neutrino Experiment	51

CONTENTS

54	3.1 Overview	51
55	3.2 Physics goals of DUNE	53
56	3.3 Far Detector	55
57	3.3.1 Horizontal Drift	56
58	3.3.2 Vertical Drift	59
59	3.3.3 FD Data Acquisition System	61
60	3.4 Near Detector	62
61	3.4.1 ND-LAr	64
62	3.4.2 TMS/ND-GAr	65
63	3.4.3 PRISM	66
64	3.4.4 SAND	68
65	3.5 LBNF beamline	68
66	4 ND-GAr	71
67	4.1 Requirements	71
68	4.2 Reference design	72
69	4.2.1 HPgTPC	72
70	4.2.2 ECal	73
71	4.2.3 Magnet	74
72	4.2.4 Muon system	75
73	4.3 GArSoft	75
74	4.3.1 Event generation	75
75	4.3.2 Detector simulation	76
76	4.3.3 Reconstruction	77
77	5 FWTPG offline software	81
78	6 Matched Filter approach to induction wire Trigger Primitives	83
79	6.1 Motivation	83
80	6.2 Signal-to-noise ratio definition	85

CONTENTS

81	6.3	Low-pass FIR filter design	87
82	6.4	Matched filters	90
83	6.5	Using simulated samples	96
84	6.5.1	Angular dependence	102
85	6.5.2	Distortion and peak asymmetry	104
86	6.5.3	Hit sensitivity	107
87	7	DM searches with neutrinos from the Sun	117
88	7.1	Motivation	117
89	7.2	Gravitational capture of DM by the Sun	117
90	7.3	Neutrino flux from DM annihilations	124
91	7.4	Computing limits from solar neutrino fluxes	125
92	7.5	Example: Kaluza-Klein Dark Matter	129
93	7.6	High energy DM neutrino signals	133
94	7.6.1	DIS events	135
95	7.6.2	Single proton QEL events	140
96	7.6.3	Results	143
97	7.7	Example: Leptophilic Dark Matter	145
98	8	Particle ID in GArSoft	151
99	8.1	dE/dx measurement in the TPC	152
100	8.1.1	Energy calibration	154
101	8.1.2	Truncated dE/dx mean	164
102	8.1.3	Mean dE/dx parametrisation	167
103	8.1.4	Particle identification	171
104	8.2	Muon and pion separation in the ECal and MuID	171
105	8.2.1	Track-ECal matching	174
106	8.2.2	Classification strategy	178
107	8.2.3	Feature selection and importance	182
108	8.2.4	Hyperparameter optimisation	193

CONTENTS

109	8.2.5 Probability calibration	197
110	8.2.6 Performance	199
111	8.3 ECal time-of-flight	199
112	8.3.1 Arrival time estimations	201
113	8.3.2 Proton and pion separation	202
114	8.4 Charged pion decay in flight	205
115	8.4.1 Track breakpoints	206
116	8.5 Neutral particle identification	213
117	8.5.1 ECal clustering	213
118	8.5.2 π^0 reconstruction	216
119	9 Event selection in ND-GAr	219
120	9.1 CAFs and CAFAna	219
121	9.2 Event selection	219
122	9.2.1 ν_μ CC selection	219
123	9.2.2 Charged pion multiplicity	219
124	10 Conclusions	221
125	A An appendix	223
126	Bibliography	225

¹²⁷ List of Figures

¹²⁸ 3.1	Schematic diagram of the DUNE experiment and the LBNF beamline [1].	52
¹²⁹ 3.2	Schematic diagram showing the operating principle of a LArTPC with wire readout	56
¹³¹ 3.3	Proposed design for the FD-1 and FD-2 modules following the HD principle.	57
¹³² 3.4	Schematic representation of an APA frames showing the U, V, X and G wires.	58
¹³⁴ 3.5	A PDS module containing 24 X-ARAPUCAs and the location of the modules on the APAs.	58
¹³⁶ 3.6	Proposed design for the FD-3 module following the VD principle.	59
¹³⁷ 3.7	Schematic representation of the electrode strip configuration for a top and bottom CRU.	60
¹³⁹ 3.8	Detailed diagram of the DUNE FD DAQ system. Figure taken from Ref. [2].	61
¹⁴¹ 3.9	Representation of the ND hall in Phase II, showing the different subcomponents.	63
¹⁴² 3.10	Schematic representation of the external components of ND-LAr, including the cryostat and the PRISM movable system and detailed drawing of one ArgonCube module.	64
¹⁴⁵ 3.11	Schematic view of the TMS detector, highlighting its main parts.	65
¹⁴⁶ 3.12	Cross section of the ND-GAr geometry, showing the HPgTPC, ECal and magnet.	66

LIST OF FIGURES

148	3.13 Predicted beam muon neutrino flux at the ND location for different off-axis	
149	positions.	67
150	3.14 Schematic longitudinal section of the LBNF beamline at Fermilab.	68
151	3.15 Predicted neutrino fluxes at the FD in FHC mode and RHC mode.	69
152	4.1 Diagram of the ALICE TPC, showing the two drift chambers, inner and	
153	outer field cages and readout chambers.	73
154	4.2 Diagram of the ALICE TPC, showing the two drift chambers, inner and	
155	outer field cages and readout chambers.	74
156	6.1 <i>Schematic representation of an APA. The black lines represent the APA</i>	
157	<i>steel frame. The green and magenta lines correspond to the direction of the</i>	
158	<i>U and V induction wires respectively. The blue lines indicate the direction</i>	
159	<i>of the X collection wires and the wire shielding G.</i>	84
160	6.2 <i>Left panel: Zoomed unfiltered waveform corresponding to channel 7840</i>	
161	<i>from the ProtoDUNE-SP raw data capture felix-2020-07-17-21:31:44</i>	
162	<i>(blue line). The green dashed lines mark the region $\pm 3\sigma_{raw}$. The resulting</i>	
163	<i>noise waveform is also shown (red line). Top right panel: ADC distribution</i>	
164	<i>for channel 7840, where the green shaded region represents $\pm \sigma_{raw}$. Bottom</i>	
165	<i>right panel: noise ADC distribution for channel 7840, where the green</i>	
166	<i>shaded region represents $\pm \sigma_{noise}$.</i>	85
167	6.3 <i>Left panel: Zoomed filtered waveform corresponding to channel 7840 from</i>	
168	<i>the ProtoDUNE-SP raw data capture felix-2020-07-17-21:31:44 (blue</i>	
169	<i>line). The filter used was the current implementation of the low-pass FIR</i>	
170	<i>filter in <code>dtp-firmware</code>. The green dashed lines mark the region $\pm 3\sigma_{raw}$.</i>	
171	<i>The resulting noise waveform is also shown (red line). Top right panel:</i>	
172	<i>ADC distribution for channel 7840 after filtering, where the green shaded</i>	
173	<i>region represents $\pm \sigma_{raw}$. Bottom right panel: noise ADC distribution for</i>	
174	<i>channel 7840 after filtering, where the green shaded region represents $\pm \sigma_{noise}$</i>	87

LIST OF FIGURES

175	6.4 Power spectrum in decibels for the current implementation of the low-pass	
176	FIR filter in <i>dtp-firmware</i> (blue line), compared to the response of an	
177	optimal filter obtained using the Parks-McClellan algorithm for the same	
178	pass-band (red line). Also for comparison I include the spectrum of the	
179	optimal filter when taking only the integer part of the coefficients (red	
180	dashed line)	88
181	6.5 Relative change in the S/N for the ProtoDUNE-SP raw data capture	
182	<i>felix-2020-07-17-21:31:44</i> , using different values of the cutoff frequency	
183	f_c and the transition width δf . The optimal Chebyshev filters were applied	
184	using just the integer part of the coefficients given by the Parks-McClellan	
185	algorithm.	89
186	6.6 Distribution of the relative change of the S/N on the different wire planes	
187	from the ProtoDUNE-SP raw data capture <i>felix-2020-07-17-21:31:44</i>	
188	after the optimal Chebyshev filter was applied. The filter was computed	
189	with the Parks-McClellan algorithm using a cutoff of $f_c = 0.068 \text{ ticks}^{-1}$	
190	and a transition width $\delta f = 0.010 \text{ ticks}^{-1}$	90
191	6.7 Left panel: Zoomed match filtered waveform corresponding to channel 7840	
192	from the ProtoDUNE-SP raw data capture <i>felix-2020-07-17-21:31:44</i>	
193	(blue line). The filter used was directly extracted from the data, being	
194	the 32 values around the first peak in the original waveform. The green	
195	dashed lines mark the region $\pm 3\sigma_{\text{raw}}$. The resulting noise waveform is	
196	also shown (red line). Top right panel: ADC distribution for channel 7840	
197	after match filtering, where the green shaded region represents $\pm \sigma_{\text{raw}}$.	
198	Bottom right panel: noise ADC distribution for channel 7840 after match	
199	filtering, where the green shaded region represents $\pm \sigma_{\text{noise}}$	91
200	6.8 Relative improvement in the S/N for the raw data capture <i>felix-2020-07-17-21:31:44</i> ,	
201	using the matched filter following the parametrisation in Eq. (6.17). The	
202	black crosses in both panels denote the location of the maximum ratio value.	94

LIST OF FIGURES

203	6.9 Left panel: Optimal matched filter coefficients for the U (blue line) and V (red line) planes. The filters were computed with our parametrisation in Eq. (6.17) for the parameter values $\delta = 0.035$, $\sigma = 0.191$ and $\delta = 0.018$, $\sigma = 0.191$ respectively. Right panel: Distribution of the relative change of the S/N on the two induction wire planes from the ProtoDUNE-SP raw data capture <i>felix-2020-07-17-21:31:44</i> after their respective optimal matched filters were applied.	97
210	6.10 Left panel: distributions of the particles track length in the liquid argon for the generated $E_k = 100$ MeV monoenergetic samples, electrons (blue), muons (red), protons (green) and neutral pions (purple). Right panel: distribution of the length of the longest photon in the neutral pion sample after the decay process $\pi^0 \rightarrow \gamma\gamma$	98
215	6.11 Left panel: schematic representation of the two new rotated reference frames used in this analysis (denoted as prime and double prime), viewed from the yz plane. The magenta stack of lines represent the wires in the U plane, whereas the green lines correspond to the wires in the V plane. Right panel: 3D representation of the momentum of one of the generated monoenergetic muons (red arrow) in the original reference frame (black lines), along with the new reference frame used for the U plane waveforms (blue lines). In the yz plane I added the projection of these three.	100
223	6.12 Distributions of the mean S/N improvement per event for the corresponding sample after applying the matched filters. Here I separated the change in the U plane (blue) and the V plane (red) channels. From top left to the right: muon, electron, proton and neutral pion. All the events have a fixed kinetic energy of $E_k = 100$ MeV.	101

LIST OF FIGURES

LIST OF FIGURES

248	6.16 Left panel: peak asymmetry distribution for the case of the monoenergetic	
249	$E_k = 100$ MeV muon sample. Each value corresponds to a single bipolar	
250	signal peak from a channel in any event. The blue distribution represents	
251	the peaks on U plane channels, whereas the red corresponds to signal peaks	
252	in V wires. Right panel: relation between the mean peak asymmetry per	
253	event with the S/N for U channel waveforms from the $E_k = 100$ MeV	
254	muon sample. The top subplot shows the decimal logarithm of the mean	
255	S/N for the raw (red) and the matched filtered (blue) waveforms. The	
256	bottom subplot contains the mean S/N improvement ratio after the matched	
257	filter was applied.	106
258	6.17 Raw data display in the plane time (in firmware ticks) vs. offline channel	
259	number for an $E_k = 100$ MeV electron event. The produced true hits are	
260	superimposed (black boxes) as well as the hits comming from the standard	
261	hit finder chain (blue circles) and the hit finder using the matched filter	
262	(green triangles).	108
263	6.18 Dependence of the precision (blue), sensitivity (red) and F_1 (green) scores	
264	on the threshold values used in the hit finder, for the FIR (left panel)	
265	and matched filter (right panel) cases. The results were obtained after	
266	matching the hits to the true hits in the case of the isotropic muon sample	
267	with kinetic energy in the range 5 to 100 MeV, taking only into account	
268	the induction plane channels. The points represent the mean value while	
269	the error bars indicate one standard deviation around that mean value. . .	110

LIST OF FIGURES

- 270 6.19 *Dependence of the averaged hit sensitivity on the kinetic energy of the events for the matched filter (blue) and standard (red) hits, for the case of the muon (left panel) and electron (right panel) samples, separated between U (top plots) and V (bottom plots) induction wire planes. The top subplots contain the hit sensitivities for the two hit finder alternatives, while the bottom subplots show the ratio between the two. The horizontal lines sit at the mean value and represent the size of the energy bins, while the vertical error bars indicate one standard deviation around that mean value.* 112
 271
 272
 273
 274
 275
 276
 277
- 278 6.20 *Distributions of the hit sensitivity in the U (top panels) and V (bottom panels) planes versus the hit sensitivity in the X plane, both for the standard hits (left panels) and the matched filter hits (right panels), in the case of the electron sample and a threshold of 30 ADC.* 113
 279
 280
 281
- 282 6.21 *Top panels: standard residual plots of the hit sensitivities between the X and U planes. Bottom panels: quantile-quantile plots of the hit sensitivity standard residuals between the X and U planes. In all cases, the left panel corresponds to the standard hits while the right panel represents the matched filter case, all from the electron sample with a 30 ADC threshold.* 114
 283
 284
 285
 286
- 287 7.1 *Input solar parameters used in our capture rate computation as functions of the Sun's radius, from left to right: temperature (with respect to the temperature at the core), mass (in solar masses) and electron number density (with respect to the electron density at the core). All quantities shown correspond to the standard solar model BS2005-OP [3].* 121
 288
 289
 290
 291
- 292 7.2 *Capture rates as a function of the DM mass for the DM-electron interactions (red lines), SD DM-nucleons interactions (green lines) and SI DM-nucleons interactions (blue lines). Solid lines represent the values computed in this work while the dashed lines are the one given in Ref. [4]. All the rates are shown for a choice of scattering cross section of $\sigma_i = 10^{-40} \text{ cm}^2$.* . . . 122
 293
 294
 295
 296

LIST OF FIGURES

297	7.3 <i>NuWro computed $\nu_\mu - {}^{40}\text{Ar}$ charged-current scattering cross section as a function of the neutrino energy E_μ. The black line shows to the total cross section, whereas the others correspond to the different contributions (in red quasi-elastic scattering, in green resonant pion exchange, in blue deep inelastic scattering and in purple meson exchange current).</i>	126
302	7.4 <i>Expected atmospheric neutrino flux as a function of the neutrino energy E_ν at Homestake at solar minimum, taken from Ref. [5]. The blue solid (dashed) line correspond to muon neutrinos (antineutrinos) and the red solid (dashed) line correspond to electron neutrinos (antineutrinos)</i>	128
306	7.5 Feynman diagrams for B^1B^1 annihilation into SM fermions.	130
307	7.6 Feynman diagrams for B^1B^1 annihilation into a Higgs boson pair. . . .	130
308	7.7 <i>Computed spectra of muon neutrinos at the DUNE FD site from B^1 annihilations in the Sun for three different values of M_{LKP}, plotted in relative energy units for legibility.</i>	131
311	7.8 <i>Projected 90% confidence level upper limit for DUNE (400 kT yr) on the spin- dependent B^1-proton scattering cross section as a function of M_{LKP} (green dots). I also show the previous limits from IceCube [6] (blue line) and Antares [7] (red line) on the LKP cross section. The shaded area represents the disfavoured region (at 95% confidence level) on the mass of the LKP from LHC data [8]</i>	132
317	7.9 <i>Computed spectra of muon neutrinos at the DUNE FD site from $\tau^+\tau^-$ (left panel) and $b\bar{b}$ (right panel) annihilations in the Sun for the DM masses $m_{\text{DM}} = 10$ GeV (red line), 50 GeV (green line) and 100 GeV (blue line), plotted in relative energy units.</i>	133
321	7.10 <i>Distribution of the muon neutrino energies from the $\tau^+\tau^-$ (left panel) and $b\bar{b}$ (right panel) annihilation channels, for $m_{\text{DM}} = 10$ GeV, separated by CC interaction type: QEL (blue), MEC (orange), RES (green) and DIS (red)</i>	135

LIST OF FIGURES

<p>325 7.11 <i>Distributions of θ_μ (left panel), θ_j (central panel) and θ_{plane} (right panel)</i> 326 <i>for the $b\bar{b}$ sample with $m_{DM} = 10$ GeV (blue) and the atmospheric</i> 327 <i>background (red).</i></p> <p>328 7.12 <i>Left panel: signal efficiencies (blue lines) and background rejections (red</i> 329 <i>lines) for events passing the cuts $\theta < \theta_{cut}$ for the jet (solid lines) and</i> 330 <i>muon (dashed lines) angles. Right panel: signal efficiency (blue line) and</i> 331 <i>background rejection (red line) for events passing the cut $\theta_{plane} < \theta_{cut}$ for</i> 332 <i>the momentum conservation plane deviation.</i></p> <p>333 7.13 <i>Signal efficiencies for the $\tau^+\tau^-$ (blue line) and $b\bar{b}$ (red line) DIS samples</i> 334 <i>as functions of the DM mass, m_{DM}, obtained by applying the optimal</i> 335 <i>angular cuts $\theta_\mu < 27^\circ$, $4^\circ < \theta_j < 26^\circ$ and $\theta_{plane} < 3.5^\circ$.</i></p> <p>336 7.14 <i>Distributions of $\cos \theta_\mu$ (left panel), $\cos \theta_p$ (central panel) and $\cos \theta_N$</i> 337 <i>(right panel) for the $\tau^+\tau^-$ QEL sample with $m_{DM} = 5$ GeV (blue) and</i> 338 <i>the atmospheric background (red).</i></p> <p>339 7.15 <i>Left panel: value of the loss function for the training sample (blue line)</i> 340 <i>and accuracy for the validation sample (red line) versus the number of</i> 341 <i>iterations for the MLP classifier training. Right panel: distributions of the</i> 342 <i>predicted probabilities assigned by the MLP classifier to the test sample</i> 343 <i>for the $\tau^+\tau^-$ QEL signal with $m_{DM} = 5$ GeV (blue) and the atmospheric</i> 344 <i>background (red).</i></p> <p>345 7.16 <i>Signal efficiencies for the $\tau^+\tau^-$ (blue line) and $b\bar{b}$ (red line) single proton</i> 346 <i>QEL samples as functions of the DM mass, m_{DM}, obtained by requiring a</i> 347 <i>minimum predicted probability from the MLP classifier of 0.97 in order to</i> 348 <i>achieve a background rejection greater than 99.8%.</i></p>	<p>136</p> <p>137</p> <p>139</p> <p>140</p> <p>141</p> <p>142</p>
---	---

LIST OF FIGURES

349	7.17 Projected 90% confidence level upper limit for DUNE (400 kT yr) on 350 the spin-dependent DM-nucleon scattering cross section as a function of 351 m_{DM} , for the annihilation channels $\tau^+\tau^-$ (blue) and $b\bar{b}$ (red) separated 352 by interaction type (up triangles denote DIS interactions whereas down 353 triangles represent QEL interactions). I also show the previous limits 354 from IceCube [9] (solid lines) and the projected sensitivities for Pingu [10] 355 (dashed lines) and Hyper-Kamiokande [11] (dash-dotted lines), as well 356 as the direct detection limits from PICASSO [12] (solid green line) and 357 PICO-60 C ₃ F ₈ [13] (dashed green line).	144
358	7.18 Left panel: Projected 90% confidence level sensitivity of DUNE (400 kT 359 yr) to the scale Λ of an EFT containing only leptophilic DM axial-axial 360 interactions (blue line). Right panel: . In both cases the corresponding 361 limits from DarkSide-50 [14] (dotted green line) and XENON1T [15] 362 (dashed red line) are also shown, together with the configurations for which 363 the correct relic density is achieved (black line), all for the coupling values 364 $c_A^e = 10^3$ and $c_A^\nu = 10^{-2}$	148
365	8.1 Distribution of the fraction of energy deposits with residual range less 366 than 20% of the total track length, and distribution of the ionisation per 367 unit length after removing the tracks with less than 30% of their energy 368 deposits in the last 20% of the track.	155
369	8.2 Distribution of the reconstructed ionisation charge per unit length for 370 different reclustering values, and distribution of the median change in 371 dQ/dx per track for the $N_{\text{group}} = 4$ reclustering.	156
372	8.3 Distribution of the Geant4-simulated energy losses per unit length versus 373 residual range for the stopping proton sample.	158
374	8.4 Fitted most probable dQ/dx values for each dE/dx bin, together with 375 best fit to the logarithmic calibration function.	159

LIST OF FIGURES

376	8.5 Fitted most probable dQ/dx values for each dE/dx bin for three different	
377	ADC bit limits.	161
378	8.6 Area normalised dE/dx distributions for the true and the reconstructed	
379	energy deposits in the stopping proton sample, both after applying the	
380	calibration and the calibration and the normalisation correction.	162
381	8.7 Fractional residuals between the true and the corrected dE/dx means	
382	and the 60% truncated means, and fractional residuals between the true	
383	and the uncorrected, corrected and uncalibrated dE/dx 60% truncated	
384	means.	164
385	8.8 Estimated values of the mean dE/dx bias and resolution for the stopping	
386	proton sample at different values of the truncation factor.	165
387	8.9 Examples of the truncated mean dE/dx LanGauss fits for various $\beta\gamma$	
388	bins, from a simulated FHC neutrino sample.	167
389	8.10 Resulting one and two dimensional projections of the posterior probability	
390	distributions of the ALEPH $\langle dE/dx \rangle$ parameters obtained by fitting the	
391	60% truncated mean dE/dx values from a FHC neutrino sample.	168
392	8.11 Truncated mean dE/dx obtained for the FHC neutrino sample as a	
393	function of the $\beta\gamma$ product, together with the fitted most probable values	
394	for each $\beta\gamma$ bin and the best fit obtained using the ALEPH parametrisation.	169
395	8.12 Distribution of the 60% truncated mean dE/dx versus reconstructed	
396	momentum for the FHC neutrino sample.	170
397	8.13 Estimated values of the mean dE/dx bias and resolution obtained for the	
398	true protons in a FHC neutrino sample.	171
399	8.14 True momentum distribution for the primary muon in ν_μ CC $N\pi^\pm$	
400	interactions inside the fiducial volume of ND-GAr, compared to the	
401	post FSI charged pion spectrum.	172
402	8.15 Distributions of energy deposits in the ECal for a muon and a charged	
403	pion with similar momenta.	173

LIST OF FIGURES

404	8.16 Left panel: comparison between the precision (blue), sensitivity (yellow) and F_1 score (red) obtained for the default (horizontal lines) and new algorithms, both with the χ^2 -based direction estimator (squares) and cheating the directions (circles), for different values of the χ^2 cut. Right panel: comparison of the performance of the new algorithm when applying the cluster t_0 correction (squares) and when (circles).	175
410	8.17 Schematics of a possible option to deal with track-ECal associations in non-zero t_0 neutrino interaction events, trying to correct for the drift direction uncertainty in a cluster-by-cluster basis using the cluster time, $t_{cluster}$	177
414	8.18 Momentum distribution for the reconstructed muons (top panel) and charged pions (bottom panel) in a FHC neutrino sample, together with the fraction of them reaching the ECal (red) and MuID (blue). Each entry corresponds to a reconstructed track, backtracked to a true muon or pion which has not produced any other reconstructed track.	179
419	8.19 Predicted truncated mean dE/dx versus momentum, for electrons, muons, charged pions and protons, obtained using the ALEPH parametrisation. The vertical dashed lines represent the boundaries of the six regions used for the muon and pion classification training.	180
423	8.20 Example ECal feature distributions for muons and charged pions in the five different momentum ranges considered.	184
425	8.21 Example MuID feature distributions for muons and charged pions in the three different momentum ranges considered.	185
427	8.22 Left panel: cumulative explained variance for the first three principal components (top panel) and contribution of the different features to the principal axes in feature space (bottom panel). Right panel: Shapley (blue) and Gini (red) feature importances for the different input features. Both figures correspond to the samples in the momentum range $0.3 \leq p < 0.8 \text{ GeV}/c$	187

LIST OF FIGURES

433	8.23 Left panel: cumulative explained variance for the first three principal	
434	components (top panel) and contribution of the different features to the	
435	principal axes in feature space (bottom panel). Right panel: Shapley	
436	(blue) and Gini (red) feature importances for the different input features.	
437	Both figures correspond to the samples in the momentum range $0.8 \leq$	
438	$p < 1.5 \text{ GeV}/c$	188
439	8.24 Evolution of the SHAP importance for the top six most important features	
440	across all five momentum ranges.	190
441	8.25 Permutation importances for the ten most important features in the	
442	different momentum ranges (from left to right, top to bottom, in increasing	
443	momentum order). The bars indicate the effect that permutations of	
444	each feature have on the purity (blue) and the sensitivity (yellow), the	
445	translucent regions representing one standard deviation around the central	
446	value.	192
447	8.26 Values of the precision and sensitivity obtained for 10000 BDT hyperparameter	
448	configurations, for the momentum regions I, III and V.	195
449	8.27 Reliability diagrams for the BDT classifier used in the momentum range	
450	$0.3 \leq p < 0.8 \text{ GeV}/c$, both for the original (blue circles) and calibrated	
451	(yellow squares) responses. For reference, the response of a perfectly	
452	calibrated classifier is also shown (black dashed line).	197
453	8.28 Uncalibrated (left panel) and calibrated (right panel) predicted probabilities	
454	assigned by the BDT classifiers for true muons (blue) and charged pions	
455	(red) in the momentum range $0.3 \leq p < 0.8 \text{ GeV}/c$	198
456	8.29 Schematic of the hit selection used for the ToF measurement. The grid	
457	represents the layers of the inner ECal, with coloured squares indicating	
458	the tiles with hits. Green squares indicate the selected hits.	200
459	8.30 Particle velocity versus momentum measured with different ECal arrival	
460	time estimations. From left to right: earliest hit time, average hit time,	
461	and fitted hit time. In all cases the time resolution is $\Delta\tau = 0.1 \text{ ns}$	202

LIST OF FIGURES

462	8.31 Mass spectra for p (blue) and π^\pm (yellow) particles, using different ECal 463 time resolution values (from top to bottom, in ascending order), and 464 arrival time estimates. From left to right: earliest hit time, average hit 465 time, and fitted hit time. The dashed lines indicate the true masses of 466 the particles.	203
467	8.32 Efficiency (top panel) and purity (bottom panel) for the proton selection 468 as a function of the momentum, for $\Delta\tau = 0.10$ ns.	204
469	8.33 Distributions of the velocities measured by ToF with the inner ECal, for 470 different momentum bins, in a FHC neutrino interaction sample. The 471 Gaussian fits are performed around the maxima for each particle species.	205
472	8.34 Left panel: number of non-decaying, decaying and decaying in the fiducial 473 volume pions for a MC sample of 100000, $p = 500$ MeV/c isotropic 474 positively charged pions inside the TPC. Right panel: event display 475 for a positive pion decaying inside the fiducial volume, with a single 476 reconstructed track for the pion and muon system.	206
477	8.35 Values of $\chi_k^{2(FB)}$ (top left panel), F_k (top right panel), $D_k^{1/R}$ (bottom 478 left panel) and D_k^ϕ (bottom right panel) versus position along the drift 479 direction for a reconstructed track in a positive pion decay event. The 480 vertical red dashed line indicates the true location of the decay point. . .	208
481	8.36 Fractional residual distributions of the true and reconstructed decay 482 position along the drift coordinate, using the position of the maximum 483 of $\chi_k^{2(FB)}$ (left panel) and F_k (right panel) as estimates of the decay 484 position. Also shown are double Gaussian fits to these points (red lines).	209
485	8.37 Distributions of the extreme values of $\chi_k^{2(FB)}$ (top left panel), F_k (top 486 right panel), $D_k^{1/R}$ (bottom left panel) and D_k^ϕ (bottom right panel) for 487 non-decaying reconstructed pion tracks (blue) and tracks which include 488 the decay inside the fiducial volume (red).	211

LIST OF FIGURES

489	8.38 Left panel: distributions of the predicted probabilities assigned by the 490 BDT classifier to a test sample of decaying pion+muon tracks (blue) and 491 non-decaying pion tracks (red). Left: signal efficiency versus background 492 acceptance (ROC curve) obtained from the BDT for the test sample.	212
493	8.39 Left panel: dependence of the decay position finding resolution on the 494 true value of the decay angle for the $\chi_k^2(FB)$ (red) and F_k (blue) methods. 495 Right panel: signal efficiency (blue line) and background rejection (red 496 line) from the BDT classifier versus true decay angle.	212
497	8.40 Mean values of the F_1 -score marginal distributions for the different 498 free parameters of the new clustering algorithm, with the error bars 499 representing one standard deviation around the mean. The F_1 -score 500 values were computed for the 6561 possible parameter configurations 501 using 1000 ν_μ CC interaction events.	215
502	8.41 Left panel: distributions of the number of ECal clusters per photon from 503 π^0 decays for the standard (red) and new (blue) clustering algorithms. 504 Right panel: reconstructed invariant mass distributions for photon pairs 505 from single π^0 events using the standard (red) and new (blue) ECal 506 clustering algorithms.	217

507 List of Tables

508	2.1	Values of T_3 and $Y/2$ assigned to the first generation of fermions.	39
509	2.2	Neutral current couplings.	40
510	2.3	Summary of neutrino oscillation parameters determined in the Neutrino	
511		Global Fit of 2020 [16].	48
512	3.1	Summary of the two-phased plan for DUNE	53
513	3.2	Exposure and time required to achieve the different physics milestones of	
514		the two phases	54
515	6.1	<i>Characteristic parameters of the two monoenergetic muon events selected, relative to the U plane: projected angles in the xz' and $y'z'$ planes, S/N values for the raw and filtered waveforms, mean improvement of the S/N and peak asymmetry.</i>	105
519	8.1	Calibration parameters obtained from the fit of the ND-GAr simulated stopping proton sample to the calibration function, for different ADC limits.	161
520			
521	8.2	Momentum ranges and description of the PID approach assumed for the muon and pion classification task.	181
522			
523	8.3	Optimal values of the hyperparameters used by the BDT, for each momentum range.	196
524			
525	8.4	Performance metrics of the BDTs with optimal hyperparameters, for the different momentum ranges.	196
526			

LIST OF TABLES

527	8.5 Summary of parameters and sampled values used in the optimisation of	
528	the clustering algorithm.	215

529

⁵³⁰ **List of Abbreviations**

ADC	Analog to Digital Converter.
ALEPH	Apparatus for LEP PHysics.
ALICE	A Large Ion Collider Experiment.
BDT	Boosted Decision Tree.
CC	Charged Current.
DM	Dark Matter.
DUNE	Deep Underground Neutrino Experiment.
ECal	Electromagnetic Calorimeter.
FD	Far Detector.
FHC	Forward Horn Current.
HPgTPC	High Pressure gaseous Time Projection Chamber.
LBL	Long BaseLine.
MuID	Muon IDentification system.
NC	Neutral Current.
ND	Near Detector.
ND-GAr	Near Detector Gaseous Argon.
ND-LAr	Near Detector Liquid Argon.
PDG	Particle Data Group.
RHC	Reverse Horn Current.

⁵³¹ Chapter 1

⁵³² Introduction

533 Chapter 2

534 Neutrino physics

535 *Little particles of inspiration sleet through the universe all the time traveling
536 through the densest matter in the same way that a neutrino passes through a
537 candyfloss haystack, and most of them miss.*

538 – Terry Pratchett, *Sourcery*

539 Ever since they were postulated in 1930 by Wolfgang Pauli to explain the continuous
540 β decay spectrum [17] and later found by F. Reines and C. Cowan at the Savannah
541 River reactor in 1953 [18], neutrinos have had a special place among all other elementary
542 particles. They provide a unique way to probe a wide range of quite different physics,
543 from nuclear physics to cosmology, from astrophysics to colliders. Moreover, there is
544 compelling evidence to believe that the study of neutrinos may be key to unveil different
545 aspects of physics beyond the SM, difficult to test elsewhere.

546 In this Chapter, I will review the basics of neutrino physics, from its role within the
547 SM to the main open questions related to the neutrino sector, paying special attention
548 to the phenomenology of neutrino oscillations.

Chapter 2. Neutrino physics

549 2.1 Historical remarks

550 2.2 Neutrinos in the SM

551 The SM of fundamental interactions was initially proposed in 1967 by S. Glashow, S.
552 Weinberg and A. Salam[19–21]. This theoretical framework describes the dynamics of
553 leptons and quarks, by introducing one scalar particle, the Higgs boson. It assumes
554 that the local $SU(3) \times SU(2)_L \times U(1)_Y$ gauge symmetry is an internal symmetry of the
555 system, with $SU(3)$ describing quantum chromodynamics, and $SU(2)_L \times U(1)_Y$ being the
556 gauge groups of the electroweak sector. For a detailed overview of the SM of electroweak
557 interactions, see Ref. [22].

558 In the SM, neutrinos appear in three flavours, namely ν_e , ν_μ , and ν_τ . These are
559 associated with the corresponding charged leptons, e , μ , and τ . Neutrinos exist only
560 as left-handed particles, grouped in doublets with the charged leptons, while the later
561 come in both chirality states:

$$\begin{pmatrix} \nu_e \\ e_L^- \end{pmatrix}, \quad \begin{pmatrix} \nu_\mu \\ \mu_L^- \end{pmatrix}, \quad \begin{pmatrix} \nu_\tau \\ \tau_L^- \end{pmatrix}, \quad e_R^-, \quad \mu_R^-, \quad \tau_R^-. \quad (2.1)$$

562 Similarly, quarks also exist in both chirality states, and are grouped as:

$$\begin{pmatrix} u_L \\ d_L \end{pmatrix}, \quad \begin{pmatrix} s_L \\ c_L \end{pmatrix}, \quad \begin{pmatrix} t_L \\ b_L \end{pmatrix}, \quad u_R, \quad d_R, \quad s_R, \quad c_R, \quad t_R, \quad b_R. \quad (2.2)$$

563 The fact that there are no right-handed neutrino fields implies that neutrinos are
564 strictly massless within the SM. This restriction follows from the experimental observation
565 that all neutrinos produced via weak interactions are pure left-handed helicity states
566 (and similarly antineutrinos are pure right-handed states). The hypothetical existence
567 of right-handed neutrinos could be indirectly inferred from the observation of non-zero
568 neutrino masses, nevertheless the existence of neutrino masses is not a sufficient condition
569 for the existence of such fields.

570 Left and right-handed fermions transform differently under $SU(2)_L \times U(1)_Y$ rotations,

2.2. Neutrinos in the SM

Table 2.1: Values of T_3 and $Y/2$ assigned to the first generation of fermions.

	e_L	ν_e	e_R	u_L	d_L	u_R	d_R
T_3	-1/2	1/2	0	1/2	-1/2	0	0
$Y/2$	-1/2	-1/2	-1	1/6	1/6	2/3	-1/3

as the right-handed particles are singlets under $SU(2)_L$. Applying a local transformation,
they change as:

$$\begin{aligned}\psi_L &\longrightarrow e^{-iY\beta(x)/2} e^{-iT_a\alpha_a(x)} \psi_L, \\ \psi_R &\longrightarrow e^{-iY\beta(x)/2} \psi_R,\end{aligned}\tag{2.3}$$

where $Y/2$ and T_a are the generators of $SU(2)_L$ and $U(1)_Y$, respectively, and $\beta(x)$ and $\alpha_a(x)$ are the parameters of the rotation.

The values of the quantum numbers $Y/2$ and T_3 , the third component of the weak isospin, have to be assigned to the different particles. The values of T_3 follow from the commutation relations of the generators of $SU(2)$. After the spontaneous symmetry breaking $SU(2)_L \times U(1)_Y \rightarrow U(1)_{EM}$, one finds the relation which determines the electric charge:

$$Q = T_3 + \frac{Y}{2},\tag{2.4}$$

Setting the electric charge to -1 for electrons, we can find the values of the hypercharge for the rest of the fermions. The resulting values for the first generation of leptons and quarks are shown in Tab. 2.1.

It is clear that the free Lagrangian of the theory is not be invariant under the gauge transformations, as the kinetic terms contain derivatives. Therefore, to make it invariant, one needs to introduce a set of gauge bosons. They appear in the so-called covariant derivative, which replaces the common derivative and transforms in the same way as the fermion fields under local rotations. This constrain fixes completely the transformations of the spin-1 fields. For left and right-handed particles, the covariant derivatives are

Chapter 2. Neutrino physics

Table 2.2: Neutral current couplings.

	u	d	ν_e	e
$2v_f$	$1 - \frac{8}{3}\sin^2\theta_W$	$-1 + \frac{4}{3}\sin^2\theta_W$	1	$-1 + 4\sin^2\theta_W$
$2a_f$	1	-1	1	-1

given by:

$$\begin{aligned} D_\mu \psi_L &= \left(\partial_\mu + ig' \frac{Y}{2} B_\mu + ig T_a W_\mu^a \right) \psi_L, \\ D_\mu \psi_R &= \left(\partial_\mu + ig' \frac{Y}{2} B_\mu \right) \psi_R, \end{aligned} \quad (2.5)$$

where W_μ^i , $i = 1, 2, 3$ and B_μ are the gauge bosons for the $SU(2)_L$ and $U(1)_Y$ factors, respectively, and g and g' are the corresponding gauge couplings. It can be shown that these fields transform in the adjoint representation of the gauge group.

So far, the theory only contains massless particles, as adding bare mass terms to the Lagrangian would spoil the gauge symmetry. Therefore, the mass terms need to be induced by a spontaneous violation of the symmetries. In the SM, the responsible for this is the Higgs mechanism. The Higgs doublet is coupled to the gauge bosons through the covariant derivative, and to the fermions through the Yukawa couplings. Upon spontaneous symmetry breaking, the vacuum expectation value of the Higgs field generate the mass terms of the particles.

In order to obtain the physical intermediate vector boson states, we need to perform the following redefinitions:

$$\begin{aligned} A_\mu &= \sin \theta_W W_\mu^3 + \cos \theta_W B_\mu, \\ Z_\mu &= \cos \theta_W W_\mu^3 - \sin \theta_W B_\mu, \\ W_\mu^\pm &= \frac{1}{\sqrt{2}} (W_\mu^1 \mp i W_\mu^2), \end{aligned} \quad (2.6)$$

where A_μ is the photon field, and Z_μ and W_μ^\pm are the neutral and the charged weak boson fields, respectively. The Weinberg angle, θ_W , relates the weak coupling constants

2.3. Massive neutrinos

604 and the electric charge:

$$e = g' \cos \theta_W = g \sin \theta_W. \quad (2.7)$$

605 At this point, the interacting part of the electroweak Lagrangian can be re-written
 606 as the sum of three contributions: the electromagnetic (EM), charged-current (CC) and
 607 neutral-current (NC) components:

$$\begin{aligned} \mathcal{L}_{\text{EW}}^{\text{int}} &= \mathcal{L}_{\text{EM}} + \mathcal{L}_{\text{CC}} + \mathcal{L}_{\text{NC}} \\ &= -e A_\mu J_{\text{EM}}^\mu - \frac{g}{2\sqrt{2}} (W^+ J_{\text{CC}}^\mu + \text{h.c.}) - \frac{g}{2\cos\theta_W} Z_\mu J_{\text{NC}}^\mu, \end{aligned} \quad (2.8)$$

608 with the currents defined as:

$$\begin{aligned} J_{\text{EM}}^\mu &= \sum_f Q_f \bar{f} \gamma^\mu f, \\ J_{\text{CC}}^\mu &= \sum_\ell \bar{\nu}_\ell \gamma^\mu (1 - \gamma_5) \ell + \sum_f \bar{u}_f \gamma^\mu (1 - \gamma_5) d_f, \\ J_{\text{NC}}^\mu &= \sum_f \bar{f} \gamma^\mu (v_f - a_f \gamma_5) f, \end{aligned} \quad (2.9)$$

609 where f denotes any SM fermion, ℓ and ν_ℓ a charged lepton and a neutrino of any flavour,
 610 and u_f and d_f an up-like and a down-like quarks of any flavour. For the NC case, the
 611 values of the v_f and a_f couplings are given in Tab. 2.2.

612 As seen in Eq. (7.8), in the electroweak theory neutrinos are coupled to the Z boson
 613 in a universal way. Therefore, by measuring the so-called invisible decay width of the Z
 614 boson we have an estimate of the number of light (i.e. lighter than the Z boson) neutrino
 615 flavours. This number was measured by LEP in a combined analysis of $e^+ e^- \rightarrow \mu^+ \mu^-$
 616 and $e^+ e^- \rightarrow \text{hadrons}$ to be $N_\nu = 2.9840 \pm 0.0082$ [23].

617 2.3 Massive neutrinos

618 The existence of neutrino oscillations imply . However, as we have seen before, within
 619 the SM neutrinos are massless, as they do not have a mass term in the Lagrangian. If
 620 one wants to give neutrinos a mass, the particle content of the SM needs to be expanded.

Chapter 2. Neutrino physics

621 A way of generating massive neutrinos while maintaining gauge invariance is by
 622 introducing an arbitrary number of sterile neutrinos $N_i, i = 1, \dots, m$. These allow for
 623 two different types of neutrino mass terms:

$$-\mathcal{L}_{M_\nu} = \sum_{i=1}^m \sum_{j=1}^3 M_D^{ij} \bar{N}_i \nu_{Lj} + \frac{1}{2} \sum_{i=1}^m \sum_{j=1}^m M_N^{ij} \bar{N}_i N_j^c + \text{h.c.}, \quad (2.10)$$

624 where M_D is a complex $m \times 3$ matrix and M_N a complex, symmetric $m \times m$ matrix.
 625 The first term, often referred to as the Dirac mass term, arises from the corresponding
 626 Yukawa interaction after the spontaneous electroweak symmetry breaking, similar to
 627 the other fermions. The second term, called the Majorana mass term, is allowed in the
 628 Lagrangian, as it is a singlet of the gauge group. However, it violates lepton number
 629 conservation by two units.

630 If one imposes lepton number symmetry conservation, the Majorana term must
 631 banish, $M_N = 0$. In this case, if $m = 3$ we can identify the sterile neutrinos as the
 632 right-handed component of the neutrino field. The Dirac mass matrix can be diagonalised
 633 using two unitary matrices, V_R^ν and V_L^ν , as:

$$M_D = V_R^\nu \text{ diag}(m_1, m_2, m_3) V_L^{\nu\dagger}, \quad (2.11)$$

634 where $m_i, i = 1, 2, 3$ are the masses of the three neutrino mass eigenstates.

635 The neutrino mass term can be written in term of the resulting eigenstates as:

$$-\mathcal{L}_{M_\nu} = \sum_{i=1}^3 m_i \bar{\nu}_{Di} \nu_{Di}, \quad (2.12)$$

636 with:

$$\nu_{Di} = \left(V_L^{\nu\dagger} \nu_L \right)_i + \left(V_R^{\nu\dagger} N \right)_i. \quad (2.13)$$

637 In this scenario, both the low energy particle budget and the symmetries of the SM
 638 have to be modified. Moreover, the masses of the neutrinos are generated exclusively
 639 through the Higgs mechanism, which does not explain why they are much smaller than

2.3. Massive neutrinos

640 those of the charged leptons.

641 Going back to the general case, we can re-write Eq. (2.10) in matrix form as:

$$-\mathcal{L}_{M_\nu} = \frac{1}{2} (\bar{\nu}_L^c, \bar{N}) \begin{pmatrix} 0 & M_D^T \\ M_D & M_N \end{pmatrix} \begin{pmatrix} \nu_L \\ N^c \end{pmatrix} + \text{h.c.} = \bar{\nu}^c M_\nu \nu + \text{h.c.}, \quad (2.14)$$

642 with $\nu = (\nu_L, N^c)^T$ being a $(3+m)$ -dimensional vector grouping the active and the
643 sterile neutrinos. The matrix M_ν , which is a complex $(3+m) \times (3+m)$ symmetric
644 matrix, can be diagonalised by means of a unitary matrix V^ν , yielding:

$$M_\nu = V^\nu \text{ diag}(m_1, m_2, \dots, m_{3+m}) V^{\nu\dagger}. \quad (2.15)$$

645 Using this eigendecomposition, the neutrino mass term can be expressed as:

$$\begin{aligned} -\mathcal{L}_{M_\nu} &= \frac{1}{2} \sum_{i=1}^{3+m} m_i \left[(\bar{\nu}^c V^\nu)_i (V^{\nu\dagger} \nu)_i + (\bar{\nu} V^\nu)_i (V^{\nu\dagger} \nu^c)_i \right] \\ &= \frac{1}{2} \sum_{i=1}^{3+m} m_i \bar{\nu}_{Mi} \nu_{Mi}, \end{aligned} \quad (2.16)$$

646 where the states ν_{Mi} , commonly referred to as Majorana neutrinos, are defined as:

$$\nu_{Mi} = (V^{\nu\dagger} \nu)_i + (V^{\nu\dagger} \nu^c)_i^c, \quad (2.17)$$

647 in such a way that the Majorana condition, $\nu_M^c = \nu_M$, holds true.

648 As a consequence of the Majorana condition, the neutrino and the antineutrino states
649 can be described in terms of a single field. As opposed to the charged leptons, which
650 need to be represented by a four-component or Dirac spinor, the Majorana neutrino is
651 described by a two-component or Weyl spinor.

652 If the eigenvalues of the Majorana mass matrix, M_N , are much larger than the
653 electroweak symmetry breaking scale, the diagonalisation of M_ν leads to 3 light and m
654 heavy neutrino states:

$$-\mathcal{L}_{M_\nu} = \frac{1}{2} \bar{\nu}_l M_l \nu_l + \frac{1}{2} \bar{\nu}_h M_h \nu_h, \quad (2.18)$$

Chapter 2. Neutrino physics

2.4 Neutrino oscillations

The evidence for neutrino oscillation [24], and therefore the existence of non-zero neutrino masses, constitutes one of the groundbreaking discoveries of modern Physics and has acted as driving force for Beyond the Standard Model (BSM) Physics. The minimal extension of the Standard Model (SM) we can do to address these phenomena is introducing distinct masses for at least two of the neutrinos. This way, we are left with three neutrino mass eigenstates ν_1 , ν_2 and ν_3 , with masses m_1 , m_2 and m_3 respectively, which in general will not coincide with the flavour eigenstates ν_e , ν_μ and ν_τ .

The way to relate these two sets of neutrino eigenstates is via a 3×3 unitary matrix, called the Pontecorvo-Maki-Nakagawa-Sakata (PMNS) matrix [25, 26], as:

$$|\nu_\alpha\rangle = \sum_{i=1}^3 U_{\alpha i}^* |\nu_i\rangle, \quad (2.19)$$

where the Greek index α denotes the flavour $\{e, \mu, \tau\}$ and the Latin index i the associated masses $\{1, 2, 3\}$. This leptonic mixing matrix may be parametrized in terms of 6 parameters, 3 of which are mixing angles θ_{12} , θ_{13} and θ_{23} , one CP-violating phase δ_{CP} and 2 Majorana phases α and β :

$$U = \begin{pmatrix} 1 & 0 & 0 \\ 0 & c_{23} & s_{23} \\ 0 & -s_{23} & c_{23} \end{pmatrix} \begin{pmatrix} c_{13} & 0 & s_{13}e^{-i\delta_{CP}} \\ 0 & 1 & 0 \\ -s_{13}e^{-i\delta_{CP}} & 0 & c_{13} \end{pmatrix} \begin{pmatrix} c_{12} & s_{12} & 0 \\ -s_{12} & c_{12} & 0 \\ 0 & 0 & 1 \end{pmatrix} \begin{pmatrix} 1 & 0 & 0 \\ 0 & e^{i\alpha} & 0 \\ 0 & 0 & e^{i\beta} \end{pmatrix}, \quad (2.20)$$

where $c_{ij} \equiv \cos \theta_{ij}$ and $s_{ij} \equiv \sin \theta_{ij}$. This matrix is analogous to the Cabibbo-Kobayashi-Maskawa (CKM) matrix in the quark sector. If neutrinos are Dirac fermions, we can drop the Majorana phases in the PMNS matrix. But, in any case, these phases play no role on the neutrino oscillations.

2.4. Neutrino oscillations

2.4.1 Oscillations in vacuum

Consider the case where a neutrino of flavour α is produced at $t = 0$, and then it propagates through vacuum. Such a state will evolve in time according to the relation:

$$|\nu_\alpha(t)\rangle = \sum_{i=1}^3 U_{\alpha i}^* e^{-iE_i t} |\nu_i(t=0)\rangle, \quad (2.21)$$

as the mass eigenstates are also eigenstates of the free Hamiltonian. Now, if we express the mass eigenstates as a superposition of flavour eigenstates, the last expression can be rewritten as:

$$|\nu_\alpha(t)\rangle = \sum_{i=1}^3 U_{\beta i} e^{-iE_i t} U_{\alpha i}^* |\nu_\beta\rangle. \quad (2.22)$$

This way, the probability for the neutrino to transition from flavour α to flavour β will be given by:

$$P(\nu_\alpha \rightarrow \nu_\beta) = |\langle \nu_\beta | \nu_\alpha(t) \rangle|^2 = \left| \sum_{i=1}^3 U_{\beta i} e^{-iE_i t} U_{\alpha i}^* \right|^2. \quad (2.23)$$

A usual approximation to take at this point is to consider ultra-relativistic neutrinos, i.e. $E \approx |\vec{p}|$, so we can write the dispersion relations as:

$$E_i = \sqrt{p^2 + m_i^2} \approx E + \frac{m_i^2}{2E}, \quad (2.24)$$

so we can write the oscillation probability as:

$$\begin{aligned} P(\nu_\alpha \rightarrow \nu_\beta) &= \sum_{i,j} U_{\alpha i}^* U_{\beta i} U_{\alpha j} U_{\beta j}^* e^{-i \frac{\Delta m_{ij}^2}{2E} t} \\ &= \delta_{\alpha\beta} - 4 \sum_{i < j} \Re [U_{\alpha i}^* U_{\beta i} U_{\alpha j} U_{\beta j}^*] \sin^2 \left(\frac{\Delta m_{ij}^2}{4E} t \right) \\ &\quad + 2 \sum_{i < j} \Im [U_{\alpha i}^* U_{\beta i} U_{\alpha j} U_{\beta j}^*] \sin \left(\frac{\Delta m_{ij}^2}{2E} t \right), \end{aligned} \quad (2.25)$$

where Δm_{ij}^2 is the difference of the squared masses of the j th and i th neutrino mass eigenvalues. At this point, it is usual to write the phase responsible for the oscillations

Chapter 2. Neutrino physics

686 as (under the approximate assumption $t \approx L$):

$$\Delta_{ij} \equiv \frac{\Delta m_{ij}^2}{4E} L \simeq 1.27 \frac{\Delta m_{ij}^2}{(\text{eV}^2)} \frac{L}{(\text{km})} \frac{(\text{GeV})}{E}. \quad (2.26)$$

687 Notice that, in the case of antineutrinos the only difference would be the sign of the
688 last term in the oscillation probability. This way, one can write the CP asymmetry as:

$$\begin{aligned} A_{CP}^{\alpha\beta} &= P(\nu_\alpha \rightarrow \nu_\beta) - P(\bar{\nu}_\alpha \rightarrow \bar{\nu}_\beta) \\ &= 4 \sum_{i < j} \Im \left[U_{\alpha i}^* U_{\beta i} U_{\alpha j} U_{\beta j}^* \right] \sin 2\Delta_{ij}. \end{aligned} \quad (2.27)$$

689 2.4.2 Oscillations in matter

690 When neutrinos propagate through matter, their oscillation can be affected in mainly
691 two ways. First, neutrinos can inelastically scatter with nuclei, thus destroying the
692 coherent propagation of their quantum state. Nevertheless, in most cases this effect is
693 negligible (even in very dense mediums like the core of the Sun). Second, neutrinos can
694 also experience coherent or forward scatterings, that can affect their oscillation but not
695 lose the coherent propagation of the state.

696 The first proposed model to account for neutrino oscillations in matter was proposed
697 by Mikhaev, Smirnov and Wolfenstein (MSW) [27]. It relies on the fact that, as the
698 only charged lepton present in ordinary matter is the electron, electron neutrinos can
699 undergo both charged and neutral-current interactions with matter whereas for muon
700 and tau neutrinos just neutral currents are possible.

701 2.4.3 Current status of neutrino oscillations

702 A wide range of neutrino experiments provide experimental input to the neutrino
703 oscillation framework, both using natural or synthetic neutrino sources. The results
704 from one of the neutrino global fit analyses, shown in Tab. 2.3¹, summarise well our
705 current understanding of the different oscillation parameters.

¹These are the results reported during M. Tórtola's talk at Neutrino 2024 (see this link). I need to keep an eye and see if they publish these or other updated results in the near future.

2.5. Open questions in the neutrino sector

706 **Solar neutrino experiments** detect neutrinos produced in thermonuclear reactions
707 inside the Sun, mainly from the so-called *pp* chain and the CNO cycle. These neutrinos
708 have a typical energy in the range from 0.1 to 20 MeV. These experiments (Homestake
709 [28], GALLEX [29], SAGE [30], Borexino [31], Super-Kamiokande [32] and SNO [33])
710 provide the best sensitivities to θ_{12} and Δm_{21}^2 .

711 **Atmospheric neutrino experiments** detect the neutrino flux produced when
712 cosmic rays scatter with particles in Earth's atmosphere. These collisions generate particle
713 showers that eventually produce electron and muon neutrinos (and antineutrinos). Their
714 energies range from few MeV to about 10^9 GeV. Experiments, like Super-Kamiokande
715 [34] and IceCube [35] use atmospheric neutrinos to measure oscillations and are specially
716 sensitive to θ_{23} and Δm_{32}^2 .

717 **Reactor neutrino experiments** look for the $\bar{\nu}_e$ spectrum produced by nuclear
718 reactors, with energies in the MeV scale. Depending on the distance to the source,
719 long-baseline experiments like KamLAND [36] are sensitive to the solar mass splitting
720 Δm_{21}^2 whereas much shorter baseline experiment such as RENO [37] or DayaBay [38]
721 measure θ_{13} and Δm_{31}^2 .

722 **Accelerator experiments** measure neutrino fluxes generated in particle accelerators.
723 Usually mesons are produced in the accelerator to be focused into a beam, then some
724 decay to muon neutrinos and the rest are absorbed by a target. Depending on the
725 configuration one can obtain a beam made of mostly neutrinos or antineutrinos. The
726 typical energies of these neutrinos are in the GeV range. Experiments such as NOvA
727 [39], T2K [40], MINOS [41], OPERA [42] and K2K [43] (and in the future DUNE [44])
728 are primarily sensitive to θ_{13} , θ_{23} and Δm_{32}^2 . Also, in the coming years DUNE [44] and
729 Hyper-Kamiokande [45] will be sensitive to δ_{CP} .

730 2.5 Open questions in the neutrino sector

731 A crucial question that remains open these days, and is of vital importance for oscillation
732 phenomena, is whether the mass eigenvalue ν_3 is the heaviest (what we call normal

Chapter 2. Neutrino physics

Table 2.3: Summary of neutrino oscillation parameters determined in the Neutrino Global Fit of 2020 [16].

Parameter	Best fit $\pm 1\sigma$	3σ range
Δm_{21}^2 [eV $^2 \times 10^{-5}$]	$7.55^{+0.22}_{-0.20}$	6.98 – 8.19
$ \Delta m_{31}^2 $ [eV $^2 \times 10^{-3}$] (NO)	$2.51^{+0.02}_{-0.03}$	2.43 – 2.58
$ \Delta m_{31}^2 $ [eV $^2 \times 10^{-3}$] (IO)	$2.41^{+0.03}_{-0.02}$	2.34 – 2.49
$\sin^2 \theta_{12}/10^{-1}$	3.04 ± 0.16	2.57 – 3.55
$\sin^2 \theta_{23}/10^{-1}$ (NO)	$5.64^{+0.15}_{-0.21}$	4.23 – 6.04
$\sin^2 \theta_{23}/10^{-1}$ (IO)	$5.64^{+0.15}_{-0.18}$	4.27 – 6.03
$\sin^2 \theta_{13}/10^{-2}$ (NO)	$2.20^{+0.05}_{-0.06}$	2.03 – 2.38
$\sin^2 \theta_{13}/10^{-2}$ (IO)	$2.20^{+0.07}_{-0.04}$	2.04 – 2.38
δ_{CP}/π (NO)	$1.12^{+0.16}_{-0.12}$	0.76 – 2.00
δ_{CP}/π (IO)	$1.50^{+0.13}_{-0.14}$	1.11 – 1.87

ordering) or the lightest (referred to as inverted ordering) of the mass eigenstates. In other words, this means that we do not know the sign of Δm_{32}^2 , so we can either have $m_1 < m_2 < m_3$ (NO) or $m_3 < m_1 < m_2$ (IO).

Another big puzzle is related to the value of δ_{CP} . Nowadays it is poorly constrained, with all values between π and 2π being consistent with data. A prospective measurement different from $\delta_{CP} = 0, \pi$ will predict CP-violation in the leptonic sector, and thus contribute along with the one measured in the quark sector to the total amount of CP-violation. Although it is true that these two contributions by themselves are not enough to explain the matter anti-matter asymmetry in our universe, the amount of CP-violation in the leptonic sector can be key to explain such imbalance.

Both of these questions, because of their nature, could be understood thanks to future oscillation experiments.

Notwithstanding, there are other mysteries that can not be unveiled just by conducting oscillation experiments, as certain quantities do not influence these phenomena. Among these there is the question of the absolute values of the neutrino masses. Depending on the value of the lightest of the neutrino masses we can have different mass spectra, from hierarchical $m_1 \ll m_2 < m_3$ (NO) or $m_3 \ll m_1 < m_2$ (IO) to quasi-degenerate

2.6. Neutrino interactions

750 $m_1 \simeq m_2 \simeq m_3$.

751 Other open question concerns the nature itself of the neutrinos. If neutrinos are Dirac
752 particles then their mass term can be generated through the usual Higgs mechanism
753 by adding right-handed neutrino fields. However, if they are Majorana particles and
754 therefore their own antiparticles, there is no need to add extra fields to have the mass
755 term in the Lagrangian. Experiments like SuperNEMO [46], SNO+ [47] and NEXT
756 [48], which search for neutrino-less double beta decay, will be able to determine whether
757 neutrinos are Dirac or Majorana.

758 2.6 Neutrino interactions

759 **Chapter 3**

760 **The Deep Underground Neutrino
761 Experiment**

762 The Deep Underground Neutrino Experiment (DUNE) is a next generation long-baseline
763 neutrino experiment [1]. It will aim to address several questions in neutrino physics,
764 study neutrinos from astrophysical sources and search for beyond the standard model
765 physics.

766 This chapter reviews the main goals of the DUNE experiment, the design of the far
767 detector modules and their data acquisition (DAQ) system, and the role that the near
768 detector plays in the physics program of DUNE.

769 **3.1 Overview**

770 The main physics goals of DUNE are:

- 771 • measure the neutrino mass hierarchy, the amount of CP violation in the leptonic
772 sector and the θ_{23} octant,
- 773 • detect rare low energy neutrino events, like neutrinos from supernova bursts, and
- 774 • search for proton decay and other beyond the standard model phenomena.

Chapter 3. The Deep Underground Neutrino Experiment

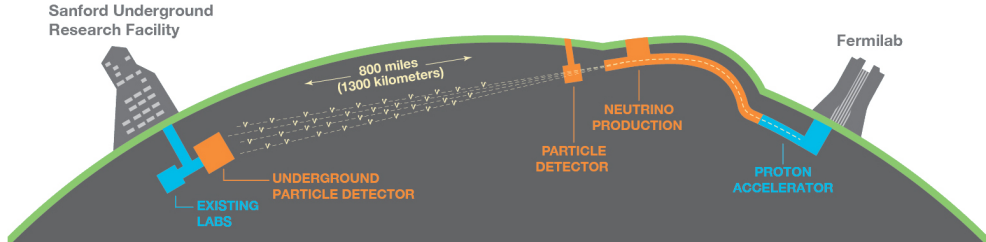


Figure 3.1: Schematic diagram of the DUNE experiment and the LBNF beamline [1].

775 The design of DUNE has bee tailored with these goals in mind. It will consist
776 of two neutrino detectors. A near detector (ND) complex will be placed in Fermilab,
777 574 m downstream of the neutrino production point, whereas a larger far detector (FD)
778 will be built in the Sandford Underground Research Facility (SURF), South Dakota,
779 approximately 1300 km away. Fig. 3.1 shows a simplified view of the various components
780 of DUNE (not to scale).

781 The beam neutrinos to be used in DUNE will be provided by the LBNF beamline,
782 the multi-megawatt wide-band neutrino beam planned for Fermilab. First, an intense
783 proton beam is extracted from the Fermilab Main Injector. Then, these protons with
784 energies between 60 GeV and 120 GeV collide with a high-power production target and
785 produce charged mesons. Two magnetic horns allow to focus the mesons and perform a
786 sign selection (thus having the capability to switch between neutrino and antineutrino
787 mode). Soon after that, the mesons decay and produce neutrinos (or antineutrinos)
788 which are then aimed to SURF.

789 Before arriving to the FD, the neutrino beam meets the ND complex, which serves as
790 the experiment's control. Its role is to measure the unoscillated neutrino energy spectra.
791 From these we can predict the unoscillated spectra at the FD, which can be compared to
792 the spectra measured at the FD in order to extract the oscillation parameters. Therefore,
793 the design of the DUNE ND is mainly driven by the needs of the oscillation physics
794 program.

795 The liquid Argon time projection chamber (LArTPC) technology has been chosen for

3.2. Physics goals of DUNE

Table 3.1: Summary of the two-phased plan for DUNE. Adapted from Ref. [49].

Parameter	Phase I	Phase II	Benefit
FD mass	20 kt fiducial	40 kt fiducial	FD statistics
Beam power	up to 1.2 MW	2.4 MW	FD statistics
ND config.	ND-LAr, TMS, SAND	ND-LAr, ND-GAr, SAND	Systematic constraints

796 the FD modules of DUNE. Its four modules will record neutrino interactions from the
 797 accelerator-produced beam arriving at predictable times. As it also aims at recording
 798 rare events, the FD requires trigger schemes which can deal with both kinds of physics,
 799 and also maximum uptime.

800 DUNE is planned to be built using a staged approach consisting on two phases,
 801 which are summarised in Tab. 3.1. Phase I consists of a FD with 50% of the total
 802 fiducial mass, a reduced version of the ND complex and a 1.2 MW proton beam. It will
 803 be sufficient to achieve some early physics goals, like the determination of the neutrino
 804 mass ordering. For its Phase II, DUNE will feature the full four FD modules, a more
 805 capable ND and a 2.4 MW proton beam. The physics milestones for the two phases are
 806 given in Tab. 3.2, in a staging scenario which assumes that Phase II is completed after
 807 6 years of operation.

808 A summary of the DUNE science program can be found in the DUNE FD Technical
 809 Design Report (TDR) Volume I [1]. For a detailed discussion on the two-phased approach
 810 the reader is referred to the DUNE Snowmass 2021 report [49].

811 3.2 Physics goals of DUNE

812 As noted in the literature (see for instance Ref. [16] for a review), the parameter space of
 813 the neutrino oscillation phenomena within the three-flavour picture is quite constrained
 814 by current experimental data. However, there are still crucial open questions, like the
 815 mass ordering, the value of δ_{CP} or the θ_{13} octant. One of the main goals of DUNE is to
 816 shed some light on the values of these parameters [50].

817 To address these questions DUNE can look to the subdominant oscillation channel
 818 $\nu_\mu \rightarrow \nu_e$ ($\bar{\nu}_\mu \rightarrow \bar{\nu}_e$) and study the energy dependence of the ν_e ($\bar{\nu}_e$) appearance probability.

Chapter 3. The Deep Underground Neutrino Experiment

Table 3.2: Exposure and time required to achieve the different physics milestones of the two phases. The predictions assume a Phase II staging scenario where FD modules 3 and 4 are deployed in years 4 and 6 and both the beam and ND are upgraded after 6 years. Adapted from Ref. [49].

Stage	Physics milestone	Exposure (kt-MW-years)	Years (staged)
Phase I	5σ MO ($\delta_{CP} = -\pi/2$)	16	1-2
	5σ MO (100% of the δ_{CP} values)	66	3-5
	3σ CPV ($\delta_{CP} = -\pi/2$)	100	4-6
Phase II	5σ CPV ($\delta_{CP} = -\pi/2$)	334	7-8
	δ_{CP} resolution of 10 degrees ($\delta_{CP} = 0$)	400	8-9
	5σ CPV (50% of the δ_{CP} values)	646	11
	3σ CPV (75% of the δ_{CP} values)	936	14
	$\sin^2(2\theta_{13})$ resolution of 0.004	1079	16

819 When we focus on the antineutrino channel $\bar{\nu}_\mu \rightarrow \bar{\nu}_e$ there is a change in the sign of δ_{CP} ,
 820 thus introducing CP-violation. Moreover, due to the fact that there are no positrons in
 821 the composition of Earth, there is a sign difference for the matter effect contribution
 822 when looking to the antineutrino channel. This asymmetry is proportional to the baseline
 823 length L and is sensitive to the sign of Δ_{31} , and thus to the neutrino mass ordering.

824 Another of the main physics goals of DUNE is the search for baryon-number violating
 825 processes. Specifically, it will try to answer the question of whether protons are stable
 826 or not. There is no symmetry argument that forbids protons from decaying, but its
 827 apparent stability seems to suggest that baryon number is conserved [51]. However,
 828 proton decay is a usual feature of grand-unified theories, where electromagnetic, weak
 829 and strong interactions are unified above a certain energy scale [52].

830 As the energy deposition scale for this kind of searches is nearly the same as the one
 831 for long-baseline neutrino oscillations, DUNE will be able to look for them. It has several
 832 advantages over other experiments, such as excellent imaging and particle identification,
 833 which can be translated to lower backgrounds.

834 The last of the main objectives of DUNE is the detection of neutrinos originated in
 835 supernovae explosions, what is called a supernova neutrino burst (SNB). These neutrinos
 836 carry with them information about the core-collapse process, from the progenitor to the
 837 explosion and the remnant; but also may have information about new exotic physics. So
 838 far, the only neutrino events ever recorded from such a process were a few dozens of $\bar{\nu}_e$

3.3. Far Detector

839 events from the 1987A supernova located in the Magellanic Cloud, 50 kpc away from
840 Earth [53, 54].

841 DUNE aims to collect also some SNB events. Although these are quite rare, as the
842 expected supernovae explosion events are about one every few decades for our galaxy
843 and Andromeda, the long lifetime of the experiment (around a few decades as well)
844 makes it reasonable to expect some. Nowadays the main sensitivity to SNB of most
845 experiments is to the $\bar{\nu}_e$ through inverse beta decay. One of the advantages of DUNE is
846 its expected sensitivity to ν_e , since the dominant channel will be ν_e CC scattering.

847 Moreover, due to the stringent requirements that the main physics goals set for
848 DUNE, it will allow also to perform searches for all kind of BSM physics. Among
849 others, DUNE will be able to look for: active-sterile neutrino mixing, non-unitarity of
850 the PMNS matrix, non-standard interactions, Lorentz and CPT violations, neutrino
851 trident production, light-mass DM, boosted DM and heavy neutral leptons. The reader
852 is referred to the DUNE FD TDR Volume II [50] for a full discussion of the physics
853 scope of DUNE.

854 3.3 Far Detector

855 The so-called DUNE FD complex will sit 1.5 km underground at SURF, South Dakota.
856 Two caverns will host the four FD modules, two of them per cavern, each embedded in
857 cryostats of dimensions 18.9 m (w) \times 17.8 m (h) \times 65.8 m (l). A central, smaller cavern
858 will host the cryogenic system.

859 Three out of the four modules will be liquid argon (LAr) time projection chamber
860 detectors, often refer to as LArTPCs, with a LAr fiducial mass of at least 10 kt each.
861 The first and second FD modules, FD-1 and FD-2, will use a Horizontal Drift (HD)
862 technology, whereas the third module, FD-3, will have a Vertical Drift (VD) direction.
863 The technology for the fourth module is still to be decided,

864 For each event, with energies ranging from a few MeV to several GeV, these detectors
865 collect both the scintillation light and the ionisation electrons created when the charged

Chapter 3. The Deep Underground Neutrino Experiment

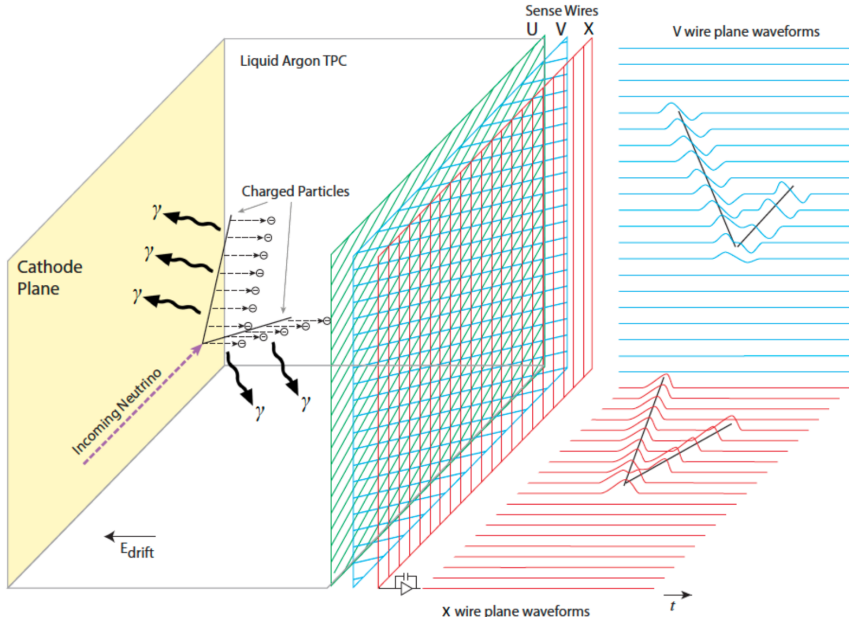


Figure 3.2: Schematic diagram showing the operating principle of a LArTPC with wire readout. Figure taken from Ref. [1].

866 particles produced in neutrino-nucleus interactions ionise the argon nuclei. In both HD
 867 and VD designs the characteristic 128 nm scintillation light of argon is collected by a
 868 photon detection system (PDS). This light will indicate the time at which electrons
 869 start to drift, thus enabling reconstruction over the drift coordinate when compared
 870 to the time when the first ionisation electron arrives to the anode. Reconstruction of
 871 the topology in the transverse direction is achieved using the charge readout. Fig. 3.2
 872 illustrates the detection principle described, for the case of a HD detector with a wire
 873 readout.

874 3.3.1 Horizontal Drift

875 Within the HD design the ionisation electrons produced as charged particles traverse the
 876 LAr drift horizontally towards the anode planes, made out of three layers of wire readout,
 877 due to the effect of an electric field. This design, previously known as single-phase (SP),
 878 was tested by the ProtoDUNE-SP detector at CERN. The prototype collected data from
 879 a hadron beam and cosmic rays, providing high-quality data sets for calibration studies
 880 and proving the excellent performance of this design.

3.3. Far Detector

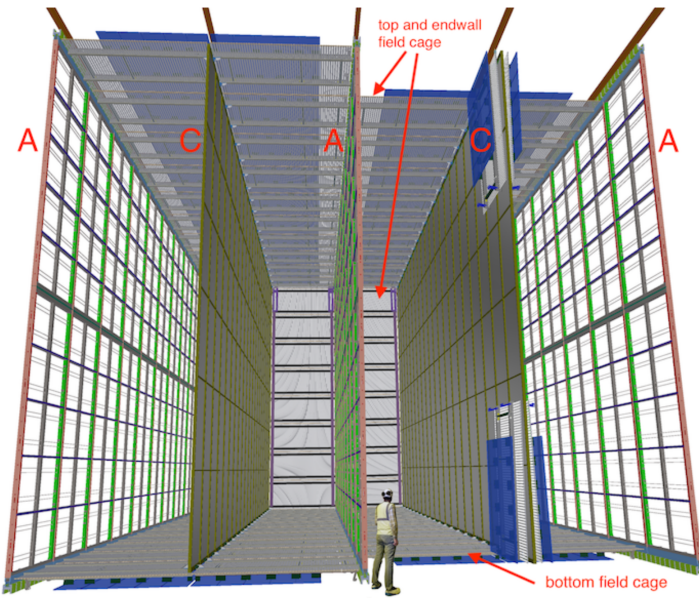


Figure 3.3: Proposed design for the FD-1 and FD-2 modules following the HD principle. Figure taken from Ref. [1].

881 Each FD HD detector module is divided in four drift regions, with a maximum drift
 882 length of 3.5 m, by alternating anode and cathode walls. The surrounding field cage
 883 ensures the uniformity of the 500 V/cm horizontal electric field across the drift volumes.
 884 The three anode walls, which constitute the charge readout of the detector, are built by
 885 stacking anode plane assemblies (APAs), 2 high times 25 wide. The design of the HD
 886 modules is shown in Fig. 3.3.

887 Each APA is made of 2560 active wires arranged in three layers, plus an extra grid
 888 layer, wrapped around a metal frame. The two induction wire planes, U and V, sit at
 889 $\pm 35.7^\circ$ to the vertical on each side of the APA. The collection and shielding plane wires,
 890 X and G, run parallel to the vertical direction. The ionisation electrons drift past the
 891 induction planes, generating bipolar signals on those wires, and are collected by the
 892 collection plane, producing a monopolar positive signal. The spacing between the wires
 893 is ~ 5 mm, and it defines the spatial resolution of the APA.

894 The front-end readout electronics, or cold electronics as they are immerse in the LAr,
 895 are attached to the top of the up APAs and the bottom of the down APAs. Mounted on
 896 the front-end mother boards we have a series of ASICs that digitize the signals from the

Chapter 3. The Deep Underground Neutrino Experiment

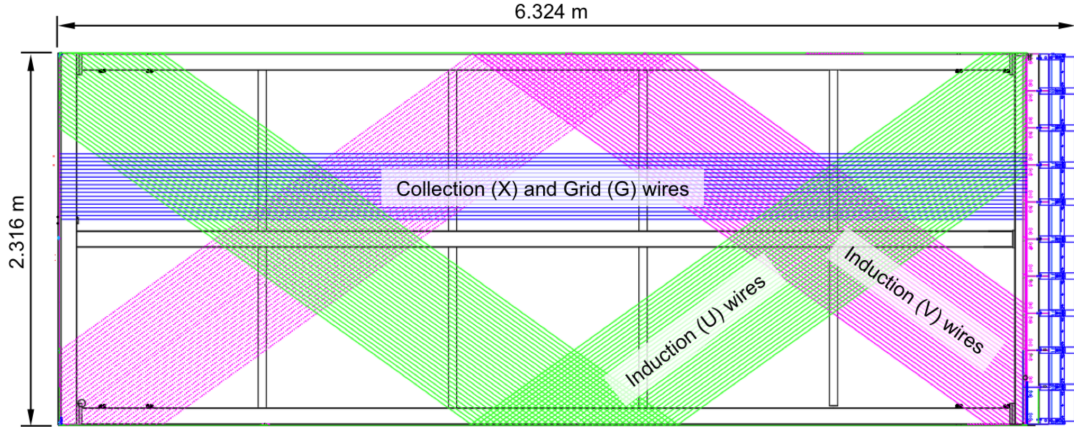


Figure 3.4: Schematic representation of an APA. The black lines represent the APA steel frame. The green and magenta lines correspond to the direction of the U and V induction wires respectively. The blue lines indicate the direction of the X collection wires and the wire shielding G. Figure taken from Ref. [1].

897 collection and induction planes. Each wire signal goes to a charge-sensitive amplifier,
 898 then there is a pulse-shaping circuit and this is followed by the analogue-to-digital
 899 converter. This part of the process happens inside the LAr to minimise the number of
 900 cables penetrating the cryostat. The digitised signals come out finally via a series of
 901 high-speed serial links to the warm interface boards (WIBs), from where the data is sent
 902 to the back-end DAQ through optical fibers.

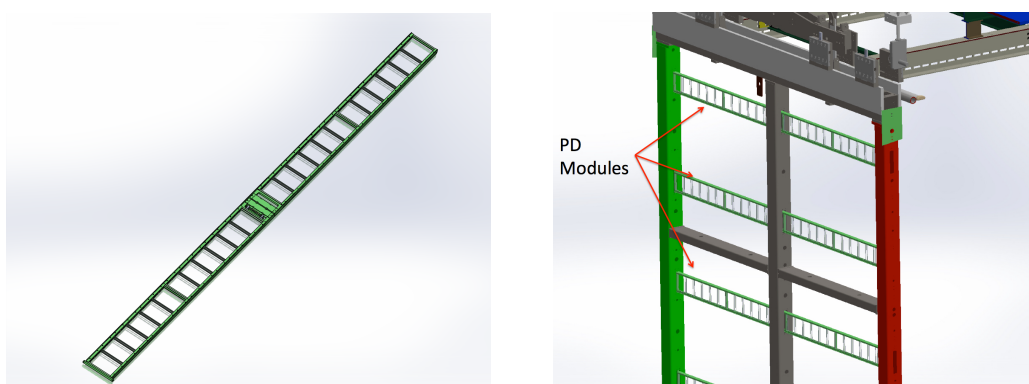


Figure 3.5: A PDS module containing 24 X-ARAPUCAs (left) and the location of the modules on the APAs (right). Figure taken from Ref. [1].

903 The PDS uses modules of X-ARAPUCA devices, mounted on the APA frames
 904 between the wire planes. Each X-ARAPUCA consists of layers of dichroic filter and

3.3. Far Detector

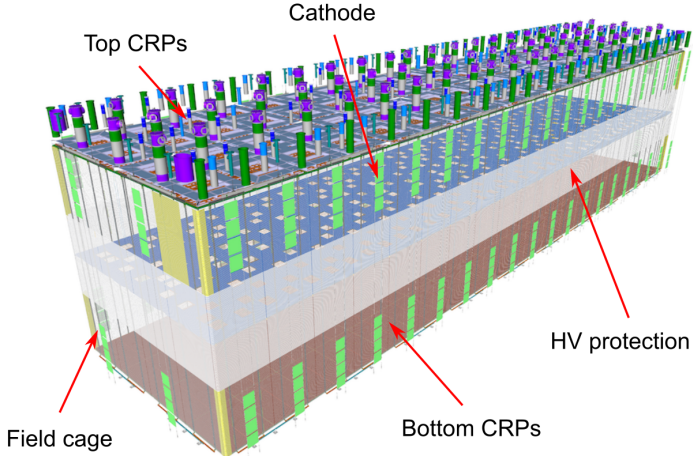


Figure 3.6: Proposed design for the FD-3 module following the VD principle. Figure adapted from Ref. [55].

wavelength-shifter. They shift the VUV scintillation light into the visible spectrum, sending then the visible photons to silicon photomultiplier (SiPM) devices. The PDS modules are $209\text{ cm} \times 12\text{ cm} \times 2\text{ cm}$ bars, containing 24 X-ARAPUCAs. There are 10 of these PDS modules per APA. Fig. 3.5 shows a PDS module (left) and the placement of the modules on the APAs (right).

3.3.2 Vertical Drift

In the VD case the ionisation electrons will drift vertically until they meet a printed circuit board-based (PCB) readout plane. It is based on the original dual-phase (DP) design deployed at CERN, known as ProtoDUNE-DP, used a vertical drift design with an additional amplification of the ionization electrons using a gaseous argon (GAr) layer above the liquid phase. The VD module incorporates the positive features of the DP design without the complications of having the LAr-GAr interface.

The current design of the FD VD module counts with two drift chambers with a maximum drift distance of 6.5 cm. A cathode plane splits the detector volume along the drift direction while the two anode planes are connected to the bottom and top walls of the detector. The layout of the VD module is shown in Fig. 3.6. Compared with

Chapter 3. The Deep Underground Neutrino Experiment

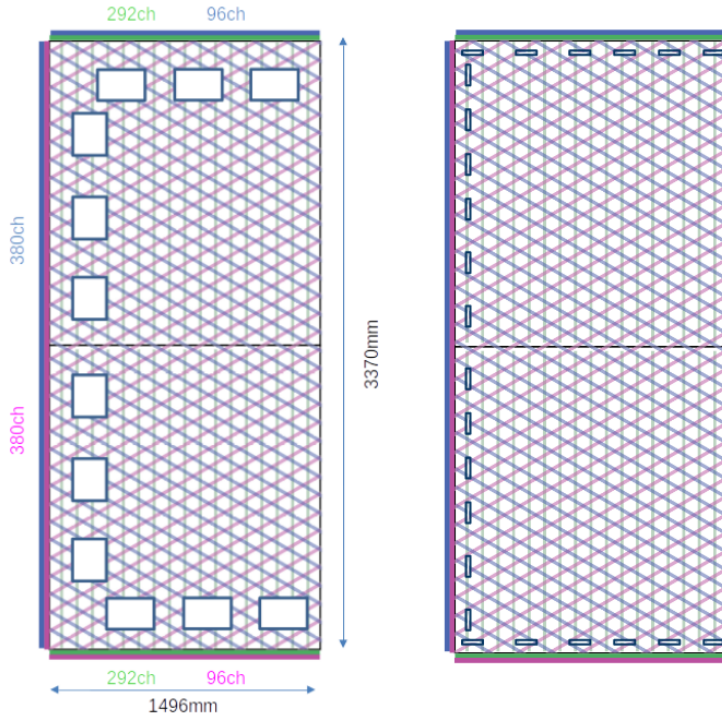


Figure 3.7: Schematic representation of the electrode strip configuration for a top (left) and bottom (right) CRU. Figure taken from Ref. [55].

the HD design, the VD option offers a slightly larger instrumented volume and a more cost-effective solution for the charge readout.

As in the HD design, each drift volume features a 500 V/cm electric field and a field cage that ensures its uniformity. The anode planes are arrays of $3.4\text{ m} \times 3\text{ m}$ charge-readout planes (CRPs). These are formed by a pair of charge-readout units (CRUs), which are built from two double-sided perforated PCBs, with their perforations aligned. The perforations allow the drift electrons to pass between the layers.

The PCB face opposite to the cathode has a copper guard plane which acts as shielding, while its reverse face is etched with electrode strips forming the first induction plane. The outer PCB has electrode strips on both faces, the ones facing the inner PCB form the second induction plane while the outermost ones form the collection plane. Fig. 3.7 shows the layout of the electrode strips for the top (left) and bottom (right) CRUs. The magenta and blue lines represent the first and second induction planes respectively, and the green lines correspond to the collection plane.

3.3. Far Detector

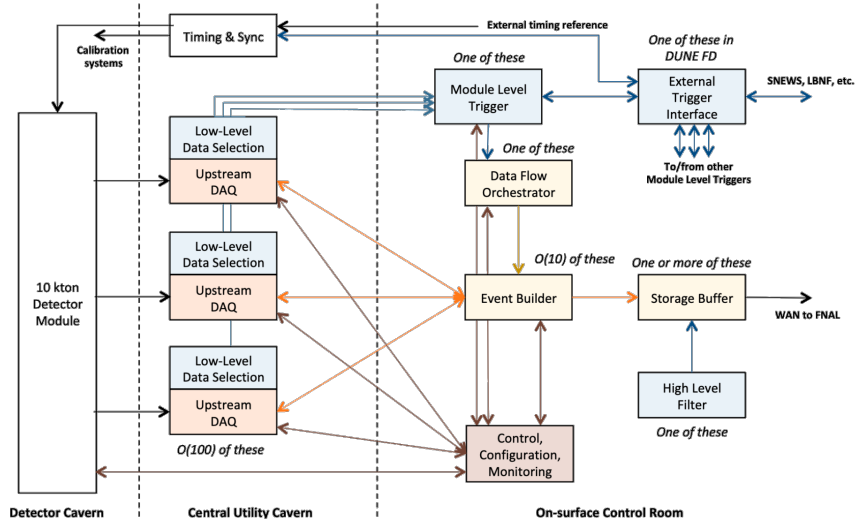


Figure 3.8: Detailed diagram of the DUNE FD DAQ system. Figure taken from Ref. [2].

935 The PDS in the VD module will use the same X-ARAPUCA technology developed
936 for the HD design. The plan is to place the PDS modules on the cryostat walls and on
937 the cathode, in order to maximise the photon yield.

938 3.3.3 FD Data Acquisition System

939 The task of the data acquisition (DAQ) system is to receive, process and store data from
940 the detector modules. In the case of DUNE the DAQ architecture is designed to work
941 for all FD modules interchangeably, except some aspects of the upstream part which
942 may depend on the specific module technology.

943 The enormous sample rate and the number of channels in TPC and PD readouts
944 will produce a very large volume of data. These pose really strong requirements and
945 challenges to the DUNE FD DAQ architecture. It will be required to read out data of
946 the order of ten thousand or more channels at rates of a few MHz. In order to cope
947 with the huge data volume, segmented readouts and compression algorithms are used to
948 reduce the data rate to manageable levels.

The DAQ system of the DUNE FD is composed of five different subsystems. The first one is the upstream DAQ, which receives the raw data from the detector, buffers it

Chapter 3. The Deep Underground Neutrino Experiment

951 and perform some low-level pre-processing. The minimally processed data is then fed
952 into a hierarchical data selection system, which then performs a module level trigger
953 decision. In case of a positive decision a trigger command is produced and executed by
954 the data flow orchestrator, located in the back-end (BE) DAQ subsystem. Subsequently
955 the DAQ BE retrieves the relevant data from the buffers located in the upstream DAQ,
956 adds all the data into a cohesive record and saves it to permanent storage. Watching
957 over all the other subsystems we also have the control, configuration and monitoring
958 subsystem and the time and synchronization subsystem. Fig. 3.8 shows a schematic
959 diagram of the DAQ system, showing the different subsystems and their relations.

960 A notorious challenge for the DUNE DAQ system comes from its broad physics
961 goals. We must be prepared to process events spanning a wide range of time windows
962 (from 5 ms in the case of beam and cosmic neutrinos and nucleon decay to 100 s in the
963 case of SNBs) and therefore this requires a continuous readout of the detector modules.
964 Moreover, because of the off-beam measurements we need to ensure the capabilities
965 of online data processing and self-triggering. Having this into account, together with
966 the technical constraints, the DUNE FD DAQ faces a series of challenges: it needs to
967 be fault tolerant and redundant to reduce downtime, accommodate new components
968 while it keeps serving the operational modules, have large upstream buffers to handle
969 SNB physics, be able to support a wide range of readout windows and last reduce the
970 throughput of data to permanent storage to be at most 30 PB/year.

971 3.4 Near Detector

972 In order to estimate the oscillation parameters we measure the neutrino energy spectra
973 at the FD. This reconstructed energy arises from a convolution of the neutrino flux, cross
974 section, detector response and the oscillation probability. Using theoretical and empirical
975 models to account for the other effects, one can extract the oscillation probability using
976 the measurement. However, these models have associated a number of uncertainties that
977 are then propagated to the oscillation parameters.

3.4. Near Detector

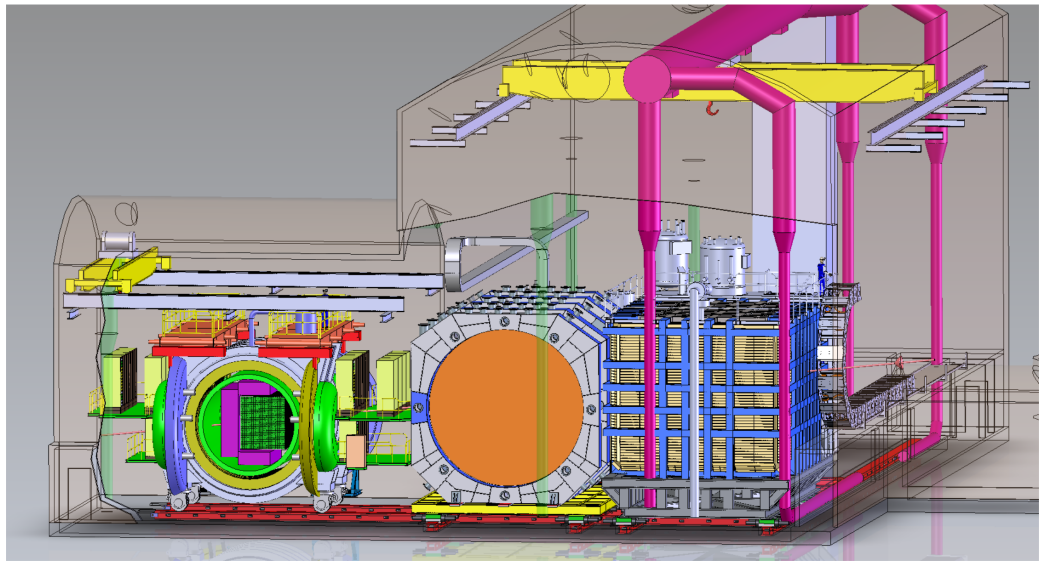


Figure 3.9: Representation of the ND hall in Phase II, showing the different subcomponents. From right to left, in the direction of the beam, we have ND-LAr, ND-GAr and SAND. Figure taken from Ref. [56].

978 One of the main roles of the ND is to measure the neutrino interaction rates before
979 the oscillation effects become relevant, i.e. close to the production point. By measuring
980 the ν_μ and ν_e energy spectra, and that of their corresponding antineutrinos, at the ND
981 we can constrain the model uncertainties. A complete cancellation of the uncertainties
982 when taking the ratio between the FD and ND measurements is not possible, as that
983 would require both detectors to have identical designs and the neutrino fluxes to be
984 the same. Because of the distance, the flux probed by the FD will have a different
985 energy and flavour composition than that at the ND, as neutrinos oscillate and the beam
986 spreads. The differences in the flux also determine the design of the detectors, therefore
987 the ND is limited in its capability to match the FD design.

988 Nevertheless, having a highly capable ND DUNE can minimise the systematic
989 uncertainties affecting the observed neutrino energy. The ND data can be used to
990 tune the model parameters by comparison with the prediction. Then, one uses the
991 tuned model to predict the unoscillated FD spectra. Comparing the prediction with the
992 measured spectra it is possible to extract the oscillation parameters.

993 Additionally, the ND will have a physics program of its own. In particular, it will

Chapter 3. The Deep Underground Neutrino Experiment

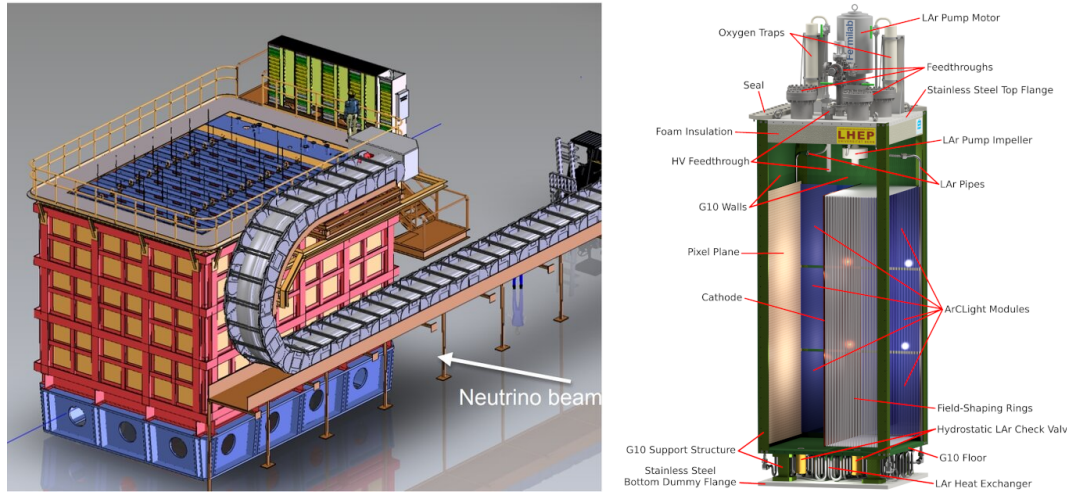


Figure 3.10: Schematic representation of the external components of ND-LAr, including the cryostat and the PRISM movable system (left) and detailed drawing of one ArgonCube module (right). Figure adapted from Ref. [1].

measure neutrino cross sections that will then be used to constrain the model used in the long-baseline oscillation analysis. It will also be used to search for BSM phenomena such as heavy neutral leptons, dark photons, millicharged particles, etc.

The DUNE ND can be divided in three main components, a LArTPC known as ND-LAr, a magnetised muon spectrometer, which will be the Temporary Muon Spectrometer (TMS) in Phase I and ND-GAr in Phase II, and the System for on-Axis Neutrino Detection (SAND). The layout of the Phase II DUNE ND can be seen in Fig. 3.9. The first two components of the ND will be able to move off-axis, in what is called the Precision Reaction-Independent Spectrum Measurement (PRISM) concept. More details on the purpose and design of the ND can be found in the DUNE ND Conceptual Design Report (CDR) [56].

3.4.1 ND-LAr

ND-LAr is a LArTPC, as the ND needs a LAr component in order to reduce cross section and detector systematic uncertainties in the oscillation analysis. However, its design differs significantly from those proposed for the FD modules. Because of the high event rates at the ND, approximately 55 neutrino interaction events per 10 μs spill,

3.4. Near Detector

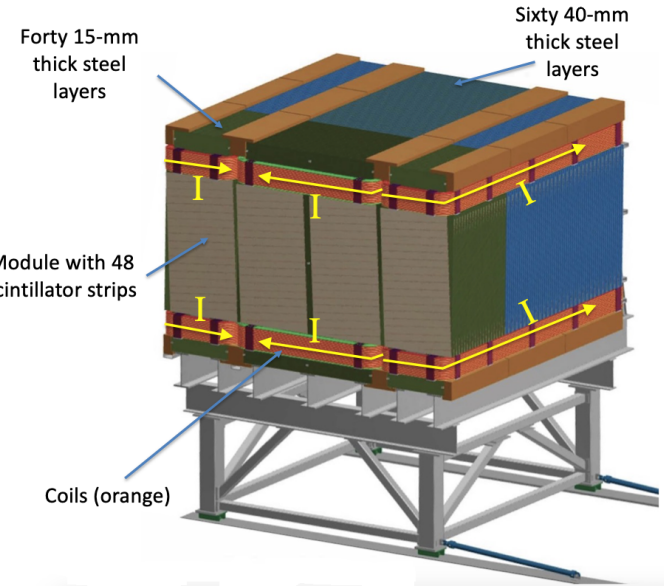


Figure 3.11: Schematic view of the TMS detector, highlighting its main parts. Figure adapted from Ref. [1].

ND-LAr will be built in a modular way. Each of the modules, based on the ArgonCube technology, is a fully instrumented, optically isolated TPC with a pixelated readout. The pixelisation allows for a fully 3D reconstruction and the optical isolation reduces the problems due to overlapping interactions. Fig. 3.10 shows a representation of the external parts of ND-LAr (left) and a detailed diagram of an ArgonCube module (right).

With a fiducial mass of 67 t and dimensions 7 m (w) \times 3 m (h) \times 5 m (l), ND-LAr will be able to provide high statistics and contain the hadronic systems from the beam neutrino interactions, but muons with a momentum higher than 0.7 GeV will exit the detector.

3.4.2 TMS/ND-GAr

In order to accurately estimate the neutrino energy, the momentum of the outgoing muons needs to be determined. That is the reason why a muon spectrometer is needed downstream of ND-LAr.

In Phase I that role will be fulfilled by TMS. It is a magnetised sampling calorimeter, with alternating steel and plastic scintillator layers. Fig. 3.11 shows a schematic view of

Chapter 3. The Deep Underground Neutrino Experiment

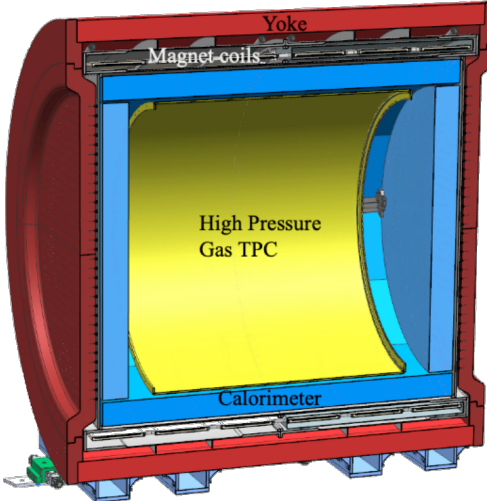


Figure 3.12: Cross section of the ND-GAr geometry, showing the HPgTPC, ECal and magnet. Figure adapted from Ref. [1].

1025 the TMS detector. The magnetic field allows a precise measurement of the sign of the
1026 muon, so one can distinguish between neutrino and antineutrino interactions.

1027 After the Phase II upgrade, TMS will be replaced with ND-GAr. This detector is
1028 a magnetised, high-pressure GAr TPC (often denoted as HPgTPC) surrounded by an
1029 electromagnetic calorimeter (ECal) and a muon tagger. A cross section of its geometry
1030 can be seen in Fig. 3.12. ND-GAr will be able to measure the momenta of the outgoing
1031 muons while also detect neutrino interactions inside the GAr volume. This allows
1032 ND-GAr to constrain the systematic uncertainties even further, as it will be able to
1033 accurately measure neutrino interactions at low energies thanks to the lower tracking
1034 thresholds of GAr.

1035 3.4.3 PRISM

1036 In general, the observed peak neutrino energy of a neutrino beam decreases as the
1037 observation angle with respect to the beam direction increases. This feature has been
1038 used in other long-baseline neutrino experiments, like T2K (2.5° off-axis) and NOvA
1039 (0.8° off-axis), in order to achieve narrower energy distributions. The DUNE PRISM
1040 concept exploits this effect using a movable ND. Within PRISM both ND-LAr and the

3.4. Near Detector

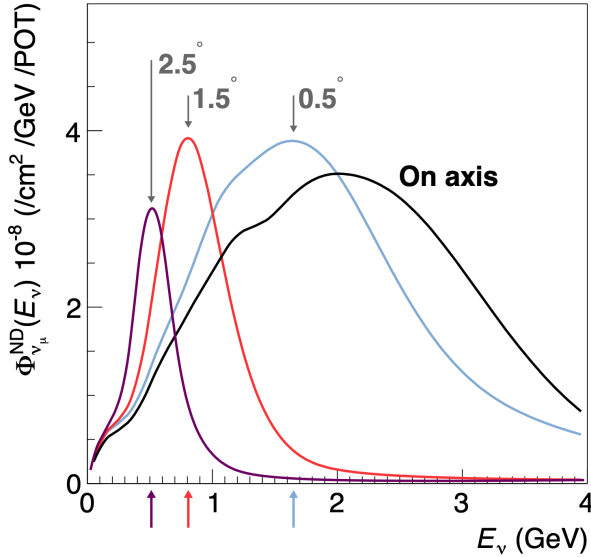


Figure 3.13: Predicted beam muon neutrino flux at the ND location for different off-axis positions. Figure taken from Ref. [56].

1041 muon spectrometer (TMS in Phase I and ND-GAr in Phase II) can be moved up to 3.2°
 1042 off-axis, equivalent to move the detectors 30.5 m laterally through the ND hall.

1043 This allows to record additional data samples with different energy compositions.
 1044 Fig. 3.13 compares the on-axis muon neutrino flux at the ND with the fluxes at different
 1045 off-axis positions. As the off-axis position increases the neutrino flux becomes closer to
 1046 a monoenergetic beam with a lower peak energy. These samples can be used to perform
 1047 a data-driven determination of the relation between true and reconstructed neutrino
 1048 energy, in order to reduce the dependence on the interaction model. The off-axis samples
 1049 are linearly combined to produce a narrow Gaussian energy distribution centered on
 1050 a target true energy. From the combination coefficients one can build a sample of
 1051 reconstructed neutrino events that will determine the energy mapping.

1052 The PRISM samples can also be used to form a flux at the ND location similar in
 1053 shape to the oscillated flux measured by the FD. This method can be used to extract
 1054 the oscillation parameters with minimal input from the neutrino interaction model.

Chapter 3. The Deep Underground Neutrino Experiment

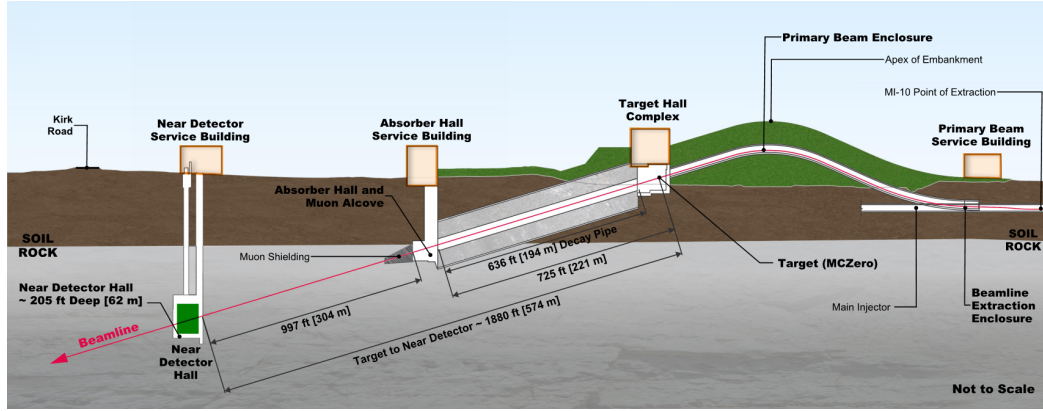


Figure 3.14: Schematic longitudinal section of the LBNF beamline at Fermilab (not to scale). Figure taken from Ref. [57].

1055 3.4.4 SAND

1056 The role of SAND is to monitor the beam stability by measuring the on-axis neutrino
 1057 energy spectra. As the PRISM program requires that ND-LAr and its downstream
 1058 muon spectrometer spend about half of the time in off-axis positions, it is not possible
 1059 to monitor the stability with the movable detectors. Moreover, for the success of PRISM
 1060 it is essential to have a stable beam configuration, or, at least, a quick assessment and
 1061 modeling of the distortions.

1062 The SAND detector is magnetised, and it counts with an inner low density tracker,
 1063 a LAr target with optical readout and surrounding sampling calorimeter.

1064 3.5 LBNF beamline

1065 The Long-Baseline Neutrino Facility (LBNF) project is responsible for producing the
 1066 neutrino beam for the DUNE detectors. A detailed discussion of the LBNF program
 1067 can be found in the DUNE/LBNF CDR Volume III [57].

1068 The LBNF beamline will provide a high-intensity neutrino beam within the adequate
 1069 energy range in order to meet the long-baseline oscillation physics goals of DUNE. A
 1070 schematic diagram of the longitudinal section of the LBNF beamline is shown in Fig.
 1071 3.14. First, a beam of $60 - 120$ GeV protons is extracted from the Fermilab Main

3.5. LBNF beamline

1072 Injector. This beam is aimed towards the target area, where it collides with a cylindrical
 1073 graphite target to produce pions and kaons.

1074 The diffuse, secondary beam of particles is focused by a pair of magnetic horns.
 1075 These select the positively charged particles when operated in Forward Horn Current
 1076 (FHC) mode, or the negatively charged ones when the current is reversed, also known as
 1077 Reverse Horn Current (RHC) mode. The focused secondary beam then enters a 194 m
 1078 decay pipe where the pions and kaons will predominantly produce $\mu^+\nu_\mu$ pairs when in
 1079 FHC mode (or $\mu^-\bar{\nu}_\mu$ in RHC mode).

1080 At the end of the decay pipe a hadron absorber removes the undecayed hadrons and
 1081 muons from the beam, which reduces the ν_e ($\bar{\nu}_e$) and $\bar{\nu}_\mu$ (ν_μ) contamination coming
 1082 from the μ^+ (μ^-) decays. The resulting neutrino flux at the FD is shown in Fig. 3.15,
 1083 both for FHC (left) and RHC (right) modes. These predictions show the intrinsic $(\bar{\nu}_e)$
 1084 contamination and wrong sign component from wrong sign and neutral meson decays,
 1085 as well as muons decaying before reaching the absorber.

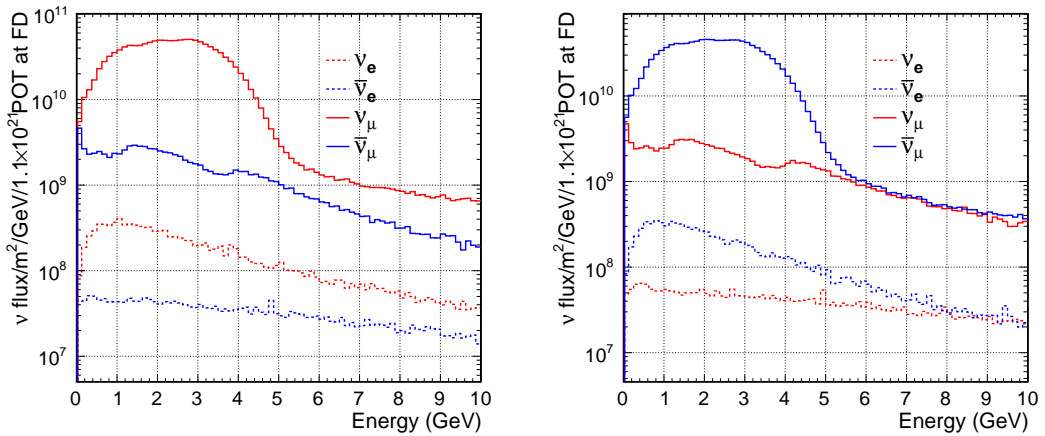


Figure 3.15: Predicted neutrino fluxes at the FD in FHC mode (left panel) and RHC mode (right panel). Figures taken from Ref. [50].

1086 **Chapter 4**

1087 **ND-GAr**

1088 ND-GAr is a magnetised, high-pressure gaseous argon TPC (HPgTPC), surrounded by
1089 an electromagnetic calorimeter (ECal) and a muon detector (commonly refer to as μ ID).
1090 A detailed discussion on the requirements, design, performance and physics of ND-GAr
1091 can be found in the DUNE ND CDR [56] and the ND-GAr whitepaper (cite).

1092 In DUNE Phase II ND-GAr will fulfill the role of TMS, measuring the momentum
1093 and sign of the charged particles exiting ND-LAr. Additionally, it will be able to measure
1094 neutrino interactions inside the HPgTPC, achieving lower energy thresholds than those
1095 of the ND and FD LArTPCs. By doing so ND-GAr will allow to constrain the relevant
1096 systematic uncertainties for the LBL analysis even further.

1097 The goal of the present chapter is to review the requirements that the physics program
1098 of DUNE impose on ND-GAr, present the current status of its design and describe the
1099 GArSoft package, its simulation and reconstruction software.

1100 **4.1 Requirements**

1101 The primary requirement for ND-GAr is to the measure the momentum and charge of
1102 muons from ν_μ and $\bar{\nu}_\mu$ CC interactions in ND-LAr, in order to measure their energy
1103 spectrum. To achieve the sensitivity to the neutrino oscillation parameters described
1104 in the DUNE FD TDR Volume II [50] ND-GAr should be able to constrain the muon

Chapter 4. ND-GAr

1105 energy within a 1% uncertainty or better. The main constraint will come from the
1106 calibration of the magnetic field, performed using neutral kaon decays in the HPgTPC.

1107 Another requirement for ND-GAr is the precise measurement of neutrino interactions
1108 on argon for the energies relevant to the neutrino oscillation program. The goal is to
1109 constrain the cross section systematic uncertainties in the regions of phase space that
1110 are not accessible to ND-LAr. This requires the kinematic acceptance for muons in
1111 ND-GAr to exceed that of ND-LAr, being comparable to the one observed in the FD.

1112 ND-GAr should also be able to the relationship between true and reconstructed energy
1113 from neutrino interactions on argon with low thresholds, being sensitive to particles that
1114 are not observed or may be misidentified in ND-LAr. In particular, ND-GAr needs to
1115 have low tracking thresholds in order to measure the spectrum of pions and protons
1116 produced in final-state interactions (FSI). It also must be able to accurately measure
1117 the pion multiplicity in 1, 2 and 3 pions final states, to inform the pion mass correction
1118 in the LArTPCs.

1119 4.2 Reference design

1120 The final design of ND-GAr is still under preparation. However, a preliminary baseline
1121 design was in place at the time of the ND CDR. This section summarises the main
1122 features of that design, as it is also the one used for the default geometry in our simulation.
1123 A DUNE Phase II whitepaper, discussing the different options under consideration for
1124 the ND-GAr design, is in progress.

1125 4.2.1 HPgTPC

1126 The reference design for the ND-GAr HPgTPC follow closely that of the ALICE TPC.
1127 It is a cylinder with a central high-voltage cathode, generating the electric field for
1128 the two drift volumes, with a maximum drift distance of 2.5 m each. The anodes will
1129 be instrumented with charge readout chambers. The original design repurposed the
1130 multi-wire proportional readout chambers of ALICE, however the current R&D efforts

4.2. Reference design

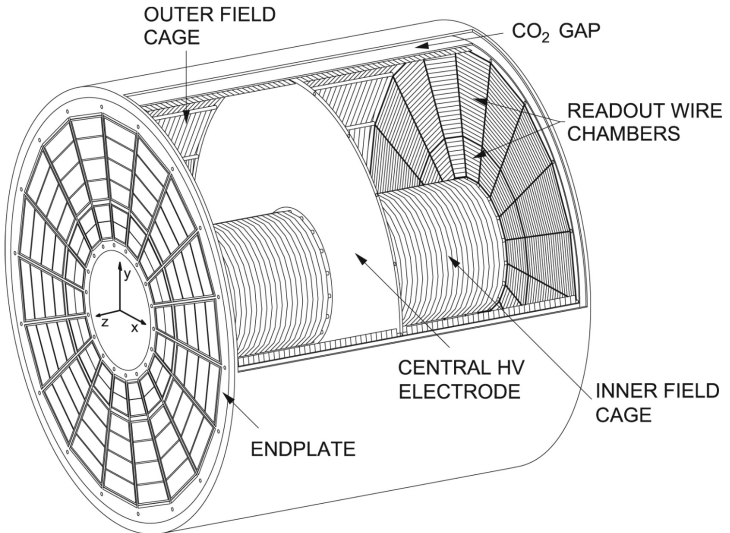


Figure 4.1: Diagram of the ALICE TPC, showing the two drift chambers, inner and outer field cages and readout chambers. Figure taken from Ref. [1].

1131 focus on a gas electron multiplier option instead. Fig. 4.1 shows a schematic diagram of
 1132 the ALICE TPC design. The basic ND-GAr geometry will resemble this, except for the
 1133 inner field cage.

1134 It will use a 90-10 molar fraction argon-CH₄ mixture at 10 bar. With this baseline
 1135 gas mixture light collection is not possible, as the quenching gas absorbs most of the
 1136 VUV photons. Additional R&D efforts are underway, to understand if different mixtures
 1137 allow for the light signal to be used to provide a t_0 while maintaining stable charge gain.

1138 4.2.2 ECal

1139 The main role of the ND-GAr ECal is the calorimetric measurement of the electron
 1140 energies and the reconstruction of photons, in particular those from neutral pion decays.
 1141 Also, the ECal is able to provide a t_0 timestamp for neutrino interactions, by associating
 1142 its activity to the tracks in the HPgTPC. The ECal will also be able to perform
 1143 neutron reconstruction using time of flight and reject external backgrounds, thanks to
 1144 its sub-nanosecond time resolution.

1145 The ECal design features three independent subdetectors, two end caps at each side
 1146 and a barrel surrounding the HPgTPC. Each of the detectors is divided in modules,

Chapter 4. ND-GAr

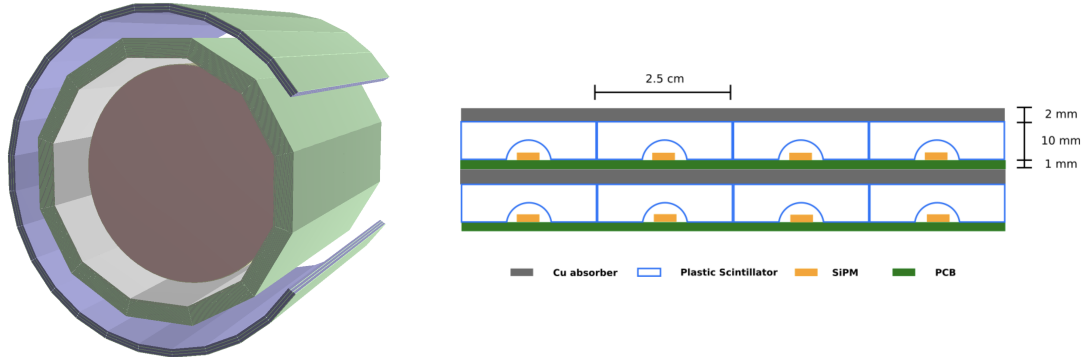


Figure 4.2: View of the 12-sided ECal barrel and outer muon tagger geometries (left) and layout of the ECal tile layers for the 2 mm Cu, 10 mm scintillator option (right). Figure adapted from Ref. [1].

which combine alternating layers of plastic scintillator and absorber material readout by SiPMs. The inner scintillator layers consist of $2.5 \times 2.5 \text{ cm}^2$ high-granularity tiles, whereas the outer ones are made out of 4 cm wide cross-strips spanning the whole module length. The current barrel geometry consists of 8 tile layers and 34 strip layers, while the end caps feature 6 and 36 respectively. The thickness of the scintillator layers is 7 mm and 5 mm for the Pb absorber layers. The 12-sided geometry of the ECal barrel (left) and the layout of the tile layers (left)¹ can be seen in Fig. 4.2.

4.2.3 Magnet

The ND-GAr magnet design, known as the Solenoid with Partial Yoke (SPY), consists of two coupled solenoids with an iron return yoke. The idea behind the design is to have a solenoid as thin as possible, as well as a return yoke mass distribution that minimises the material budget between ND-LAr and ND-GAr. The magnet needs to provide a 0.5 T field in the direction perpendicular to the beam, parallel to the drift electric field. It needs to host the pressure vessel and the surrounding ECal, which points to an inner diameter of $\sim 6.4 \text{ m}$.

The solenoid is a single layer coil, based on niobium titanium superconducting

¹The figure shows the layout of the tile layers for a previous design with 2 mm Cu absorber and 10 mm plastic scintillator, as mentioned in the text the current choice is 5 mm Pb absorber and 7 mm scintillator.

4.3. GArSoft

1163 Rutherford cable. The total length of the coil is 7.5 m. The bobbin will be split in four
1164 segments grouped in pairs with two identical cryostats, connected in series. The iron
1165 yoke features an aperture in the upstream side to allow the muons coming from ND-LAr.
1166 Still, its material will be enough to reduce the magnetic field reaching SAND, and also
1167 stop the charged pions produced inside the HPgTPC.

1168 4.2.4 Muon system

1169 The design of the ND-GAr muon system is still in a preliminary stage. Its role is to
1170 distinguish between muons and pions punching through the ECal. This is especially
1171 important for wrong-sign determination, to separate these from neutral current events.

1172 In its current form, the muon system consists of three layers of longitudinal sampling
1173 structures. It alternates 10 cm Fe absorber slabs with 2 cm plastic scintillator strips.

1174 The transverse granularity required is still under study.

1175 4.3 GArSoft

1176 GArSoft is a software package developed for the simulation and reconstruction of events
1177 in ND-GAr. It is inspired by the LArSoft toolkit used for the simulation of LArTPC
1178 experiments, like the DUNE FD modules. It is based on `art`, the framework for event
1179 processing in particle physics experiments [58]. Other of its main dependencies are `ROOT`,
1180 `NuTools`, `GENIE` and `Geant4`. It allows the user to run all the steps of a generation-
1181 simulation-reconstruction workflow using FHiCL configuration files.

1182 4.3.1 Event generation

1183 The standard generator FHiCLs in GArSoft run the event generation and particle
1184 propagation simulation (i.e. Geant4) in the same job by default. However, it is possible
1185 to split them up if needed. The current version of GArSoft provides five different event
1186 generators, each of them producing `simb::MCTruth` products defined in `NuTools`. The
1187 available modules are:

Chapter 4. ND-GAr

- 1188 • **SingleGen**: particle gun generator. It produces the specified particles with a given
1189 distribution of momenta, initial positions and angles.
- 1190 • **TextGen**: text file generator. The input file must follow the `hepevt` format², the
1191 module simply copies this to `simb::MCTruth` data products.
- 1192 • **GENIEGen**: GENIE neutrino event generator. The module runs the neutrino-nucleus
1193 interaction generator using the options specified in the driver FHiCL file (flux file,
1194 flavour composition, number of interactions per event, t_0 distribution, ...). Current
1195 default version is `v3_04_00`.
- 1196 • **RadioGen**: radiological generator. It produces a set list of particles to model
1197 radiological decays. Not tested.
- 1198 • **CRYGen**: cosmic ray generator. The module runs the CRY event generator with a
1199 configuration specified in the FHiCL file (latitude and altitude of detector, energy
1200 threshold, ...). Not tested.

1201 The module `GArG4` searches for all the generated `simb::MCTruth` data products, using
1202 them as inputs to the Geant4 simulation with the specified detector geometry. A constant
1203 0.5 T magnetic field along the drift coordinate is assumed. The main outputs of this step
1204 are `simb::MCParticle` objects for the generated Geant4 particles, `gar::EnergyDeposit`
1205 data products for the energy deposits in the HPgTPC and `gar::CaloDeposit` data
1206 products for the energy deposits in the ECal and muon system.

1207 4.3.2 Detector simulation

1208 The standard detector simulation step in GArSoft is all run with a single FHiCL, but
1209 the different modules can be run independently as well. First the `IonizationReadout`

²In brief, each event contains at least two lines. The first line contains two entries, the event number and the number of particles in the event. Each following line contains 15 entries to describe each particle. The entries are: status code, pdg code for the particle, entry of the first mother for this particle, entry of the second mother for this particle, entry of the first daughter for this particle, entry of the second daughter for this particle, x component of the particle momentum, y component of the particle momentum, z component of the particle momentum, energy of the particle, mass of the particle, x component of the particle initial position, y component of the particle initial position, z component of the particle initial position and time of the particle production.

4.3. GArSoft

1210 module simulates the charge readout of the HPgTPC, and later the `SiPMReadout` module
1211 runs twice, once for the ECal and then for the muon system, with different configurations.

1212 The `IonizationAndScintillation` module collects all the `gar::EnergyDeposit`
1213 data products, to compute the equivalent number of ionization electrons for each energy
1214 deposit. The `ElectronDriftAlg` module simulates the electron diffusion numerically
1215 both in the longitudinal and transverse directions and applies an electron lifetime
1216 correction factor. The induced charge on the nearest and neighbouring readout pads
1217 is modeled using the provided pad response functions. The digitisation of the data is
1218 then simulated with the `TPCReadoutSimAlg` module. By default, the ADC sampling
1219 rate used is 50.505 MHz. The resulting raw waveforms for each channel are stored with
1220 zero-suppression, in order to save memory and CPU time. The algorithms keep blocks
1221 of ADC values above a certain threshold, plus some adjustable additional early and late
1222 tick counts. The results of these three steps are `gar::raw::RawDigit` data products.

1223 For the ECal and the muon system the `SiPMReadout` module calls either the
1224 `ECALReadoutSimStandardAlg` or `MuIDReadoutSimStandardAlg` modules. These take
1225 all the `gar::CaloDeposit` data products in the corresponding detector and do the
1226 digitisation depending on whether the hit was in a tile or strip layer. They include single
1227 photon statistics, electronic noise, SiPM saturation and time smearing. The resulting
1228 objects are `gar::raw::CaloRawDigit` data products.

1229 4.3.3 Reconstruction

1230 The reconstruction in GArSoft is also run as a single job by default. It first runs the hit
1231 finding, clustering, track fitting and vertex identification in the HPgTPC, followed by
1232 the hit finding and clustering in the ECal and muon system. After those it produces the
1233 associations between the associations between the tracks and the ECal clusters.

1234 Focusing first on the HPgTPC reconstruction, the `CompressedHitFinder` module
1235 takes the zero-suppressed ADCs from the `gar::raw::RawDigit` data products. The
1236 reconstructed hits largely correspond to the above threshold blocks, however the hit
1237 finder identifies waveforms with more than one maximum, diving them in multiple hits

Chapter 4. ND-GAr

1238 if they dip below a certain threshold. The data products produced are of the form
1239 `gar::rec::Hit`. These are the inputs to the clustering of hits in the `TPCHitCluster`
1240 module. Hits close in space and time are merged, and the resulting centroids are found.
1241 This module outputs `gar::rec::TPCClusters` objects and associations to the input
1242 hits.

1243 The following step prior to the track fitting is pattern recognition. The module
1244 called `tpcvechitfinder2` uses the `gar::rec::TPCClusters` data products to find track
1245 segments, typically called vector hits. They are identified by performing linear 2D fits
1246 to the positions of the clusters in a 10 cm radius, one fit for each coordinate pair. A
1247 3D fit defines the line segment of the vector hit, using as independent variable the one
1248 whose sum of (absolute value) slopes in the 2D fits is the smallest. The clusters are
1249 merged to a given vector hit if they are less than 2 cm away from the line segment. The
1250 outputs are `gar::rec::VecHit` data products, as well as associations to the clusters. The
1251 `tpcpatrec2` module takes the `gar::rec::VecHit` objects to form the track candidates.
1252 The vector hits are merged together if their direction matches, their centers are within
1253 60 cm and their direction vectors point roughly to their respective centers. Once
1254 the clusters of vector hits are formed they are used to make a first estimation of the
1255 track parameters, simply taking three clusters along the track. The module produces
1256 `gar::rec::Track` data products and associations between these tracks and the clusters
1257 and vector hits.

1258 The track is fitted by means of a Kalman filter in the `tpctrackfit2` module, using
1259 the position along the drift direction as the independent variable. Two different fits are
1260 performed per track, a forward and a backwards fit, each starting from one of the track
1261 ends. The Kalman filter state vector ($y, z, R, \phi, \tan\lambda$) is estimated at each point along
1262 the track using a Bayesian update. The track parameters reported in the forward and
1263 backwards fits are the ones computed at the opposite end where the fit started. The
1264 main outputs of the track fit are the `gar::rec::Track` objects. Additionally, the module
1265 stores the fitted 3D positions along the track in the `gar::rec::TrackTrajectory` data
1266 products and the total charge and step sizes for each point also get stored in the form of

4.3. GArSoft

1267 `gar::rec::TrackIonization` objects.

1268 After the tracking step, the `vertexfinder1` module looks at the reconstructed
1269 `gar::rec::Track` products, creating vertex candidates with the track ends that are
1270 within 12 cm of each other. The vertices are then fitted using linear extrapolations from
1271 the different track ends associated. The results are `gar::rec::Vertex` data products,
1272 and associations to the tracks and corresponding track ends.

1273 For the ECal and muon tagger, the `SiPMHitFinder` module runs twice with different
1274 configurations, adapted to the particular capabilities of both. The module simply takes
1275 the `gar::raw::CaloRawDigit` products, applies a calibration factor to convert the ADC
1276 counts to MeV and for the strip layer hits it calculates the position along the strip using
1277 the times recorded of both SiPMs. This module produces `gar::rec::CaloHit` data
1278 products. Next, these objects are used as inputs to the `CaloClustering` module. It
1279 merges the hits based on a simple nearest neighbours (NN) algorithm. For the resulting
1280 clusters it also computes the total energy and position of the centroid. The results are
1281 stored as `gar::rec::Cluster` data products, with associations to the hits.

1282 The last step in the reconstruction is associating the reconstructed tracks in the
1283 HPgTPC to the clusters formed in the ECal and muon system. The `TPCECALAssociation`
1284 module checks first the position of the track end points, considering only the points
1285 that are at least 215 cm away from the cathode or have a radial distance to the center
1286 greater than 230 cm. The candidates are propagated up to the radial position, in the
1287 case of clusters in the barrel, or the drift coordinate position, for the end cap cluster, of
1288 the different clusters in the collection using the track parameters computed at the end
1289 point. The end point is associated to the cluster if certain proximity criteria are met.
1290 This module creates associations between the tracks, the end points and the clusters.
1291 The criteria for the associations are slightly different for the ECal and the muon tagger.

₁₂₉₂ Chapter 5

₁₂₉₃ FWTPG offline software

1294 Chapter 6

1295 Matched Filter approach to
1296 induction wire Trigger Primitives

1297 6.1 Motivation

1298 The filter implemented in the firmware of the upstream DUNE FD DAQ is a 32nd-order
1299 low-pass finite impulse-response (FIR) filter. The output of such filter for a discrete
1300 system can be written as:

$$y[i] = \sum_{j=0}^N h[j]x[i-j], \quad (6.1)$$

1301 where N is the order of the filter, y is the output sequence, x is the input sequence and h
1302 is the set of coefficients of the filter. The current implementation within `dtp-firmware`
1303 [59] uses a set of 16 non-zero integer coefficients.

1304 Filtering is a vital step in the hit finder chain. It helps to suppress the noise and
1305 enhance the signal peaks with respect to the noiseless baseline. A good filtering strategy
1306 allows us to use lower thresholds when forming the trigger primitives (TPs) and thus
1307 increasing the sensitivity of our detector to low energy physics events. In such events,
1308 the hits produced by the ionisation electrons tend to have lower amplitudes than those
1309 of interest to the baseline physics programme of the DUNE experiment.

1310 This is particularly important for the induction planes. In general, signal peaks in

Chapter 6. Matched Filter approach to induction wire Trigger Primitives

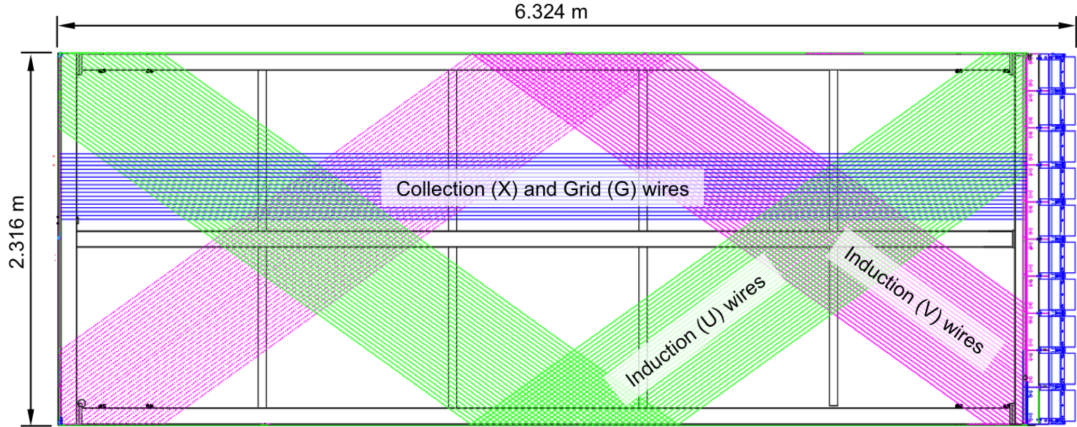


Figure 6.1: Schematic representation of an APA. The black lines represent the APA steel frame. The green and magenta lines correspond to the direction of the U and V induction wires respectively. The blue lines indicate the direction of the X collection wires and the wire shielding G.

the induction wires have smaller amplitude than the ones in the induction plane. This, together with the fact that the pulse shapes are bipolar, reduces our capacity to detect the hits on these channels. The inefficiency of detecting TPs in the induction planes (denoted as U and V planes) lead trigger algorithms to focus mainly on the TPs from the collection plane (so-called X plane). As a result, the possibility of making trigger decisions based on the coincidence of TPs across the three wire planes remains nowadays unexploited in DUNE. Fig. 6.1 shows a schematic view of an anode plane assembly (APA), with the different wire plane orientations highlighted.

A possible improvement of the current hit finder chain could require optimising the existing or choosing a new filter implementation. A filter strategy which improves the induction signals may be able to enhance the detection efficiency of TPs from the induction planes and ideally make it comparable to that of the collection plane.

The goal is to implement a better finite-impulse response filter design and to evaluate its performance relative to the current filter. To do so, we need to take into account the limitations of the firmware: the FIR filter shall have maximum 32 coefficients (so-called taps) whose values are 12-bit unsigned integers. Although it is technically possible to include non-integer coefficients, it would be a technical challenge as we have 40 FIR

6.2. Signal-to-noise ratio definition

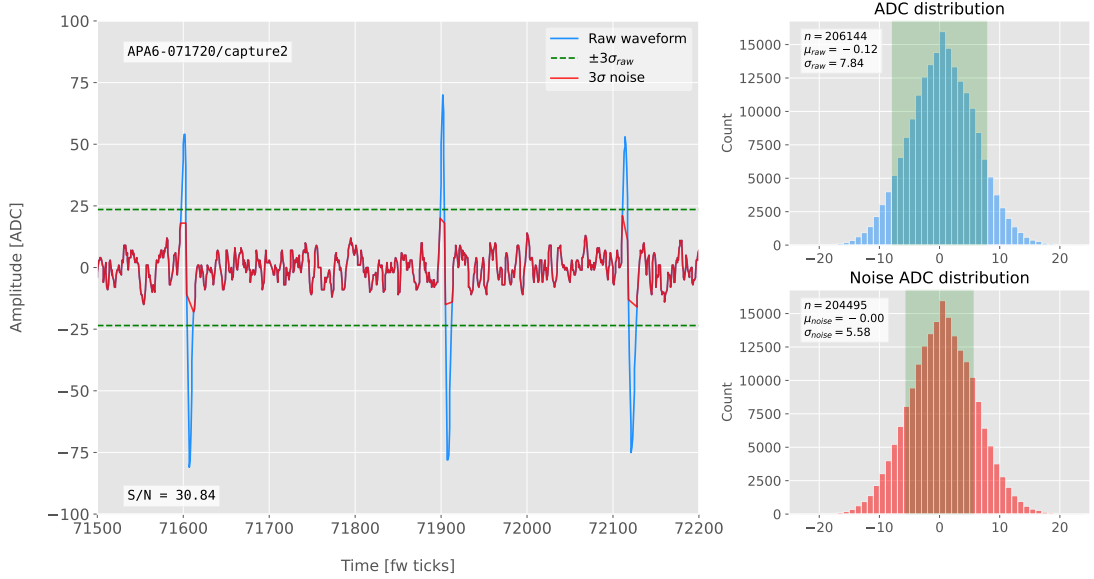


Figure 6.2: Left panel: Zoomed unfiltered waveform corresponding to channel 7840 from the ProtoDUNE-SP raw data capture `felix-2020-07-17-21:31:44` (blue line). The green dashed lines mark the region $\pm 3\sigma_{\text{raw}}$. The resulting noise waveform is also shown (red line). Top right panel: ADC distribution for channel 7840, where the green shaded region represents $\pm \sigma_{\text{raw}}$. Bottom right panel: noise ADC distribution for channel 7840, where the green shaded region represents $\pm \sigma_{\text{noise}}$.

1328 instances per APA, as there are 4 FIR per optical link and 10 optical links per APA.
 1329 With these restrictions, the task is to provide a set of 32 coefficients which yield an
 1330 optimal filter performance for the induction wires.

1331 6.2 Signal-to-noise ratio definition

1332 I introduce the signal to noise ratio (S/N) as a measure of the FIR filter performance
 1333 and demonstrate how to extract its value for a set of ProtoDUNE-SP data. The S/N
 1334 metrics allow us to compare different filter implementations and serve as a basis for more
 1335 detailed studies presented later in this document. Specifically, I use the ADC capture
 1336 `felix-2020-07-17-21:31:44` (data capture taken for firmware validation purposes). I
 1337 defined S/N as the height of the signal peaks relative to the size of the noise peaks.
 1338 To quantify this quantity channel by channel one first need to estimate the standard
 1339 deviation of the ADC data for each channel, σ_{ADC} . Then, I define the corresponding

Chapter 6. Matched Filter approach to induction wire Trigger Primitives

noise waveform to be the ADC values in the range $\pm 3\sigma_{ADC}$. From this new noise data one can estimate again the mean and standard deviation, μ_{noise} and σ_{noise} , so I can write the S/N for any given channel as:

$$S/N = \frac{\max [ADC] - \mu_{noise}}{\sigma_{noise}}, \quad (6.2)$$

where $\max [ADC]$ is simply the maximum ADC value found in the corresponding channel.

One can apply this definition of the S/N with a waveform from one of the channels of the data capture¹. Fig. 6.2 shows a zoomed region of the waveform corresponding to channel 7840 (blue line), where one can clearly see three signal peaks and continuous additive noise (we actually see 6 peaks, 3 positive and 3 negative, but, because by design for induction channels the expected signal pulse shapes are bipolar, I treat them as a collection of 3 individual signal peaks). I estimated the standard deviation of this raw waveform to be $\sigma_{raw} = 7.84$ ADC, so I am able to define the noise waveform (red line) as the ADC values in the range ± 23.52 ADC. This way one obtains $\mu_{noise} = 0$ and $\sigma_{noise} = 5.58$ ADC, which gives $S/N = 30.84$.

We can repeat this calculation now for the corresponding filtered waveform (using the current firmware FIR filter). In Fig. 6.3 I plotted the same time window for the filtered waveform from channel 7840 (blue line). In this case, the standard deviation of the waveform is larger than before, giving $\sigma_{raw} = 10.99$ ADC. The resulting noise waveform (red line) results from selection the ADC values in the range ± 32.91 ADC, giving now $\mu_{noise} = -0.47$ ADC and $\sigma_{noise} = 7.03$ ADC. Finally, one obtains $S/N = 24.68$. Notice that the value of S/N decreases after the filtering. Clearly, one can see that the noise baseline has increased by a factor of 1.35 when we applied the FIR filter and at the same time the amplitude of the signal peaks has remained almost unchanged, leading to this poorer S/N value.

¹All the original work was done within the `dtp-simulation` package [60], which offers a variety of tools to read raw data and emulate the TPG block (pedestal subtraction, filtering and hit finder). However, the results shown in this report were re-worked later using the C++ based `dtpemulator` package [61]. Its main purpose is the emulation of the TPG block and, in the same way as its predecessor, it has been cross-checked against the current firmware implementation.

6.3. Low-pass FIR filter design

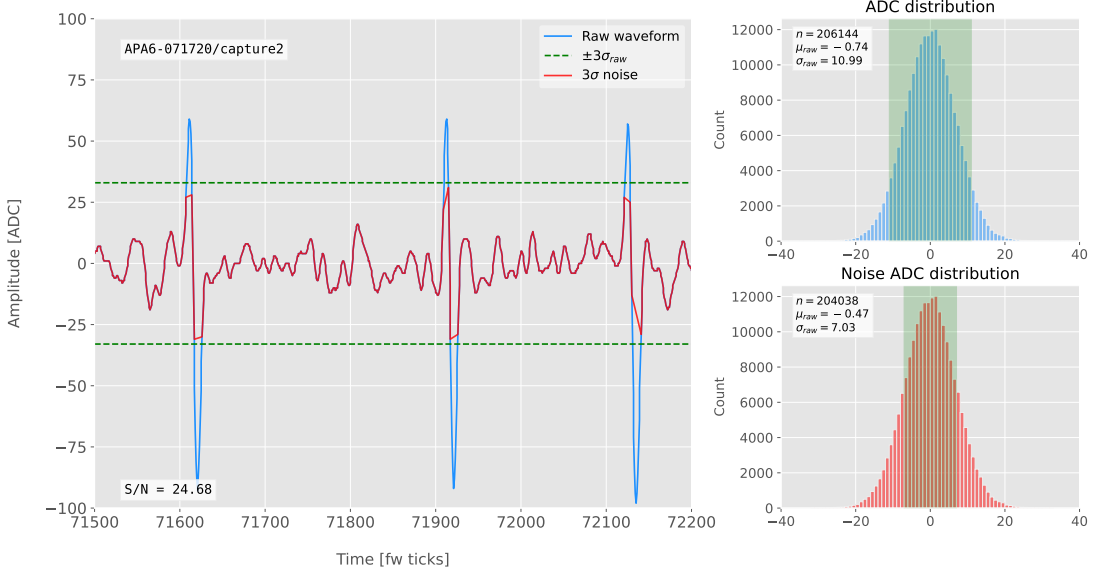


Figure 6.3: Left panel: Zoomed filtered waveform corresponding to channel 7840 from the ProtoDUNE-SP raw data capture `felix-2020-07-17-21:31:44` (blue line). The filter used was the current implementation of the low-pass FIR filter in `dtp-firmware`. The green dashed lines mark the region $\pm 3\sigma_{\text{raw}}$. The resulting noise waveform is also shown (red line). Top right panel: ADC distribution for channel 7840 after filtering, where the green shaded region represents $\pm \sigma_{\text{raw}}$. Bottom right panel: noise ADC distribution for channel 7840 after filtering, where the green shaded region represents $\pm \sigma_{\text{noise}}$

1363 6.3 Low-pass FIR filter design

1364 In general, when one uses a method to optimize the frequency response of a digital filter,
 1365 such as the Parks-McClellan algorithm, one finds a set of N real coefficients that give
 1366 the best response for the specified pass-band and order of the filter [62].

1367 In our case, as the sampling frequency is defined as 1 ticks^{-1} , the Nyquist frequency
 1368 will simply be $1/2 \text{ ticks}^{-1}$. The current implementation of the filter seems to have as
 1369 pass-band the range $[0, 0.1] \text{ ticks}^{-1}$. This can be seen in Fig. 6.4, where I show the
 1370 power spectrum, in decibels, of such filter implementation (blue solid line). For instance,
 1371 the Park-McClellan algorithm finds the optimal Chebyshev FIR filter taking as input
 1372 the boundaries of the target pass-band and stop-band, which can be written in the form:

$$\left\{ \begin{array}{l} [0, f_c] \\ [f_c + \delta f, f_N] \end{array} \right. , \quad (6.3)$$

Chapter 6. Matched Filter approach to induction wire Trigger Primitives

where f_c is the cut-off frequency, δf is the transition width and f_N is the aforementioned Nyquist frequency. A similar behaviour to the one in the current filter can be obtained by setting $f_c = 0$ and $\delta f = 0.1 \text{ ticks}^{-1}$. The response of the resulting filter is also shown in Fig. 6.4 (blue solid line). Notice that the suppression of the stop-band is enhanced for this optimal filter. For comparison I included the power response of the filter obtained by taking the integer part of the coefficients resulting from the Parks-McClellan method (red dashed line). One can see that it does not suppress that much the stop-band, in a similar way to the current implementation of the filter.

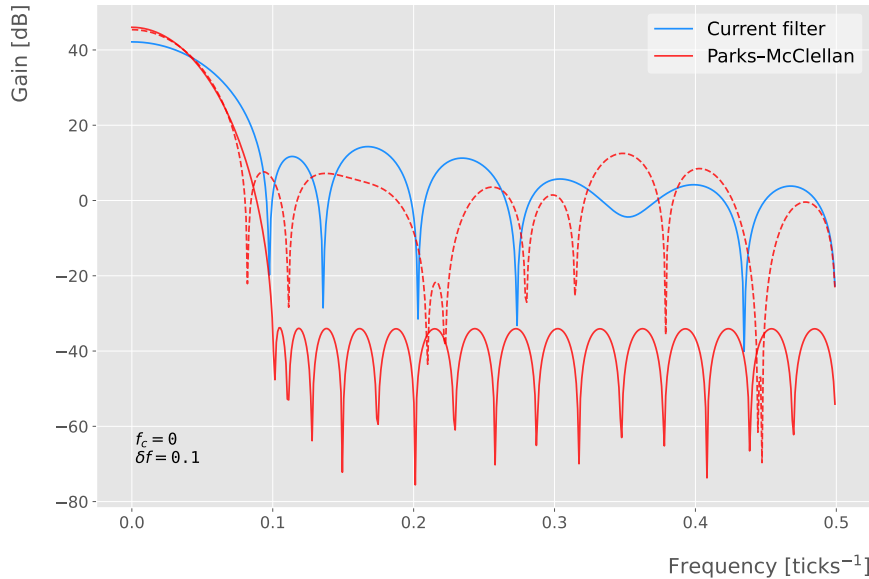


Figure 6.4: Power spectrum in decibels for the current implementation of the low-pass FIR filter in `dtp-firmware` (blue line), compared to the response of an optimal filter obtained using the Parks-McClellan algorithm for the same pass-band (red line). Also for comparison I include the spectrum of the optimal filter when taking only the integer part of the coefficients (red dashed line).

At this point, I tried to improve the performance of the FIR filter using the Parks-McClellan method, i.e. maximize the overall S/N, using the available data captures. I did so by varying the values of the two quantities that parametrize the pass-band and stop-band, the cut-off frequency f_c and the transition width δf .

Fig. 6.5 shows the average relative change in the S/N (i.e. the ratio between the value of the S/N after and before the filtering) for capture `felix-2020-07-17-21:31:44`,

6.3. Low-pass FIR filter design

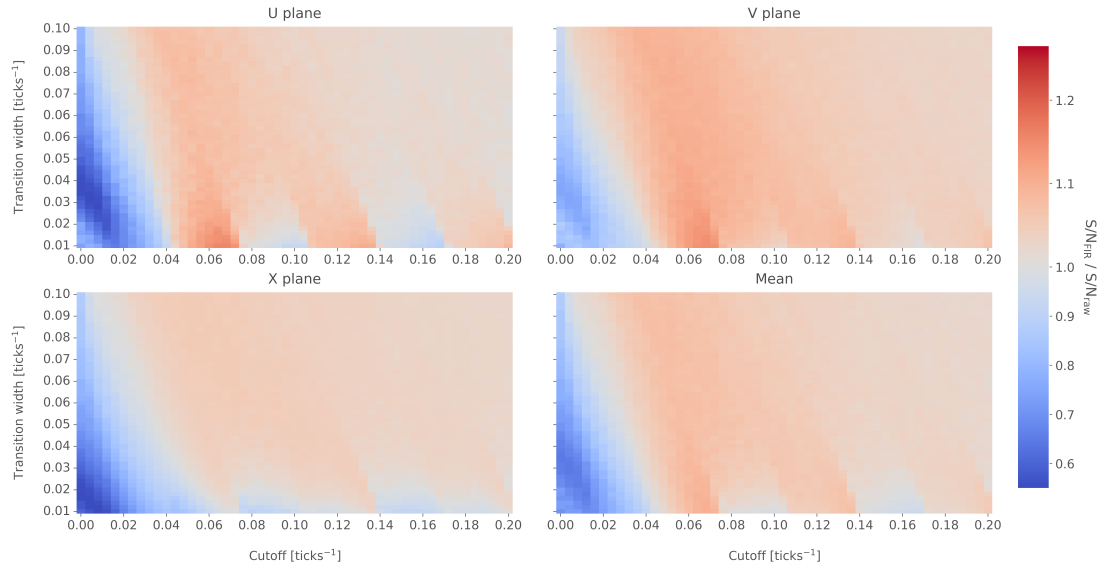


Figure 6.5: Relative change in the S/N for the ProtoDUNE-SP raw data capture `felix-2020-07-17-21:31:44`, using different values of the cutoff frequency f_c and the transition width δf . The optimal Chebyshev filters were applied using just the integer part of the coefficients given by the Parks-McClellan algorithm.

when using filters designed with the Parks-McClellan algorithm for the specified values of the cut-off frequency f_c and the transition width δf , restricted to integer values for the filter coefficients. One can clearly distinguish different regions where we get an improvement of up to a factor of 1.35 for the U plane. For large values of $f_c + \delta f$ the ratio tends to 1, as expected (in that limit the width of the stop-band goes to 0, meaning that no frequencies are filtered out and thus the waveform remains the same).

Using the configuration which gives the best mean performance for the three planes (see bottom right panel of Fig. 6.5), i.e. $f_c = 0.068 \text{ ticks}^{-1}$ and $\delta f = 0.010 \text{ ticks}^{-1}$, we can see how such filter affects the different channels. Fig. 6.6 shows the distribution of the S/N improvement values for all the channels in the raw ADC capture `felix-2020-07-17-21:31:44`, separated by wire plane, after the optimal Chebyshev filter was applied. One can see that there is a clear improvement for both U and V induction wire planes, obtaining a mean change of 1.25 and 1.30 for them respectively. However, in the case of the collection plane X the mean of this distribution is roughly 1, meaning that a good fraction of channels in that plane get a slightly worse S/N after the

Chapter 6. Matched Filter approach to induction wire Trigger Primitives

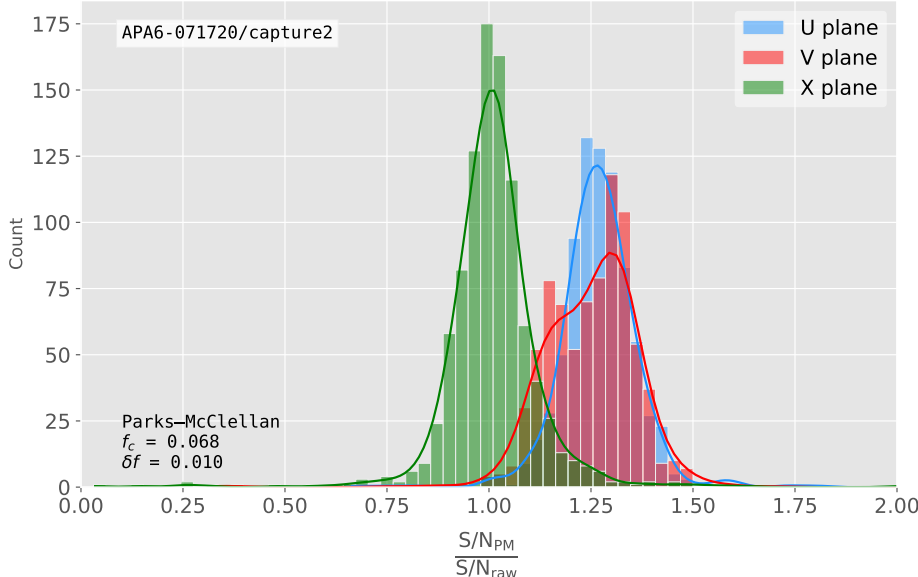


Figure 6.6: Distribution of the relative change of the S/N on the different wire planes from the ProtoDUNE-SP raw data capture *felix-2020-07-17-21:31:44* after the optimal Chebyshev filter was applied. The filter was computed with the Parks-McClellan algorithm using a cutoff of $f_c = 0.068 \text{ ticks}^{-1}$ and a transition width $\delta f = 0.010 \text{ ticks}^{-1}$.

filter is applied. In any case, this is not a big issue as the S/N for collection channels is usually much higher than the one for induction channels.

The results I obtained optimising the low pass filter with the Parks-McClellan method are promising. Nonetheless, the improvement found is rather marginal so I wondered if there could be an alternative approach to the filtering problem which yields better outputs. At this point, I found a possible alternative in matched filters. By construction, this kind of filters offer the best improvement on the S/N.

6.4 Matched filters

In the context of signal processing, a matched filter is the optimal linear filter for maximising the signal-to-noise ratio (S/N) in the presence of additive noise, obtained by convolving a conjugated time-reversed known template with an unknown signal to detect the presence of the template in the signal [63].

Given a known signal sequence $s(t)$ and another (a priori unknown) noise sequence

6.4. Matched filters

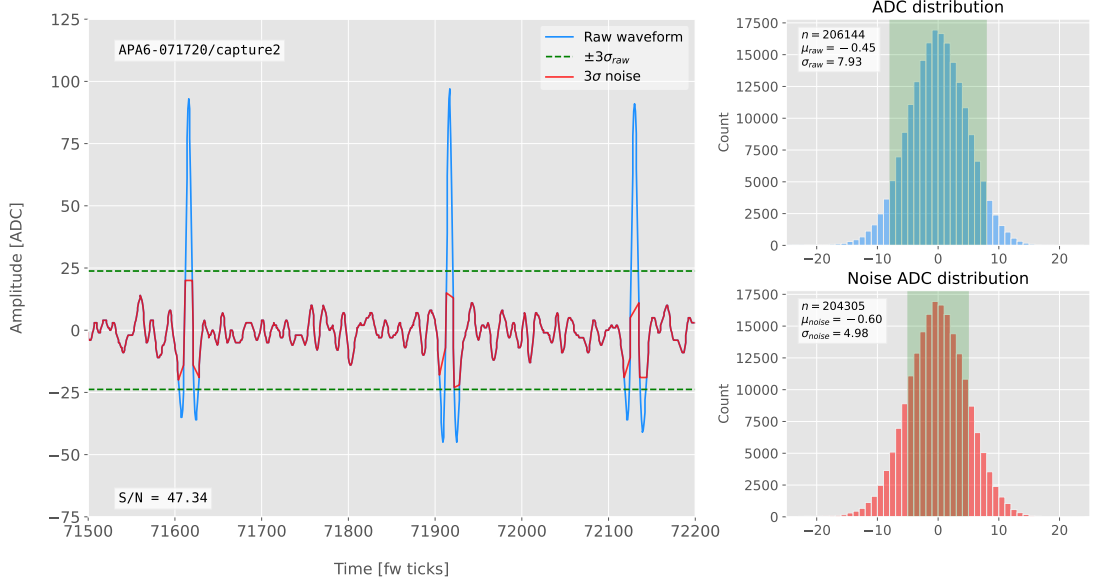


Figure 6.7: Left panel: Zoomed match filtered waveform corresponding to channel 7840 from the ProtoDUNE-SP raw data capture felix-2020-07-17-21:31:44 (blue line). The filter used was directly extracted from the data, being the 32 values around the first peak in the original waveform. The green dashed lines mark the region $\pm 3\sigma_{\text{raw}}$. The resulting noise waveform is also shown (red line). Top right panel: ADC distribution for channel 7840 after match filtering, where the green shaded region represents $\pm \sigma_{\text{raw}}$. Bottom right panel: noise ADC distribution for channel 7840 after match filtering, where the green shaded region represents $\pm \sigma_{\text{noise}}$

1415 $n(t)$, the input signal can be written as:

$$x(t) = s(t) + n(t). \quad (6.4)$$

1416 Now, considering a linear time-invariant filter, whose impulse-response function I
1417 will refer to as $h(t)$, one can write the output signal as:

$$\begin{aligned} y(t) &= x(t) * h(t) \\ &= (s(t) + n(t)) * h(t) \\ &= y_s(t) + y_n(t), \end{aligned} \quad (6.5)$$

1418 where $y_s(t)$ and $y_n(t)$ are simply the outputs of the filter due to the signal and the noise
1419 components respectively.

Chapter 6. Matched Filter approach to induction wire Trigger Primitives

1420 The goal of the matched filter is to detect the presence of the signal $s(t)$ in the input
 1421 sample $x(t)$ at a certain time t_0 , which effectively means we need to maximise the S/N.
 1422 This way, what one wants is to have a filter which gives a much bigger output when the
 1423 known signal is present than when it is not. Putting it in other words, the instantaneous
 1424 power of the signal output $y_s(t)$ should be much larger than the average power of the
 1425 noise output $y_n(t)$ at some time t_0 .

1426 For the case of the filtered signal, one can easily re-write it as an inverse Fourier
 1427 transform:

$$y_s(t) = \frac{1}{2\pi} \int_{-\infty}^{\infty} d\omega H(\omega)S(\omega)e^{i\omega t}, \quad (6.6)$$

1428 where $H(\omega)$ and $S(\omega)$ are the Fourier transforms of the impulse-response function (i.e.
 1429 the transfer function of the filter) and of the input signal, respectively.

1430 Now focusing on the noise, we can use the Wiener-Khinchin theorem [64] to write
 1431 the mean power of the noise after filtering as:

$$E|y_n(t)|^2 = \frac{1}{2\pi} \int_{-\infty}^{\infty} d\omega |H(\omega)|^2 S_n(\omega), \quad (6.7)$$

1432 where $S_n(\omega)$ is the power spectral density of the noise.

1433 Having these, one can write the instantaneous S/N at time t_0 as:

$$\begin{aligned} \left(\frac{S}{N} \right)_{t_0} &= \frac{|y_s|^2}{E|y_n(t)|^2} \\ &= \frac{1}{2\pi} \frac{\left| \int_{-\infty}^{\infty} d\omega H(\omega)S(\omega)e^{i\omega t_0} \right|^2}{\int_{-\infty}^{\infty} d\omega |H(\omega)|^2 S_n(\omega)}. \end{aligned} \quad (6.8)$$

1434 Once we have this expression, we need to find the upper limit of it to determine what
 1435 would be the optimal choice for the transfer function. One can use the Cauchy-Schwarz
 1436 inequality, which in the present case takes the form:

$$\left| \int_{-\infty}^{\infty} dx f(x)g(x) \right|^2 \leq \int_{-\infty}^{\infty} dx |f(x)|^2 + \int_{-\infty}^{\infty} dx |g(x)|^2, \quad (6.9)$$

6.4. Matched filters

1437 for any two analytical functions $f(x)$ and $g(x)$. One can prove that making the choice:

$$\begin{aligned} f(x) &= H(\omega) \sqrt{S_n(\omega)} e^{i\omega t_0}, \\ g(x) &= \frac{S(\omega)}{\sqrt{S_n(\omega)}}, \end{aligned} \quad (6.10)$$

1438 leads to the following upper bound for the S/N:

$$\left(\frac{S}{N} \right)_{t_0} \leq \frac{1}{2\pi} \int_{-\infty}^{\infty} d\omega \frac{|S(\omega)|^2}{S_n(\omega)}. \quad (6.11)$$

1439 From Eqs. (6.8), (6.9) and (6.10) one can also derive the form of the transfer function

1440 such that the upper bound is exactly reached [65]:

$$H(\omega) \propto \frac{S^*(\omega) e^{-i\omega t_0}}{S_n(\omega)}. \quad (6.12)$$

1441 From this last expression we can clearly see the way the matched filter acts. As the
1442 transfer function is proportional to the Fourier transform of the signal it will try to only
1443 pick the frequencies present in the signal [66].

1444 The matched filter transfer function can be greatly simplified if the input noise is
1445 Gaussian. In that case, the power spectral density of the noise is a constant, so it can be
1446 re-absorbed in the overall normalisation of the transfer function. Moreover, considering
1447 that the input signal is a real function, one can simply set $S^*(\omega) = S(-\omega)$, which gives:

$$H(\omega) \propto S(-\omega) e^{-i\omega t_0}. \quad (6.13)$$

1448 For a discrete signal, one can think of the input and impulse-response sequences as
1449 vectors of \mathbb{R}^N . Then, the matched filter tries to maximise the inner product of the signal
1450 and the filter while minimising the output due to the noise by choosing a filter vector
1451 orthogonal to the later. In the case of additive noise, that leads to the impulse-response
1452 vector:

$$h = \frac{1}{\sqrt{s^\dagger R_n^{-1} s}} R_n^{-1} s, \quad (6.14)$$

Chapter 6. Matched Filter approach to induction wire Trigger Primitives

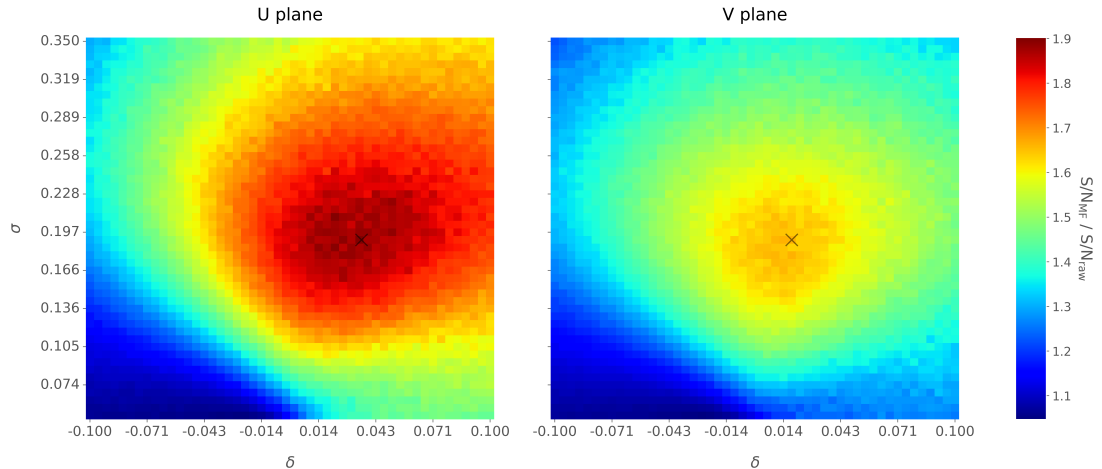


Figure 6.8: Relative improvement in the S/N for the raw data capture `felix-2020-07-17-21:31:44`, using the matched filter following the parametrisation in Eq. (6.17). The black crosses in both panels denote the location of the maximum ratio value.

1453 where s is a reversed signal template sequence of length N equal to the order of the filter
 1454 and R_n is the covariance matrix associated with the noise sequence n . For the Gaussian
 1455 noise case, the covariance matrix is simply the unit matrix, so the above expression
 1456 simplifies again to:

$$h = \frac{s}{|s|}. \quad (6.15)$$

1457 For this first stage of the study, I use a definition of the S/N per channel given by:

$$\text{S/N} = \frac{\max [ADC] - \mu_{noise}}{\sigma_{noise}}, \quad (6.16)$$

1458 where the subscript *noise* refers to a subset of the data obtained by only taking into
 1459 account waveform values within a $\pm 3\sigma$ range around the mean of the data and $\max [ADC]$
 1460 is the maximum of the original waveform. This definition is further discussed in App.
 1461 6.2, where I also show examples of its application to raw data and to a waveform filtered
 1462 with the current low-pass FIR filter.

1463 To test whether this choice of filter is appropriate one needs to choose a signal
 1464 template. As an example of how a matched filter would affect our signal, I simply took
 1465 the filter coefficients to be the 32 ADC values around a signal peak present in the data.

6.4. Matched filters

1466 In Fig. 6.7 (left panel) I plotted a zoomed region for channel 7840 in the raw data capture
1467 `felix-2020-07-17-21:31:44`, after applying the matched filter described before (blue
1468 line). When compared to the raw and FIR filtered case (see App. 6.2), after applying
1469 the match filter the standard deviation of the noise waveform (red line) decreases and at
1470 the same time the signal peaks are enhanced. This leads to an improvement of the S/N
1471 by a factor of 1.92 when compared to the raw waveform.

1472 In order to obtain the matched filter that is more suitable for our data, I explored
1473 different configurations of signal templates. In order to perform this exploration, I
1474 parametrised the signal using the bipolar function:

$$f(x) = -A(x + \delta) e^{-x^2/\sigma^2}, \quad (6.17)$$

1475 where the parameter δ controls the asymmetry between the positive and negative peaks
1476 and σ controls their width. The amplitude parameter A is set such that it keeps the
1477 height of the biggest peak to be less than 200 ADC in absolute value.

1478 As this parametrisation is only adequate for bipolar signals I will focus exclusively
1479 on the induction channels. Also, the optimal configurations I found for the U and V
1480 plane will be kept separate, i.e. I will have two sets of coefficients that will be applied to
1481 either the U and V planes of wires. I do so as I found this was the choice giving the
1482 best performance. Even so, as I will discuss, the differences are not very pronounced. In
1483 case it is not technically possible to separate channels in the firmware according to the
1484 wire plane they come from and use different sets of filter coefficients for them, we can
1485 just find a common unique set of coefficients. In such case, I do not expect our results
1486 to change dramatically.

1487 In Fig. 6.8 I present the results of our parameter scan, for channels in the induction
1488 planes U (left panel) and V (right panel). For each configuration of σ and δ the resulting
1489 matched filter was applied to all channels in the corresponding plane within the data
1490 capture `felix-2020-07-17-21:31:44`, the S/N improvement was computed with respect
1491 to the raw waveforms and then the S/N mean value was kept as a score for such filter.

Chapter 6. Matched Filter approach to induction wire Trigger Primitives

1492 One can see that the improvement obtained for the U plane is in general higher than the
1493 one for the V plane. In any case, I got substantially higher ratios than the ones obtained
1494 for the low-pass FIR filters. For the optimal configurations I attained improvements up
1495 to a factor of 1.85 for the U plane and 1.65 for the V plane.

1496 The sets of optimal matched filter coefficients were obtained for the parameters
1497 $\delta = 0.035$, $\sigma = 0.191$ for the U plane and $\delta = 0.018$, $\sigma = 0.191$ for the V plane. I
1498 show these two sets of coefficients in Fig. 6.9 (left panel). Also in Fig. 6.9 (right
1499 panel) I plot the distribution of the S/N improvement after the optimal match filters
1500 for the U and V were applied to the corresponding channels in the raw data capture
1501 `felix-2020-07-17-21:31:44`. As mentioned before, the mean improvement achieved
1502 for the U plane channels is slightly bigger than the one for the V channels. Note, however,
1503 that the spread of the distribution for the V plane is also smaller than the one for the U
1504 plane.

1505 I also performed a similar scan for the case of a low-pass FIR filter using the Parks-
1506 McClellan algorithm. In that case, the parameters to check were the cutoff frequency
1507 and the transition width of the filter. A summary of the results is given in App. 6.3.

1508 Overall, one can see that the improvements on the S/N are much more significant in
1509 the case of the matched filter than it is for the low-pass FIR filters. The analysis of this
1510 and other raw data captures from ProtoDUNE-SP suggest that matched filters increase
1511 the S/N of induction channels by a factor of 1.5 more than the optimal low-pass FIR
1512 filters.

1513 Although these results are by themselves great points in favour of the matched
1514 filter, more studies are needed to completely assess the robustness of this approach. I
1515 proceeded then to test the matched filter with simulated data samples.

1516 6.5 Using simulated samples

1517 In order to further test the matched filter, the next step was to generate and process
1518 data samples using *LArSoft* [67]. In this way, one can control the particle content of

6.5. Using simulated samples

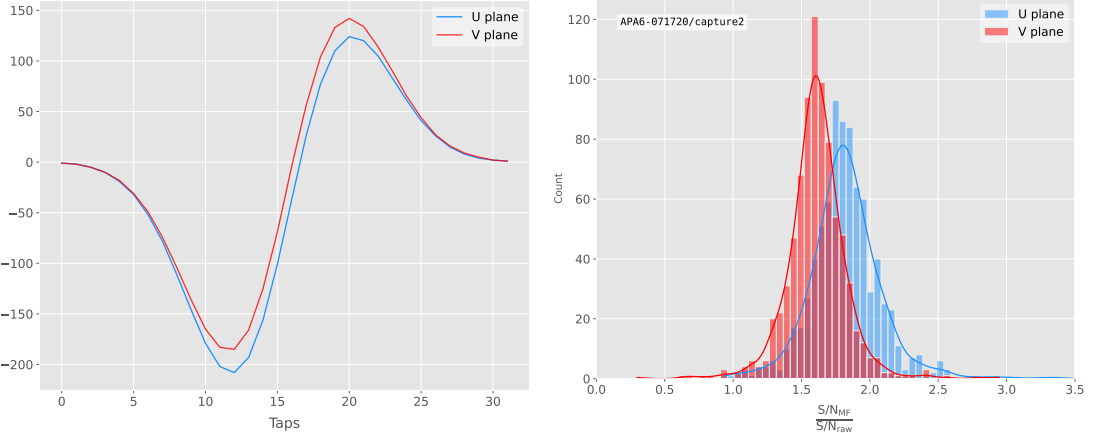


Figure 6.9: Left panel: Optimal matched filter coefficients for the U (blue line) and V (red line) planes. The filters were computed with our parametrisation in Eq. (6.17) for the parameter values $\delta = 0.035$, $\sigma = 0.191$ and $\delta = 0.018$, $\sigma = 0.191$ respectively. Right panel: Distribution of the relative change of the S/N on the two induction wire planes from the ProtoDUNE-SP raw data capture *felix-2020-07-17-21:31:44* after their respective optimal matched filters were applied.

1519 the samples, the orientation of the tracks and their energy, and therefore see how the
1520 matched filter behaves in various situations.

1521 To begin with, I prepared different monoenergetic and isotropic samples containing
1522 a single particle per event. Each sample contains a different particle species, namely
1523 electrons, muons, protons and neutral pions all with a kinetic energy of $E_k = 100$ MeV.
1524 I chose these because of the fairly different topologies they generate in the liquid argon,
1525 ranging from shower-like to track-like. The procedure I followed to generate the samples
1526 and process them is discussed in detail in App. ??.

1527 These were generated with the single particle gun and the Geant4 stage of the
1528 *LArSoft* simulation [67] was performed with the standard configuration for the DUNE
1529 FD 10kt module.

1530 For simplicity, I restricted the particles to start drifting in a single TPC volume
1531 (in this case TPC 0), so I can focus exclusively on the signals coming from one APA.
1532 The chosen kinetic energy for all the particles in my first trial is $E_k = 100$ MeV, so a
1533 necessary check is to see if all our tracks will be typically contained in one TPC volume.
1534 Fig. 6.10 (left panel) shows the distributions of the track lengths in the liquid argon

Chapter 6. Matched Filter approach to induction wire Trigger Primitives

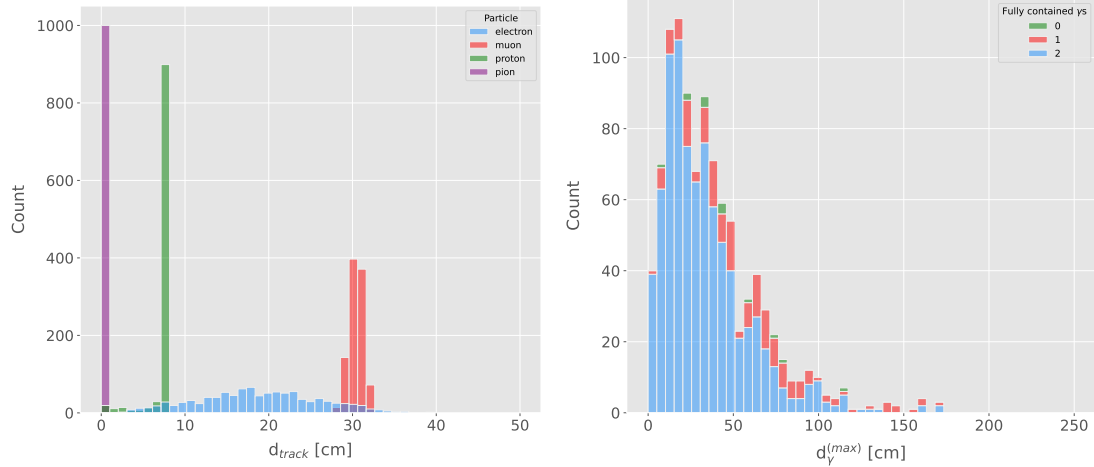


Figure 6.10: Left panel: distributions of the particles track length in the liquid argon for the generated $E_k = 100$ MeV monoenergetic samples, electrons (blue), muons (red), protons (green) and neutral pions (purple). Right panel: distribution of the length of the longest photon in the neutral pion sample after the decay process $\pi^0 \rightarrow \gamma\gamma$.

of all generated particles with $E_k = 100$ MeV. One can see that, in the case of the track-like particles (i.e. muons and protons), their length distributions are quite sharp and centered at relatively low distances (30 and 8 cm, respectively). For electrons, the distribution is quite broad but it does not extend past ~ 30 cm. The case of neutral pions can be misleading, as they decay promptly the track length associated with the true Monte Carlo particle is always < 1 cm. In Fig. 6.10 (right panel) I show the effective length distribution of the longest photon after the pion decays as $\pi^0 \rightarrow \gamma\gamma$, highlighting the number of fully contained photons in the TPC volume per event (either zero, one or both). One can see that the vast majority of events has both photons contained and that just a negligible number of them has none of them contained in the TPC volume. In any case, for the sake of caution, I will only keep the pion events with both photons contained.

Once I have prepared a sample at the Geant4 level, I need to process it through the detector simulation. In order to make adequate estimations of the noise levels and run the filtering and hit finder as I did with the ProtoDUNE data, one needs to turn off the default zero-suppression of the waveforms produced by the simulation. At this first stage I am only concerned with the waveforms with the noise added, so I keep the noise

6.5. Using simulated samples

addition option as true in the configuration. However, for studies related to the hit finder performance one will also need to store the noiseless waveforms in order to retrieve the truth information of the hits. I will discuss this approach next.

After the detector simulation stage, one needs to extract the no zero-suppressed noisy waveforms, along with their offline channel numbers, and store them in a certain format to be analysed later. To reduce the amount of data that will go for processing, I used the information from the Geant4 step of the simulation to select only the active channels, i.e. the channels where some ionisation electrons arrive. Moreover, as said previously, I only extract the waveforms from APA 0 and exclusively the ones coming from induction channels. The resulting ROOT file contains a tree with two branches, one containing the waveforms for each event and channel and the other with the corresponding offline channel numbers.

Finally, to extract the truth values for the orientation of the tracks and the energies of the particles I used a modified analysis module. This gives a ROOT file with a single tree, containing several branches with different information such as the components of the initial momentum of the particles, initial and final xyz location, track length, etc.

For the analysis of the resulting waveforms and truth values I used a custom set of Python libraries (available at [??]). Among other functionalities, these enable the user to read the ROOT files, export the raw data as pandas objects, apply the filters and compute the S/N of both the raw and filtered signals. So far, the default configuration for the filtering uses the set of optimal matched filter coefficients that I found using the ProtoDUNE data samples.

Additionally, for the analysis of the samples it was necessary to use two different reference frames, to study separately the signals coming from the U and V induction wire planes. As I am focussing on a single APA, the U and V wires have a different orientation in the yz plane. In the case of U wires, these are tilted 35.7° clockwise from the vertical (y direction), whereas the V wires are at the same angle but in the counter clockwise direction. Because of this, the best option is to deal with two new coordinate systems rotated by $\pm 35.7^\circ$ along the x axis, so the new y' and y'' directions are aligned with the

Chapter 6. Matched Filter approach to induction wire Trigger Primitives

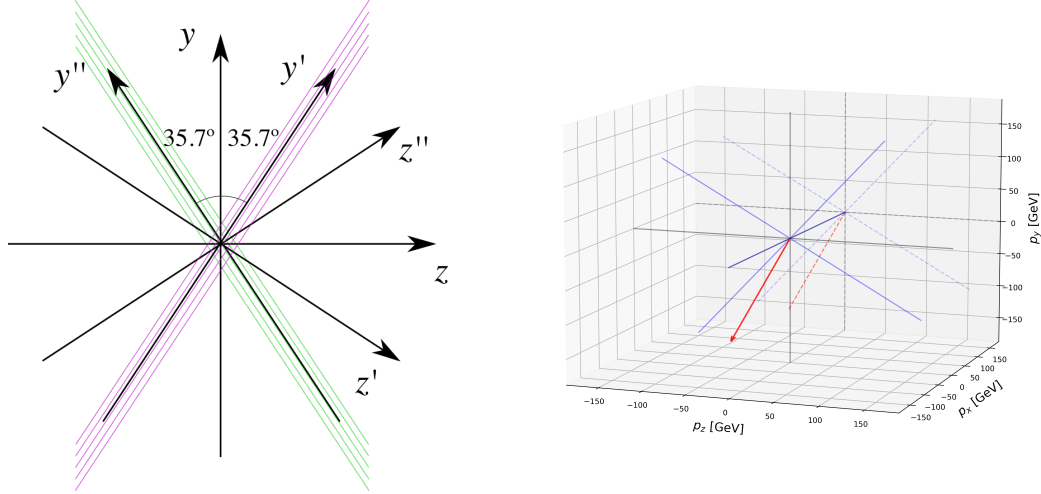


Figure 6.11: Left panel: schematic representation of the two new rotated reference frames used in this analysis (denoted as prime and double prime), viewed from the yz plane. The magenta stack of lines represent the wires in the U plane, whereas the green lines correspond to the wires in the V plane. Right panel: 3D representation of the momentum of one of the generated monoenergetic muons (red arrow) in the original reference frame (black lines), along with the new reference frame used for the U plane waveforms (blue lines). In the yz plane I added the projection of these three.

1581 U and V induction wires. Fig. 6.11 (left panel) shows a schematic representation of
 1582 the original reference frame together with the two rotated ones (denoted by primed and
 1583 double primed). This way, one can easily understand how parallel was a track to the
 1584 wires in the two induction planes. Fig. 6.11 (right panel) shows a 3D representation of
 1585 the momentum of a track (red arrow) in the original reference frame (black lines), along
 1586 with the new reference frame for U wires (blue lines). I added the projection in the yz
 1587 plane of this three, to show the usefulness of the new reference frame to tell whether a
 1588 track is parallel or normal to the wires in the induction plane.

1589 Fig. 6.12 shows the distribution of the average S/N improvement per event when one
 1590 applies the optimal matched filters. I produced separate distributions for the channels
 1591 in the U (red) and V (blue) induction wire planes. Notice that the S/N distributions
 1592 for the track-like particles, i.e. muons (top left panel) and protons (bottom left panel),
 1593 have significantly larger mean values than the distributions of the shower like particles,
 1594 i.e. electrons (top right panel) and neutral pions (bottom right panel). An important

6.5. Using simulated samples

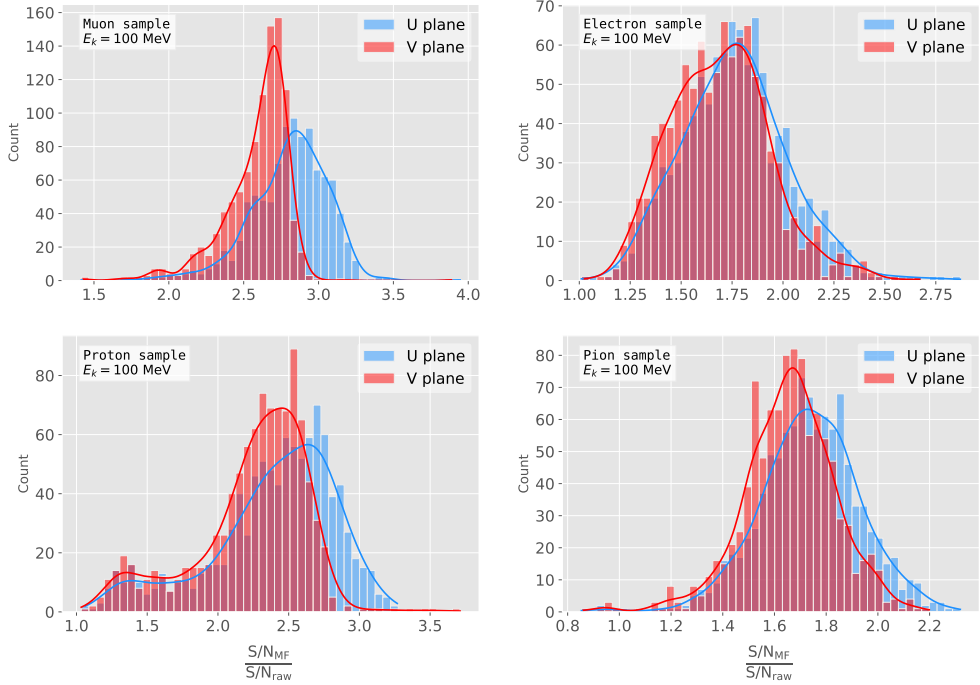


Figure 6.12: Distributions of the mean S/N improvement per event for the corresponding sample after applying the matched filters. Here I separated the change in the U plane (blue) and the V plane (red) channels. From top left to the right: muon, electron, proton and neutral pion. All the events have a fixed kinetic energy of $E_k = 100 \text{ MeV}$.

difference between these results and the ones seen before for ProtoDUNE data is that, overall, the improvements that I get for simulated data are bigger. This could be due either to the default noise model used in the *LArSoft* simulation or to the simulated hits having higher energy than the ones in the recorded data. Nonetheless, the concluding message is that the previously optimised matched filters give an overall significant improvement of the S/N for the different samples.

About the convention I followed for the plots and results, in the case of the raw and filtered S/N of each event in the sample I simply took the average of the quantities over all the active channels in the event. That is, if a certain event has N_{chan} active channels these two quantities are computed as:

$$(S/N_{fir})_{event} = \frac{\sum_{i=0}^{N_{chan}} (S/N_{fir})_i}{N_{chan}},$$

$$(S/N_{raw})_{event} = \frac{\sum_{i=0}^{N_{chan}} (S/N_{raw})_i}{N_{chan}}.$$
(6.18)

Chapter 6. Matched Filter approach to induction wire Trigger Primitives

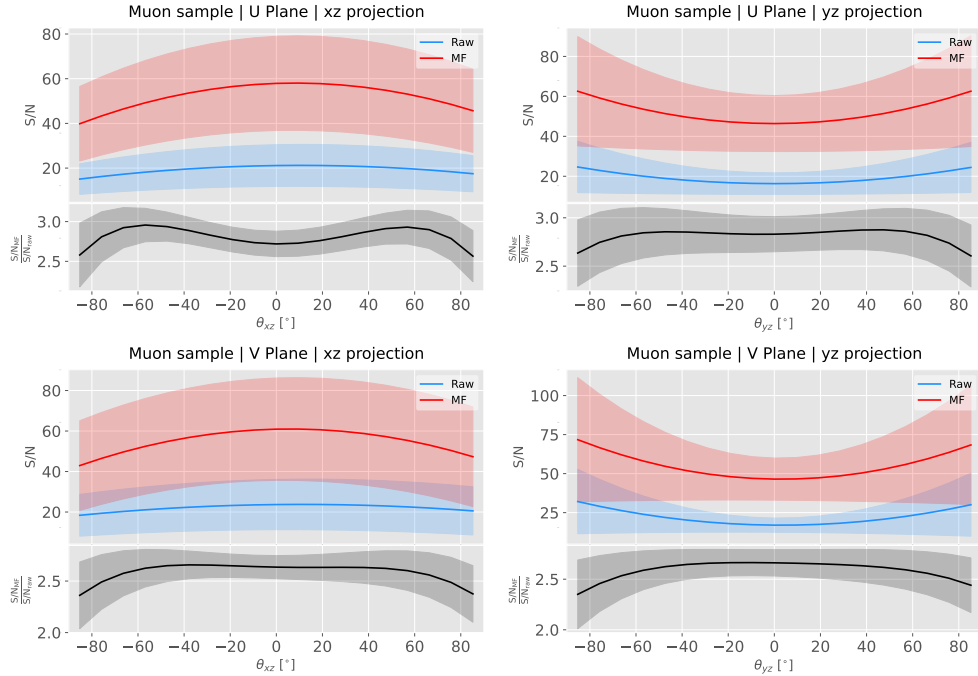


Figure 6.13: Angular dependence of the mean S/N and the S/N improvement, for the different monoenergetic samples considered (from top to bottom: electrons, muons, protons and neutral pions). The two columns on the left represent the values for the U plane waveforms. The top subplots show the mean S/N for raw (green) and filtered (red) waveforms whereas the bottom subplots depict the averaged S/N improvement (black).

1605 However, for the ratio of the raw and filtered S/N (what I called the S/N improvement)
 1606 per event I am not just taking the ratio of the previous two quantities but computing
 1607 the average of the individual ratios per channel in the event:

$$\left(\frac{S/N_{fir}}{S/N_{raw}} \right)_{event} = \frac{\sum_{i=0}^{N_{chan}} \left(\frac{S/N_{fir}}{S/N_{raw}} \right)_i}{N_{chan}}, \quad (6.19)$$

1608 and so:

$$\left(\frac{S/N_{fir}}{S/N_{raw}} \right)_{event} \neq \frac{(S/N_{fir})_{event}}{(S/N_{raw})_{event}}. \quad (6.20)$$

1609 6.5.1 Angular dependence

1610 Having these monoenergetic samples, one can also study the angular dependence of the
 1611 performance of the matched filter. This is an important point, as it is a well established
 1612 fact that for certain configurations (an extreme case configuration being signals normal

6.5. Using simulated samples

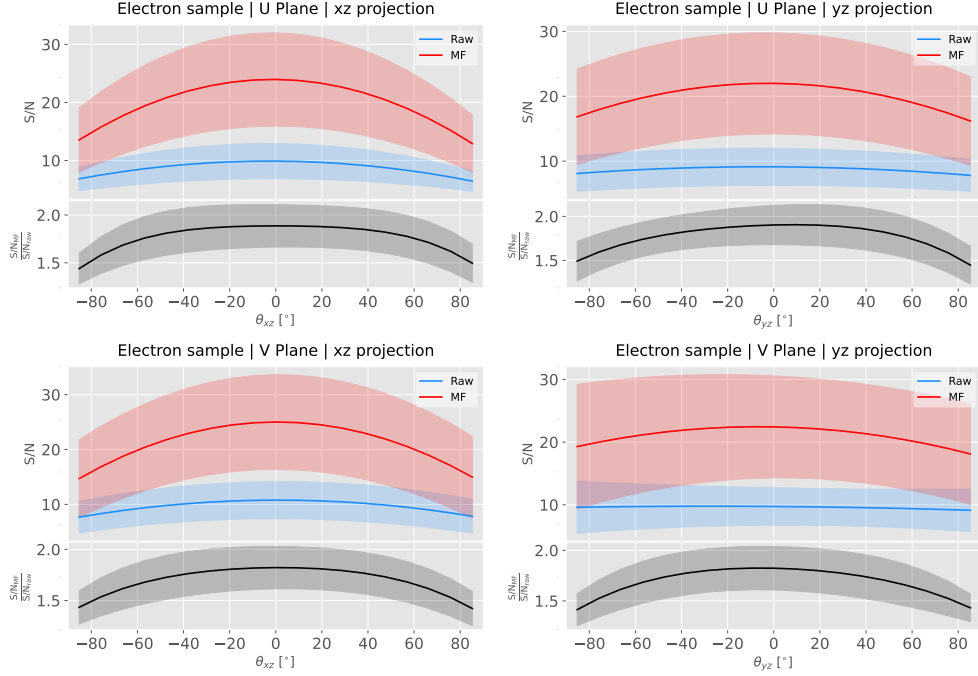


Figure 6.14: Angular dependence of the mean S/N and the S/N improvement, for the different monoenergetic samples considered (from top to bottom: electrons, muons, protons and neutral pions). The two columns on the left represent the values for the U plane waveforms. The top subplots show the mean S/N for raw (green) and filtered (red) waveforms whereas the bottom subplots depict the averaged S/N improvement (black).

to the wire plane and perpendicular to the induction wires at the same time) the S/N is
 much lower than average as the corresponding waveforms are severely distorted. In this
 sense, I am interested to see how the matched filter behaves for these cases and how the
 S/N improvement on those compare to the average.

Fig. 6.13 shows the angular dependence of the S/N for the monoenergetic $E_k = 100$ MeV isotropic muons, for the different induction wire planes and projections. The angles for each event are given by the components of the initial value of the momentum of the particles, taking the angles of the projections on the xz and yz planes with respect to the z axis (more accurately, one needs to compute these angles twice for each event, a pair for the $xy'z'$ coordinate system and the other for the $xy''z''$). The top row shows the dependence on the angles corresponding to the U plane, i.e. $\theta_{xz'}$ and $\theta_{y'z'}$, whereas the bottom row shows the angular dependence viewed from the V plane, $\theta_{xz''}$ and $\theta_{y''z''}$. In each plot, the top subplot represents the mean values of the S/N for the raw (blue) and

Chapter 6. Matched Filter approach to induction wire Trigger Primitives

1626 matched filtered (red) signals, and the bottom subplot the averaged S/N improvement
1627 (black). The solid lines represent the mean value obtained for the corresponding angular
1628 value, whereas the semitransparent bands represent one standard deviation around the
1629 mean at each point.

1630 As expected, the S/N is in general higher when tracks are parallel to the APA (i.e.
1631 $\theta_{xz} \sim 0$) and lower when it is normal to the plane ($\theta_{xz} \sim \pm 90^\circ$). In the same way, tracks
1632 parallel to the wires ($\theta_{yz} \sim \pm 90^\circ$) tend to have higher S/N than those perpendicular to
1633 these ($\theta_{yz} \sim \pm 0$).

1634 Fig. 6.14 shows the corresponding angular dependence information for the $E_k =$
1635 100 MeV electrons sample. Notice that, in this case, the S/N behaviour discussed above
1636 does not hold. A possible explanation can be that, because most hits in these events
1637 are produced by the secondary particles generated in the EM shower, the signal peaks
1638 whose S/N ratios were computed do not correspond to the directional information of
1639 the primary electron.

1640 6.5.2 Distortion and peak asymmetry

1641 As a little case of study, I selected two of the simulated $E_k = 100$ MeV monoenergetic
1642 muon events. With respect to the U induction plane, one is parallel to the APA (low
1643 $\theta_{xz'}$) and to the wires (high $\theta_{y'z'}$) and the other is normal to the APA plane (high $\theta_{xz'}$)
1644 and perpendicular to the wires (low $\theta_{y'z'}$). As expected from the results on the angular
1645 dependence discussed above, the former has a higher S/N (before and after the filtering)
1646 when compared to the latter. An interesting thing to notice about these two samples
1647 is that, even though one has a much bigger S/N than the other, it is the one with the
1648 smallest S/N the one that got the biggest averaged S/N improvement. In Table 6.1
1649 I included all the relevant parameters of these two $E_k = 100$ MeV muon events I am
1650 considering, namely, the angles with respect to the $xy'z'$ reference frame, the values of
1651 the S/N, the S/N improvement and also the so-called peak asymmetry Δ_{peak} that I will
1652 discuss next.

1653 One can try to understand better what is going on with these two events by looking

6.5. Using simulated samples

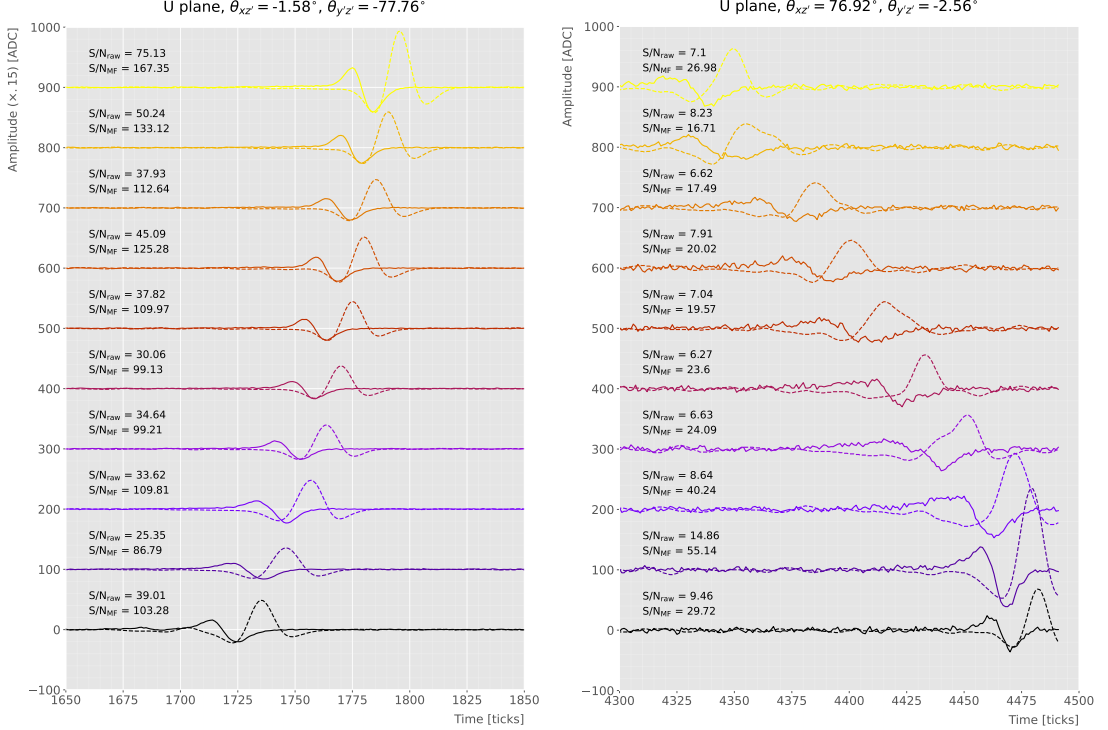


Figure 6.15: Selected consecutive waveforms corresponding to two monoenergetic $E_k = 100$ MeV muon events, one is parallel to the APA and to the wires in the U plane (left panel) and the other is normal to the APA plane and perpendicular to the U plane wires (right panel). The solid lines represent the raw waveforms whereas the dashed lines correspond to the waveforms after the matched filter was applied. The waveforms on the left panel have been scaled by a factor of 0.15 to have similar amplitude to the ones on the right panel.

Table 6.1: Characteristic parameters of the two monoenergetic muon events selected, relative to the U plane: projected angles in the xz' and yz' planes, S/N values for the raw and filtered waveforms, mean improvement of the S/N and peak asymmetry.

	$\theta_{xz'} (\circ)$	$\theta_{yz'} (\circ)$	S/N _{raw}	S/N _{MF}	$\frac{S/N_{MF}}{S/N_{raw}}$	Δ_{peak} (ADC)
High ("parallel")	-1.58	-77.76	41.65	112.44	2.83	-35.73
Low ("normal")	76.92	-2.56	8.07	25.46	3.12	-10.38

at the raw and filtered data from some of their active channels. Fig. 6.15 shows a selection of consecutive raw and filtered U plane waveforms from the event with high S/N (left panel) and the one with low S/N (right panel). Notice that to show both collections of waveforms at a similar scale I had to apply a factor of 0.15 to the waveforms with high S/N. Additionally, next to each waveform I included the values of the raw and matched filtered S/N for the corresponding channel. The first thing to notice in this plot

Chapter 6. Matched Filter approach to induction wire Trigger Primitives

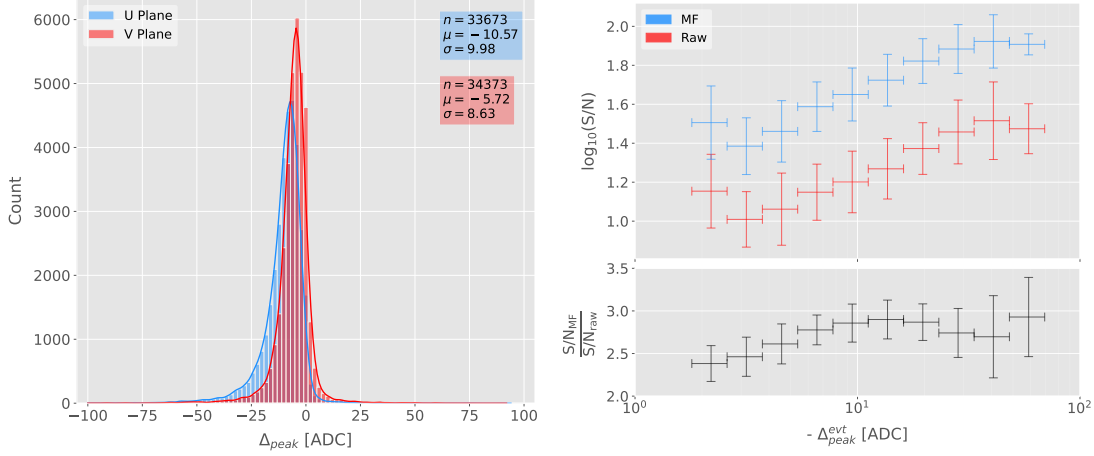


Figure 6.16: Left panel: peak asymmetry distribution for the case of the monoenergetic $E_k = 100$ MeV muon sample. Each value corresponds to a single bipolar signal peak from a channel in any event. The blue distribution represents the peaks on U plane channels, whereas the red corresponds to signal peaks in V wires. Right panel: relation between the mean peak asymmetry per event with the S/N for U channel waveforms from the $E_k = 100$ MeV muon sample. The top subplot shows the decimal logarithm of the mean S/N for the raw (red) and the matched filtered (blue) waveforms. The bottom subplot contains the mean S/N improvement ratio after the matched filter was applied.

is that the amplitude of the signal peaks from the normal track have a much smaller
 amplitude, and also appear quite distorted when compared to the others. On the other
 hand, although the matched filtered S/N is still smaller, the relative improvement is
 bigger than in the parallel case.

A way I found to quantify the difference between the shapes within these two events
 is their different peak asymmetry. One can define the peak asymmetry as the (signed)
 difference between the positive and the negative peaks of the bipolar shape, i.e.:

$$\Delta_{peak} \equiv h_+ - h_-, \quad (6.21)$$

where both heights h_+ and h_- are positive defined. Fig. 6.16 (left panel) shows the distribution of this peak asymmetry for all the waveforms corresponding to channels in the U (blue) and V (red) planes for the monoenergetic muon sample. One can see that these distributions are clearly shifted to negative values (with mean values $\mu_\Delta^U = -10.57$ ADC and $\mu_\Delta^V = -5.72$ ADC respectively). It is interesting to notice

6.5. Using simulated samples

that the peak asymmetry value of the sample with high S/N sits at the left tail of the distribution whereas the corresponding value of the sample with low S/N lies around the mean.

Now, one can try to correlate the peak asymmetry with the S/N and the S/N change per event. Fig. 6.16 (right panel) shows the result of comparing (minus) the mean peak asymmetry per event to the averaged raw (red) and matched filtered (blue) S/N per event (top subplot). The horizontal lines sit at the mean value obtained in the fit and represent the width of the $-\Delta_{peak}$ bins used, while the vertical lines indicate one standard deviation around that mean value. Notice that, when taking decimal logarithm on both, there is an approximate linear relation between these quantities, except for peak asymmetry values bigger than -5 ADC where the S/N remains constant.

Also, in the bottom subplot of Fig. 6.16 (right panel) I show the relation between the peak asymmetry and the mean S/N improvement. In this case, one see that there is a maximum at $\Delta_{peak} \sim -10$ ADC. As mentioned previously, this is also the value of the mean of the peak asymmetry distribution. In fact, it is expected that our filter favours the signal peaks with the most common values of the peak asymmetry, as this was one of the features I target in our filter coefficient optimisation through the parameter δ .

These results suggest that events with poorer values of the mean S/N, usually associated to non-favourable track orientations, tend to have smaller values of the mean peak asymmetry (in absolute value). Nonetheless, because our matched filters have been optimised to account for these asymmetries, the improvement on the S/N for these events is sizeable if not better than the one for events which already had a high S/N.

6.5.3 Hit sensitivity

One of the advantages of the matched filter, directly related to increasing the S/N, is the capability of picking hits that before fell below the threshold. For instance, Fig. 6.17 shows the raw ADC data from an example event (electron, $E_k = 100$ MeV) with the produced true hits superimposed (black boxes), together with the hits produced by the standard hit finder chain (blue circles), i.e. using the current FIR filter, and the hits

Chapter 6. Matched Filter approach to induction wire Trigger Primitives

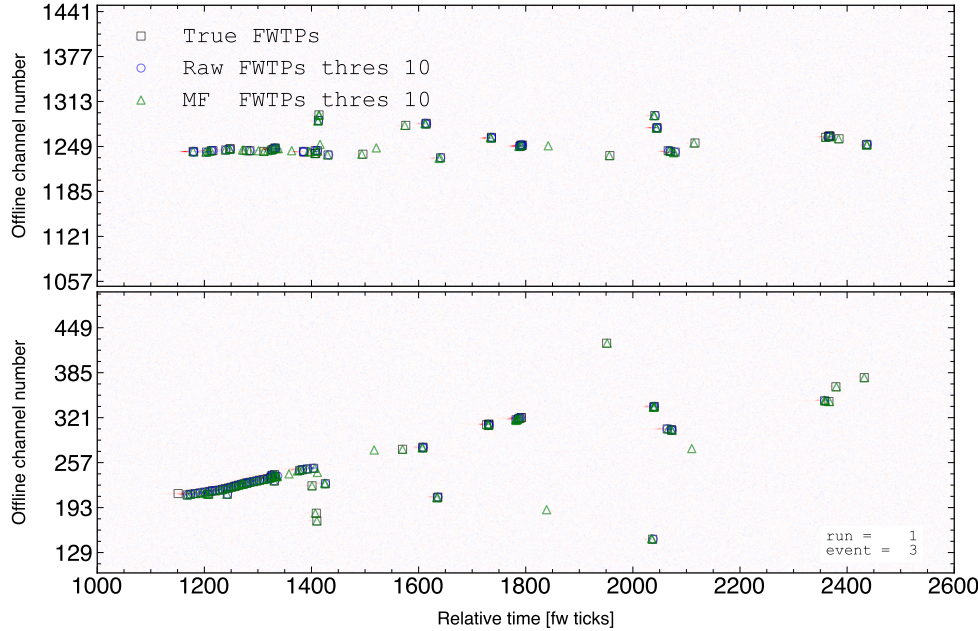


Figure 6.17: Raw data display in the plane time (in firmware ticks) vs. offline channel number for an $E_k = 100$ MeV electron event. The produced true hits are superimposed (black boxes) as well as the hits coming from the standard hit finder chain (blue circles) and the hit finder using the matched filter (green triangles).

1700 obtained using the matched filters (green triangles). Both the standard and the matched
 1701 filter hit finders were run with a threshold of 10 ADC. Notice that the standard hits
 1702 match well the true ones at the initial part of the event (where we have a track-like
 1703 object), but they miss most of the hits produced by the EM shower at later times. On
 1704 the other hand, the hits produced with the matched filter have a better agreement with
 1705 the true hits even for the more diffuse shower activity.

1706 Notwithstanding that now I get more hits with this combination of matched filter
 1707 and low threshold as a results of the enhancement of the signal peaks relative to the
 1708 noise level, it is also true that I pick some spurious hits not related to any real activity
 1709 if one lowers the thresholds too much. Therefore, some optimisation of the threshold is
 1710 needed. Basically one will need to make a trade-off between precision and sensitivity.

1711 Having this in mind, I tried to compare the produced hits one gets from the standard
 1712 hit finder and the ones resulting from applying the matched filter with the true hits.
 1713 By running the hit finders on our samples with different values of the threshold one

6.5. Using simulated samples

1714 can understand, for instance, how low one can set the threshold without getting mostly
1715 spurious hits and then evaluate the gains obtained from this.

1716 Because now I am also interested in seeing how the hit sensitivity changes with the
1717 energy, I prepared new isotropic samples with the same types of particles as before
1718 (muons, electrons, protons and neutral pions) but with a flat kinetic energy distribution
1719 ranging from 5 to 100 MeV.

1720 In order to estimate the hit sensitivity, given a certain sample, one needs to recover
1721 the set of true hits to be able to compare these with the ones produced. To do so,
1722 a modification in the procedure I was using to extract the raw waveforms is needed.
1723 For this kind of study I run the detector simulation in two steps, first I produce the
1724 waveforms without noise and extract them in the same format I used for the raw data,
1725 then the noise is added and the noisy waveforms are then written to a file as well.

1726 To have a better comparison between the true hits and the ones produced from
1727 the raw waveforms after applying the two filters, I applied also the FIR filter and the
1728 matched filters to the noiseless waveforms and then I run the hit finder with a minimal
1729 threshold (in this case I used 1 ADC) on these noiseless filtered waveforms. In this way
1730 I generated two sets of true hits, I will refer to them as standard true hits (with the
1731 current/default FIR filter) and matched filter true hits respectively. This allows a more
1732 precise matching between the different groups of hits produced, as it will account for
1733 any delays and distortions introduced by the FIR and the matched filters.

1734 In the case of the raw waveforms (with noise), I run the hit finder on them, with
1735 different values of the threshold, after applying either the FIR or the matched filters. I
1736 will name them simply standard hits and matched filter hits respectively. Then, I match
1737 the generated hits to the true hits (the standard hits with the standard true hits and
1738 the matched filter hits with the matched filter true hits). The matching is performed by
1739 comparing the channel number and the timestamp of the hits. To count as a match,
1740 I require that all hits with the same channel number and timestamp have overlapping
1741 hit windows, i.e. the time windows between their hit end and hit start times need to
1742 overlap. If more than one hit in one of the groups have hit overlap with the same hit in

Chapter 6. Matched Filter approach to induction wire Trigger Primitives

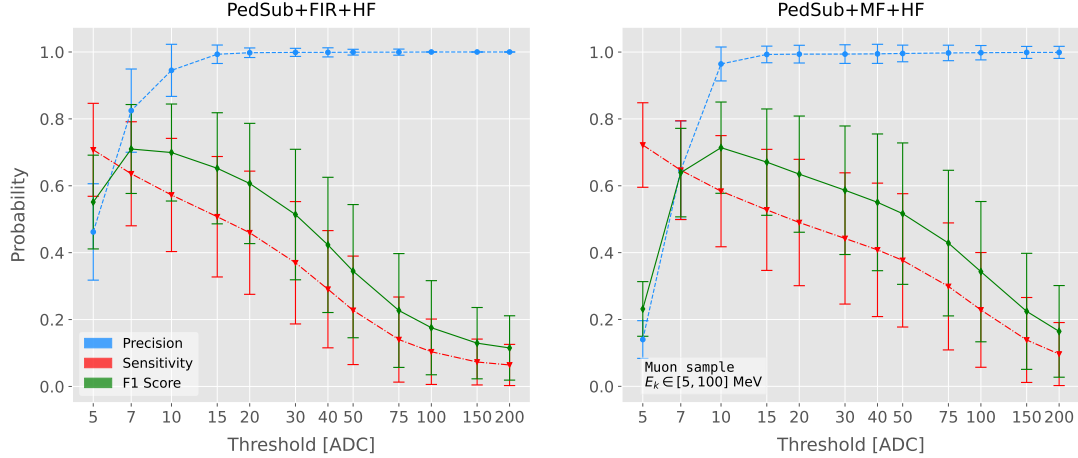


Figure 6.18: Dependence of the precision (blue), sensitivity (red) and F_1 (green) scores on the threshold values used in the hit finder, for the FIR (left panel) and matched filter (right panel) cases. The results were obtained after matching the hits to the true hits in the case of the isotropic muon sample with kinetic energy in the range 5 to 100 MeV, taking only into account the induction plane channels. The points represent the mean value while the error bars indicate one standard deviation around that mean value.

1743 the other group I only count the hit with closer hit peak time value.

1744 The generation of the samples, the procedure to produce the standard hits (with the
 1745 default FIR filter) and matched filter hits and the matching of these with the true hits
 1746 is described in detail in App. ??.

1747 To quantify the performance of the two hit finder approaches, I use a classical method
 1748 from statistical classification known as confusion matrix [68]. This is basically a way of
 1749 sorting the outputs of a binary classifier, considering the true values of the classification
 1750 and the predicted values. It divides the outputs in four categories: true positive (TP,
 1751 both true and predicted values are 1), false negative (FN, true value is 1 but predicted
 1752 is 0), false positive (FP, true value is 0 but predicted is 1) and true negative (TN, both
 1753 true and predicted values are 0)).

1754 The contents of the confusion matrix allow us to compute other derived scores to
 1755 judge the performance of our classifiers. In this study, I will make use of three of these
 1756 metrics, namely the precision or positive predictive value:

$$\text{PPV} = \frac{\text{TP}}{\text{TP} + \text{FP}}, \quad (6.22)$$

6.5. Using simulated samples

1757 the sensitivity or true positive rate:

$$\text{TPR} = \frac{\text{TP}}{\text{TP} + \text{FN}}, \quad (6.23)$$

1758 and the F_1 score [69]:

$$F_1 = \frac{2\text{TP}}{2\text{TP} + \text{FP} + \text{FN}}, \quad (6.24)$$

1759 which is the harmonic mean of the precision and the sensitivity.

1760 In our specific case I am not going to make use of the true negative value, as its
1761 definition in this context can be ambiguous because one does not have clear instances in
1762 the classification process. This way, I will only count the number of true positives as the
1763 total amount of hits I can match between true and raw populations, the number of false
1764 negatives will be the number of missing true hits and the false positive the number of
1765 hits which do not match any true hit.

1766 In Fig. 6.18 I show the precision (blue), sensitivity (red) and F_1 (green) scores I
1767 obtained for different values of the threshold used in the hit finder for the case of the
1768 muon sample. Because the matched filters are only applied to induction channels, I only
1769 consider here hits coming from the U and V planes. The panel on the left corresponds
1770 to the scores I got when I ran the hit finder on the FIR filtered waveforms, whereas the
1771 right panel contains the scores for the matched filter case. The points are centered at
1772 the threshold value used and represent the mean value obtained for each score using all
1773 the generated events, while the error bars indicate one standard deviation around the
1774 mean value.

1775 One can see that the precision for the matched filter case is lower when the thresholds
1776 are very low, as the noise baseline is slightly amplified, but then rises to high values
1777 quicker than for the FIR case. The other difference one can spot is that the sensitivity
1778 in the FIR case starts dropping faster at around the same threshold values where the
1779 precision stabilizes around 1, while in contrast for the matched filter this rapid decrease
1780 starts at higher threshold values. A similar scan for the same thresholds was performed
1781 for the electron sample in the same energy range, yielding similar results.

Chapter 6. Matched Filter approach to induction wire Trigger Primitives

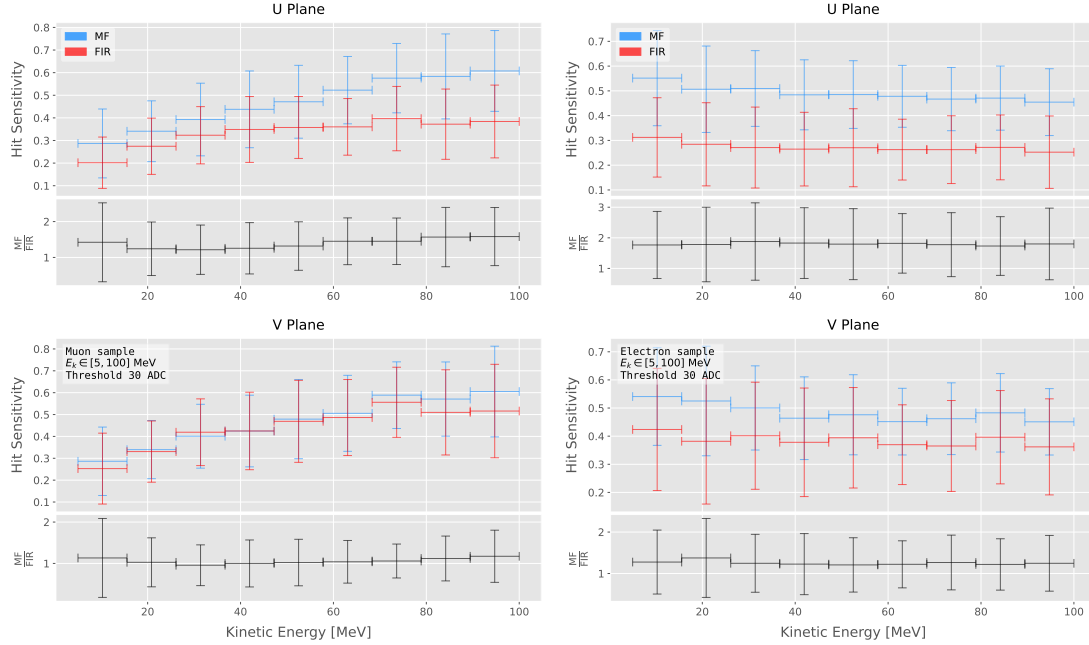


Figure 6.19: Dependence of the averaged hit sensitivity on the kinetic energy of the events for the matched filter (blue) and standard (red) hits, for the case of the muon (left panel) and electron (right panel) samples, separated between U (top plots) and V (bottom plots) induction wire planes. The top subplots contain the hit sensitivities for the two hit finder alternatives, while the bottom subplots show the ratio between the two. The horizontal lines sit at the mean value and represent the size of the energy bins, while the vertical error bars indicate one standard deviation around that mean value.

1782 In Fig. 6.19 I show the averaged hit sensitivity versus the kinetic energy of the
 1783 events, both for the matched filter hits (blue) and the standard hits (red). The left
 1784 panel corresponds to the muon sample, whereas the one on the right corresponds to the
 1785 electron sample, both with kinetic energies between 5 and 100 MeV. In each panel the
 1786 top plot corresponds to hits in the U plane, while the bottom plot contains the same
 1787 information for the V plane. Each plot contains two subplots, the one on the top shows
 1788 the hit sensitivity values for the matched filter and standard hits separate, while the
 1789 bottom subplot depicts the ratio between the matched filter and standard sensitivities.
 1790 The horizontal lines are placed at the mean value obtained in the fit and represent the
 1791 width of the E_k bins used, while the vertical error bars indicate one standard deviation
 1792 around that mean value. In both cases the threshold used was 30 ADC, as I required
 1793 the precision to be higher than 0.99 for both matched filter and standard cases.

6.5. Using simulated samples

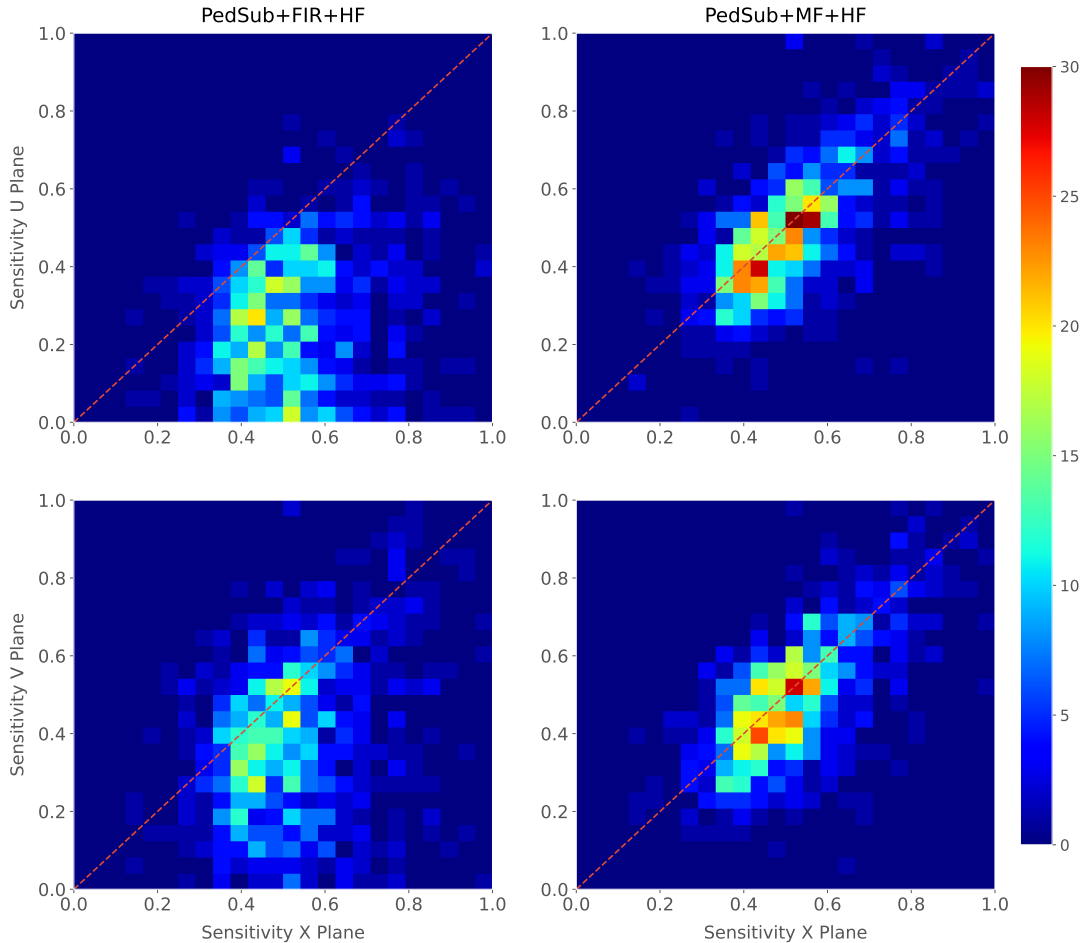


Figure 6.20: Distributions of the hit sensitivity in the U (top panels) and V (bottom panels) planes versus the hit sensitivity in the X plane, both for the standard hits (left panels) and the matched filter hits (right panels), in the case of the electron sample and a threshold of 30 ADC.

1794 One can see that, in general, the improvements are better for the U than for the V
 1795 plane. While for the U channels I achieved a mean improvement of 50% and 80% for
 1796 muons and electrons respectively, the improvement in the V plane is stalled at 10% and
 1797 25%. Nevertheless, if I look at the sensitivities for the matched filter hits in both planes
 1798 one can see these have similar mean values for each energy bin, while on the contrary
 1799 for the standard hits the sensitivity remains relatively high for the V plane. This way, it
 1800 looks there was a less significant gain because the hit sensitivity was already high.

1801 Another interesting observation is the different behaviors for muons and electrons.
 1802 While hit sensitivity for muons grows significantly with energy, in the case of electrons

Chapter 6. Matched Filter approach to induction wire Trigger Primitives

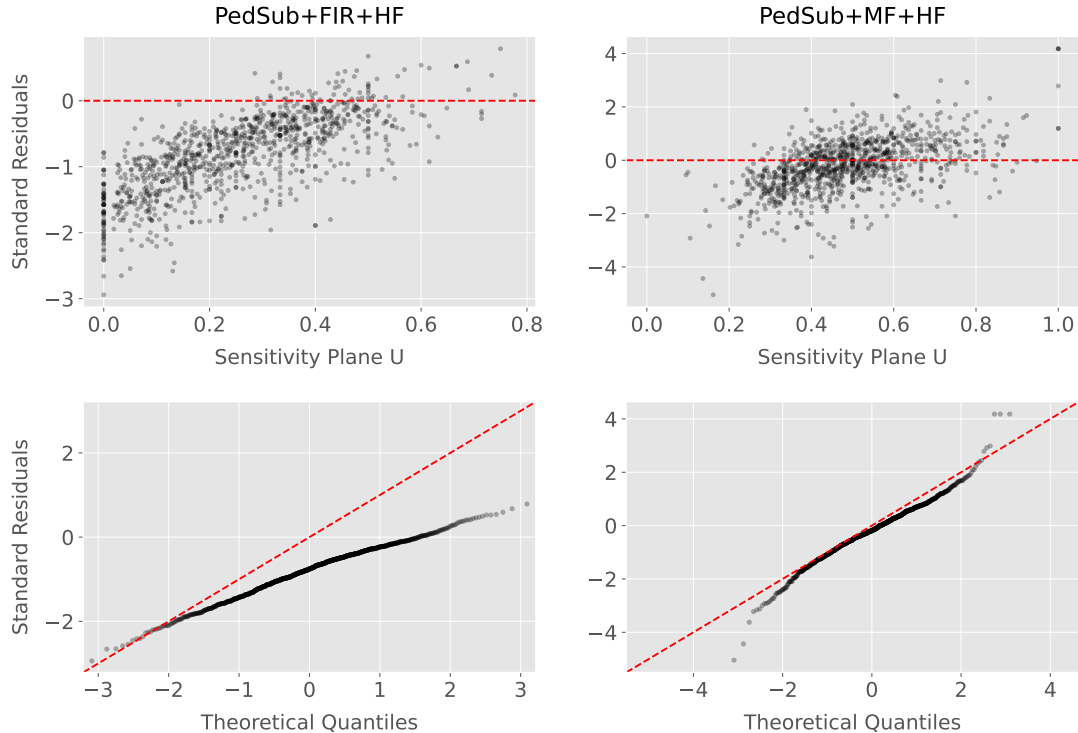


Figure 6.21: Top panels: standard residual plots of the hit sensitivities between the X and U planes. Bottom panels: quantile-quantile plots of the hit sensitivity standard residuals between the X and U planes. In all cases, the left panel corresponds to the standard hits while the right panel represents the matched filter case, all from the electron sample with a 30 ADC threshold.

1803 this slightly decreases the higher the kinetic energy of the event is. In any case, when it
 1804 comes to the improvement on the sensitivities, this remains almost constant in all cases.

1805 Furthermore, we can look at how the concurrence of hits between the different wire
 1806 planes has changed. For any given event, I expect to have a similar number of hits in the
 1807 three planes. As the ionisation electrons need to cross the U and V planes prior to reach
 1808 the collection plane X they will induce current in those wire planes. A way to check the
 1809 concurrence of hits across planes is looking at the relation between the hit sensitivities
 1810 for each individual event. One cannot expect the sensitivities to be exactly equal across
 1811 planes, but ideally they should be normally distributed around the diagonal.

1812 Fig. 6.20 shows the hit sensitivity in the U (top panels) and V (bottom panels)
 1813 planes versus the hit sensitivity in the X plane, for the case of the standard hits (left
 1814 panels) and the matched filter hits (right panels). All plots were generated for the

6.5. Using simulated samples

1815 electron sample and a threshold of 30 ADC. From these one can see a clear trend,
1816 when I use the standard hit finder chain the sensitivities in the induction planes are
1817 systematically lower than the hit sensitivity in the X plane, i.e. most of the points sit
1818 below the diagonal (red dashed line). In contrast, when the matched filters are applied,
1819 the majority of the events are distributed around the diagonal. This points out that the
1820 concurrence of hits across planes has improved.

1821 To exemplify the improvement I obtained, one can consider the residuals of the hit
1822 sensitivities for the X and U planes. Assuming the diagonal hypothesis, i.e. given a
1823 dataset of the form (x, y) for any x I take the predicted y value to be equal to the value
1824 of x , I can compute the standard residuals for the hit sensitivities in U given the ones for
1825 X. In Fig. 6.21 (top panels) I show these standard residuals against the corresponding
1826 values of the hit sensitivity in the U plane, for our electron sample with kinetic energy
1827 between 5 and 100 MeV. If I compare the scatter points in the case of the standard
1828 hits (left panel) and the matched filter hits (right panel), I see that the residuals of the
1829 standard hit finder case follow a certain pattern and their mean deviates from 0.

1830 To see clearly if the residuals are normally distributed, in Fig. 6.21 (bottom panels)
1831 I plot the corresponding quantile-quantile plot for both the standard (left panel) and
1832 matched filter (right panel) standard residuals. One can clearly see that the points for
1833 the standard case follow a strongly non-linear pattern, suggesting that the residuals
1834 do not follow a normal distribution. In contrast, for the matched filter hits the points
1835 conform to a roughly linear path, implying that in this case the normality condition is
1836 fulfilled.

1837 All these results hint at the fact that the concurrence of hits across the wire planes
1838 can be strengthened by applying the matched filters.

1839 **Chapter 7**

1840 **DM searches with neutrinos from
1841 the Sun**

1842 **7.1 Motivation**

1843 The idea of detecting neutrino signals coming from the Sun’s core to probe DM is not new.
1844 The main focus of these searches has usually been high-energy neutrinos originated from
1845 DM annihilations into heavy particles [70–73], although recent studies have proposed to
1846 look at the low-energy neutrino flux arising from the decay of light mesons at rest in the
1847 Sun [74–77] previously thought undetectable.

1848 In this chapter I try to demonstrate the capability of DUNE to constrain different
1849 DM scenarios. I used the neutrino fluxes arising from DM annihilations in the core
1850 of the Sun to compute the projected limits that DUNE would be able to set on the
1851 annihilation rates in the Sun and the DM scattering cross sections.

1852 **7.2 Gravitational capture of DM by the Sun**

1853 The Sun and the centre of the Earth are possible sources of DM annihilations, specially
1854 interesting because of their proximity. Their gravitational attraction ensured the capture
1855 of DM from the local halo through repeated scatterings of DM particles crossing them.

Chapter 7. DM searches with neutrinos from the Sun

1856 Only neutrinos produced from DM annihilations can escape the dense interior of these
1857 objects. Therefore, neutrino telescopes are the most useful experimental layouts to
1858 pursue DM searches from their cores.

1859 The neutrino flux from DM annihilations inside the Sun depends on the DM capture
1860 rate, which is proportional to the DM scattering cross section, and the annihilation rate,
1861 which is proportional to the velocity-averaged DM annihilation cross-section. The total
1862 number of DM particles inside the Sun follows the Boltzmann equation [74]:

$$\frac{dN_{DM}}{dt} = C_{\odot} - A_{\odot} N_{DM}^2, \quad (7.1)$$

1863 where C_{\odot} and A_{\odot} are the total Sun DM capture and annihilation rates respectively.
1864 In this expression I neglected the evaporation term, proportional to N_{DM} , which only
1865 contribute for $m_{DM} \lesssim 4$ GeV [78]. As the current threshold of neutrino telescopes is
1866 a few GeV, this region falls below the probed range but can be important in future
1867 low-energy projects.

1868 This equation has an equilibrium solution:

$$N_{DM}^{eq} = \sqrt{\frac{C_{\odot}}{A_{\odot}}}, \quad (7.2)$$

1869 which represents the amount of DM inside the Sun if the capture and annihilation have
1870 reached equilibrium. As the Sun is approximately 4.6 Gyr old, it is usually assumed that
1871 equilibrium has been achieved. Therefore, the anomalous neutrino flux from the Sun
1872 would only depend on the DM scattering cross section, enabling us to set limits on this
1873 quantity. If one does not assume equilibrium, some assumptions on the DM annihilation
1874 cross section are necessary to extract predictions from neutrino signals.

1875 Here, I am going to consider three possible scenarios for the DM interactions: DM
1876 scattering off electrons, spin-dependent (SD) and spin-independent interactions off nuclei.
1877 For the case of these last two, the cross sections will be given in terms of the SD and
1878 SI elastic scattering DM cross section off protons (assuming that DM interactions off

7.2. Gravitational capture of DM by the Sun

1879 protons and neutrons are identical), σ_p^{SD} and σ_p^{SI} , as [4, 74]:

$$\sigma_i^{\text{SD}} = \left(\frac{\tilde{\mu}_{A_i}}{\tilde{\mu}_p} \right)^2 \frac{4(J_i + 1)}{3J_i} |\langle S_{p,i} \rangle + \langle S_{n,i} \rangle|^2 \sigma_p^{\text{SD}}, \quad (7.3)$$

$$\sigma_i^{\text{SI}} = \left(\frac{\tilde{\mu}_{A_i}}{\tilde{\mu}_p} \right)^2 A_i^2 \sigma_p^{\text{SI}}, \quad (7.4)$$

1880 where $\tilde{\mu}_{A_i}$ is the reduced mass of the DM-nucleus i system, $\tilde{\mu}_p$ is the reduced mass of
1881 the DM-proton system, A_i and J_i the mass number and total angular momentum of
1882 nucleus i and $\langle S_{p,i} \rangle$ and $\langle S_{n,i} \rangle$ the expectation value of the spins of protons and neutrons
1883 averaged over all nucleons, respectively (see Ref. [79] for a review on spin expectation
1884 values).

1885 Since the Sun is mainly composed of Hydrogen, the capture of DM from the halo
1886 is expected to occur mainly through spin-dependent scattering. However, since the
1887 spin-independent cross section is proportional to the square of the atomic mass, heavy
1888 elements can contribute to the capture rate (even though they constitute less than 2%
1889 of the mass of the Sun). Heavy elements can also contribute to the spin-dependent cross
1890 section if the DM has also momentum-dependent interactions.

1891 DM particles can get captured by the Sun if after repeated scatterings off solar
1892 targets their final velocity is lower than the escape velocity of the Sun. In the limit of
1893 weak cross sections, this capture rate can be approximately written as [4]:

$$C_{\odot}^{\text{weak}} = \sum_i \int_0^{R_{\odot}} dr 4\pi r^2 \int_0^{\infty} du_{\chi} \frac{\rho_{\chi}}{m_{\chi}} \frac{f_{v_{\odot}}(u_{\chi})}{u_{\chi}} \omega(r) \int_0^{v_e(r)} dv R_i^-(\omega \rightarrow v) |F_i(q)|^2, \quad (7.5)$$

1894 where the summation extends over all possible nuclear targets. In this expression, R_{\odot}
1895 is the radius of the Sun, ρ_{χ} is the local DM density, m_{χ} the mass of the DM particle,
1896 $f_{v_{\odot}}(u_{\chi})$ the DM velocity distribution seen from the Sun's reference frame, $R_i^-(\omega \rightarrow v)$
1897 is the differential rate at which a DM particle with velocity v scatters a solar target of
1898 mass m_i to end up with a velocity ω and $|F_i(q)|$ is the nuclear form factor of target i .

1899 The differential scattering rate takes a rather simple form when considering velocity-

Chapter 7. DM searches with neutrinos from the Sun

1900 independent and isotropic cross sections. In that case, this quantity is given by [4, 80]:

$$R_i^-(\omega \rightarrow v) = \frac{2}{\sqrt{\pi}} \frac{\mu_{i,+}^2}{\mu_i} \frac{v}{\omega} n_i(r) \sigma_i \left[\chi(-\alpha_-, \alpha_+) + \chi(-\beta_-, \beta_+) e^{\mu_i(\omega^2 - v^2)/u_i^2(r)} \right], \quad (7.6)$$

1901 where μ_i is the ratio between the DM mass and the mass of target i , $\mu_{i,\pm}$ is defined as:

$$\mu_{i,\pm} \equiv \frac{\mu_i \pm 1}{2}, \quad (7.7)$$

1902 $n_i(r)$ is the density profile of target i in the solar medium, $u_i(r)$ is the most probable

1903 velocity of target i given by:

$$u_i(r) = \sqrt{\frac{2T_\odot(r)}{m_i}}, \quad (7.8)$$

1904 where $T_\odot(r)$ is the temperature of the Sun, the quantities α_\pm and β_\pm are defined as:

$$\alpha_\pm \equiv \frac{\mu_{i,+}v \pm \mu_{i,-}\omega}{u_i(r)}, \quad (7.9)$$

$$\beta_\pm \equiv \frac{\mu_{i,-}v \pm \mu_{i,+}\omega}{u_i(r)}, \quad (7.10)$$

1905 and the function $\chi(a, b)$ is a Gaussian integral of the form:

$$\chi(a, b) \equiv \int_a^b dx e^{-x^2}. \quad (7.11)$$

1906 Finally, if one assumes the DM halo velocity distribution in the galactic rest frame

1907 to be a Maxwell-Boltzmann distribution, one can write the halo velocity distribution for

1908 an observer moving at the speed of the Sun with respect to the DM rest frame as:

$$f_{v_\odot}(u_\chi) = \sqrt{\frac{3}{2\pi}} \frac{u_\chi}{v_\odot v_d} \left(e^{-\frac{3(u_\chi - v_\odot)^2}{2v_d^2}} - e^{-\frac{3(u_\chi + v_\odot)^2}{2v_d^2}} \right), \quad (7.12)$$

1909 where:

$$\omega^2 = u_\chi + v_e(r)^2, \quad (7.13)$$

1910 is the DM velocity squared, v_\odot the relative velocity of the Sun from the DM rest frame

7.2. Gravitational capture of DM by the Sun

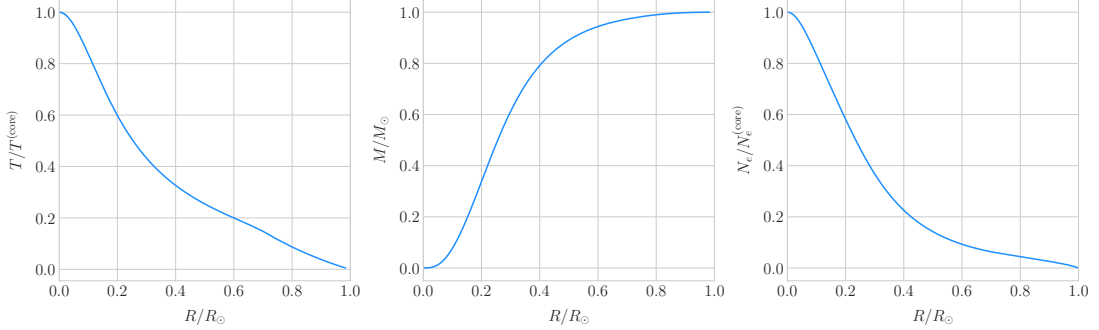


Figure 7.1: Input solar parameters used in our capture rate computation as functions of the Sun's radius, from left to right: temperature (with respect to the temperature at the core), mass (in solar masses) and electron number density (with respect to the electron density at the core). All quantities shown correspond to the standard solar model BS2005-OP [3].

and $v_d \simeq \sqrt{3/2}v_\odot$ the velocity dispersion.

For the case of strong scattering cross section, Eq. (7.5) ceases to be valid, as it escalates indefinitely with the cross section. In that limit, the capture rate saturates to the case where the probability of interaction is equal to one, which can be written as:

$$C_\odot^{\text{geom}} = \pi R_\odot^2 \left(\frac{\rho_\chi}{m_\chi} \right) \langle v \rangle \left(1 + \frac{3}{2} \frac{v_e^2(R_\odot)}{v_d^2} \right) \xi(v_\odot, v_d), \quad (7.14)$$

where $v_d = \sqrt{8/3\pi}v_\odot$ is the mean velocity in the DM rest frame and the factor $\xi(v_\odot, v_d)$ accounts for the suppression due to the motion of the Sun:

$$\xi(v_\odot, v_d) = \frac{v_d^2 e^{-\frac{3v_\odot^2}{2v_d^2}} + \sqrt{\frac{\pi}{6}} \frac{v_d}{v_\odot} (v_d^2 + 3v_e^2(R_\odot) + 3v_\odot^2) \text{Erf} \left(\sqrt{\frac{3}{2}} \frac{v_\odot}{v_d} \right)}{2v_d^2 + 3v_e^2(R_\odot)}. \quad (7.15)$$

Having these into account, one can write the total capture rate as a combination of both contributions, allowing a smooth transition between the two, as:

$$C_\odot = C_\odot^{\text{weak}} \left(1 - e^{C_\odot^{\text{geom}}/C_\odot^{\text{weak}}} \right). \quad (7.16)$$

I computed the capture rate from Eq. (7.16) in the case of interactions with electrons. To do so, I used the standard solar model BS2005-OP [3]. Fig. 7.1 shows the

Chapter 7. DM searches with neutrinos from the Sun

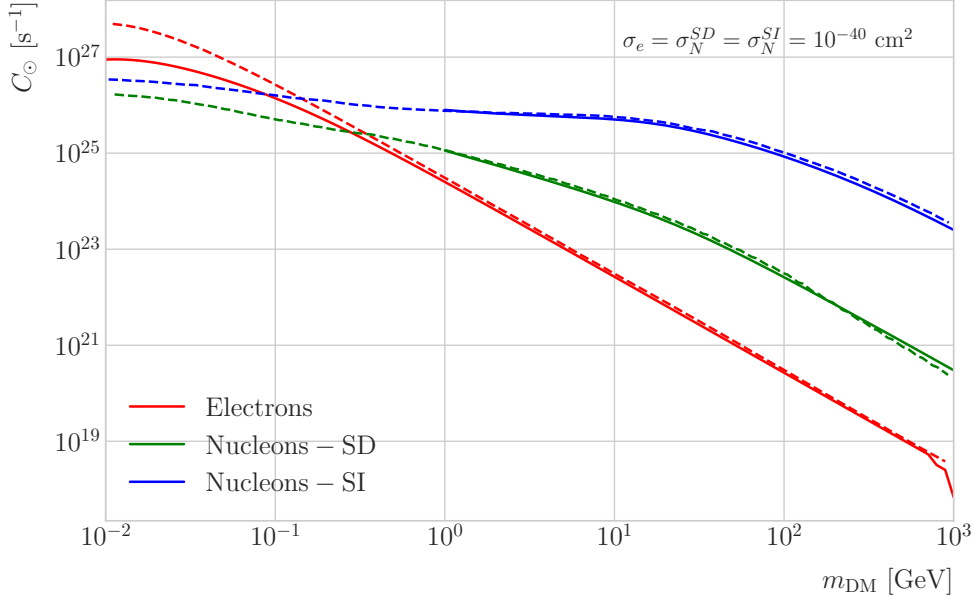


Figure 7.2: Capture rates as a function of the DM mass for the DM-electron interactions (red lines), SD DM-nucleons interactions (green lines) and SI DM-nucleons interactions (blue lines). Solid lines represent the values computed in this work while the dashed lines are the one given in Ref. [4]. All the rates are shown for a choice of scattering cross section of $\sigma_i = 10^{-40} \text{ cm}^2$.

1921 three parameters from the solar model that are needed for the computation, the solar

1922 temperature (left panel), mass (central panel) and electron density (right panel) profiles.

1923 For the case of the interactions off nuclei, the computations are more convoluted

1924 as one needs to add up the contributions of the different most abundant nuclei in

1925 the Sun. Also, in contrast to the electron scenario where the form factor is trivially

1926 $|F_e(q)|^2 = 1$, for any nucleus i one would need to consider some appropriate nuclear

1927 density distribution (either a Gaussian approximation, a Woods-Saxon distribution, etc)

1928 which would complicate the calculations even further.

1929 That is the reason why, at this stage of our study, I decided to take an alternative

1930 approach to the computation of the DM-nucleus capture rates. I used the **DarkSUSY**

1931 software, that allows us to compute these quantities performing a full numerical

1932 integration over the momentum transfer of the form factors. The default standard

1933 solar model used by **DarkSUSY** is BP2000¹ [81].

¹This is what they say in their manual, but I fear it is somewhat outdated. It appears to me this

7.2. Gravitational capture of DM by the Sun

1934 In Fig. 7.2 I show the results I obtained for the capture rates, for the case of
 1935 interactions off electrons (red solid line), SD (green solid line) and SI (blue solid line)
 1936 interactions of nucleons. In all cases I used a value of the scattering cross sections of
 1937 $\sigma_i = 10^{-40} \text{ cm}^2$. Note here one of the limitations of the **DarkSUSY** approach, one can
 1938 not extend the computation below $m_{\text{DM}} = 1 \text{ GeV}$. Nevertheless, this is not something
 1939 to worry about in this case, as I will discuss next. As a comparison, I added also the
 1940 values computed in Ref. [4] (same color scheme, dashed lines). One can see there is good
 1941 agreement between these and the **DarkSUSY** computation of the SD and SI interactions
 1942 for $m_{\text{DM}} \geq 1 \text{ GeV}$. In this regime their computations also matches quite well our
 1943 result for the electron capture rate. However, these start to differ significantly below
 1944 $m_{\text{DM}} = 1 \text{ GeV}$, being their estimate up to a factor of 5 bigger than ours for low masses.

1945 Let us comment briefly about the assumption I made before about not including
 1946 an evaporation term in the Boltzmann equation. If I include this term in the equation
 1947 (which will be proportional to the number of DM particles) the equilibrium solution
 1948 takes the form:

$$N_{\text{DM}}^{eq} = \sqrt{\frac{C_\odot}{A_\odot}} \frac{1}{\kappa + \frac{1}{2} E_\odot \tau_{eq}}, \quad (7.17)$$

1949 where E_\odot is the total evaporation rate, τ_{eq} is the equilibrium time in the absence of
 1950 evaporation:

$$\tau_{eq} = \frac{1}{\sqrt{C_\odot A_\odot}}, \quad (7.18)$$

1951 and κ is defined as:

$$\kappa \equiv \sqrt{1 + \left(\frac{E_\odot \tau_{eq}}{2} \right)^2}. \quad (7.19)$$

1952 Now, it is easy to proof that in case evaporation dominates $\kappa \gg 1$ and therefore:

$$N_{\text{DM}}^{eq} \simeq \frac{C_\odot}{E_\odot}. \quad (7.20)$$

1953 In contrast, if evaporation is irrelevant $\kappa \simeq 1$ and one recovers Eq. (7.2).

model is relatively old and do not see why they are not using others like [3]. Maybe one can double-check in the code to make sure.

Chapter 7. DM searches with neutrinos from the Sun

1954 In this way, one can define the evaporation mass as the mass for which the number
1955 of DM particles in equilibrium approaches Eq. (7.20) at 10% level:

$$\left| N_{DM}^{eq}(m_{\text{evap}}) - \frac{C_{\odot}(m_{\text{evap}})}{E_{\odot}(m_{\text{evap}})} \right| = 0.1 N_{DM}^{eq}(m_{\text{evap}}). \quad (7.21)$$

1956 This can be regarded as the minimum testable mass one can reach using the annihilation
1957 products of the DM in the Sun.

1958 It was reported in Ref. [4] that, in the case of both SD and SI DM interactions
1959 off nuclei, this value ranges from 2 to 4 GeV depending on the specific scattering
1960 cross section value, compatible with the usual assumptions in the literature. What is
1961 interesting is the case of the electron capture. It was found that, when one applies a
1962 cutoff in the velocity distribution of the DM trapped in the Sun slightly below the escape
1963 velocity, the evaporation mass for the DM-electron interaction decreases remarkably. For
1964 a moderate choice of $v_c(r) = 0.9v_e(r)$ one gets an evaporation mass of around 200 to
1965 600 MeV. This possibility opens a region of the parameter space that could be tested
1966 with neutrino detectors.

1967 7.3 Neutrino flux from DM annihilations

1968 When WIMPs annihilate inside the Sun a flux of high-energy neutrinos is expected from
1969 heavy quarks, gauge bosons and $\tau^+\tau^-$ final states, which decay before losing energy
1970 in the dense solar medium, as they will produce a continuum spectra up to $E_{\nu} \sim m_{\chi}$
1971 (in the case of direct annihilation to neutrinos one would have a line at $E_{\nu} = m_{\chi}$) [75].
1972 This kind of signal has been extensively studied in the literature, allowing to put strong
1973 limits on the SD WIMP-proton cross section for large m_{χ} . However, the number of
1974 high-energy neutrinos per WIMP annihilation is small and the spectrum depends on the
1975 unknown final state. Moreover, background rejection is easier for large m_{χ} but neutrinos
1976 with $E_{\nu} \gtrsim 100$ GeV are significantly attenuated by interactions in the Sun.

1977 Nevertheless, most WIMP annihilation final states eventually produce a low-energy
1978 neutrino spectrum. In this case one does not just consider the more massive final

7.4. Computing limits from solar neutrino fluxes

states but also annihilations into e^+e^- , $\mu^+\mu^-$ and light quarks [74]. In particular, light mesons would be produced and stopped in the dense medium, thus decaying at rest and producing a monoenergetic neutrino signal. The decay-at-rest of kaons will produce a $E_\nu = 236$ MeV ν_μ while in the case of pions one would have a $E_\nu = 29.8$ MeV ν_μ . In practice only K^+ and π^+ contribute to these signals, as K^- and π^- are usually Coulomb-captured in an atomic orbit and get absorbed by the nucleus. There is also a low-energy neutrino signal coming from muon decays, which are produced in kaon or pion decays, leptonic decays of other hadrons and heavy leptons or even directly from WIMP annihilations, which can decay at rest and contribute to the previous low-energy neutrino flux with a well known spectrum below 52.8 MeV.

These monoenergetic MeV neutrinos were previously considered undetectable but, due to the large yield, the known spectra and the modern advances in the detector technology, these low-energy neutrino flux can be a good probe of the SD WIMP-proton cross-section in standard solar WIMP capture scenario, as it is sensitive to low WIMP masses and insensitive to the particular final state. A good place to look for these signals are next-generation neutrino experiments such as DUNE.

7.4 Computing limits from solar neutrino fluxes

In order to use the neutrino fluxes from DM annihilations in the Sun, the first thing I need to do is to determine the expected number of atmospheric background events, for a given exposure, after directionality selection has been applied. I can write this number as:

$$N_B = \eta_B \int d\Omega \int_{E_{min}}^{E_{max}} dE_\nu \frac{d^2\Phi_{atm}^\mu}{dE_\nu d\Omega} \times \left(A_{eff}^{(\mu)}(E_\nu) T \right), \quad (7.22)$$

where η_B is the background efficiency, E_{min} and E_{max} the minimum and maximum energies to integrate over, $d^2\Phi_{atm}^\mu/dE_\nu d\Omega$ the differential flux of atmospheric muon neutrinos, $A_{eff}^{(\mu)}$ is the effective area of DUNE to muon neutrinos and T is the exposure time. The effective area can be expressed as the product of the neutrino-nucleus scattering cross section and the number of nuclei in the fiducial volume of the detector. This way

Chapter 7. DM searches with neutrinos from the Sun

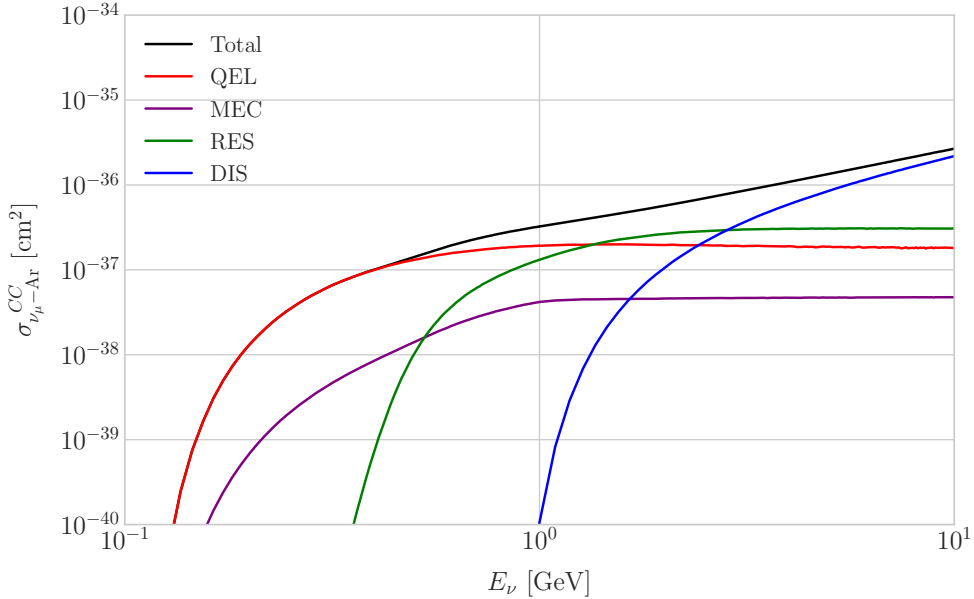


Figure 7.3: *NuWro* computed $\nu_\mu - {}^{40}\text{Ar}$ charged-current scattering cross section as a function of the neutrino energy E_μ . The black line shows to the total cross section, whereas the others correspond to the different contributions (in red quasi-elastic scattering, in green resonant pion exchange, in blue deep inelastic scattering and in purple meson exchange current).

2005 for DUNE I can write:

$$A_{eff}^{(\mu)}(E_\nu) = (6.0 \times 10^{-10} \text{ m}^2) \left(\frac{\sigma_{\nu - \text{Ar}}^{(\mu)}(E_\nu)}{10^{-38} \text{ cm}^2} \right) \left(\frac{M_{target}}{40 \text{ kT}} \right), \quad (7.23)$$

2006 where $\sigma_{\nu - \text{Ar}}^{(\mu)}$ is the $\nu_\mu - {}^{40}\text{Ar}$ charged-current scattering cross section. In Fig. 7.3 I
2007 show the computed value of this cross section as a function of the neutrino energy E_ν ,
2008 in the range of interest both for the atmospheric background and signal events. It was
2009 computed using the **NuWro** Monte Carlo neutrino event generator [82], including the
2010 charged-current contributions of the quasi-elastic scattering (red line), resonant pion
2011 exchange (green line), deep inelastic scattering (blue line) and meson exchange current
2012 (purple line).

2013 The background rejection will depend on the resolution of the detector and the
2014 selection one applies on the events. A geometry argument can be used to estimate
2015 the maximum background rejection one can achieve in this case, considering one can

7.4. Computing limits from solar neutrino fluxes

2016 efficiently discriminate all events coming from a direction different from that of the
 2017 Sun. In that case, the optimal background efficiency will simply be the relative angular
 2018 coverage of the Sun. Taking the angular diameter of the Sun as seen from the Earth to
 2019 be 0.5° , I have:

$$\eta_B^{(opt)} \approx \frac{\pi \left(\frac{0.5}{2}\right)^2}{360 \times 180} \simeq 3.03 \times 10^{-6}. \quad (7.24)$$

2020 This value will give a very optimistic estimate of the number of background events.
 2021 However, it can be regarded as a lower limit, as it represents the best case scenario.

2022 In Fig. 7.4 I show the fluxes of atmospheric neutrinos at the Homestake mine during
 2023 solar minimum, taken from Ref. [5]. The values are averaged over the two angular
 2024 directions. In blue I have the flux of muon neutrinos while in red I indicate the flux
 2025 of electron neutrinos. Additionally, the dashed lines correspond to both antineutrino
 2026 species.

2027 Using these values for the muon neutrino and the corresponding total CC cross
 2028 section, one can compute the number of expected background events by integrating over
 2029 the given energy range (as in this case the angular integral is trivial). As for the energy
 2030 range to integrate over, I choose the range for DUNE specified in [50], $E_{min} = 10^{-1}$ GeV
 2031 and $E_{max} = 10$ GeV. Taking all these into account, I found the number of background
 2032 events to be:

$$N_B \simeq \eta_B \times (3.827 \times 10^4) \times \left(\frac{\text{exposure}}{400 \text{ kT yr}} \right). \quad (7.25)$$

2033 In order to estimate the sensitivity of DUNE to this kind signal, one can consider a
 2034 hypothetical data set where the number of observed neutrinos is taken to be the expected
 2035 number of background events rounded to the nearest integer, $N_{obs} = \text{round}(N_B)$ [83].
 2036 Now, if I assume that the number of signal and background events seen by DUNE are
 2037 given by Poisson distributions with means equal to the expected number of signal and
 2038 background events, N_S and N_B , one can denote by N_S^{90} to the number of expected
 2039 signal events such that the probability of having an experimental run with a number of
 2040 events greater than N_{obs} is 90%. This number can be obtained as the numerical solution

Chapter 7. DM searches with neutrinos from the Sun

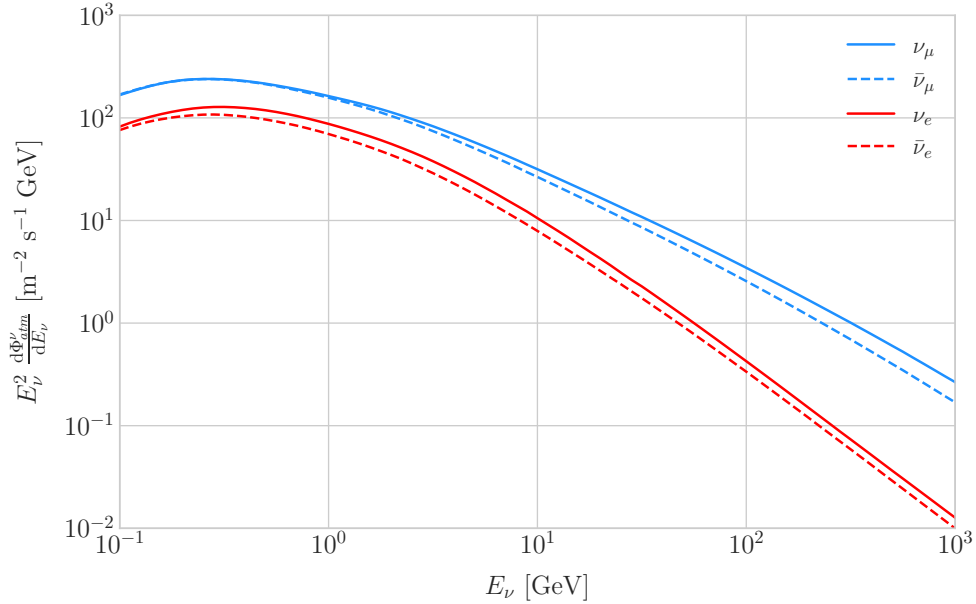


Figure 7.4: Expected atmospheric neutrino flux as a function of the neutrino energy E_ν at Homestake at solar minimum, taken from Ref. [5]. The blue solid (dashed) line correspond to muon neutrinos (antineutrinos) and the red solid (dashed) line correspond to electron neutrinos (antineutrinos).

2041 to the equation:

$$1 - \frac{\Gamma(N_{obs} + 1, N_S^{90} + N_B)}{N_{obs}!} = 0.9, \quad (7.26)$$

2042 where $\Gamma(x, y)$ is the upper incomplete gamma function.

2043 The number of signal events is related to the neutrino flux from DM annihilations in
2044 a similar way as the background events to the atmospheric neutrino flux. In this case I
2045 have:

$$N_S = \eta_S \Gamma_A^{eq} \int_{z_{min}}^{z_{max}} dz \frac{dN_\nu}{dAdN_A dz} \times (A_{eff}^\mu(z)T), \quad (7.27)$$

2046 where η_S is the signal efficiency, Γ_A^{eq} is the total annihilation rate of DM particles at
2047 equilibrium, $\Gamma_A^{eq} = A_\odot (N_{DM}^{eq})^2$, z_{min} and z_{max} the minimum and maximum relative
2048 energies to integrate over (in such a way that $z_{min,max} \leq E_{min,max}/m_{DM}$ for each m_{DM})
2049 and $dN_\nu/dAdN_A dz$ the muon neutrino flux per DM annihilation in the Sun.

2050 Knowing N_S^{90} one can use the relation in Eq. (7.27) to obtain $\Gamma_A^{eq,90}$ for different
2051 values of the DM mass. From there I can directly translate those values into the

7.5. Example: Kaluza-Klein Dark Matter

2052 upper limits for DUNE on the DM scattering cross sections, for a given exposure. The
2053 relation between the annihilation rate and the DM-nucleon cross section comes from the
2054 equilibrium condition through the solar DM capture rate. The details of the evolution
2055 of the number of DM particles inside the Sun and the computation of the capture rates
2056 are discussed in App. 7.2.

2057 7.5 Example: Kaluza-Klein Dark Matter

2058 Even though there are plenty of BSM theories which provide viable dark matter
2059 candidates, Kaluza-Klein type of models [84, 85] within the universal extra dimensions
2060 (UED) paradigm naturally predict the existence of a massive, stable particle that can
2061 play the role of the dark matter. In the UED scenario all the SM fields can propagate
2062 in one or more compact extra dimensions [86], as opposed to the idea of brane worlds
2063 [87, 88], where just gravity can propagate in the bulk while SM particles live at fixed
2064 points.

2065 Furthermore, in UED there is no violation of the translational invariance along the
2066 extra dimensions, thus leading to degenerate KK modes masses and also the conservation
2067 of the KK number in the effective four dimensional theory. At loop level, radiative
2068 corrections and boundary terms shift the masses of the KK modes and break KK
2069 number conservation into a KK parity. As a result, this theory only contains interactions
2070 between an even number of odd KK modes and therefore the lightest among the first KK
2071 excitations will be stable. This particle is usually denoted as the lightest Kaluza-Klein
2072 particle (LKP) and its mass is proportional to $1/R$, being R the size of the extra
2073 dimension.

2074 A viable DM candidate needs to be electrically neutral and non-baryonic, therefore
2075 good candidates among the first Kaluza-Klein excitations would be the KK neutral
2076 gauge bosons and the KK neutrinos [89]. Another possible candidate is the first KK
2077 excitation of the graviton, which receives negligible radiate contributions and therefore
2078 has a mass almost equal to $1/R$, but it has been shown that the lightest eigenstate from

Chapter 7. DM searches with neutrinos from the Sun

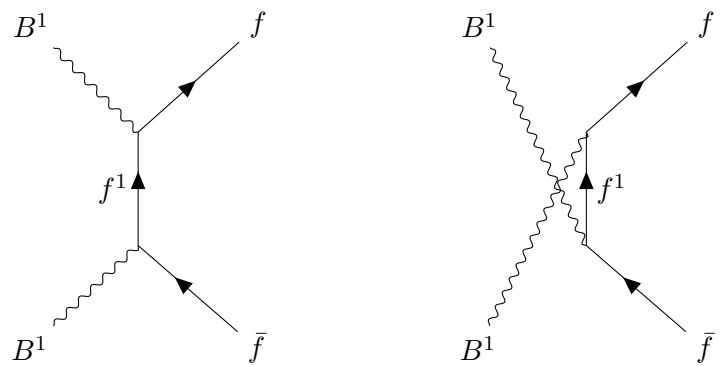


Figure 7.5: Feynman diagrams for $B^1 B^1$ annihilation into SM fermions.

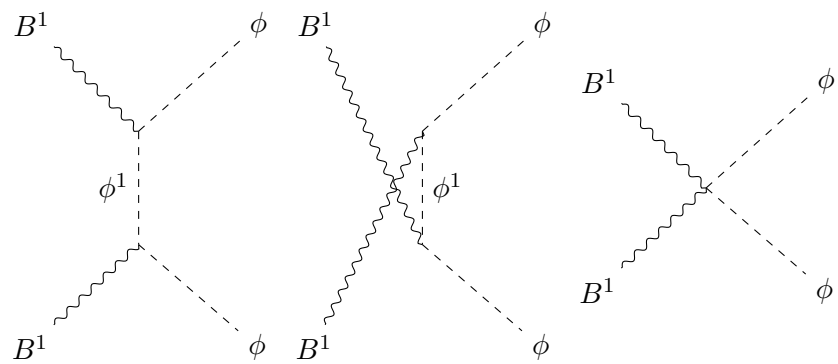


Figure 7.6: Feynman diagrams for $B^1 B^1$ annihilation into a Higgs boson pair.

7.5. Example: Kaluza-Klein Dark Matter

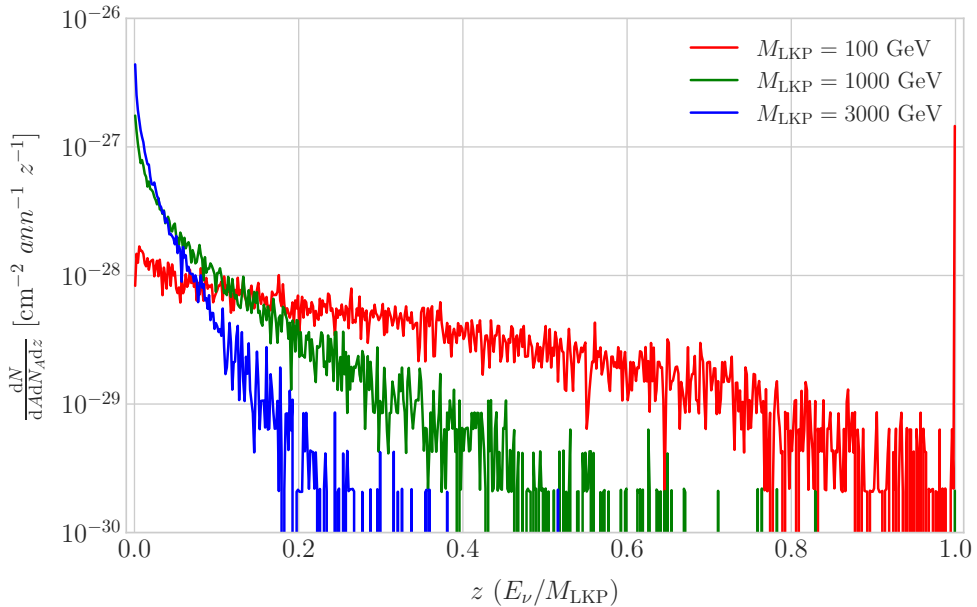


Figure 7.7: Computed spectra of muon neutrinos at the DUNE FD site from B^1 annihilations in the Sun for three different values of M_{LKP} , plotted in relative energy units for legibility.

the mixing of the gauge mass states (B^1, W_3^1) would be lighter, as B^1 and W_3^1 receive negative radiative corrections [90]. It is also understood that, when these corrections become sizeable, the eigenstates become approximately pure B^1 and W_3^1 states as the Weinberg mixing angle grows small with the KK number [90]. In that case, the LKP can be well-approximated as being entirely B^1 .

I need to compute the neutrino flux produced by the annihilations of the LKP in the core of the Sun, taking into account their propagation in the solar medium, as well as neutrino oscillations. To this end I used `WimpSim` [91, 92] to generate one million annihilation events in the Sun over a time span of four years and propagate them to the DUNE FD location ($44^\circ 20' \text{ N}, 103^\circ 45' \text{ W}$), for different values of M_{LKP} . In Fig. 7.7 I show the obtained muon neutrino spectra arriving to the detector from LKP annihilations in the Sun, per unit area and per annihilation, plotted in relative energy units for different values of the mass. As one could expect the spectra get steeper the higher is the mass, due to the absorption of high-energy neutrinos in the solar medium. Also, one can see the peak at $z = 1$ due to the direct annihilation into neutrinos $\chi\chi \rightarrow \nu\bar{\nu}$.

Chapter 7. DM searches with neutrinos from the Sun

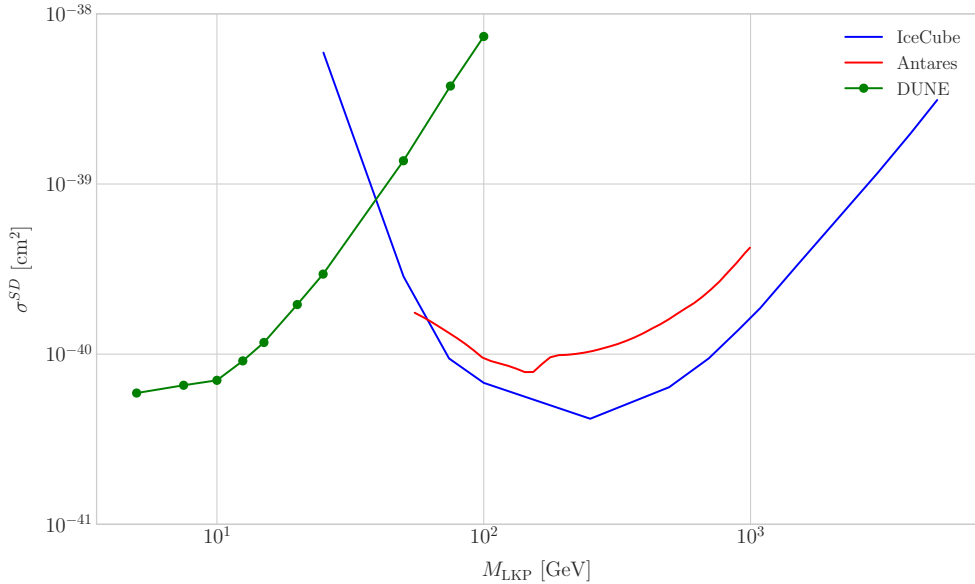


Figure 7.8: Projected 90% confidence level upper limit for DUNE (400 kT yr) on the spin-dependent B^1 -proton scattering cross section as a function of M_{LKP} (green dots). I also show the previous limits from IceCube [6] (blue line) and Antares [7] (red line) on the LKP cross section. The shaded area represents the disfavoured region (at 95% confidence level) on the mass of the LKP from LHC data [8].

Now, one can estimate the sensitivity of DUNE to this particular model by using the methods I previously discussed. To begin with, I will use the optimistic estimation of the background efficiency in Eq. (7.24) to get our upper bound. Using it, one can directly compute the number of expected background events to be $N_B = 0.1101$ for an exposure of 400 kT yr. Then, Eq. (7.26) give us a value of $N_S^{90} = 2.20$ for the 90% exclusion number of expected signal events. By using the NuWro generated cross sections and the computed neutrino fluxes from B^1 annihilations in the Sun I can estimate the limits on the SD and SI DM-nucleus cross section using the relation in Eq. (7.2) and the capture rates I computed with DarkSUSY.

In Fig. 7.8 I show the projected sensitive for DUNE on the spin-dependent B^1 -proton scattering cross section versus the mass of the DM particle, for a exposure of 400 kT yr (green dots). I also include the previous results from IceCube [6] (blue line) and Antares [7] (red line). The shaded area represents the disfavoured region from combined searches for UED by ATLAS and CMS [8].

7.6. High energy DM neutrino signals

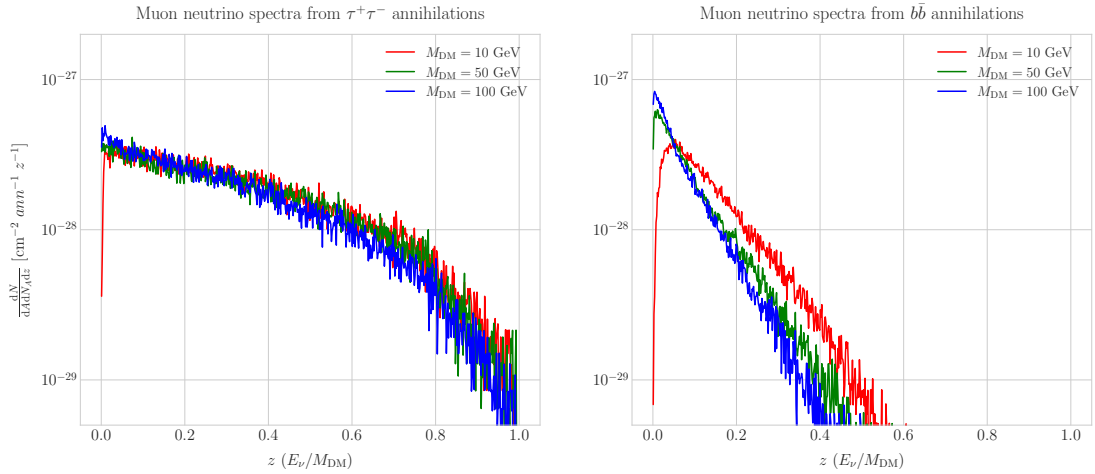


Figure 7.9: Computed spectra of muon neutrinos at the DUNE FD site from $\tau^+\tau^-$ (left panel) and $b\bar{b}$ (right panel) annihilations in the Sun for the DM masses $m_{\text{DM}} = 10 \text{ GeV}$ (red line), 50 GeV (green line) and 100 GeV (blue line), plotted in relative energy units.

From the experimental point of view, this estimation lacked a detailed simulation of the detector response and thus this must be considered as a mere optimistic sensitivity computation. However, it shows the potential of DUNE to constrain this kind of exotic scenarios, showing the region where it will be in a position to compete with other neutrino telescopes. A more detailed analysis is needed if I am to make a realistic estimation. Even though the region of the parameter space where DUNE would be sensitive to this particular model is quite constrained by collider searches [8] and other rare decay measurements [93, 94], it still constitutes an alternative indirect probe.

7.6 High energy DM neutrino signals

To have better estimates on the capability of the DUNE FD to constrain the parameter space of DM using solar neutrino fluxes, I need to start accounting for the detector resolution effects and the topologies of the different signatures. As a starting point, I will focus on specific annihilation channels. For the case of DUNE, the relevant ones are mainly the hard channels $\tau^+\tau^-$ and $\nu\bar{\nu}$ and the soft channel $b\bar{b}$. These are the open annihilation channels for relatively low mass WIMPs that will actually give neutrino fluxes. Other channels, like W^+W^- and ZZ , are open for more massive WIMPs, but

Chapter 7. DM searches with neutrinos from the Sun

2124 those will produce usually a higher energy neutrino flux that will be out of reach for
2125 DUNE (usually the maximum neutrino energy is taken to be $E_{max} = 10$ GeV).

2126 In Fig. 7.9 I show the `WimpSim` [91, 92] generated muon neutrino spectra at the
2127 DUNE FD location ($44^\circ 20' N, 103^\circ 45' W$) from $\tau^+\tau^-$ (left panel) and $b\bar{b}$ (right panel)
2128 annihilations in the core of the Sun, for different DM masses. Here, one can clearly see
2129 the meaning of the previous distinction between hard and soft channels. For the same
2130 DM mass value, the muon neutrino spectrum from the $\tau^+\tau^-$ channel is more flat and
2131 reaches higher energies than the one from the $b\bar{b}$ channel, which drops faster.

2132 In this case, I prepared two sets of files, one for $\tau^+\tau^-$ and the other for $b\bar{b}$, for DM
2133 masses in the range from 5 to 100 GeV (actually for $b\bar{b}$ the first mass point I took is
2134 7.5 GeV, as a WIMP with $m_{DM} = 5$ GeV can not kinematically self annihilate into $b\bar{b}$).
2135 Then, I prepared the `WimpSim` output fluxes in a specific way to use them as inputs to
2136 `NuWro`, which simulates the neutrino interaction with the argon.

2137 Because `WimpSim` outputs an event list together with the fluxes, I can use the former
2138 to generate the events. The direction of these is given in terms of the azimuth and
2139 altitude angles viewed from the specified location, so first I need to convert these into the
2140 DUNE FD coordinates. Once I have done it, each event can be processed with `NuWro`.
2141 To increase the number of samples and optimise the computation time, I generate 100
2142 interactions (i.e. `NuWro` events) for each `WimpSim` event². I restrict the event generation
2143 to charged current interactions, but I allow all the different contributions to the CC
2144 cross section, i.e. quasielastic scattering (QEL), meson exchange current process (MEC),
2145 resonant pion production (RES) and deep inelastic scattering (DIS). I just take into
2146 account the CC contribution because I am only interested in final states with charged
2147 leptons, as we have better chances of reconstructing the kinematics of CC events.

2148 For the atmospheric fluxes I follow a similar procedure, only that this time I do not
2149 have a set of events but the fluxes binned in azimuth and altitude angles. This way, I
2150 transform these to DUNE coordinates and process the fluxes for each bin separated with

²This also solves a problem related with the generation of the neutrino interactions in `NuWro`, as if you only produce one event each time you launch `NuWro` it will always produce an interaction of the dominant interaction type for that particular energy.

7.6. High energy DM neutrino signals

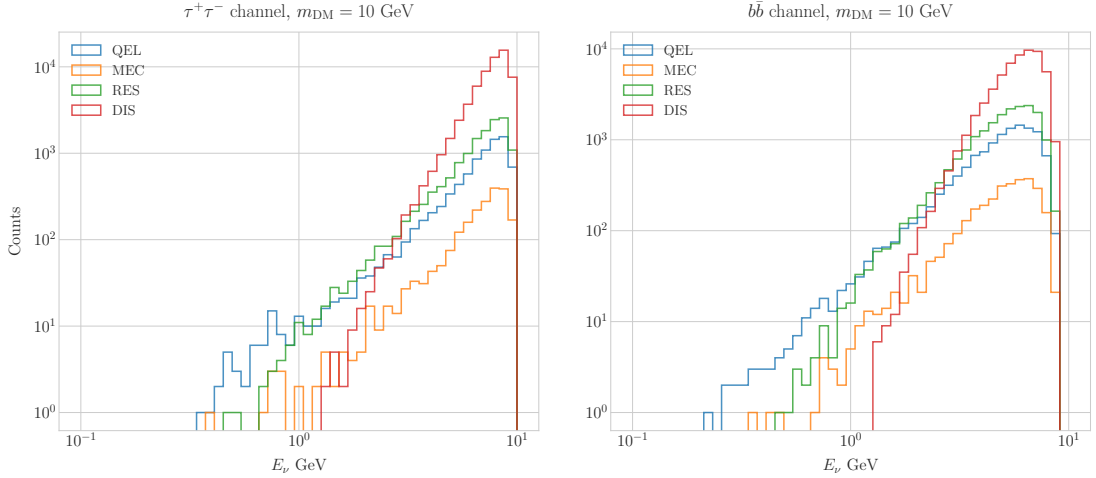


Figure 7.10: Distribution of the muon neutrino energies from the $\tau^+\tau^-$ (left panel) and $b\bar{b}$ (right panel) annihilation channels, for $m_{\text{DM}} = 10 \text{ GeV}$, separated by CC interaction type: QEL (blue), MEC (orange), RES (green) and DIS (red).

2151 NuWro.

2152 At this point, I have two sets of events with different energies and final states.
 2153 In Fig. 7.10 one can see the distribution of the muon neutrino energies for the case
 2154 $m_{\text{DM}} = 10 \text{ GeV}$, both for the $\tau^+\tau^-$ (left panel) and $b\bar{b}$ (right panel) channels, separated
 2155 by interaction. One can clearly see that there are different energy regimes where the
 2156 primary interaction type is different. This leads to a plurality of event topologies,
 2157 therefore making it difficult to implement a general approach to the selection of events
 2158 in detriment of the background. As a way to proceed, I decided to split our samples,
 2159 based on the different interaction modes and contents of the final state, into a CC DIS
 2160 sample and a single proton CC QEL sample.

2161 7.6.1 DIS events

2162 To begin with, I consider the high energy part of the spectrum. In this region DIS events
 2163 dominate, i.e. interactions of the form $\nu_\mu + q_d(\bar{q}_u) \rightarrow \mu^- + q_u(\bar{q}_d)$. Therefore, our final
 2164 estates will contain a muon and a hadronic jet from the fragmentation of the outgoing
 2165 quark. As all these events have $E_\nu \gtrsim 1 \text{ GeV}$ the momentum transfer to the remnant
 2166 nucleus is negligible, for this reason the neutrino energy can be effectively reconstructed

Chapter 7. DM searches with neutrinos from the Sun

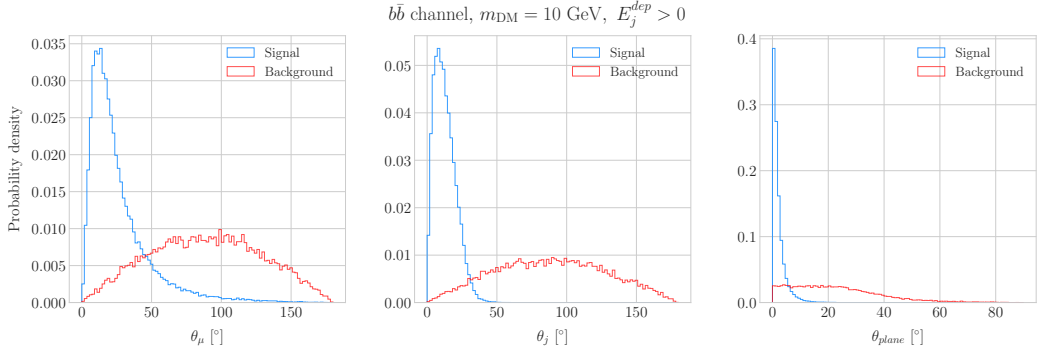


Figure 7.11: Distributions of θ_μ (left panel), θ_j (central panel) and θ_{plane} (right panel) for the $b\bar{b}$ sample with $m_{\text{DM}} = 10$ GeV (blue) and the atmospheric background (red).

just taking into account the momenta of the muon and the jet. This technique was successfully used in Ref. [95] to select monoenergetic DM solar neutrino events from $\nu\bar{\nu}$ annihilation channels.

Using momentum conservation one sees that the plane generated by the momenta of the muon and the jet needs to also contain the momentum of the neutrino. As we are interested in neutrinos coming from the Sun, the momentum of the neutrino can be regarded as known beforehand. This will allow us to define the angle of the outgoing muon and jet with respect to the incoming neutrino. Moreover, one can also use that information to reject poorly reconstructed jets, checking for deviations of these from the momentum conservation plane.

To account for the limited angular resolution of the detector, I smeared the momenta of the muons and hadrons. In a liquid argon TPC muons are expected to be tracked with high precision, therefore I take the associated angular resolution to be 1° . In the case of jets, it is expected that for the hadrons dominating the cascade a detector like DUNE has an angular resolution between 1° to 5° [50], so I take the latter, more conservative, estimate.

As a first selection step, I will just take into account particles with kinetic energies above the detection threshold of DUNE. For muons and photons the specified threshold energy is 30 MeV, for charged pions 100 MeV and for other hadrons 50 MeV [50]. This way, if the outgoing muon in a certain event has an energy lower than the required

7.6. High energy DM neutrino signals

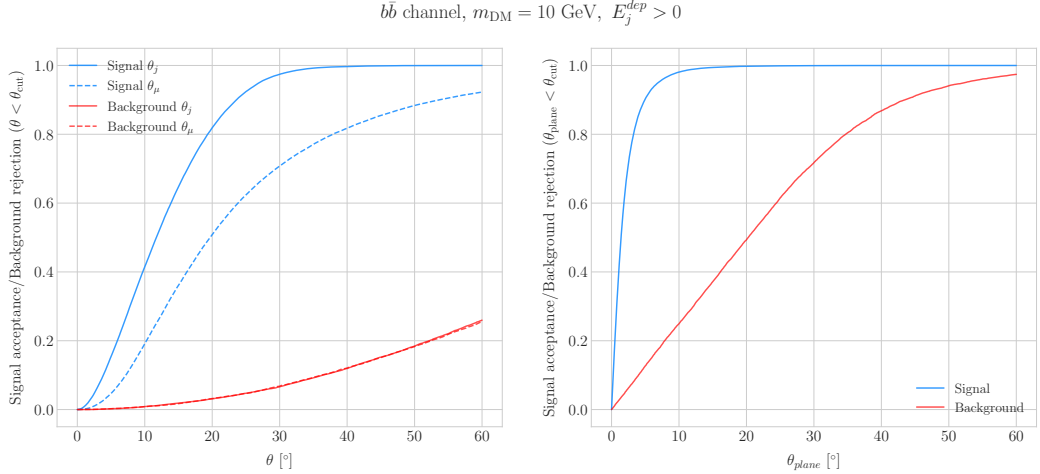


Figure 7.12: Left panel: signal efficiencies (blue lines) and background rejections (red lines) for events passing the cuts $\theta < \theta_{\text{cut}}$ for the jet (solid lines) and muon (dashed lines) angles. Right panel: signal efficiency (blue line) and background rejection (red line) for events passing the cut $\theta_{\text{plane}} < \theta_{\text{cut}}$ for the momentum conservation plane deviation.

threshold I will drop such event. For the case of hadrons and photons, I will only require to have at least one particle above the energy threshold, so then one can compute the jet momentum using the (smeared) momenta of the N particles above threshold as:

$$\vec{p}_j = \sum_{i=1}^N \vec{p}_i. \quad (7.28)$$

Additionally, I will also define an estimation of the deposited hadronic energy as:

$$E_j^{\text{dep}} = m_{^{39}\text{Ar}} - m_{^{40}\text{Ar}} + \sum_{i=1}^N \sqrt{|\vec{p}_i|^2 + m_i^2}. \quad (7.29)$$

This quantity is useful to select events with enough hadronic visible energy in the detector. For events where most of the hadronic energy is scattered across plenty of hadrons with individual energies below the detection threshold, this estimation will give $E_j^{\text{dep}} \leq 0$. In these cases it could be expected that the jet momentum is poorly reconstructed, and therefore I require events to pass the cut $E_j^{\text{dep}} > 0$.

For the events I can compute the angles for the muon and jet with respect to the

Chapter 7. DM searches with neutrinos from the Sun

2197 incoming neutrino as:

$$\cos \theta_\mu = \hat{p}_\nu \cdot \hat{p}_\mu, \quad (7.30)$$

$$\cos \theta_j = \hat{p}_\nu \cdot \hat{p}_j, \quad (7.31)$$

2198 and the deviation from the momentum conservation plane as:

$$\sin \theta_{plane} = \left| \frac{\hat{p}_\mu \times \hat{p}_\nu}{|\hat{p}_\mu \times \hat{p}_\nu|} \cdot \hat{p}_j \right|. \quad (7.32)$$

2199 In Fig. 7.11 I show some distributions of these quantities for the case of the $b\bar{b}$ sample
2200 with $m_{DM} = 10$ GeV (blue histograms) and for the atmospheric backgrounds (red).
2201 In order to select the atmospheric events I followed the same criteria as for the signal
2202 events. However, because in the signal case I used the true direction of the neutrino
2203 as input, as it should be that of the Sun at that time and therefore known, in the
2204 atmospheric case I used a set of solar positions as our ansatz for the neutrino direction.
2205 From the distributions, one can see that the muon and the jet for the signal events are
2206 predominantly forward and also that the deviations from the momentum conservation
2207 plane are peaked at zero, as one should expect.

2208 Now, I can start applying cuts to maximise our signal selection efficiency while at
2209 the same time I try to minimise the amount of atmospheric background events passing
2210 the selection. To this end, I will need to find some lower and upper cuts for θ_j and
2211 θ_μ and an upper bound for θ_{plane} . In Fig. 7.12 I show how upper bound cuts in the
2212 different angular variables affect the signal efficiency (blue lines) and the background
2213 rejection (red lines). Notice that the signal efficiency behaves in a quite different way
2214 when I apply cuts in the jet and the muon angles. On the contrary, the cuts on both
2215 variables have a similar effect on the background rejection.

2216 In order to obtain the optimal set of cuts, I perform a multidimensional scan. I
2217 do this separately for the $\tau^+\tau^-$ and the $b\bar{b}$ samples. For each case, I scan the possible
2218 cuts for each mass point and then I take the mean value of the signal efficiency for

7.6. High energy DM neutrino signals

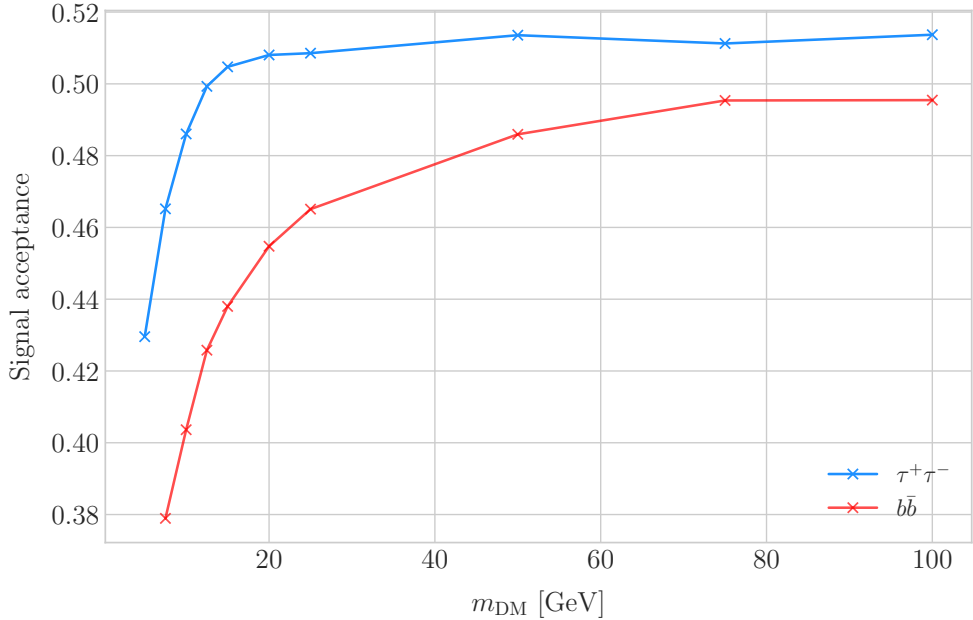


Figure 7.13: Signal efficiencies for the $\tau^+\tau^-$ (blue line) and $b\bar{b}$ (red line) DIS samples as functions of the DM mass, m_{DM} , obtained by applying the optimal angular cuts $\theta_\mu < 27^\circ$, $4^\circ < \theta_j < 26^\circ$ and $\theta_{\text{plane}} < 3.5^\circ$.

each configuration, to get the mean efficiency for each set of cuts. I do a similar scan for the atmospheric sample independently. Then, I take the sets of cuts such that the background rejection achieved is greater than 99.8% and search for the one which maximises the $\tau^+\tau^-$ and $b\bar{b}$ sample mean efficiencies. I found that with the cuts $\theta_\mu < 27^\circ$, $4^\circ < \theta_j < 26^\circ$ and $\theta_{\text{plane}} < 3.5^\circ$ I get a background rejection of 99.80% while achieving a 49.40% and 44.92% mean signal efficiencies for the $\tau^+\tau^-$ and $b\bar{b}$ signals respectively.

In Fig. 7.13 I show the signal efficiencies as a function of the DM mass for the $\tau^+\tau^-$ (blue line) and the $b\bar{b}$ (red line) DIS events, after applying the cuts discussed above, as well as the energy threshold and hadronic visible energy selections. One can see that the efficiency grows with the mass, as annihilations of more massive DM particles will produce a neutrino spectrum centered at higher energies, where DIS events dominate. Notice also that the efficiency is higher for the $\tau^+\tau^-$ case at every mass point, as in general this channel produces neutrinos at higher energies than the corresponding $b\bar{b}$ channel.

Chapter 7. DM searches with neutrinos from the Sun

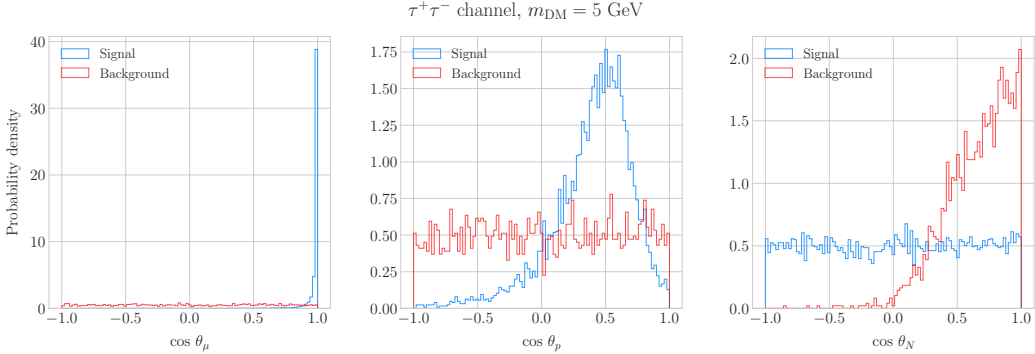


Figure 7.14: Distributions of $\cos \theta_\mu$ (left panel), $\cos \theta_p$ (central panel) and $\cos \theta_N$ (right panel) for the $\tau^+\tau^-$ QEL sample with $m_{\text{DM}} = 5 \text{ GeV}$ (blue) and the atmospheric background (red).

2233 7.6.2 Single proton QEL events

2234 Now, one can try to explore the low energy tail of the neutrino energy distributions. This
 2235 regime is dominated by the QEL interactions, i.e. events of the type $\nu_\mu + n \rightarrow \mu^- + p$.
 2236 In this case, as the typical energies are $E_\nu \lesssim 1 \text{ GeV}$, the momentum transfer to the
 2237 remnant nucleus is sizeable. Therefore, I can not make the approximation I did before
 2238 and assume that the momentum of the muon and the proton will give an adequate
 2239 estimation of the reconstructed neutrino energy.

2240 In any case, as before, I can take the direction of the incoming neutrino as known.
 2241 That way, one can estimate the energy of the neutrino as:

$$E_\nu^{reco} = E_\mu + E_p + m_{^{39}\text{Ar}} - m_{^{40}\text{Ar}}, \quad (7.33)$$

2242 and using momentum conservation I can write the momentum of the remnant nucleus
 2243 as:

$$\vec{p}_N = \hat{p}_\nu (E_\mu + E_p + m_{^{39}\text{Ar}} - m_{^{40}\text{Ar}}) - \vec{p}_\mu - \vec{p}_p. \quad (7.34)$$

2244 As in the previous case, I need to drop the events where the muon or the proton fall
 2245 below the kinetic energy detection threshold [50]. Also, I again apply a smearing to the
 2246 momenta of the particles, a 1% for muons and 5% for protons.

2247 Having done that, one can compute the following angular variables for our selected

7.6. High energy DM neutrino signals

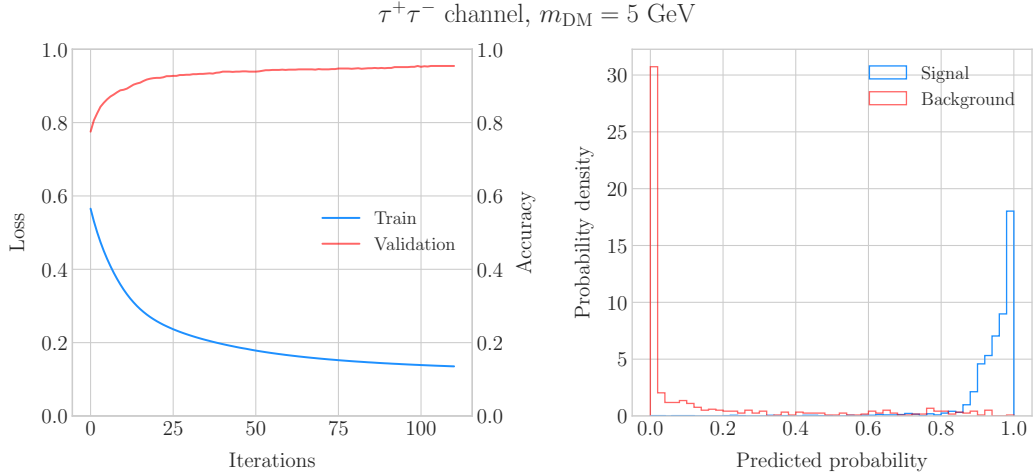


Figure 7.15: Left panel: value of the loss function for the training sample (blue line) and accuracy for the validation sample (red line) versus the number of iterations for the MLP classifier training. Right panel: distributions of the predicted probabilities assigned by the MLP classifier to the test sample for the $\tau^+\tau^-$ QEL signal with $m_{\text{DM}} = 5 \text{ GeV}$ (blue) and the atmospheric background (red).

2248 events:

$$\cos \theta_\mu = \hat{p}_\nu \cdot \hat{p}_\mu, \quad (7.35)$$

$$\cos \theta_p = \hat{p}_\nu \cdot \hat{p}_p, \quad (7.36)$$

$$\cos \theta_N = \hat{p}_\nu \cdot \hat{p}_N. \quad (7.37)$$

2249 Fig. 7.14 shows the distributions of these angular variables for the $\tau^+\tau^-$ QEL
 2250 sample with $m_{\text{DM}} = 5 \text{ GeV}$ (blue) and the atmospheric background (red). Again, for
 2251 the atmospheric events I used a random solar position as the ansatz for the incoming
 2252 neutrino direction. Notice that now, opposed to the DIS case where the signal had very
 2253 sharp distributions for the variables considered, the shapes of the angular distributions
 2254 for signal and background are not that much different.

2255 This effectively means that the usual approach of applying simple angular cuts would
 2256 not work as well as in the previous situation. Therefore, as a possible solution, I tried to
 2257 use a multilayer perceptron (MLP) classifier to separate between signal and background
 2258 events. Thus, the power of the hypothesis test will serve as an estimate of the signal

Chapter 7. DM searches with neutrinos from the Sun

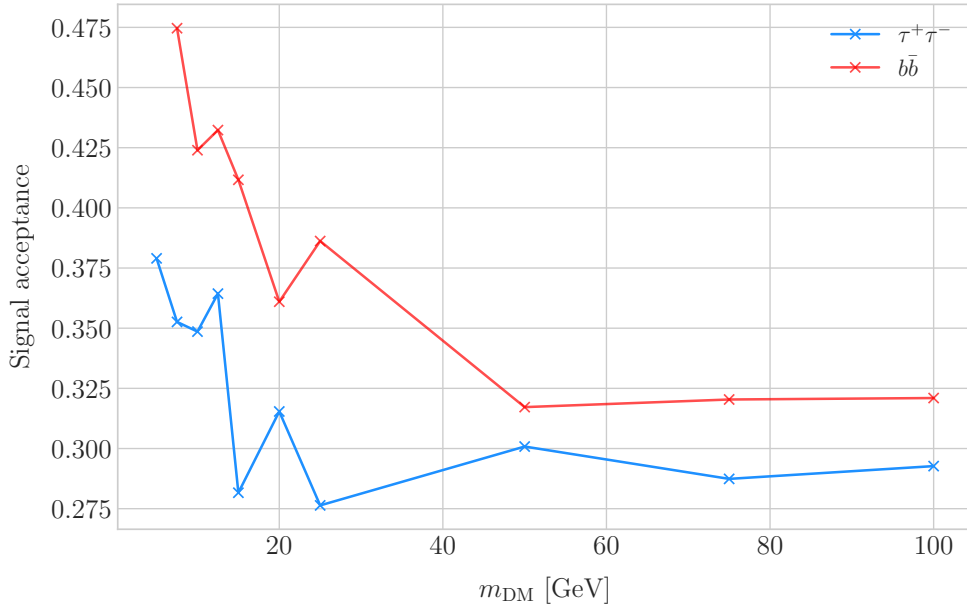


Figure 7.16: Signal efficiencies for the $\tau^+\tau^-$ (blue line) and $b\bar{b}$ (red line) single proton QEL samples as functions of the DM mass, m_{DM} , obtained by requiring a minimum predicted probability from the MLP classifier of 0.97 in order to achieve a background rejection greater than 99.8%.

efficiency, and in the same way one can take the size of the test to be our background rejection.

For each DM mass value and channel, as well as for the background sample, I divide our events into training, validation and test samples. The input variables for the classifier were the reconstructed neutrino energy from Eq. (7.33) and the angular variables defined in Eqs. (7.35 - 7.37). I used the MLP classifier implemented in `scikit-learn` [96], with a total of five hidden layers, the rectified linear unit activation function and adaptive learning rate. In order to account for fluctuations due to artifacts in the training process I repeated the training a thousand times for each sample, redefining each time the training, validation and test subsets, so one can take as our signal efficiency and background rejection the mean values of the powers and sizes of the tests.

The results of one of these training processes for the $\tau^+\tau^-$ QEL signal with $m_{\text{DM}} = 5$ GeV is shown in Fig. 7.15. On the left panel I show the loss function values (blue) and accuracy (red) at each iteration for the training and the validation samples respectively.

7.6. High energy DM neutrino signals

2273 The training stops either when the maximum number of iterations is reached (1000 in
2274 this case) or when the accuracy for the validation sample reaches a certain tolerance
2275 (I chose 10^{-4} as our tolerance). On the right panel I have the distributions for the
2276 predicted probability by the model, separated in true signal (blue) and background
2277 (red) events, for the test sample. One can see that both populations are well separated,
2278 obtaining a power of 44.97% and a size of 0.17% when I require a predicted probability
2279 greater than 0.97.

2280 Applying this criteria for each sample, I obtain the mean signal efficiencies shown in
2281 Fig. 7.16. Notice that the efficiencies for the channel $\tau^+\tau^-$ (blue line) are consistently
2282 lower than the ones for the $b\bar{b}$ channel (red line). This can be due to the fact that, for
2283 each DM mass point, the neutrino spectrum coming from the $b\bar{b}$ annihilation channel is
2284 centered at lower energies when compared to the $\tau^+\tau^-$ spectrum. This directly translates
2285 into more low energy neutrinos undergoing QEL interactions, which give signals that
2286 can be easily separated from the atmospheric background. This explanation also help us
2287 understand why in both cases the signal acceptance drops when the DM mass increases.
2288 In all cases, the background rejection took values between 99.8% to 99.9%. I will assume
2289 a 99.8% background rejection value in all cases to keep our estimation conservative.

2290 7.6.3 Results

2291 In order to estimate the DM-nucleon cross section sensitivities in the present case I need
2292 again to compute the expected number of background events. As I am now separating
2293 events by interaction type Eq. (7.25) does not hold anymore, as in that case I integrated
2294 over the total neutrino-argon cross section. In this instance, the expected background
2295 events for DIS events is approximately given by:

$$N_B^{DIS} \simeq \eta_B^{DIS} \times (4.655 \times 10^3) \times \left(\frac{\text{exposure}}{400 \text{ kT yr}} \right), \quad (7.38)$$

Chapter 7. DM searches with neutrinos from the Sun

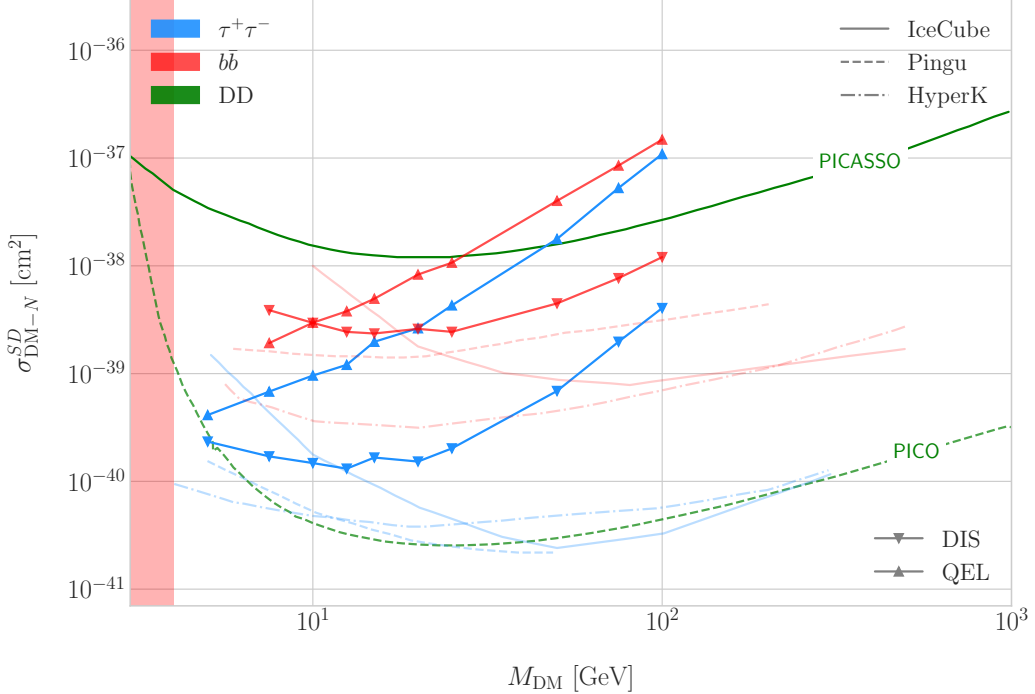


Figure 7.17: Projected 90% confidence level upper limit for DUNE (400 kT yr) on the spin-dependent DM-nucleon scattering cross section as a function of m_{DM} , for the annihilation channels $\tau^+\tau^-$ (blue) and $b\bar{b}$ (red) separated by interaction type (up triangles denote DIS interactions whereas down triangles represent QEL interactions). I also show the previous limits from IceCube [9] (solid lines) and the projected sensitivities for Pingu [10] (dashed lines) and Hyper-Kamiokande [11] (dash-dotted lines), as well as the direct detection limits from PICASSO [12] (solid green line) and PICO-60 C₃F₈ [13] (dashed green line).

2296 whereas for QEL events we have:

$$N_B^{QEL} \simeq \eta_B^{QEL} \times (2.248 \times 10^4) \times \left(\frac{\text{exposure}}{400 \text{ kT yr}} \right). \quad (7.39)$$

2297 Now, using these together with Eqs. (7.26) and (7.27) one can obtain the 90% C.L.
 2298 upper limit on the total annihilation rate at equilibrium for both kind of events. Then,
 2299 applying the computed DM-nucleons capture rates I can translate these into limits on
 2300 the DM-nucleon cross section by means of Eqs. (7.2), (7.5) and (7.6).

2301 Fig. 7.17 shows the obtained limits on the SD DM-nucleon cross section for DUNE,
 2302 using the DIS (up triangles) and QEL (down triangles) events both for the $\tau^+\tau^-$ (blue)
 2303 and the $b\bar{b}$ (red) samples, for an exposure of 400 kT yr. I also include the corresponding

7.7. Example: Leptophilic Dark Matter

2304 current limits from IceCube [9] (solid lines), as well as the projected sensitivities of Pingu
2305 [10] (dashed lines) and Hyper-Kamiokande [11] (dash-dotted lines). For comparison, I
2306 also show the reported direct detection limits from PICASSO [12] (solid green line) and
2307 PICO-60 C₃F₈ [13] (dashed green line).

2308 Notice that, for most of the mass range, the limits one can set by using the DIS
2309 events are stronger than those of the QEL interactions, except for the low mass part
2310 of both the $\tau^+\tau^-$ and the $b\bar{b}$ curves where the QEL events dominate. In general, the
2311 expected sensitivity of DUNE for DM masses $\lesssim 25$ GeV surpasses the stronger current
2312 indirect limits. However, experiments like Hyper-Kamiokande are foreseen to have an
2313 overall better sensitivity in this kind of searches, as they have a bigger active volume
2314 and accept a broader energy range.

2315 A pending question is what happens when we add the RES and MEC charged-current
2316 interaction contributions. In that case it would probably be more convenient to split
2317 the samples by final state interaction topologies. Also, another necessary improvement
2318 would be adding a full detector simulation and reconstructions. This will also require
2319 considering the effect of poorly reconstructed events or final states containing neutral
2320 particles such that they mimic the desired topology at the reconstruction level.

2321 7.7 Example: Leptophilic Dark Matter

2322 In general, the capture rate of DM particles by the Sun via interactions with electrons is
2323 several orders of magnitude smaller than the capture via DM-nucleus scattering. Thus,
2324 it would be sub-leading even when nucleon capture is loop suppressed. As I showed in
2325 Fig. 7.2, the capture rate via scattering off electrons only surpasses the capture rates
2326 via DM-nucleons interactions for DM masses $\lesssim 100 - 500$ MeV.

2327 However, if one considers a model where DM-nucleon interactions are forbidden even
2328 at loop level, then electron interactions will be the sole contributor to DM capture in
2329 the Sun. One can describe such scenario where the DM particles couple to leptons but
2330 not to the quark sector using effective operators.

Chapter 7. DM searches with neutrinos from the Sun

2331 In general, assuming that the DM particle is a Dirac fermion, the dimension six
 2332 operators describing the interaction between two DM particles and two leptons can be
 2333 written as:

$$\mathcal{L}_{eff} = G \sum_i (\bar{\chi} \Gamma_\chi^i \chi) (\bar{\ell} \Gamma_\ell^i \ell), \quad (7.40)$$

2334 where $G = 1/\Lambda^2$ is the effective coupling strength, Λ the cut-off of the effective field
 2335 theory and ℓ denotes any lepton. In principle, one should consider all the possible
 2336 Lorentz structures Γ_f^i in order to have a complete set of effective operators.

2337 However, some combinations will induce interactions with nucleons at loop level. As
 2338 we are specifically interested in interactions which forbid any communication with the
 2339 quark sector, I will not consider those [97]. In addition, some of the effective operators
 2340 give rise to velocity-suppressed scattering cross sections between DM particles and
 2341 leptons. I will also neglect those, as the suppression goes with the square of the DM
 2342 halo velocity which in units of the speed of light is $\sim 10^{-6}$.

2343 This way, the only Lorentz tensor structure that do not induce interactions with
 2344 quarks at loop level and gives a contribution to the scattering cross section that is not
 2345 velocity suppress is the axial-axial interaction. The effective Lagrangian is then given
 2346 by:

$$\mathcal{L}_{eff} = \frac{c_A^\chi c_A^\ell}{\Lambda^2} (\bar{\chi} \gamma^\mu \gamma^5 \chi) (\bar{\ell} \gamma_\mu \gamma^5 \ell), \quad (7.41)$$

2347 where c_A^χ and c_A^ℓ are the couplings for the different species. As the DM coupling appears
 2348 as a common factor for any lepton choice, I will redefine the corresponding coupling c_A^ℓ
 2349 to absorb c_A^χ . Also, for simplicity, I will assume that the couplings between the DM
 2350 particles and the leptons are flavour independent, i.e. I have just two couplings, c_A^e for
 2351 charged leptons and c_A^v for neutrinos.

2352 In the case of a scalar DM particle, the lowest order effective interaction with
 2353 leptons happens through a dimension five operator, generating scalar and pseudoscalar
 2354 interactions. However, the former induces interactions with quarks at two loop level
 2355 whereas the latter gives a velocity suppressed scattering cross section.

2356 From the effective Lagrangian in Eq. (7.41) it can be shown that the axial-axial

7.7. Example: Leptophilic Dark Matter

2357 contribution to the scattering cross section for the fermionic DM and a charged lepton
2358 is given by:

$$\sigma_{\text{DM}-e}^{AA} = 3(c_A^e)^2 \frac{m_e^2}{\pi \Lambda^4}. \quad (7.42)$$

2359 If the DM interacts exclusively with fermions, then the only annihilation channels
2360 that will give us a measurable neutrino flux coming out of the Sun are $\tau^+\tau^-$ and $\nu\bar{\nu}$. The
2361 former channel, already explored previously in the more mainstream scenario of the DM
2362 capture via scattering off nucleons, is open only for $m_{\text{DM}} > m_\tau \simeq 1776.86 \pm 0.12$ MeV
2363 [98], a mass region where the solar DM capture by electrons is at least one order of
2364 magnitude smaller than the capture via interactions with nucleons. On the contrary, the
2365 latter allows us to explore a region where the capture rate via scattering off electrons
2366 dominates over the rest.

2367 One downside of focusing in such low mass range is that it falls below the usual
2368 limit of $m_{\text{evap}} \sim 4$ GeV usually explored in the literature. The pretext to explore this
2369 region is the result discussed previously reported in Ref. [4], where DM evaporation in
2370 the Sun for the case of capture via electron scattering could be negligible for masses
2371 as low as $m_{\text{evap}} \sim 200$ MeV. This result is quite sensitive to the high velocity tail of
2372 the DM velocity distribution in equilibrium inside the Sun, and therefore full numerical
2373 simulations would be needed to assess the impact of this effect. However, this falls out of
2374 the scope of our work.

2375 In this case, as I have a specific realisation of the interaction between the DM
2376 and leptons, one can estimate the relic density of our DM for different values of the
2377 couplings and the effective field theory scale Λ . The first step to do so is compute the
2378 self-annihilation cross section. Because I consider cold relics, at the freeze-out time our
2379 DM particles were non-relativistic and so one can expand the annihilation cross section
2380 in terms of the relative velocity v between two annihilating DM particles as [99]:

$$\sigma_{\text{ann}}^{AA}|v| \approx \frac{1}{2\pi\Lambda^4} \sum_\ell \left(c_A^\ell\right)^2 m_\chi^2 \sqrt{1 - \frac{m_\ell^2}{m_\chi^2} \left[\frac{m_\ell^2}{m_\chi^2} + \frac{1}{12} \left(2 - \frac{m_\ell^2}{m_\chi^2}\right) v^2 \right]}, \quad (7.43)$$

Chapter 7. DM searches with neutrinos from the Sun

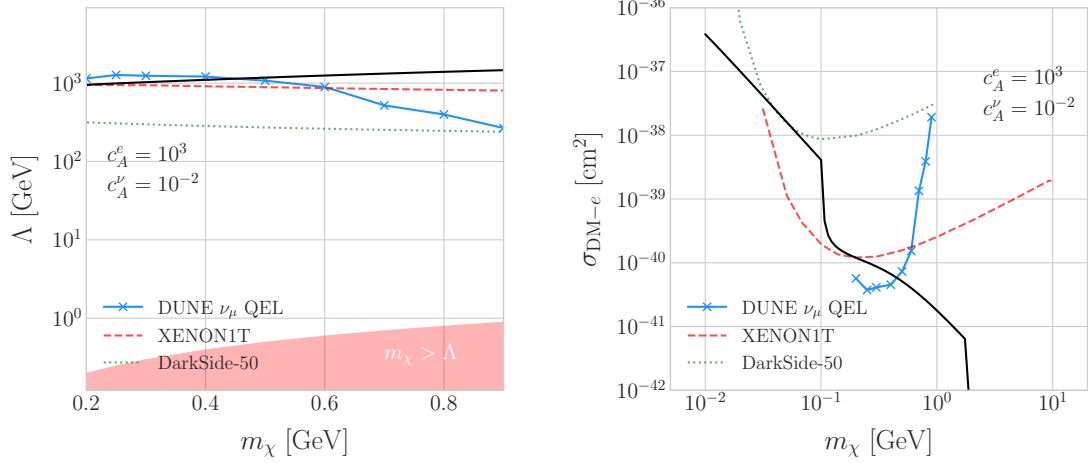


Figure 7.18: Left panel: Projected 90% confidence level sensitivity of DUNE (400 kT yr) to the scale Λ of an EFT containing only leptophilic DM axial-axial interactions (blue line). Right panel: . In both cases the corresponding limits from DarkSide-50 [14] (dotted green line) and XENON1T [15] (dashed red line) are also shown, together with the configurations for which the correct relic density is achieved (black line), all for the coupling values $c_A^e = 10^3$ and $c_A^\nu = 10^{-2}$.

2381 where the sum includes all the possible lepton final states with mass m_ℓ .
 2382 Solving the Boltzmann equation for the evolution of the DM density gives as a
 2383 solution a relic density of:

$$\Omega_\chi h^2 \approx \frac{(1.04 \times 10^9) x_F}{M_{Pl} \sqrt{g_*} (a + 3b/x_F)}, \quad (7.44)$$

2384 where $x_F = m_\chi/T_F$ being T_F the freeze-out temperature, g_* the number of relativistic
 2385 degrees of freedom at freeze-out and a and b the terms in the annihilation cross section
 2386 expansion $\sigma_{ann}|v| \approx a + bv^2 + \mathcal{O}(v^4)$. Using the current best fit for the relic DM density
 2387 $\Omega_\chi h^2 = 0.1198 \pm 0.0012$ [100] one can use these relations to compute the required
 2388 effective theory scale Λ at which the correct density is achieved for any combinations of
 2389 m_χ and c_A^ℓ .

2390 As discussed before, in the low DM mass region QEL interactions dominate. Moreover,
 2391 if I focus on direct annihilation to neutrinos, the energy of the muon neutrino flux is
 2392 known as it must be equal to the mass of the DM particle, $E_\nu = m_\chi$. That way, now
 2393 I do not need to use Eq. (7.33) in order to estimate the momentum transfer to the

7.7. Example: Leptophilic Dark Matter

2394 remnant nucleus, I can simply take:

$$\vec{p}_N = \hat{p}_\nu m_\chi - \vec{p}_\mu - \vec{p}_p. \quad (7.45)$$

2395 To estimate the signal efficiency and background rejection for this case I used again
2396 the MLP classifier from `scikit-learn`, using the same specifications as before. The
2397 only difference now is that I add also the reconstructed neutrino energy as one of the
2398 features to train the classifier with, because the characteristic monoenergetic flux for
2399 each m_χ value will help to distinguish between signal and background events.

2400 In this case, for masses below ~ 500 MeV I obtain a signal efficiency close to unity
2401 while keeping a background rejection of 99.9%. For bigger values of the mass, the signal
2402 efficiency drops significantly if I require to keep the background acceptance under 0.01%.
2403 However, because this kind of search is dominated by the background, sacrificing the
2404 signal acceptance to keep the background rejection to a minimum enhances the reach
2405 of the analysis. This way, for DM masses of the order of $m_\chi \sim 1$ GeV I end up with
2406 efficiencies as low as 1%.

2407 Now, estimating the number of background events using Eq. (7.39) one can go on
2408 and apply Eqs. (7.26) and (7.27) together with Eq. (7.42) to derive the sensitivity of
2409 DUNE to this kind of model. Fig. 7.18 (left panel) shows the potential reach of DUNE
2410 to constrain the EFT scale Λ this model containing only leptophilic DM axial-axial
2411 interactions (blue line), for a choice of couplings $c_A^e = 10^3$ and $c_A^\nu = 10^{-2}$. I also included
2412 the current limits on the DM-electron scattering cross section from DarkSide-50 [14]
2413 (dotted green line) and XENON1T [15] (dashed red line), reworked with Eq. (7.42) to
2414 show their implications for the EFT scale. The values of Λ for which the correct DM relic
2415 density value is achieved for each mass are also shown (black line). This tells us that,
2416 for that specific choice of couplings, DUNE would be sensitive to DM configurations
2417 allowed by the relic density constraint up to a mass of $m_\chi \sim 400$ MeV.

2418 In Fig. 7.18 (right panel) I show the same upper limits but for the DM-electron
2419 scattering cross section. From this view one can see that DUNE would be able to

Chapter 7. DM searches with neutrinos from the Sun

2420 offer complementary information to the low energy DM-electron interaction searches
2421 performed by direct detection experiments, in a slightly higher mass range.

2422 With the present example, although it focuses on a very specific realisation of the DM
2423 interactions, I show the potential of DUNE to constrain exotic DM scenarios. Thanks
2424 to its low backgrounds and superb angular resolution DUNE will be able to help with
2425 the systematic searches for dark sectors physics.

2426 Chapter 8

2427 Particle ID in GArSoft

2428 ND-GAr is a magnetised, high-pressure gaseous argon TPC (HPgTPC), surrounded by
2429 an electromagnetic calorimeter (ECal) and a muon detector (commonly refer to as μ ID).
2430 A detailed discussion on the requirements, design, performance and physics of ND-GAr
2431 can be found in the DUNE ND CDR [56] and the ND-GAr whitepaper (cite).

2432 In DUNE Phase II ND-GAr will fulfill the role of TMS, measuring the momentum
2433 and sign of the charged particles exiting ND-LAr. Additionally, it will be able to measure
2434 neutrino interactions inside the HPgTPC, achieving lower energy thresholds than those
2435 of the ND and FD LArTPCs. By doing so ND-GAr will allow to constrain the relevant
2436 systematic uncertainties for the LBL analysis even further.

2437 The goal of the present chapter is to review the requirements that the physics program
2438 of DUNE impose on ND-GAr, present the current status of its design and describe the
2439 GArSoft package, its simulation and reconstruction software.

2440 As decided during the DUNE Phase II workshop in June 2023 [reference], we want
2441 to build ND-GAr physics case by showing:

- 2442 • That ND-GAr can constrain systematic uncertainties that ND-LAr might miss.
- 2443 • The impact on the neutrino oscillation results if such systematic uncertainties are
2444 missed.
- 2445 • That ND-GAr is necessary to reach DUNE's main physics goals.

Chapter 8. Particle ID in GArSoft

2446 This way, the design of ND-GAr will be physics driven.

2447 In order to study the effects of final state interactions (FSI) in CC interactions,
2448 ND-GAr should be able to measure the spectrum of protons and charged pions at low
2449 energies. ND-GAr also needs to be able to measure the pion multiplicity, specially for
2450 energies above 100 MeV as at these energies the pions shower in the LAr, to inform the
2451 pion mass correction in the ND and FD LArTPCs.

2452 In order to correctly identify electrons, muons, pions, kaons and protons ND-GAr
2453 can use a combination of: dE/dx measurements in the HPgTPC, E_{ECAL}/p using the
2454 ECAL total energy and the momentum obtained from magnetic spectroscopy in the
2455 HPgTPC and penetration information through the ECAL and muon tagger.

2456 8.1 dE/dx measurement in the TPC

2457 Among the parameters extracted from the track fitting, ionisation is particularly useful
2458 for particle identification, as it is a function of the particle velocity. Although for the
2459 case of relativistic particles this dependence is not very strong, measuring the track on
2460 a large number of points may allow us to estimate the amount of ionisation accuratel.
2461 This, paired with a measurement of the momentum, may allow us to identify the particle
2462 type.

2463 The first calculation of the energy loss per unit length of relativistic particles using a
2464 quantum-mechanical treatment is due to Bethe [101]. Using this approach, the mean
2465 ionisation rate of a charged particle traveling through a material medium is (using
2466 natural units $G = \hbar = c = 1$):

$$\left\langle \frac{dE}{dx} \right\rangle = \frac{4\pi Ne^4}{m_e \beta^2} z^2 \left(\log \frac{2m_e \beta^2 \gamma^2}{I} - \beta^2 \right), \quad (8.1)$$

2467 where N is the number density of electrons in the medium, e the elementary charge, m_e
2468 is the electron mass, z the charge of the particle in units of e , β is the velocity of the
2469 particle, $\gamma = (1 - \beta^2)^{-1}$ and I denotes the effective ionisation potential averaged over
2470 all electrons. This relation is known as the Bethe-Bloch formula.

8.1. dE/dx measurement in the TPC

From Eq. (8.1) one can see that the ionisation loss does not depend explicitly on the mass of the charged particle, that for non-relativistic velocities it falls as β^{-2} , then goes through a minimum and increases as the logarithm of γ . This behaviour at high velocities is commonly known as the relativistic rise. The physical origin of this effect is partly due to the fact that the transverse electromagnetic field of the particle is proportional to γ , therefore as it increases so does the cross section.

It was later understood that the relativistic rise could not grow indefinitely with γ . A way to add this feature in the Bethe-Bloch formula is by introducing the so-called density effect term. It accounts for the polarisation effect of the atoms in the medium, which effectively shield the electromagnetic field of the charged particle halting any further increase of the energy loss [102]. Denoting the correction as $\delta(\beta)$, one can rewrite Eq. (8.1) as:

$$\left\langle \frac{dE}{dx} \right\rangle = \frac{4\pi Ne^4}{m_e \beta^2} z^2 \left(\log \frac{2m_e \beta^2 \gamma^2}{I} - \beta^2 - \frac{\delta(\beta)}{2} \right). \quad (8.2)$$

In general, the form of $\delta(\beta)$ depends on the medium and its state of aggregation, involving the usage of tabulated parameters and implicit relations [103].

Another standard method to compute the amount of ionisation a charged particle produces is the so-called photo-absorption ionisation (PAI) model proposed by Allison and Cobb [104]. Within their approach, the mean ionisation is evaluated using a semiclassical calculation in which one characterises the continuum material medium by means of a complex dielectric constant $\epsilon(k, \omega)$. However, in order to model the dielectric constant they rely on the quantum-mechanical picture of photon absorption and collision. Therefore, in the PAI model the computation of the ionisation loss involves a numerical integration of the measured photo-absorption cross-section for the relevant material.

In a particle physics experiment, the typical way of determining the energy loss per unit length as a function of the particle velocity is studying identified particles over a range of momenta. Once we have established this relation we can use it for other, unknown particles. In this sense, it makes sense to have a regular mathematical expression for this relation that one can use.

Chapter 8. Particle ID in GArSoft

2498 It happens that neither the Bethe-Bloch theory nor the PAI model from Allison and
2499 Cobb offer a close mathematical form for the ionisation curve. This is the reason why a
2500 full parametrisation of the ionisation curves can be useful. A parametrisation originally
2501 proposed for the ALEPH TPC [105] and later used by the ALICE TPC [106] group that
2502 manages to capture the features of the ionisation energy loss is:

$$f(\beta\gamma) = \frac{P_1}{\beta^{P_4}} \left(P_2 - \beta^{P_4} - \log \left[P_3 + \frac{1}{(\beta\gamma)^{P_5}} \right] \right), \quad (8.3)$$

2503 where P_i are five free parameters. Hereafter, we will refer to Eq. (8.3) as the ALEPH
2504 dE/dx parametrisation.

2505 8.1.1 Energy calibration

2506 In order to obtain the amount of energy loss by a charged particle due to ionisation
2507 in our TPC we need to determine the conversion between the charge deposited in our
2508 readout planes and the actual energy depositions. This procedure is known as energy
2509 calibration.

2510 In a general, the first step of the calibration involves a non-uniformity correction,
2511 to make sure that the detector response is uniform throughout the TPC. These are
2512 typically divided into three categories, non-uniformities in the transverse YZ plane,
2513 non-uniformities along the drift direction X and variations of the detector response
2514 over time (would not apply to us as the detector is not built yet). These would correct
2515 for effects such as electron diffusion and attenuation, space charge effects or channel
2516 misconfiguration. However, because at the moment I am only interested in making sure
2517 we recover a sensible result from our simulation, I will not apply uniformity corrections
2518 to our charge deposits.

2519 Other effects, like electron-ion recombination or ADC saturation, lead to a non-linear
2520 relation between the observed charge and the deposited energy in the detector, with the
2521 observed readout charge saturating at high ionisation energies. In this case, because we
2522 are dealing with gaseous argon and therefore recombination is not as important as in

8.1. dE/dx measurement in the TPC

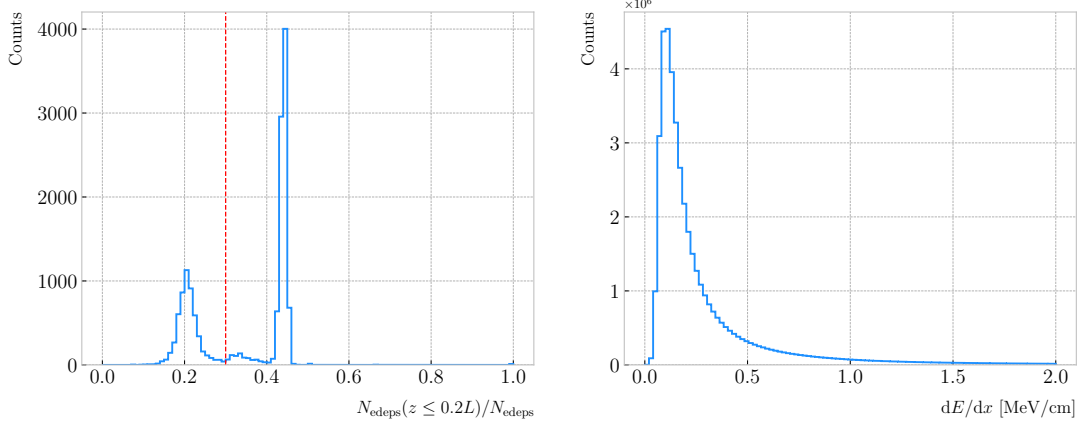


Figure 8.1: Left panel: distribution of the fraction of Geant4-level energy deposits per track with residual range less than 20% of the total track length, for the isotropic proton sample. Right panel: distribution of the ionisation per unit length of the energy deposits in the proton sample after removing the tracks with less than 30% of their energy deposits in the last 20% of the track.

2523 liquid, we do not simulate recombination effects in the TPC. Even so, the simulation of
 2524 the electronic response will still introduce charge saturation, and one needs to correct
 2525 for it in order to obtain the exact amount of energy loss due to ionisation.

2526 By default, the track fitting algorithm in GArSoft provides a `TrackIonization`
 2527 object associated to each reconstructed track. It contains two collections of charge
 2528 deposits, one for each fitting direction, consisting on pairs of charge values (dQ , in ADC)
 2529 and step sizes (dx , in cm).

2530 In order to estimate the ionisation loss in the ND-GAr TPC, I have used an MC
 2531 sample consisting of single, isotropic protons propagating in the TPC. The starting points
 2532 of the protons were sampled inside a $50 \times 50 \times 25$ cm box centered at $(100, -150, 1250)$,
 2533 and their momenta are uniformly distributed in the range $0.25 - 1.75$ GeV. I ran the
 2534 simulated sample through GArSoft's default detector simulation and reconstruction, and
 2535 then a custom analyser module that extracts the ionisation data together with other
 2536 reconstructed track information from the Kalman fit.

2537 For studying the energy loss of the protons I select the reconstructed tracks that
 2538 range out (i.e. slow down to rest) inside the TPC. A characteristic feature of the energy
 2539 loss profile of any stopping ionising particle is the so-called Bragg peak, a pronounced

Chapter 8. Particle ID in GArSoft

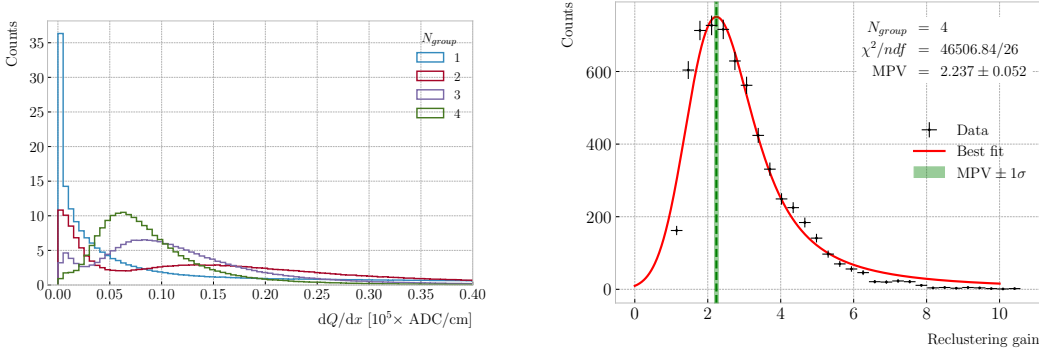


Figure 8.2: Left panel: distribution of the reconstructed ionisation charge per unit length for our MC stopping proton sample. The different colors indicate how many consecutive dQ/dx pairs were grouped together. Right panel: distribution of the median change in dQ/dx per track after $N_{group} = 4$ clusters were reclustered together.

peak that occurs immediately before the particle comes to rest. From Eq. (8.1) we can see that this behaviour is expected, as the energy loss for non-relativistic particles is inversely proportional to β^2 . In data, a way of identifying the Bragg peak, and thus select the stopping particles, is checking the number of energy deposits towards the end of the track. In this case, I count the fraction of the Geant4 simulated energy deposits with a residual range value (the distance from a given energy deposit to the last deposit in the track trajectory) less than a 20% of the corresponding track length¹. The distribution of this fraction of energy deposits for our proton sample is shown in Fig. 8.1 (left panel). We can clearly see two well separated peaks in this distribution, one centered at 0.2 and another, narrower, one centered at a higher value. The first one corresponds to non-stopping protons, as in that case the number of energy deposits towards the end of the track is uniformly distributed due to the absence of the Bragg peak. In that way, I apply a cut in this distribution, requiring that at least 30% of the simulated energy deposits sit in the last 20% of the tracks, to ensure that the Bragg peak is present.

Figure 8.1 (right panel) shows the distribution of the energy loss per unit length for the Geant4 simulated energy deposits of the selected stopping protons. We can see that

¹As we are applying this selection at the Geant4 level we could have simply selected the stopping protons using the `EndProcess` labels from the simulation. However, the Bragg peak identification method displayed here could serve as a starting point for a selection of stopping protons in real data.

8.1. dE/dx measurement in the TPC

it follows the expected shape of a Landau distribution, which describes the fluctuations of the ionisation energy losses [107]. This distribution has a characteristic asymmetric PDF, with a long right tail that translates into a high probability for high-energy ionisation losses. The origin of these fluctuations is mainly the possibility of transferring a high enough energy to an electron, so it becomes a ionising particle itself.

Now, from the point of view of the reconstruction, the objects that we have available to extract the ionisation information for the different reconstructed tracks are the collections of dQ and dx pairs, as stated before. The dQ values come from adding up the amplitude of all the reconstructed hits in a cluster, which is the input object to the Kalman fit.

Figure 8.2 (left panel) shows the distribution of the ionisation charge deposits per unit length for the track in the stopping proton sample (blue line). As one can notice, this distribution does not resemble the expected shape of the Landau PDF. This distribution peaks sharply at 0 and has a heavy tailed behaviour. Notice, however, how the distribution changes its shape as we group together N_{group} consecutive charge deposit pairs (red, purple and green lines). The distribution in the $N_{group} = 4$ case already has a shape which resembles that of the Geant4-level ionisation per unit length, so I will proceed using this amount of reclustering for the reconstruction-level depositions.

An extra factor I need to account for, when reclustering is applied, is how the overall dQ/dx per track changes. To do so, we can look at the ratio between the median dQ/dx after and before the reclustering. Figure 8.2 (right panel) shows the median enhancement in dQ/dx per track for the stopping proton sample in the case $N_{group} = 4$. Fitting a Landau distribution convolved with a Gaussian², I estimate the most probable value of this ratio to be $G_{group} = 2.24 \pm 0.05$.

At this point, I am left with determining the conversion between the charge deposits per unit length dQ/dx and the energy deposits per unit length dE/dx . To this end, we need a way of comparing the two. I can use the residual range z to get a prediction of

²In the literature, this distribution is often referred to as Landau+Gaussian or langau. In the following, I will use LanGauss to refer to such PDF.

Chapter 8. Particle ID in GArSoft

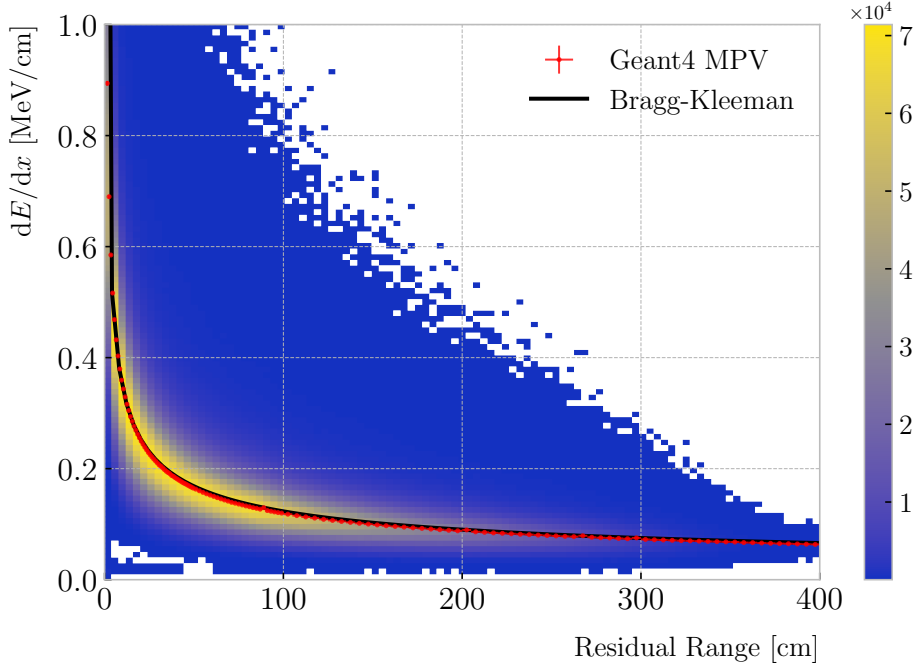


Figure 8.3: Distribution of the Geant4-simulated energy losses per unit length versus residual range for the stopping proton sample. The overlaid points represent the fitted most probable value of the dE/dx distribution in each residual range bin, whereas the curve is their best fit to the Bragg-Kleeman formula from Eq. (8.4).

2584 the most probable dE/dx by using the following empirical parametrisation [108]:

$$\frac{dE}{dx}(z) = \frac{z^{\frac{1}{p}-1}}{p\Lambda^{\frac{1}{p}}}, \quad (8.4)$$

2585 which is quoted in the literature as the Bragg-Kleeman formula. In order to obtain the
 2586 p and Λ parameters I perform a fit using the energy losses and the residual ranges given
 2587 by the Geant4 stage of our proton sample.

2588 Within our simulation, the residual range is sampled with a maximum size of
 2589 5 mm. Therefore, to perform the fit to the Bragg-Kleeman formula, we can use a
 2590 fine-grained residual range binning. For each of the residual range bins I extract the
 2591 dE/dx distribution and fit it to a LanGauss distribution, to obtain the value of the
 2592 most probable dE/dx in the bin together with a statistical uncertainty. I then fit Eq.
 2593 (8.4) to these most probable values and the centres of the residual range bins. This

8.1. dE/dx measurement in the TPC

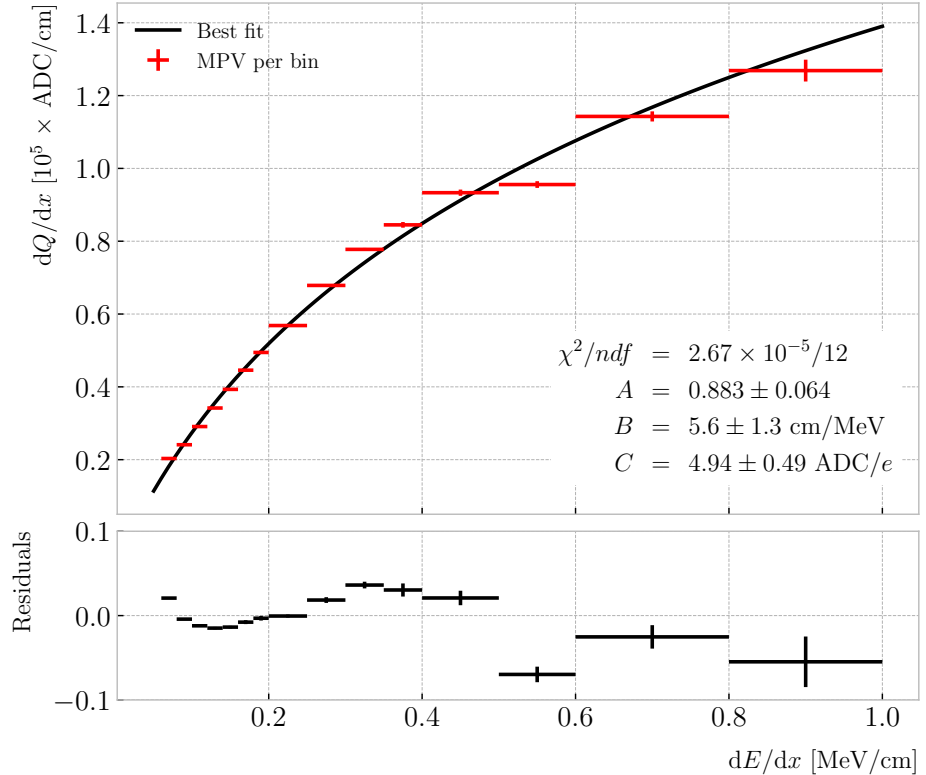


Figure 8.4: Fitted most probable dQ/dx values for each dE/dx bin (red points), obtained from the stopping proton sample. The overlaid curve (black line) represents the best fit to the logarithmic calibration function from Eq. (8.5).

procedure is depicted in Fig. 8.3, where I show the distribution of the energy loss per unit length versus the residual range, together with the most probable dE/dx values and their uncertainty in each bin (red points) and the curve with the best fit of the Bragg-Kleeman relation to those values (black line). The best fit is obtained for the parameter values $p = 1.8192 \pm 0.0005$ and $\Lambda = 0.3497 \pm 0.0008$ cm/MeV³.

Having an analytical expression that relates the residual range to dE/dx , I can take our reconstruction-level residual ranges from the stopping proton sample and compute the most probable energy loss associated.

In order to parametrise the charge saturation, we can use the following logarithmic

³These strange units for Λ come from dimensional analysis, just to keep the Bragg-Kleeman formula (8.4) consistent.

Chapter 8. Particle ID in GArSoft

2603 function inspired by the modified box model for recombination:

$$\frac{dE}{dx} = \frac{e^{\frac{dQ}{dx}B\frac{W_{ion}}{G_{group}C}} - A}{B}, \quad (8.5)$$

2604 where A and B are the calibration parameters we need to determine, W_{ion} is the average
 2605 energy to produce an electron-ion pair, G_{group} is the gain from the reclustering discussed
 2606 above and C is the calibration constant to convert number of electrons to ADC counts,
 2607 commonly refer to as gain (also to be obtained in the fit). In this case, I use a value
 2608 for the electron-ion production energy of $W_{ion} = 26.4$ eV [109]. This value, used in our
 2609 simulation as well, was measured for gaseous argon in normal conditions, and therefore
 2610 should be checked in the future to describe correctly the high-pressure argon-CH₄ mixture
 2611 of ND-GAr.

2612 For the calibration fit I follow a procedure similar to the previous one for Eq. (8.4).
 2613 Binning the dE/dx range, I fit a LanGauss distribution to the corresponding dQ/dx
 2614 distribution to obtain the most probable value. The resulting data points (red bars) are
 2615 shown in Fig. 8.4 (top panel), the horizontal error bars depict the width of the dE/dx
 2616 bin whereas the vertical bars represent the error associated to the most probable value
 2617 estimation. A fit to the logarithmic function in Eq. (8.5) is also shown (black line).
 2618 For this I weighted the data points using the inverse of their relative error, obtaining
 2619 a reduced chi-square value of $\chi^2/ndf = 2.22 \times 10^{-6}$. The best fit parameters I found
 2620 from this fit are $A = 0.883 \pm 0.064$, $B = 5.6 \pm 1.3$ cm/MeV and $C = 4.94 \pm 0.49$ ADC/e.
 2621 Figure 8.4 (bottom panel) shows the residuals between the data points and the fit.

2622 The value for the gain I obtained from the fit is in reasonable agreement with our
 2623 expectation. This value is set in GArSoft to 5 ADC/e by default.

2624 One interesting thing to check is what induces this non-linear relation between charge
 2625 and energy. The only effects that modify the amount of electrons reaching the readout
 2626 planes in the simulation are the transverse diffusion and the finite electron lifetime.
 2627 Once the electrons reach the readout chambers, the pad response functions are applied,
 2628 together with an electrons-to-ADC conversion and the ADC saturation limit.

8.1. dE/dx measurement in the TPC

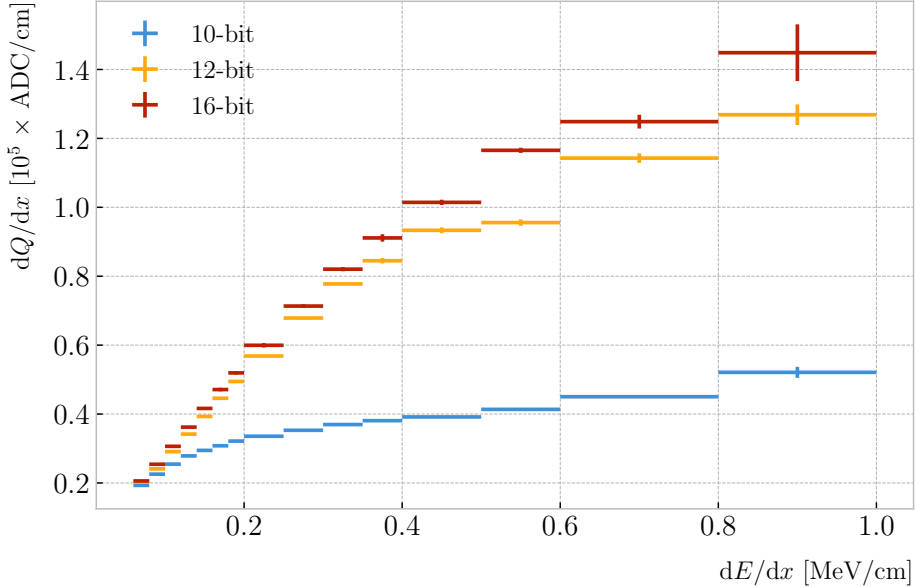


Figure 8.5: Fitted most probable dQ/dx values for each dE/dx bin for three different ADC bit limits, 10 (blue points), 12 (default, yellow points) and 16-bit (red points).

Table 8.1: Calibration parameters obtained from the fit of the ND-GAr simulated stopping proton sample to the calibration function from Eq. (8.5). The fits were performed for the 10, 12, and 16-bit ADC limits.

	χ^2/ndf	Best fit $\pm 1\sigma$		
		A	B (cm/MeV)	C (ADC/e)
10-bit	$1.83 \times 10^{-6}/12$	-9.3 ± 3.9	270 ± 69	27.1 ± 5.4
12-bit	$2.67 \times 10^{-5}/12$	0.883 ± 0.064	5.6 ± 1.3	4.94 ± 0.49
16-bit	$1.44 \times 10^{-5}/12$	0.949 ± 0.024	3.53 ± 0.58	4.52 ± 0.29

By default, GArSot applies a 12-bit ADC limit, which can be changed in the simulation configuration. However, it can only be increased up to 16-bit, as we represent the ADC collection as a `std::vector<short>`. This way, I tried to change the saturation parameter to see how it affects the relation between reconstructed charge and energy. Figure 8.5 shows a comparison between the most probable dQ/dx for 10, 12 and 16-bit ADC limits. As expected, the lower the limit is the sooner the charge saturates. For higher ADC limits the relation between energy and charge remains linear up to higher dE/dx values, but even for the 16-bit limit the saturation is noticeable for values $\gtrsim 0.5$ MeV/cm.

Chapter 8. Particle ID in GArSoft

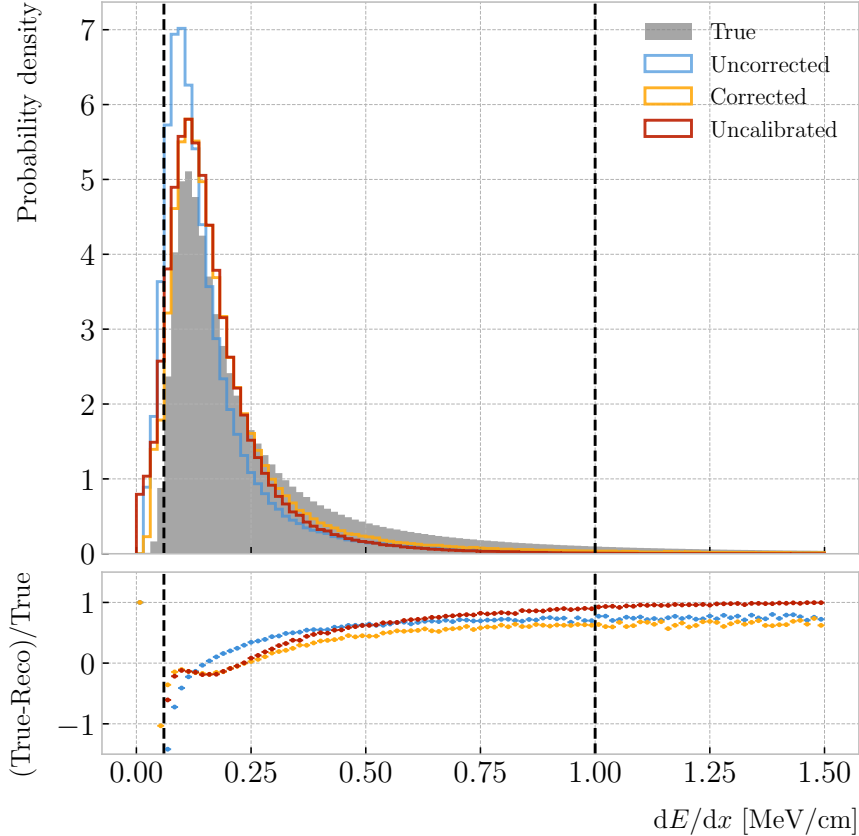


Figure 8.6: Top panel: area normalised dE/dx distributions for the true (solid grey) and the reconstructed energy deposits in the stopping proton sample, both after applying the calibration (blue) and the calibration and the normalisation correction (yellow). Also shown is the distribution obtained by applying a correction factor to the dQ/dx values but not the calibration (red). Bottom panel: fractional residuals for the uncorrected (blue), corrected (yellow) and uncalibrated (red) samples.

Table 8.1 shows the results of fitting the samples with 10 and 16-bits ADC limits to the calibration function from Eq. (8.5), using the weights based on their relative error as described previously. One interesting feature to notice is how different the best fit points look for the 10-bit ADC saturation when compared to the other two, which are consistent with each other.

At this point we can compare the dE/dx distribution one gets from Geant4, i.e. the true energy loss distribution, and the distribution I found by applying the calibration function to our collection of reconstructed dQ/dx values. Figure 8.6 (top panel) shows the true (solid grey) and reconstructed (blue, labeled as uncorrected) distributions

8.1. dE/dx measurement in the TPC

2647 together. The dashed vertical lines indicate the region of validity of the calibration fit, i.e.
2648 the left and right edges of the first and last dE/dx bin respectively. Notice that these
2649 histograms are area-normalised, as the total number of true energy deposits is much
2650 higher than the number of reconstructed charge deposits. This is due to a combination
2651 of effects, like the finite spatial resolution of the detector, the hit clustering used in the
2652 track fitting and the reclustering we have applied here.

2653 The two distributions are significantly different. That can be seen clearly when
2654 looking at the fractional residuals, shown in Fig. 8.6 (bottom panel). In particular,
2655 the position of the peak is off, which could bias the mean energy loss predictions. It
2656 seems like the difference between these may be due to an overall scaling factor. One
2657 possibility is to scale the most probable value of the reconstructed distribution to
2658 the most probable value predicted by Geant4. I do this by fitting both distributions
2659 using a LanGauss function, obtaining $dE/dx_{MPV, true} = 0.1145 \pm 0.0005$ MeV/cm and
2660 $dE/dx_{MPV, reco} = 0.0928 \pm 0.0005$ MeV/cm for the true and reconstructed most probable
2661 values respectively. These can be translated into an scaling factor $S = 0.579 \pm 0.006$.

2662 The result of applying the scaling correction can be seen in Fig. 8.6 (top panel).
2663 The corrected dE/dx distribution (yellow, labeled as corrected) peaks around the same
2664 value the true distribution does, as expected. Moreover, the high energy region is also
2665 slightly better described. For low ionisations, below the lower limit of the calibration
2666 fit, the differences between true and reconstructed are still significant. This low energy
2667 excess may be migration of some events from the peak region. The overall effect of the
2668 correction can be seen in the fractional residual plot in Fig. 8.6 (bottom panel).

2669 One can also check what happens if instead of applying the logarithmic calibration we
2670 simply scale the dQ/dx distribution (post reclustering) to have the same most probable
2671 value as the true dE/dx distribution. In this case, following an analogous procedure to the
2672 one described earlier, I found the scaling factor $S_{uncalibrated} = 0.414 \pm 0.002$ MeV/ADC⁴.
2673 The resulting distribution (red, labeled as uncalibrated) is also shown in in Fig. 8.6 (top
2674 panel). The behaviour of the new distribution is similar to the corrected case at low

⁴Notice that now the scaling factor is not dimensionless, as it acts more like a conversion factor here.

Chapter 8. Particle ID in GArSoft

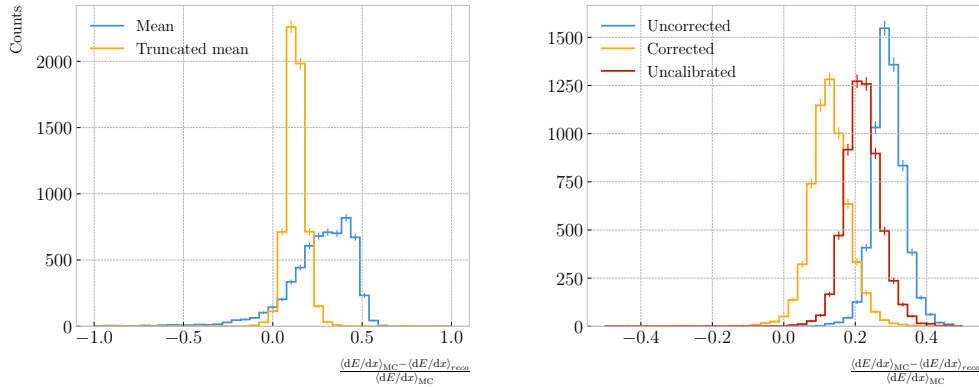


Figure 8.7: Left panel: fractional residuals between the true and the corrected $\text{d}E/\text{d}x$ means (blue) and the 60% truncated means (yellow), for each event in the stopping proton sample. Right panel: fractional residuals between the true and the uncorrected (blue), corrected (yellow) and uncalibrated (red) $\text{d}E/\text{d}x$ 60% truncated means, for each event in the stopping proton sample.

2675 energy losses, around the peak of the true distribution, but it is worse at describing the
 2676 high energy tail. This is expected, it is in the high ionisation regime where saturation
 2677 effects apply and therefore calibration is needed.

2678 8.1.2 Truncated $\text{d}E/\text{d}x$ mean

2679 Once we have a collection of $\text{d}E/\text{d}x$ values for each reconstructed track, we can compute
 2680 the corresponding most probable ionisation loss per unit length of the particle. This
 2681 is the value predicted by the Bethe-Bloch or the PAI models, and together with a
 2682 measurement of the momentum it allows for particle identification.

2683 However, estimating the most probable $\text{d}E/\text{d}x$ value for each reconstructed track
 2684 is not a trivial task. As mentioned before, the $\text{d}E/\text{d}x$ distributions follow Landau-like
 2685 distributions. Therefore, one should perform e.g. a LanGauss fit to correctly estimate
 2686 the most probable values. Automating this kind of fits is often problematic, as they
 2687 usually incur in convergence problems. Moreover, the reconstructed $\text{d}E/\text{d}x$ distributions
 2688 we obtain tend to have relatively small statistics, which may also produce poor fits. In
 2689 practice, doing these unsupervised fits may degrade our performance, and a more robust
 2690 method is preferred.

8.1. dE/dx measurement in the TPC

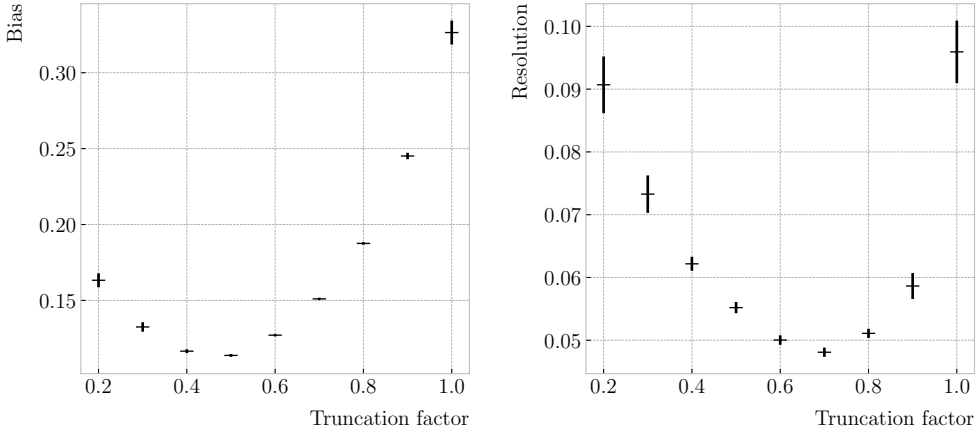


Figure 8.8: Estimated values of the mean dE/dx bias (left panel) and resolution (right panel) obtained using the corrected data from the stopping proton sample, for different values of the truncation factor.

A possibility could be taking the mean of the reconstructed dE/dx distribution for each particle. The problem with this approach is that the high energy Landau tail, combined with our limited statistics, can induce large fluctuations in the computation of the mean. Imagine you have two protons with the same kinetic energy, but due to reconstruction problems in one case you did not get as many charge deposits reconstructed in its high ionisation loss region. If you do not remove the tails the computed dE/dx means will be significantly different.

In order to avoid those fluctuations, one can compute the mean of a truncated dE/dx distribution instead. By keeping only a given fraction of the lowest energy deposits we obtain an estimate of the mean energy loss that is more resilient to reconstruction inefficiencies and statistical effects. Figure 8.7 (left panel) shows a comparison between the $\langle dE/dx \rangle$ computed by taking the mean of the full distribution (blue line) and the 60% lowest energy clusters (yellow line), for the stopping proton sample. The fractional residuals are computed for each proton, taking the corresponding means using their collections of true and reconstructed energy deposits. One can see that using the simple mean translates into a high bias and uncertainty in the $\langle dE/dx \rangle$ estimation, whereas applying the truncation reduces both significantly.

Additionally, I performed a comparison between the 60% truncated mean dE/dx

Chapter 8. Particle ID in GArSoft

2709 obtained using the different calibration methods discussed earlier, namely the uncorrected
 2710 (blue), corrected (yellow) and uncalibrated (red) distributions. The results are shown
 2711 in Fig. 8.7 (right panel). While the widths of these distributions are similar, the bias
 2712 obtained for the corrected sample, i.e. calibration function and correction factor applied,
 2713 is a factor of ~ 2 lower than in the uncalibrated case and almost three times smaller
 2714 than for the uncorrected sample.

2715 The next step is to optimise the level of truncation we are going to apply to our
 2716 data. To do so, I used different truncation factors, i.e. the percentage of energy-ordered
 2717 reconstructed energy deposits we keep to compute the mean, on the corrected dE/dx
 2718 sample of the stopping protons. Then, following the same procedure of computing the
 2719 fractional residuals as before, I fitted the resulting histograms using a double Gaussian
 2720 function. This is simply the sum of two Gaussian functions of the type:

$$g(x; \mu, \sigma, A) = A e^{-\frac{(x-\mu)^2}{2\sigma^2}}. \quad (8.6)$$

2721 I do not add the classical normalisation factor of the Gaussian, $1/\sqrt{2\pi}\sigma$, therefore
 2722 the amplitude A simply represents the maximum of the function. One of the two
 2723 Gaussian functions describes the core part of the distribution, while the other captures
 2724 the behaviour of the tails.

2725 For each truncation factor, I look at the bias and the resolution I obtain. I define
 2726 these as the weighted means of the corresponding parameters in the fits:

$$\bar{x} = \frac{A_{core} x_{core} + A_{tail} x_{tail}}{A_{core} + A_{tail}}, \quad (8.7)$$

2727 where A_{core} and A_{tail} are the amplitudes of the core and tail distributions respectively
 2728 and x is either the mean μ or the width σ of said distributions.

2729 Figure 8.8 shows the bias (left panel) and the resolution (right panel) I obtained
 2730 for the stopping proton sample, using different values of the truncation. From these, it
 2731 can be seen that a truncation factor of 50% minimises the bias in the estimation, while

8.1. dE/dx measurement in the TPC

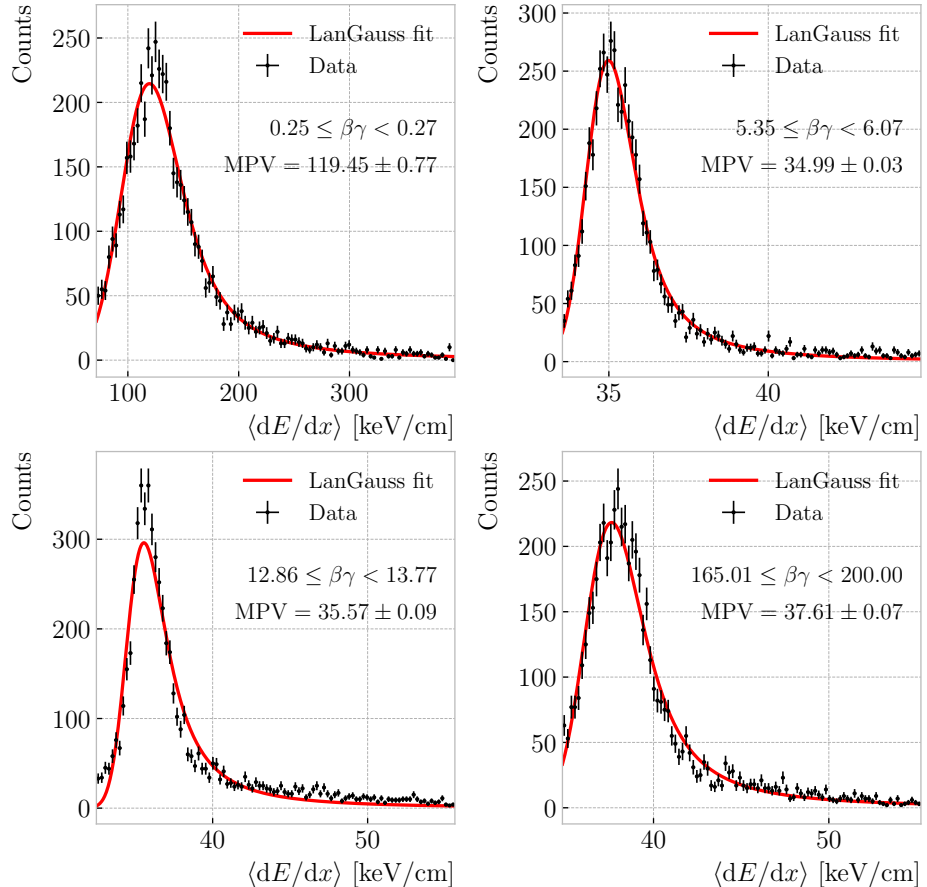


Figure 8.9: Examples of the truncated mean dE/dx LanGauss fits for various $\beta\gamma$ bins, from a simulated FHC neutrino sample.

2732 70% gives the best resolution. That way, I settled on the intermediate value of 60%
 2733 truncation, which yields a $\langle dE/dx \rangle$ resolution of 5.00 ± 0.08 % for stopping protons.

2734 8.1.3 Mean dE/dx parametrisation

2735 Now that we have a way to estimate the mean energy loss of a particle in the HPgTPC,
 2736 we can determine the value of the free parameters in the ALEPH formula, Eq. (8.3).
 2737 For this, I used a sample of 10^5 reconstructed FHC neutrino events inside ND-GAr. In
 2738 this case I cannot use the stopping proton sample, as we need to cover the full kinematic
 2739 range of interest for the neutrino interactions in our detector.

2740 The original data does not contain an estimation of the velocity of the tracks, instead
 2741 the tracks have a value for the reconstructed momentum and the associated PDG code

Chapter 8. Particle ID in GArSoft

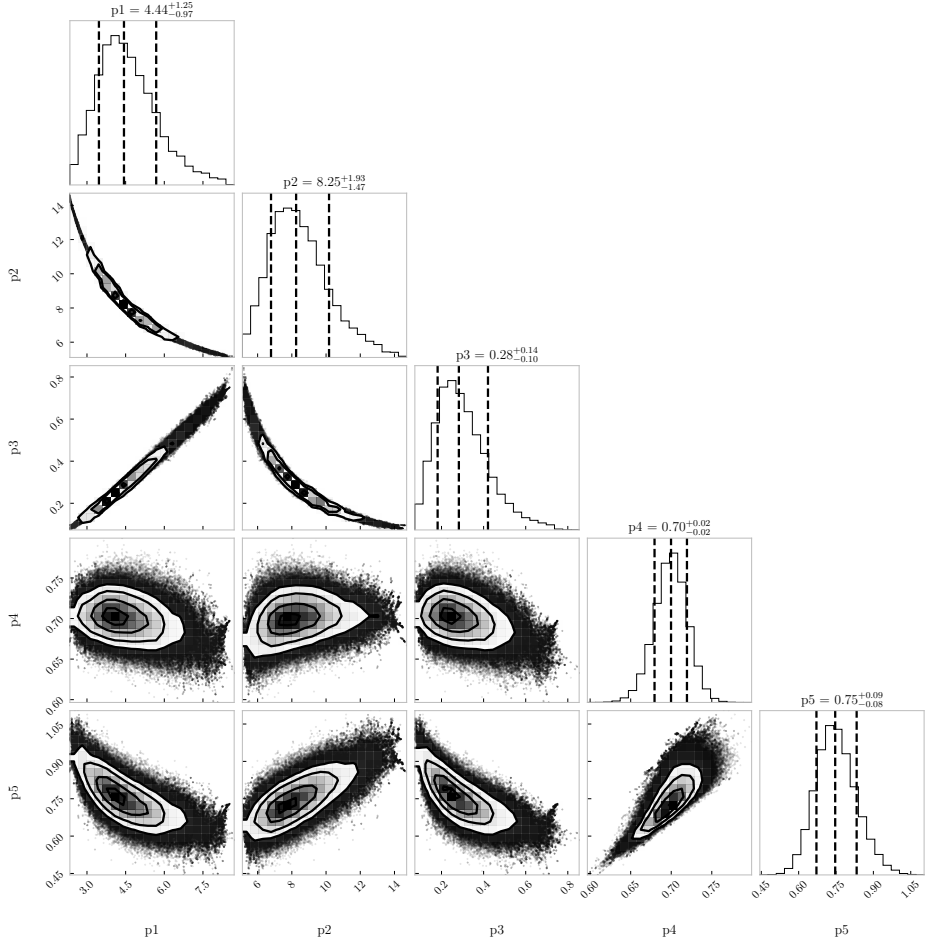


Figure 8.10: Resulting one and two dimensional projections of the posterior probability distributions of the ALEPH $\langle dE/dx \rangle$ parameters obtained by fitting the 60% truncated mean dE/dx values from a FHC neutrino sample in ND-GAr. The vertical dashed lines in the 1D distributions represent the 16th, 50th and 84th percentiles.

2742 of the Geant4-level particle that created the track. Therefore, one can select some of the
 2743 particles in the data, in this case I selected electrons, muons, pions and protons, and
 2744 compute β and γ using the reconstructed momentum and their mass. In terms of $\beta\gamma$
 2745 the mean dE/dx does not depend on the particle species, so one can consider all the
 2746 dataset as a whole. For this fit, I will express β in terms of the $\beta\gamma$ product as:

$$\beta = \frac{\beta\gamma}{\sqrt{1 + (\beta\gamma)^2}}, \quad (8.8)$$

2747 which can be easily proven from the definition of γ .

8.1. dE/dx measurement in the TPC

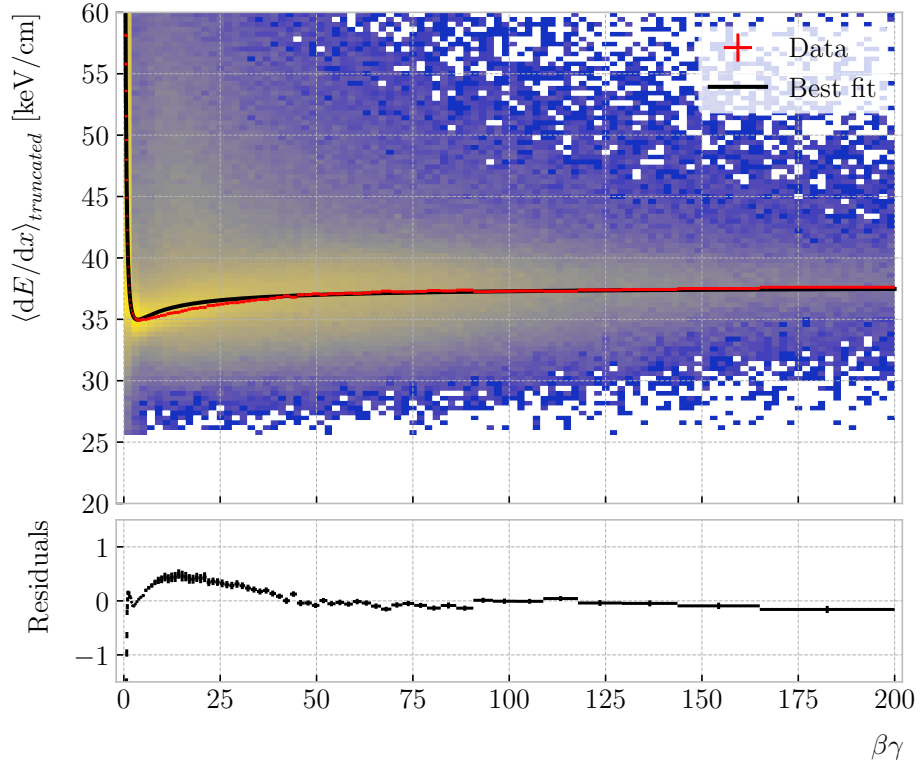


Figure 8.11: Truncated mean dE/dx obtained for the FHC neutrino sample as a function of the $\beta\gamma$ product (upper panel). Also shown are the fitted most probable values for each $\beta\gamma$ bin (red points) and the best fit obtained using the ALEPH parametrisation (black line). The residuals resulting from the fit are shown in the lower panel.

2748 Next, I bin the data in $\beta\gamma$. I chose a fine binning so as to capture the different
 2749 features of the ionisation curve. Instead of fixing the bin width, I select them so each one
 2750 has approximately the same statistics. Then, for each $\beta\gamma$ slice, I compute the median
 2751 and the interquartile range (IQR) of the $\langle dE/dx \rangle$ distribution. Using these, I make a
 2752 histogram in the range [median – IQR, median + 5 IQR], which I fit to a LanGauss
 2753 function in order to extract the MPV. Using this range accounts for the asymmetric
 2754 nature of the distributions, while also helps avoiding a second, lower maximum present
 2755 at low $\beta\gamma$, probably a result of reconstruction failures.

2756 A few examples of these fits are shown in Fig. 8.9. The chosen values of $\beta\gamma$ sit in
 2757 very distinct points along the $\langle dE/dx \rangle$ curve, going from the high ionisation region at
 2758 low velocities (top left panel), to the minimum point (top right panel), the beginning of

Chapter 8. Particle ID in GArSoft

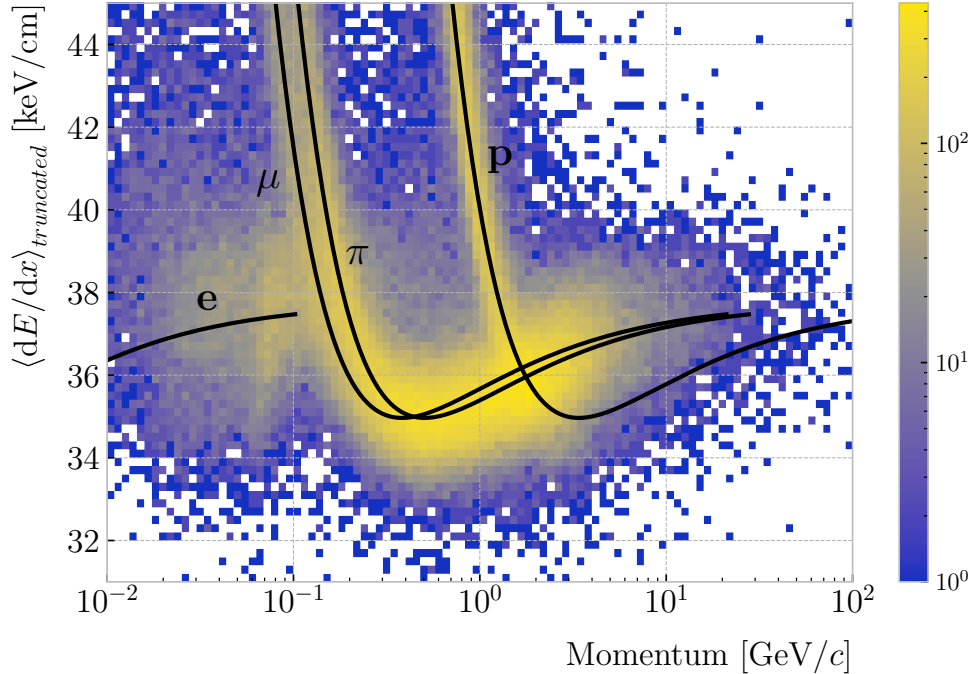


Figure 8.12: Distribution of the 60% truncated mean $\langle dE/dx \rangle$ versus reconstructed momentum for the FHC neutrino sample. The black lines indicate the predictions of the ALEPH parametrisation for electrons, muons, charged pions and protons.

2759 the relativistic rise (bottom left panel), and the plateau produced by the density effect
 2760 (bottom right panel).

2761 I used the resulting most probable $\langle dE/dx \rangle$ values and the centres of the $\beta\gamma$ bins as
 2762 the points to fit to the ALEPH formula. For this particular fit I used the least-squares
 2763 method to get a first estimation of the ALEPH parameters. Applying some uniform
 2764 priors, I then used these values as the starting point of a 100000 steps MCMC. Figure 8.10
 2765 shows the posterior probability distributions I obtain for each parameter. The reported
 2766 best fit points are based on the 16th, 50th, and 84th percentiles in the marginalised
 2767 distributions.

2768 The resulting fit (black line), compared to the data points (red points) and the
 2769 underlying distribution is shown in Fig. 8.11 (top panel). The overall fit is good, with a
 2770 reduced chi-squared of $\chi^2/ndf = 1.02$. However, there are some regions where the fit
 2771 does not describe the data correctly, like the very low $\beta\gamma$ regime, where the fit severely
 2772 underestimates for energy losses $\gtrsim 50$ keV/cm, and the start of the relativistic raise,

8.2. Muon and pion separation in the ECal and MuID

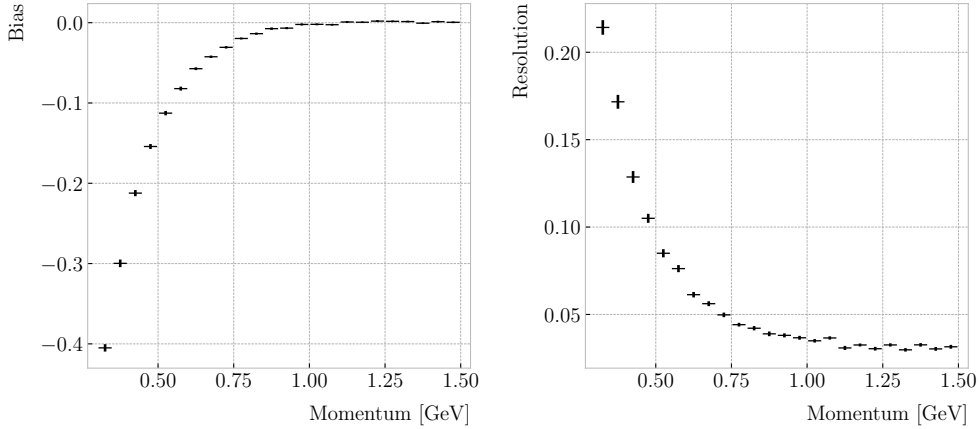


Figure 8.13: Estimated values of the mean dE/dx bias (left panel) and resolution (right panel) obtained for the true protons in a FHC neutrino sample.

where we have a slight overestimation. This is a result of those points having a larger uncertainty when compared to the ones around the dip or the plateau areas. These differences can be better seen in the residual plot, Fig. 8.11 (bottom panel).

8.1.4 Particle identification

8.2 Muon and pion separation in the ECal and MuID

As it could be seen from Fig. 8.12, it is not possible to separate muons and charged pions in the HPgTPC using dE/dx for momenta $\gtrsim 300 \text{ MeV}/c$. In ND-GAr, approximately 70% of the interactions in FHC mode will be ν_μ CC (compared to the 47% of $\bar{\nu}_\mu$ CC interactions when operating in RHC mode), while 24% are neutral currents. Out of these, around 53% and 47% of them will produce at least one charged pion in the final state, respectively. Figure 8.14 shows a comparison between the spectra of the primary muons and the charged pions for ν_μ CC interactions in ND-GAr producing one or more charged pions. From this, one can see that (i) the majority of muons and charged pions are not going to be distinguishable with a $\langle dE/dx \rangle$ measurement, and that (ii) particle identification is necessary both to classify correctly the ν_μ CC events and identify the primary muon within them.

ND-GAr features two other subdetectors which can provide additional information

Chapter 8. Particle ID in GArSoft

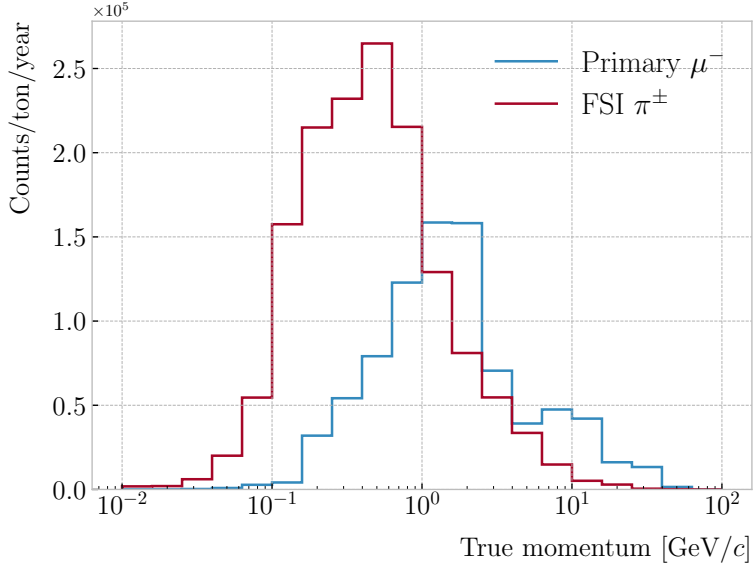


Figure 8.14: True momentum distribution for the primary muon in ν_μ CC $N\pi^\pm$ interactions inside the fiducial volume of ND-GAr (blue line), compared to the post FSI charged pion spectrum (red line).

for this task, namely the ECal and MuID. The current ECal design, described in (ref section), consists of 42 layers, made of 5 mm of Pb, 7 mm of plastic scintillator and a 1 mm PCB board. The total thickness of this calorimeter is 1.66 nuclear interaction lengths or 1.39 pion interaction lengths. The MuID design is in a more conceptual stage, however it is envisioned to feature layers with 10 cm of Fe and 2 cm of plastic scintillator⁵. With its three layers, it will have a thickness of 1.87 or 1.53 nuclear or pion interaction lengths, respectively.

Because pion showers are dominated by inelastic nuclear interactions, the signatures of these particles in the calorimeter will look significantly different from those of muons. Although our ECal is not thick enough to fully contain the hadronic showers of the charged pions at their typical energies in FHC neutrino interactions, they can still be used to understand whether the original particle was more hadron-like or MIP-like. In Fig. 8.15 I show two examples of energy distributions created by a muon (left panel) and a charged pion (right panel) of similar momenta interacting in the ECal. These

⁵It is not mentioned anywhere, but I assume that there should also be another layer of PCB board of 1 mm. However, in this case its contribution to the total thickness of the sampling calorimeter would be negligible.

8.2. Muon and pion separation in the ECal and MuID

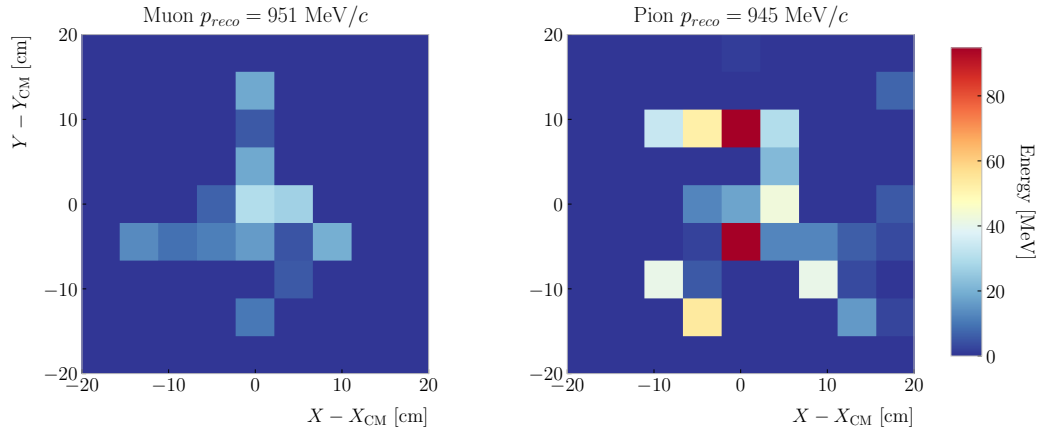


Figure 8.15: Distributions of energy deposits in the ECal for a muon (left panel) and a charged pion (right panel) with similar momenta. The energy is projected onto the plane perpendicular to the principal component of the hits, and the positions are relative to the center of the interaction.

2804 figures represent the transverse development of the interactions. For each of them, I
 2805 computed the principal component and centre of mass of the interaction, projecting
 2806 the position of the hits onto the plane perpendicular to that direction, and taking the
 2807 distances relative to the centre. It can be seen that the muon follows an almost MIP-like
 2808 behaviour, being the central bin in the histogram the one with the highest deposited
 2809 energy. On the other hand, the pion not only deposits more energy overall, but also this
 2810 energy is more spread-out among the different hits. It is this kind of information that
 2811 would allow us to tell apart muons from pions.

2812 This way, I identify three main action points that need to be addressed if one wants
 2813 to use these detectors to distinguish between muons and charged pions. These are:

- 2814 1. the way we make the associations between tracks in the HPgTPC to the activities
 2815 (what in GArSoft we call clusters) in the ECal and the MuID,
- 2816 2. what variables or features one can extract from the calorimeters that encapsulate
 2817 the information we are interested about,
- 2818 3. and how to carry out the classification problem.

Chapter 8. Particle ID in GArSoft

2819 8.2.1 Track-ECal matching

2820 One of the main players in the muon and pion separation is the way we associate clusters
2821 in the ECal to reconstructed tracks in the TPC. Missing some associations or making
2822 wrong ones can bias the ECal quantities that we can use for classifying particles. The
2823 current algorithm in GArSoft provides precise associations, i.e. most of the associations
2824 that it produces are correct, but it appears to miss an important number of associations
2825 (at least when using the default configuration).

2826 The current TPC track-ECal cluster association algorithm is divided in four parts.
2827 It first checks whether the track end point fulfils certain conditions to be extrapolated.
2828 There are two cut values in this step, one for the drift direction and other radial.

2829 If the point can be extrapolated, the code computes the coordinates of the centre
2830 of curvature using the Kalman fit estimates at the track end ($y, z, 1/R, \phi, \tan\lambda$). It
2831 then compares the distance between this and the cluster in the (z, y) plane with R . This
2832 introduces another cut in the perpendicular direction.

2833 The next step is different for clusters in the barrel or in one of the end caps. If it
2834 is a barrel cluster the algorithm extrapolates the track up to the radial distance of the
2835 cluster. There are three possible outcomes, the extrapolated helix can cut the cylinder
2836 of radius r_{clus} two, one or zero times. I get the cut point that is closer to the cluster and
2837 check that it is either in the barrel or the end caps. Computing the difference between
2838 the x coordinates of the cluster and the extrapolated point, the module checks that this
2839 is not greater than a certain cut. If the cluster is in an end cap, I propagate the track
2840 up to the x position of the cluster. Then, the algorithm computes the angle in the (z, y)
2841 plane between the centre of curvature and the cluster, α , and the centre of curvature
2842 and the propagated point, α' . A cut is applied to the quantity $(\alpha - \alpha')R$.

2843 If the cluster contains more than a certain number N of hits, I apply an extra cut to
2844 the dot product of the direction of the track at the propagated x value and the cluster
2845 direction.

2846 The code makes sure to only associate one end of the track (if any) to a cluster.

8.2. Muon and pion separation in the ECal and MuID

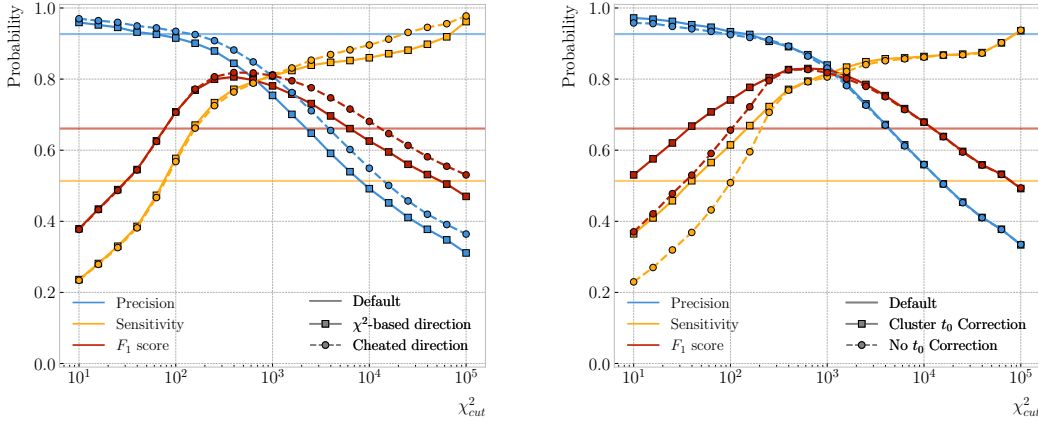


Figure 8.16: Left panel: comparison between the precision (blue), sensitivity (yellow) and F_1 score (red) obtained for the default (horizontal lines) and new algorithms, both with the χ^2 -based direction estimator (squares) and cheating the directions (circles), for different values of the χ^2 cut. Right panel: comparison of the performance of the new algorithm when applying the cluster t_0 correction (squares) and when (circles).

2847 However, it can associate more than one track to the same cluster. This makes sense,
2848 as different particles can contribute to the same cluster in the ECal, but it makes it
2849 difficult to quantify the relative contributions of the tracks to a certain cluster.

2850 As a way of comparing the performance of this algorithm, a new, simpler association
2851 module was written. The goal was to have a simple and robust algorithm, which depends
2852 on as few parameters as possible and that can produce a one-to-one matching between
2853 tracks and ECal clusters.

2854 For each reconstructed track, the new algorithms applies the same procedure to the
2855 forward and the backward fits irrespective of their end point positions. It first gets the
2856 Kalman fit parameters at the corresponding end point together with the X position, x_0 ,
2857 (y_0 , z_0 , $1/R$, ϕ_0 , $\tan\lambda$).

2858 For each ECal cluster, I compute the radial distance to the centre of the TPC and
2859 find the ϕ value in the range $[\phi_0, \phi_0 + \text{sign}(R)\phi_{max}]$ that makes the propagated helix
2860 intersect with the circle defined with such radius. The (x, y, z) position of the helix for
2861 the ϕ value found (if any) is then computed. In case there are two intersections, I keep
2862 the one that minimises the distance between (y, z) and (y_c, z_c) .

2863 I then calculate χ^2 value based on the Euclidean distance between the propagated

Chapter 8. Particle ID in GArSoft

2864 point and the cluster:

$$\chi^2/ndf = \frac{\sum_{n=0}^2 (x^{(n)} - x_c^{(n)})^2}{3}. \quad (8.9)$$

2865 If there was no intersection I store a -1 instead. In the end, for each reconstructed track
2866 in the event one ends up with two collections of χ^2 values, one for each ECal cluster
2867 and fit directions.

2868 The current code only supports having ECal clusters associated to one end of each
2869 track. We have two options to decide what track end to keep. The first one tries to
2870 cheat the selection, looking at the distance between the two track ends and the true
2871 start position of the associated MC particle. The second one keeps the track end with
2872 more χ^2 entries below the cut.

2873 This feature of only considering one track end limits the algorithm, making it not
2874 suitable for reconstructing events with particles originating outside the TPC. However,
2875 as for the moment the main concern of the group is the study of neutrino interactions
2876 off the gaseous argon, this is an acceptable assumption.

2877 In order to associate a cluster to a track, I take all clusters with a χ^2 value in the
2878 range $[0, \chi_{cut}^2]$. If a cluster has been assigned to more than one track we leave it with
2879 the one with the lowest χ^2 .

2880 This default behaviour of the algorithm can be modified to associate more than one
2881 track to each cluster. Not only that, but the χ^2 values can be used to assign relative
2882 weights to the different contributions.

2883 To evaluate the performance of the association method, I use a binary classification
2884 approach. In this case, I check the leading MC Track IDs associated to the reconstructed
2885 tracks and ECal clusters. I count an association as true positive (TP) if both Track
2886 IDs coincide. An association is considered false positive (FP) when the Track IDs are
2887 different. If a cluster has not been associated to any track but it shares the Track ID
2888 with a reconstructed track it is counted as a false negative (FN).

2889 For the testing, I used a sample of 10000 FHC neutrino events inside the HPgTPC.
2890 Figure 8.16 (left panel) shows the precision (blue line), sensitivity (yellow line), and F_1

8.2. Muon and pion separation in the ECal and MuID

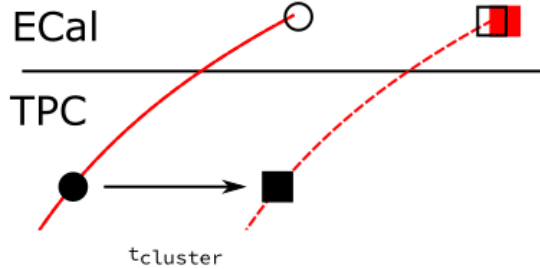


Figure 8.17: Schematics of a possible option to deal with track-ECal associations in non-zero t_0 neutrino interaction events, trying to correct for the drift direction uncertainty in a cluster-by-cluster basis using the cluster time, $t_{cluster}$.

2891 score (red line) I obtained for different values of χ^2_{cut} . For comparison, the same metrics
 2892 computed for the default algorithm with the current configuration are also shown (dashed
 2893 lines). In the case of the new algorithm, I used both the χ^2 -based method to estimate
 2894 the track direction described earlier (square markers) and the cheated direction from the
 2895 Geant-level information (circle markers). For either of these we achieve similar values of
 2896 the precision compared to the old code, while having a considerably higher sensitivity.
 2897 It can be seen that cheating the direction of the tracks only makes a difference at high
 2898 χ^2_{cut} , past the optimal value of the cut around the F_1 score maximum. Therefore, I set
 2899 the χ^2 method as the default.

2900 One of the possible weak points of this approach is that it relies on the position along
 2901 the drift direction to make the decisions. Within the current ND-GAr design implemented
 2902 in GArSoft, the timing information is provided by the ECal. That effectively means
 2903 that prior to make the track-ECal associations the reconstructed x positions of the track
 2904 trajectories differ from the simulated ones by an amount:

$$x_{reco}^{(n)} - x_{sim}^{(n)} = v_{drift} t_0, \quad (8.10)$$

2905 where v_{drift} is the mean drift velocity in our medium and the initial time is in the range
 2906 $t_0 \in [0, t_{spill}]$ where t_{spill} is the spill length. For a 10 μs spill this translates into a
 2907 maximum 30 cm uncertainty on the drift direction position.

2908 The current default in GArSoft sets $t_0 = 0$, but the functionality to randomly sample

Chapter 8. Particle ID in GArSoft

2909 this within the spill time is in place. Therefore, we need to understand what is the impact
2910 of a non-zero t_0 on the associations algorithm and foresee possible ways of minimising a
2911 loss in performance.

2912 Figure 8.17 represents a possible option to tackle the association problem when
2913 having events with a non-zero initial time t_0 . The black and white circles represent the
2914 original points, whereas the squares indicate the corrected positions. The end points of
2915 the track and the propagated points up to the cluster radius are indicated using filled
2916 and unfilled markers respectively. The red square represents the position of the cluster.

2917 Here I try to correct for the drift coordinate position using the time associated to the
2918 cluster. Assuming that the drift time is much larger than the propagation time, $t_{cluster}$
2919 could be used as a good estimation of the t_0 . An alternative can be using the earliest
2920 time associated to a hit in said cluster. Doing this for each cluster before computing
2921 the χ^2 value could be used as an alternative to knowing the specific value of the t_0 , as
2922 when the association is correct this will provide the right correction but its impact is
2923 small enough to not change the position significantly in the case the cluster does not
2924 correspond to a given track.

2925 I tested the effect of this correction again using a sample of 10000 FHC neutrino
2926 events. Figure 8.16 (right panel) shows the precision (blue line), sensitivity (yellow line),
2927 and F_1 score (red line) for the case the cluster t_0 correction is applied (square markers)
2928 and for the no correction case (circle markers), as a function of χ^2_{cut} . In this case, the
2929 differences are particularly notorious at low values of the cut. It makes sense, as the t_0
2930 effect becomes subdominant when the distance we consider grows large. Overall, the
2931 correction increases the sensitivity while keeping the precision almost unchanged. As a
2932 result, I apply the t_0 correction to the generated samples as the default.

2933 8.2.2 Classification strategy

2934 The problem of the muon and charged pion separation has to be viewed in the broader
2935 context of the particle identification in our detector. Focusing on the beam neutrino
2936 interactions, it is clear that we are going to have muons and pions spanning a broad

8.2. Muon and pion separation in the ECal and MuID

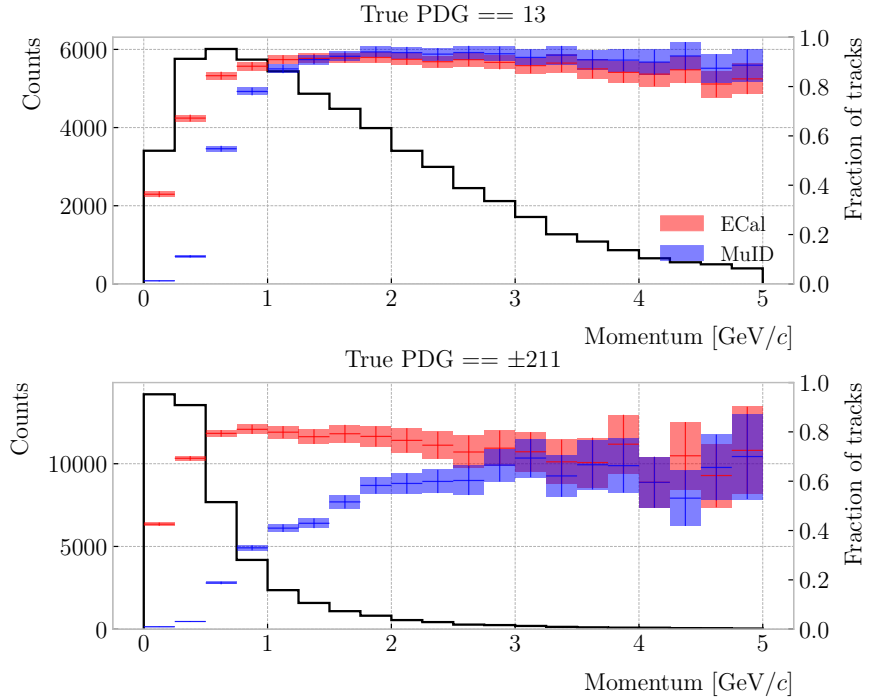


Figure 8.18: Momentum distribution for the reconstructed muons (top panel) and charged pions (bottom panel) in a FHC neutrino sample, together with the fraction of them reaching the ECal (red) and MuID (blue). Each entry corresponds to a reconstructed track, backtracked to a true muon or pion which has not produced any other reconstructed track.

2937 momentum range. Not only that, but we will also have other particles with similar
 2938 characteristics that will make the classification even more challenging. Therefore, we are
 2939 presented with a task that will depend heavily on the kinematic range we are looking at
 2940 each time, as both the available information and the possible impurities of other particle
 2941 species vary.

2942 For instance, distinguishing muons from pions could be difficult at low momenta, as
 2943 a great number of them do not reach the ECal. Therefore, we could think of tailoring a
 2944 version of the classification for that particular case, which could be complemented with
 2945 a dE/dx measurement. Likewise, for momenta $\gtrsim 1$ GeV muons and pions reach the
 2946 calorimeters efficiently, but so do protons. Because of this, one can try to train another
 2947 classifier for this energy range, and rely on other methods to remove as many of the
 2948 protons as possible.

Chapter 8. Particle ID in GArSoft

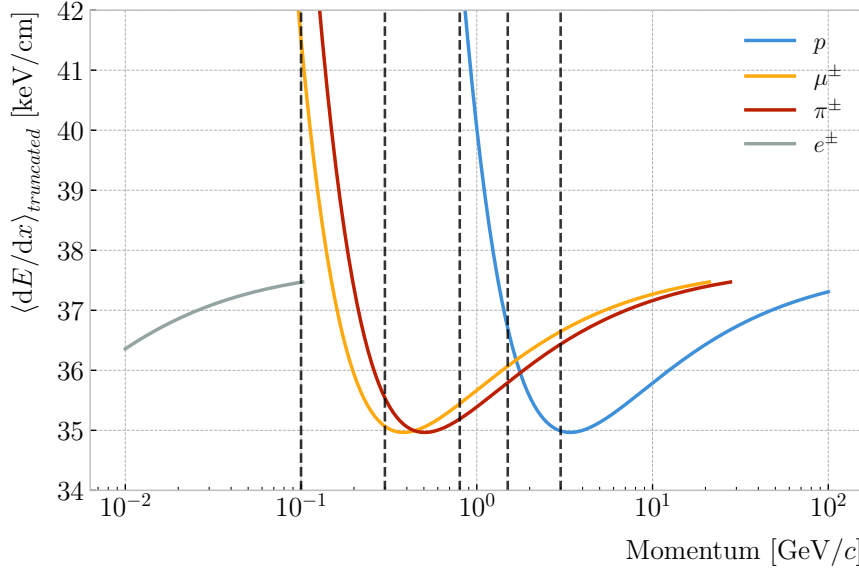


Figure 8.19: Predicted truncated mean dE/dx versus momentum, for electrons, muons, charged pions and protons, obtained using the ALEPH parametrisation. The vertical dashed lines represent the boundaries of the six regions used for the muon and pion classification training.

2949 Figure 8.18 shows the momentum distribution of the reconstructed muons (top) and
 2950 pions (bottom) in a FHC sample. It also contains the fraction of particles reaching the
 2951 ECal (red) and MuID (blue), for the different momentum bins. In Fig. 8.19 I show the
 2952 mean dE/dx of different particles as a function of the momentum, computed using the
 2953 ALEPH parametrisation with the best fit parameters found in Subsec. 8.1.2.

2954 Using these two figures as references, I decided to approach the classification by
 2955 dividing the problem into six different momentum regions. A summary of these can be
 2956 found in Tab. 8.2. The basic idea is to exploit all the information that is available in
 2957 each region and . For the problem at hand, I prepared separated samples of isotropic
 2958 single muons and pions, with momenta uniformly distributed along the corresponding
 2959 momentum range. Each sample contains 50000 events of the corresponding particle
 2960 species. I did not generate samples for the first region, as it is assumed that the separation
 2961 can be achieved using dE/dx only. For the last region, I generated particles up to a
 2962 momentum of 10 GeV/c, as that is well above the typical energies of muons and pions
 2963 from FHC neutrino interactions in ND-GAr.

8.2. Muon and pion separation in the ECal and MuID

Table 8.2: Momentum ranges and description of the PID approach assumed for the muon and pion classification task.

Momentum range	Description
$< 0.1 \text{ GeV}/c$	All tracks can be separated with dE/dx
$[0.1, 0.3) \text{ GeV}/c$	Use ECal for reaching muons and pions, dE/dx for the rest
$[0.3, 0.8) \text{ GeV}/c$	Use ECal for muons and pions, dE/dx for protons
$[0.8, 1.5) \text{ GeV}/c$	Use ECal and MuID for muons and pions, dE/dx for protons
$[1.5, 3.0) \text{ GeV}/c$	Use ECal and MuID for muons and pions, ToF for protons
$\geq 3.0 \text{ GeV}/c$	Use ECal and MuID for muons and pions, dE/dx and ToF for protons

2964 Additionally, I prepared another sample of 100000 FHC neutrino events. For each
 2965 interaction, I select the reconstructed particles which were backtracked to true muons or
 2966 charged pions. I use this dataset to perform validation checks, to see how the models
 2967 trained with the single particle data generalise to a more realistic scenario.

2968 To tackle this classification problem, I make use of Boosted Decision Trees (BDT). A
 2969 decision tree uses a flowchart-like structure to make decisions based on some input data.
 2970 It starts from a root node, which represents the complete dataset, and then it splits
 2971 this based on the variable or feature which gives the best separation between classes,
 2972 creating two new nodes. The process repeats for each node until it reaches a certain
 2973 limit, like a maximum number of splits or some tolerance criteria. The last set of nodes
 2974 are often called leave nodes, and represent the final prediction of the classifier.

2975 Boosting refers to a family of methods to combine the predictions from multiple
 2976 classifiers, following a sequential approach where each new model learns from the errors
 2977 of the previous one. The process starts with a simple decision tree, which is used to
 2978 make predictions on the training data. Then, the data points misclassified by the first
 2979 model are assigned higher weights, and another decision tree is trained on the data with
 2980 adjusted weights. The predictions of the two trees are then combined, and the cycle
 2981 repeats for a predefined number of iterations. Gradient boosting uses the direction of
 2982 the steepest error descent to guide the learning process and improve the accuracy with
 2983 each iteration.

Chapter 8. Particle ID in GArSoft

2984 8.2.3 Feature selection and importance

2985 Using the reconstructed tracks as a starting point, I compute a number of ECal and
2986 MuID variables for each of them. As there can be more than one cluster associated to a
2987 track, what I do is collect all associated clusters and compute these variables from the
2988 complete collection of associated hits. For the MuID, because it only features three layers
2989 and typically there will be less hits, I also allow single hits to be associated with tracks⁶.
2990 I can roughly divide the variables in three types: energy-related, geometry-related and
2991 statistical. In the following, I briefly describe the variables related exclusively to the
2992 ECal:

2993 • Energy-related ECal

- 2994 – ECal total energy (ClusterTotalEnergy): sum of the energy of all the ECal
2995 hits.
- 2996 – Mean ECal hit energy (HitMeanEnergy): mean of the hit energy distribution.
- 2997 – Standard deviation ECal hit energy (HitStdEnergy): standard deviation of
2998 the hit energy distribution.
- 2999 – Maximum ECal hit energy (HitMaxEnergy): maximum of the hit energy
3000 distribution.

3001 • Geometry-related ECal

- 3002 – Mean distance hit-to-cluster (DistHitClusterMean): mean of the distance
3003 distribution between the hits and the corresponding cluster's main axis.
- 3004 – RMS distance hit-to-cluster (DistHitClusterRMS): root mean square of the
3005 distance distribution between the hits and the corresponding cluster's main
3006 axis.
- 3007 – Maximum distance hit-to-centre (DistHitCenterMax): maximum of the
3008 distance distribution between the hits and the centre of the TPC.

⁶At the reconstruction level what happens is that non-clustered hits are put into single hit clusters, instead of being thrown away. This is necessary to keep the consistency of the track-cluster association code.

8.2. Muon and pion separation in the ECal and MuID

- 3009 – Time-of-Flight velocity (TOFVelocity): slope obtained when fitting a straight
3010 line to the hit time versus hit distance to the centre (i.e. $d = v \times t$).

3011 • Energy and geometry ECal

- 3012 – Radius 90% energy (Radius90E): distance in the hit-to-cluster distribution
3013 for which 90% of the total energy is contained in the hits that are closer to
3014 the axis (i.e. radius that contains 90% of the energy).

3015 • Statistical ECal

- 3016 – Number of hits (NHits): total number of hits associated to the track.
3017 – Number of layers with hits (NLayers): not really a count of all layers with
3018 hits but the difference between the last and the first layer with hits.

3019 Figure 8.20 shows the distributions of three different ECal variables, separating true
3020 muons (blue) and charged pions (red), for the five momentum ranges considered. I chose
3021 to show one feature from each category, namely the mean energy per hit (left column),
3022 the mean distance between the hits and the centre of the cluster (middle column), and
3023 the number of ECal layers with hits (right column). These give an idea of the separating
3024 power of the different features, and how it changes considerably with the energy. In
3025 the number of layers with hits distributions, the peak at 6 is due to the fact that the
3026 first six ECal layers sit inside the pressure vessel⁷. Therefore, some of the particles get
3027 stopped crossing it, never making it to the seventh layer.

3028 In the case of the MuID, because at low momenta a significant fraction of the particles
3029 do not make it past the ECal, I only consider the information coming from this detector
3030 for momenta ≥ 0.8 GeV/ c , i.e. for the last three momentum regions. The variables I
3031 extract from it are the following:

3032 • Energy-related MuID

⁷Note to self: check this. I thought the ECal barrel had 8 layers of tiles, and that all of them were inside the pressure vessel.

Chapter 8. Particle ID in GArSoft

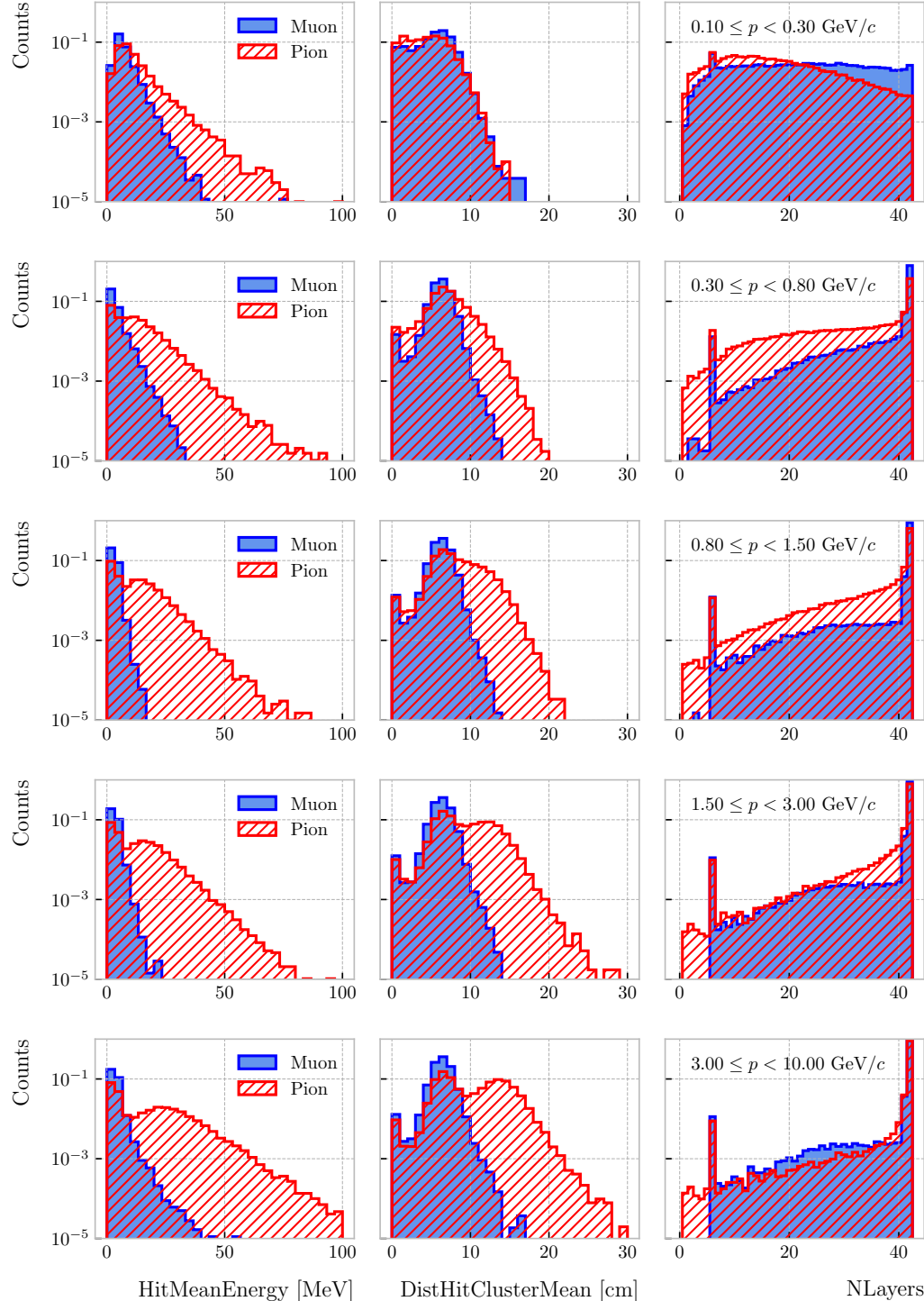


Figure 8.20: Example ECal feature distributions for muons (blue) and charged pions (red) in the five different momentum ranges considered (from top to bottom, in ascending momentum order). From left to right: mean hit energy, mean distance hit-to-cluster, and number of layers with hits.

8.2. Muon and pion separation in the ECal and MuID

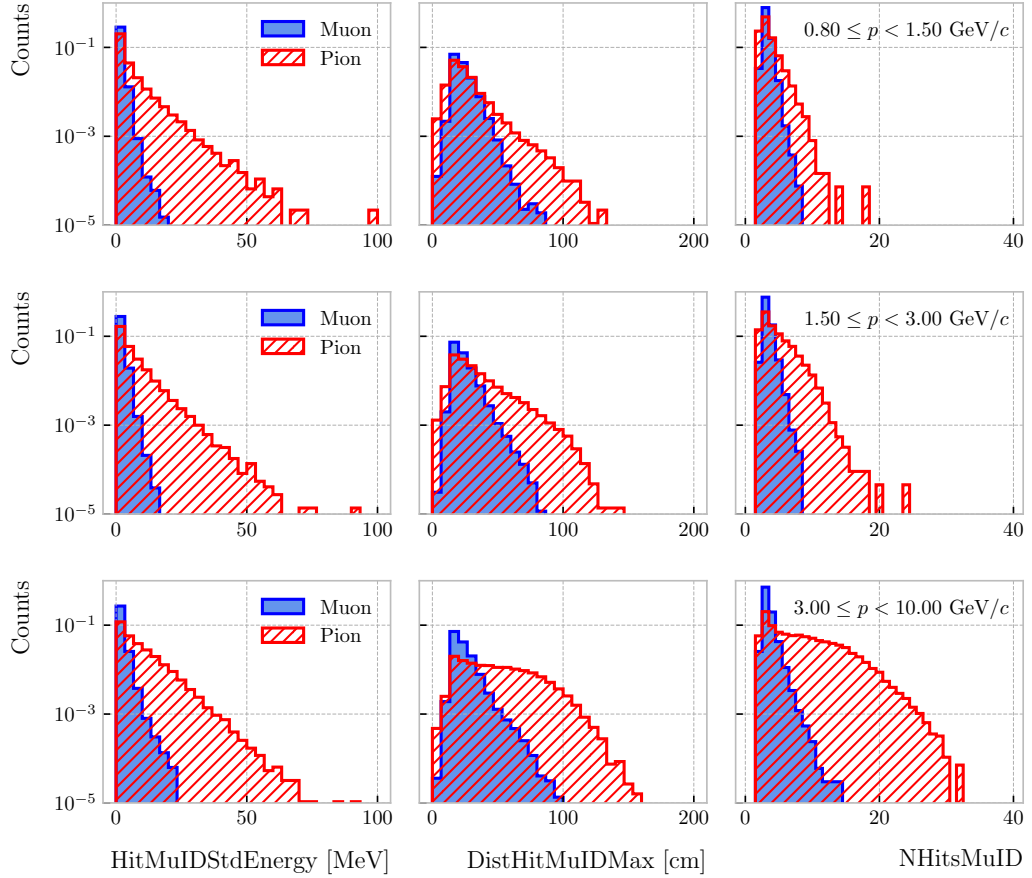


Figure 8.21: Example MuID feature distributions for muons (blue) and charged pions (red) in the three different momentum ranges considered (from top to bottom, in ascending momentum order). From left to right: standard deviation hit energy, maximum distance hit-to-hit, and number of hits.

- 3033 – MuID total energy (ClusterMuIDTotalEnergy): sum of the energy of all the
- 3034 MuID hits.
- 3035 – Mean MuID hit energy (HitMuIDMeanEnergy): mean of the MuID hit energy
- 3036 distribution.
- 3037 – Standard deviation MuID hit energy (HitMuIDStdEnergy): standard deviation
- 3038 of the MuID hit energy distribution.
- 3039 – Maximum MuID hit energy (HitMuIDMaxEnergy): maximum of the MuID
- 3040 hit energy distribution.

- 3041 • **Geometry-related MuID**

Chapter 8. Particle ID in GArSoft

- 3042 – Maximum distance MuID hit-to-hit (DistHitMuIDMax): maximum distance
3043 between pairs of MuID hits (not sure this is a good variable, distribution
3044 looks nuts).
3045 – Maximum distance MuID hit-to-centre (DistHitCenterMuIDMax): maximum
3046 of the distance distribution between the MuID hits and the centre of the
3047 TPC.

3048 • **Statistical MuID**

- 3049 – Number of hits (NHitsMuID): total number of MuID hits associated to the
3050 track.
3051 – Number of layers with hits (NLayersMuID): not really a count of all layers
3052 with MuID hits but the difference between the last and the first layer with
3053 MuIDhits.

3054 Figure 8.21 shows the distributions of three different MuID variables, separating true
3055 muons (blue) and charged pions (red), for the three momentum ranges which use the
3056 muon tagger information. In this case I decided to standard deviation of the MuID hit
3057 energy distribution (left column), the maximum distance between the MuID hit pairs
3058 (middle column), and the number of MuID hits (right column). These variables are used
3059 together with the ECal features at high momenta, providing additional disambiguation
3060 power.

3061 Once our features have been defined, one can do some exploratory analysis to
3062 understand how well the variables describe the target class, and avoid the black-box
3063 approach by what features are most relevant for the learning process. This way, I
3064 performed a feature analysis for each of the momentum ranges I divided this classification
3065 problem into. It follows three steps: first a principal component analysis (PCA), followed
3066 by a feature importance study using Gini and Shapley values, and finally a feature
3067 permutation importance analysis.

3068 The PCA is useful to understand the variance of the feature space. It is an
3069 unsupervised machine learning technique that allows the user to perform a dimensionality

8.2. Muon and pion separation in the ECal and MuID

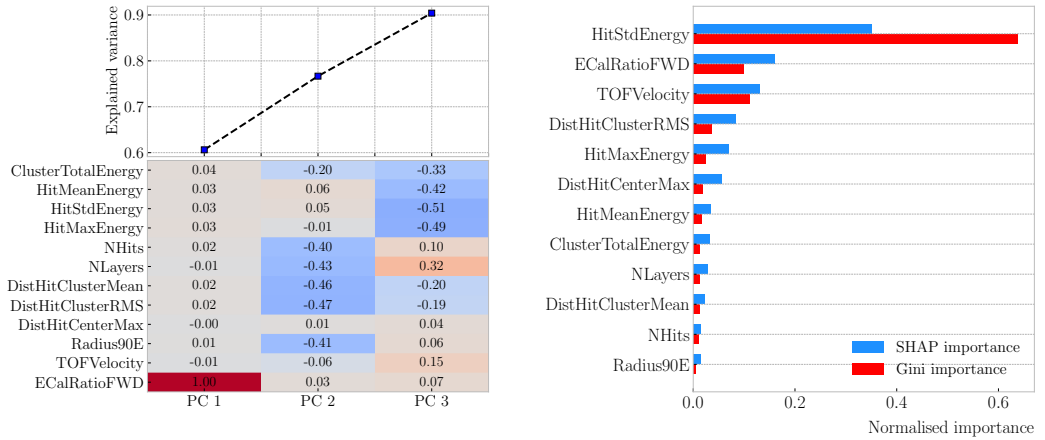


Figure 8.22: Left panel: cumulative explained variance for the first three principal components (top panel) and contribution of the different features to the principal axes in feature space (bottom panel). Right panel: Shapley (blue) and Gini (red) feature importances for the different input features. Both figures correspond to the samples in the momentum range $0.3 \leq p < 0.8$ GeV/c.

reduction. It uses a singular value decomposition of the input features to project them into a lower dimensional space. The idea is to find the matrix \mathbf{C}_m , whose columns are the first m orthonormal eigenvectors of the input covariance matrix. Consider the $n \times p$ real matrix of input data \mathbf{X} , where n is the number of samples and p the number of features. If \mathbf{X} is centred, i.e. the means of its columns are equal to zero, we can write the covariance matrix of \mathbf{X} as $\mathbf{C} = \mathbf{X}^\top \mathbf{X} / (n - 1)$. This matrix can be diagonalised, yielding:

$$\mathbf{C} = \mathbf{V} \mathbf{L} \mathbf{V}^\top, \quad (8.11)$$

where \mathbf{V} is a matrix of eigenvectors and \mathbf{L} a diagonal matrix with eigenvalues λ_i . Then, performing SVD on \mathbf{X} gives us:

$$\mathbf{X} = \mathbf{U} \mathbf{S} \mathbf{W}^\top, \quad (8.12)$$

where \mathbf{U} is a unitary matrix, whose columns are called left singular vectors, \mathbf{S} is a diagonal matrix of single values s_i , and \mathbf{W} is another unitary matrix, its columns known as right singular vectors. This way, we can write:

$$\mathbf{C} = \mathbf{W} \mathbf{S} \mathbf{U}^\top \mathbf{U} \mathbf{S} \mathbf{W}^\top / (n - 1) = \mathbf{W} \frac{\mathbf{S}^2}{n - 1} \mathbf{W}^\top. \quad (8.13)$$

Chapter 8. Particle ID in GArSoft

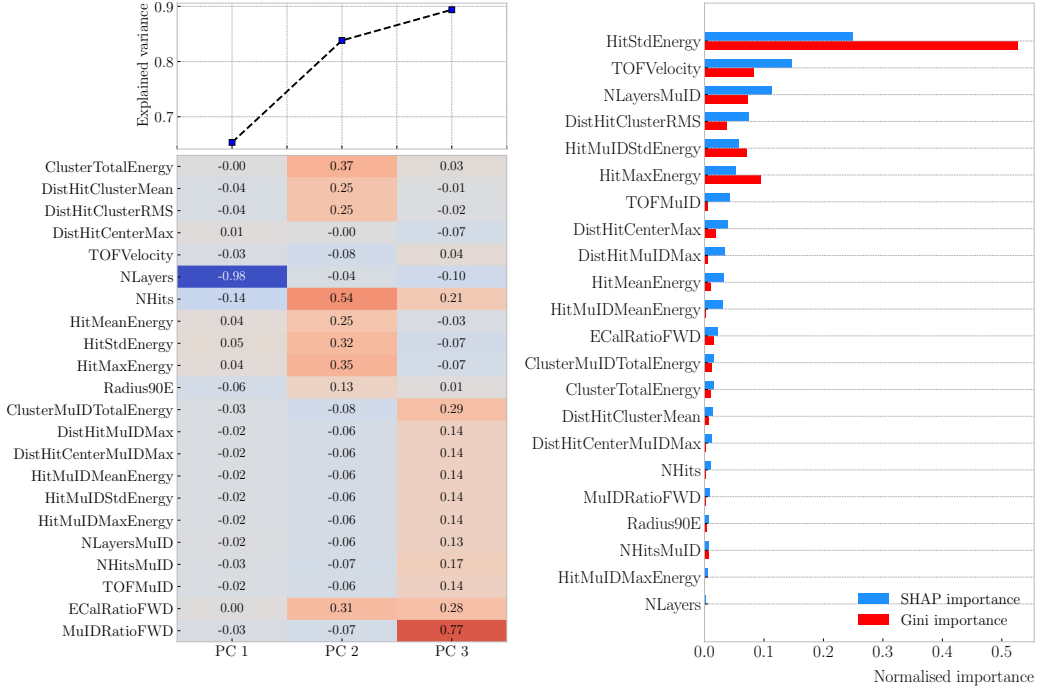


Figure 8.23: Left panel: cumulative explained variance for the first three principal components (top panel) and contribution of the different features to the principal axes in feature space (bottom panel). Right panel: Shapley (blue) and Gini (red) feature importances for the different input features. Both figures correspond to the samples in the momentum range $0.8 \leq p < 1.5$ GeV/c.

meaning that the right singular vectors are also the eigenvectors of the covariance matrix.

The SVD can be computed numerically following an iterative approach.

This way, taking an input data vector $X \in \mathbb{R}^n$, the resulting feature vector $Y \in \mathbb{R}^m$

is given by:

$$Y = \mathbf{C}_m^\top X. \quad (8.14)$$

The new features capture most of the variance of the original sample, while being lower dimensional, as $m < n$.

Before applying the PCA reduction one needs to centre and scale the input data.

Centring is necessary when using SVD to obtain the eigenvectors of the covariance matrix, as only in that case we can do the identification with the right singular vectors from the input data. Scaling is needed when variables are on different scales, as some can then dominate the PCA procedure.

8.2. Muon and pion separation in the ECal and MuID

3092 I used the PCA module of `scikit-learn`, together with the `RobustScaler`, which
 3093 centres the data and scales it based on the interquartile range. In Fig. 8.22 (left panel)
 3094 and Fig. 8.23 (left panel) I show the results I obtained from the PCA for the momentum
 3095 ranges $0.3 \leq p < 0.8 \text{ GeV}/c$ and $0.8 \leq p < 1.5 \text{ GeV}/c$, respectively. Notice that in
 3096 the second case the number of features increases considerably, as this is the first region
 3097 which uses the MuID variables. I found that, in all the cases, adding a fourth PC does
 3098 not add additional information. As it can be seen in the top panels of the figures, the
 3099 cumulative explained variance is already over 80% with three PCs.

3100 The bottom panels show the contribution of the variables to the principal axes. For
 3101 the two first momentum regions, I observe a tendency of the energy-related and the
 3102 geometry-related ECal variables to be clustered together. For the other ranges, when
 3103 I include the MuID variables, there seems to be a division between ECal and MuID
 3104 variables. For these, it seems like the number of ECal layers with hits also plays an
 3105 important role.

3106 The next step in the analysis is to quantify the importance of the features based on
 3107 two additional metrics, namely the Gini and the Shapley values. The Gini importance,
 3108 often called mean decrease impurity, is based on how much a feature contributes to the
 3109 purity improvement at the splits in each decision tree. The purity is measured in terms
 3110 of the Gini impurity index, defined as:

$$I_G = 1 - \sum_i f_i, \quad (8.15)$$

3111 where f_i is the fractional abundance of the i -th class. Then, for each split one can
 3112 compute the weighted decrease in impurity as:

$$\Delta_G = \frac{N_t}{N} \left(I_G - \frac{N_t^R}{N_t} I_G^R - \frac{N_t^L}{N_t} I_G^L \right), \quad (8.16)$$

3113 where N represents the total number of samples, N_t the number of samples at the current
 3114 node, N_t^R and N_t^L the number of samples in the right and left children respectively,

Chapter 8. Particle ID in GArSoft

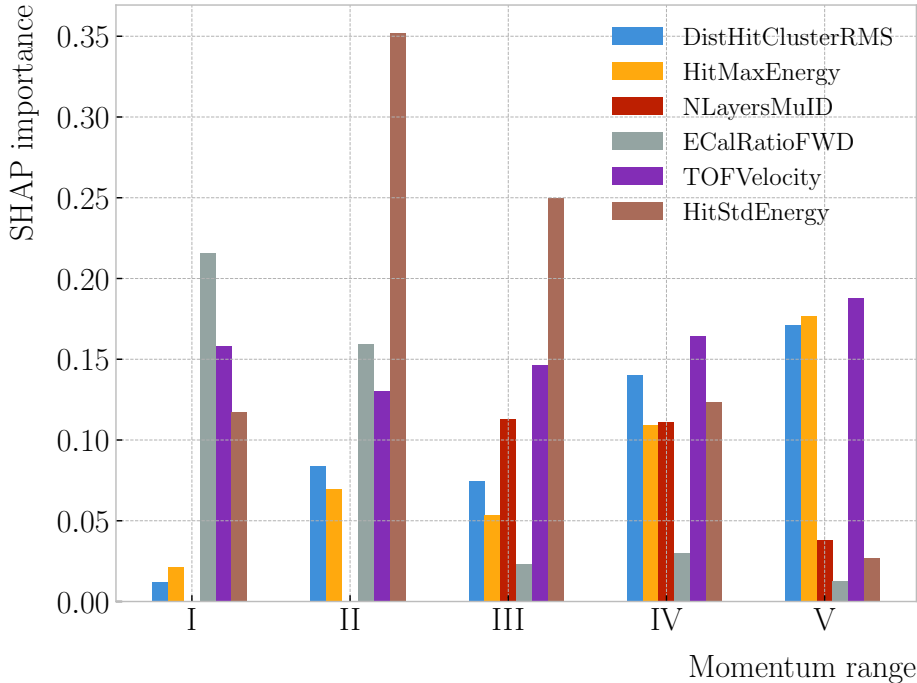


Figure 8.24: Evolution of the SHAP importance for the top six most important features across all five momentum ranges.

3115 I_G is the Gini impurity at the current node, and I_G^R and I_G^L the Gini impurities of the
3116 resulting right and left children.

3117 For each decision tree, one will have a normalised vector with the accumulated
3118 decrease in Gini impurity for each feature. In the case of a BDT, the feature importances
3119 are simply the mean for all the estimators in the ensemble⁸.

3120 The concept of Shapley values originated in the context of game theory, and it
3121 measures the marginal contribution of a feature in enhancing the accuracy of a classifier.
3122 Take F to be the set of all features in a problem, and $S \subseteq F$ the subset of features. To
3123 compute the Shapley value of the i -th feature, one has to train a model with that feature
3124 present, $f_{S \cup \{i\}}$, and another model trained without it, f_S . This has to be repeated for
3125 all possible combinations of subsets $S \subset F \setminus \{i\}$, and evaluating the models predictions

⁸Note to self: this appears not to be the case. If you get the `feature_importance` for each tree in the BDT and take the average, the result is not the same to be one reported in the `feature_importance` attribute of the BDT.

8.2. Muon and pion separation in the ECal and MuID

3126 on the appropriate sets of data x_S . This way, the Shapley value results:

$$\varphi_i = \sum_{S \subset F \setminus \{i\}} \frac{|S|! (|F| - |S| - 1)!}{|F|!} [f_{S \cup \{i\}}(x_{S \cup \{i\}}) - f_S(x_S)]. \quad (8.17)$$

3127 I trained the `GradientBoostingClassifier` from `scikit-learn` with the default
 3128 configuration in order to evaluate both the Gini and Shapley importances. The Gini
 3129 scores are automatically computed by `scikit-learn`, using the training data. For the
 3130 Shapley importance, I used the implementation from the `SHAP` package, computing
 3131 it using the test sample. The results can be seen in Fig. 8.22 (right panel) and
 3132 Fig. 8.23 (right panel), again for the momentum ranges $0.3 \leq p < 0.8 \text{ GeV}/c$ and
 3133 $0.8 \leq p < 1.5 \text{ GeV}/c$. The length of the bars denote either the SHAP (blue) or the Gini
 3134 (red) importance of the feature. One interesting thing to notice is that, when looking at
 3135 the Gini importance, there is always one feature that dominates over the rest. This is
 3136 not the case for the SHAP importance, where importances tend to be more balanced.

3137 Across all momentum ranges, I observe that the most important features are. For
 3138 the five momentum ranges considered, only six variables sit in the top five at least once.
 3139 Figure 8.24 shows the evolution of the SHAP importance of these six features. It is
 3140 interesting to see that the time-of-flight variable keeps its importance almost unchanged
 3141 for all momenta. Also, it looks like the ECal energy ratio gets less relevant the higher the
 3142 momentum is, but the RMS of the hit-to-cluster distance distribution and the maximum
 3143 ECal hit energy become more important in the last momentum ranges.

3144 The last step in the feature selection analysis is the feature permutation. This
 3145 technique measures the contribution of each feature to the performance of a model by
 3146 randomly shuffling its values and checking how some scores degrade. For the present
 3147 case, I am interested in the precision or purity, and the sensitivity or efficiency, as these
 3148 two are the most relevant metrics from a physics point of view. The `scikit-learn`
 3149 module provides the user with a method to perform the permutation scans.

3150 The results of these are shown in Fig. 8.25. For the different momentum ranges
 3151 I show the permutation importances for the ten most important features. For each

Chapter 8. Particle ID in GArSoft

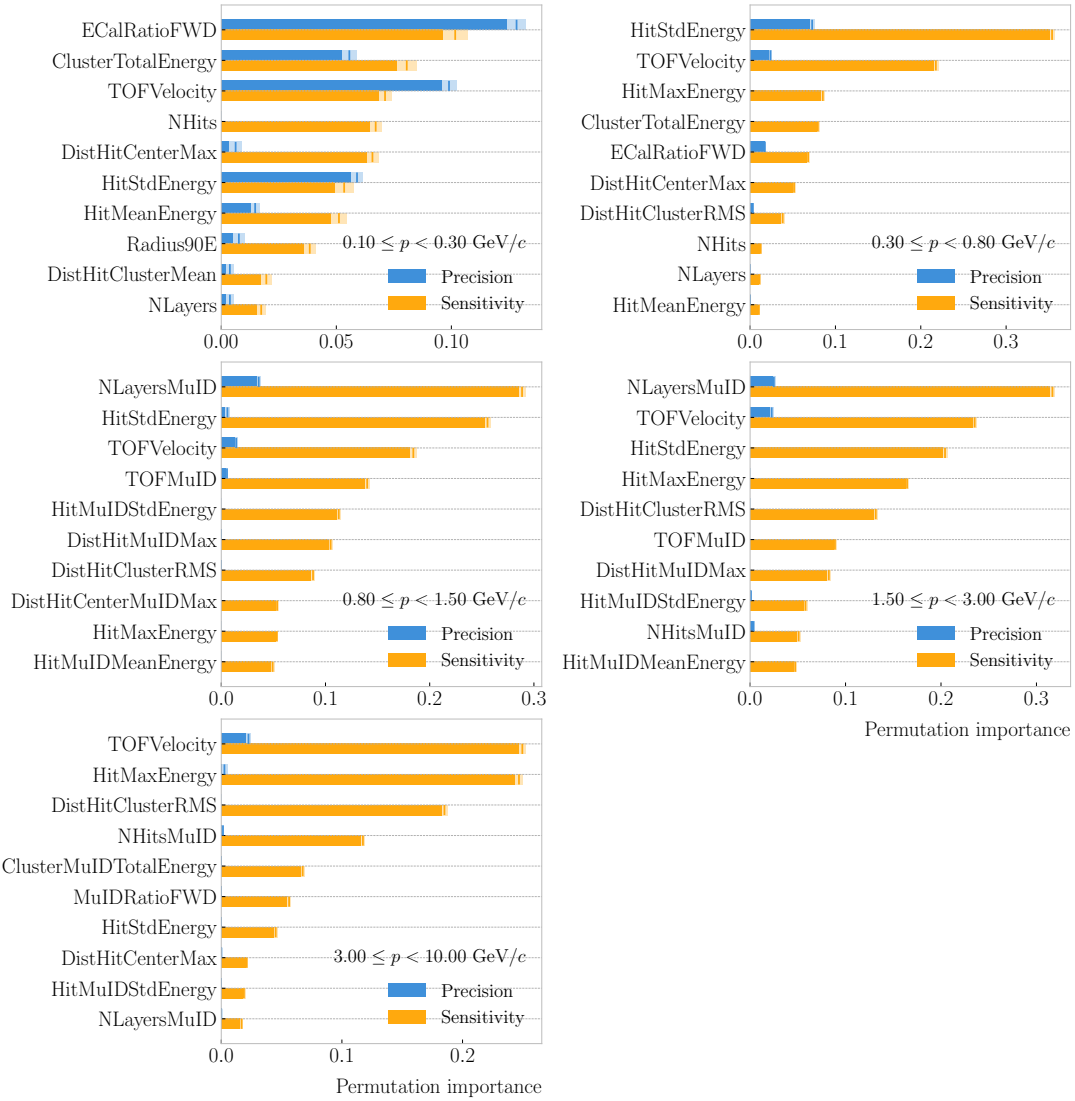


Figure 8.25: Permutation importances for the ten most important features in the different momentum ranges (from left to right, top to bottom, in increasing momentum order). The bars indicate the effect that permutations of each feature have on the purity (blue) and the sensitivity (yellow), the translucent regions representing one standard deviation around the central value.

8.2. Muon and pion separation in the ECal and MuID

3152 of the variables I report the effect the permutations have on the precision (blue) and
3153 sensitivity (yellow) of the models. The bars indicate the importance value, with the
3154 lighter part representing one standard deviation around the mean (hinted as an additional
3155 vertical line). Something to notice is that, in the first momentum region, the feature
3156 permutations have an effect on both the precision and the sensitivity. However, for the
3157 rest the precision is almost unaffected, while the sensitivity changes are considerably
3158 larger.

3159 It is also interesting to see that most of the variables identified as important here
3160 are the same I found when looking at the Shapley values. The behaviour of these across
3161 the momentum ranges is also similar, with the same patterns of some features being
3162 important at low momenta and then dropping in importance for the high momentum
3163 ranges.

3164 Wit this, I conclude the study of the features. I have prepared the training and
3165 testing datasets and understood what features are likely to have the largest impact on
3166 the performance of the classifiers.

3167 8.2.4 Hyperparameter optimisation

3168 Any BDT requires the user to specify a number of parameters that will dictate its
3169 behaviour. They can be divided into two categories: (i) tree-specific parameters, which
3170 affect each individual tree in the model, and (ii) boosting parameters, which control the
3171 boosting operation in the model. The value of these so-called hyperparameters affect the
3172 performance and predictive power of the models. Therefore, one needs to carefully select
3173 their optimal values in order to extract as much information as possible from the data.

3174 From all the parameters used to define a tree in the `scikit-learn` implementation
3175 of the BDT classifier, I only consider a subset of them. This is due to the fact that some
3176 are mutually exclusive, but also because I noticed that others have little effect on the
3177 problem at hand. Therefore, the parameters I investigate are the following:

- 3178 • `min_samples_split`: defines the minimum number of samples required in a node
3179 to be considered for splitting. Higher values prevent a model from learning relations

Chapter 8. Particle ID in GArSoft

3180 which might be highly specific to the particular sample, but may lead to under-fitting
3181 if the value is too low.

3182 • `min_samples_leaf`: defines the minimum samples required in a leaf node. For
3183 imbalanced problems it should take a low value, as there will not be many cases
3184 where the minority class dominates.

3185 • `max_depth`: maximum depth of a tree. Useful to prevent over-fitting, as higher
3186 depth will allow a model to learn relations specific to the training sample.

3187 In the case of the boosting parameters, the ones I look at are:

3188 • `learning_rate`: determines the impact of each tree on the final outcome. Low
3189 values make the model robust to the specific characteristics of a tree, and thus
3190 allow it to generalise well. However, that usually requires a large number of trees
3191 to model the data properly.

3192 • `n_estimators`: number of sequential trees to be trained. In general, BDTs are
3193 fairly robust at higher number of trees but it can still overfit at a point.

3194 • `subsample`: fraction of observations to be selected for each tree. Values slightly
3195 less than 1 make the model robust by reducing the variance.

3196 In general, hyperparameters depend on each other. Thus, it is not possible to
3197 optimise them independently. In the literature, we find two main strategies to explore
3198 the hyperparameter space. We could use a grid search, in which one discretises a
3199 portion of the space of hyperparameters and evaluates the model at each point. Another
3200 approach is the randomised search, where a certain number of random configurations of
3201 hyperparameters are explored.

3202 In this case, I used the random search to scan the hyperparameter space. Also,
3203 because it is not guaranteed that a set of hyperparameters can be efficiently applied
3204 across different datasets, I perform the optimisation for each of the momentum ranges
3205 considered. Table 8.3 shows the list of hyperparameters considered, and the range within

8.2. Muon and pion separation in the ECal and MuID

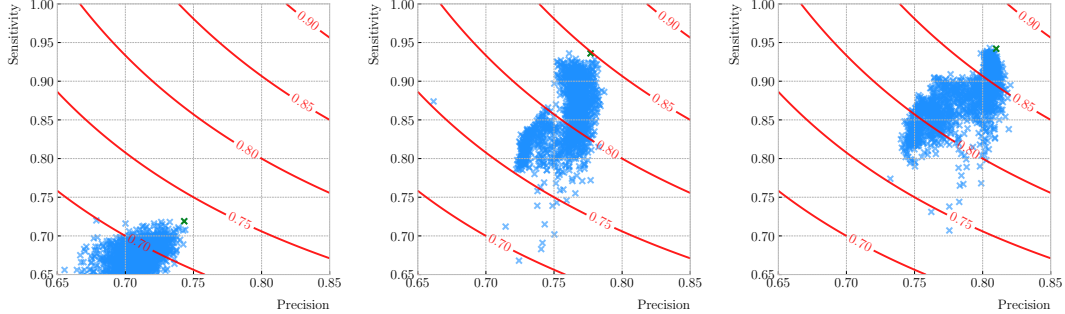


Figure 8.26: Values of the precision and sensitivity obtained for 10000 BDT hyperparameter configurations, for the momentum regions I, III and V. The red contours indicate the curves of equal F_1 -score, while the green crosses are the selected configurations.

which I let them vary. I decided to fix the number of estimators to 400 in all cases, as its value is correlated with that of the learning rate.

I evaluate 10000 different hyperparameter configurations for each momentum range. For the hyperparameter tuning, I used subsamples containing 10% of the full datasets, keeping the original proportions between classes, in order to reduce the computational load. The performance of the models was assessed using a stratified 3-fold cross-validation with replacement. Cross-validation involves dividing the data in a number of subsets, training the model using some of them, and testing it with the rest. In our case, I divide the data in 3 equal-sized subsets, maintaining the class proportions of the original dataset. Then, for 3 consecutive iterations, I train the models using 2 of the subsets while I compute the precision and sensitivity scores with the other. This approach provides a more robust estimate of the performance on unseen data.

Figure 8.26 shows the results in the precision versus sensitivity plane, for the momentum regions I, III and V (from left to right). The contours represent the curves of equal F_1 -score, i.e. the harmonic mean of the precision and the sensitivity. In order to select the optimal configurations (indicated in the plots with a green cross), I chose the point with the highest F_1 -score.

The results for the different momentum ranges are summarised in Tab. 8.3. One can see some consistency in hyperparameter choices, with models generally preferring

Chapter 8. Particle ID in GArSoft

Table 8.3: Optimal values of the hyperparameters used by the BDT, for each momentum range.

Hyperparameter	Range	Best value				
		I	II	III	IV	V
<code>min_samples_split</code>	[0.001, 1]	0.10	0.06	0.05	0.27	0.06
<code>min_samples_leaf</code>	[0.001, 1]	0.02	0.03	0.01	0.02	0.07
<code>max_depth</code>	{2, 3, ..., 8}	8	2	4	2	7
<code>learning_rate</code>	[0.05, 1]	0.10	0.23	0.07	0.13	0.09
<code>subsample</code>	[0.01, 1]	0.75	0.65	0.79	0.86	0.95

Table 8.4: Performance metrics of the BDTs with optimal hyperparameters, for the different momentum ranges.

Metric	Value $\pm 1\sigma$				
	I	II	III	IV	V
Accuracy	0.779 ± 0.003	0.812 ± 0.003	0.846 ± 0.002	0.861 ± 0.003	0.874 ± 0.002
Precision	0.769 ± 0.003	0.752 ± 0.005	0.788 ± 0.002	0.805 ± 0.003	0.815 ± 0.003
Sensitivity	0.745 ± 0.009	0.921 ± 0.006	0.965 ± 0.002	0.967 ± 0.002	0.976 ± 0.001
F_1 -score	0.757 ± 0.004	0.828 ± 0.003	0.867 ± 0.002	0.879 ± 0.002	0.889 ± 0.002
ROC AUC	0.868 ± 0.003	0.865 ± 0.003	0.899 ± 0.002	0.902 ± 0.002	0.911 ± 0.001

3225 small values for the tree-specific parameters, small learning rate, and relatively large
 3226 subsample sizes.

3227 Now that I have obtained the optimal values of the hyperparameters, I can train
 3228 the different BDTs. In this case I use the complete datasets, keeping 20% of the data
 3229 for testing. Table 8.4 shows the values of the different performance metrics obtained
 3230 using the selected hyperparameters and 5-fold cross-validation. The last row indicates
 3231 the value of the area under the receiver operating characteristic (ROC) curve. This
 3232 represents the sensitivity of a model as a function of the false positive rate. I have
 3233 included it here as it is a classic model metric used in the machine learning community.
 3234 Overall, there is a clear trend of models performing better at higher momentum.

8.2. Muon and pion separation in the ECal and MuID

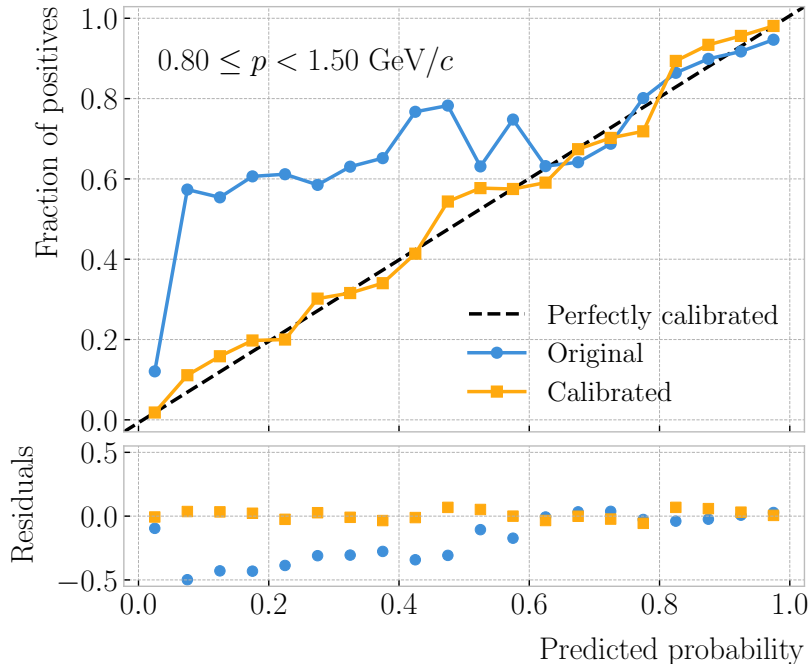


Figure 8.27: Reliability diagrams for the BDT classifier used in the momentum range $0.3 \leq p < 0.8$ GeV/ c , both for the original (blue circles) and calibrated (yellow squares) responses. For reference, the response of a perfectly calibrated classifier is also shown (black dashed line).

8.2.5 Probability calibration

So far, the trained BDTs are able to provide predictions of the class labels. Ideally, one would like the output of a classifier to give a confidence level about the prediction. However, it is not straightforward to interpret the outputs of our BDTs in terms of probabilities.

A way to visualise how well the predictions of a classifier are calibrated is using reliability diagrams [110]. They represent the probability of the positive label versus the probability predicted by the classifier. These can be obtained by binning the predicted probabilities, and then compute the conditional probability $P(y_{true} = 1 | y_i \leq y_{pred} < y_{i+1})$ by checking the fraction of true positive instances in each bin. The reliability diagram of a perfectly calibrated classifier would be a diagonal line.

In this case, I try to correct the raw response of the classifiers by applying a sigmoid

Chapter 8. Particle ID in GArSoft

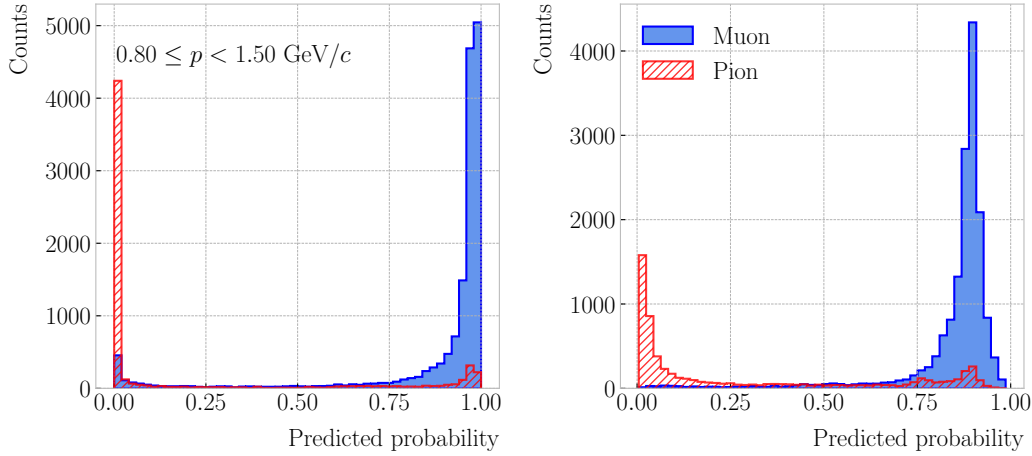


Figure 8.28: Uncalibrated (left panel) and calibrated (right panel) predicted probabilities assigned by the BDT classifiers for true muons (blue) and charged pions (red) in the momentum range $0.3 \leq p < 0.8 \text{ GeV}/c$.

3247 function:

$$\sigma(x; A, B) = \frac{1}{1 + e^{Ax+B}}, \quad (8.18)$$

3248 where the parameters A and B are real numbers determined using the method of least
3249 squares.

3250 For each classifier, I perform a grid search to obtain the optimal values of A and B .

3251 For any pair, I compute the predicted probabilities as $y_{pred} = \sigma(y_{raw}; A, B)$, where y_{raw}
3252 are the raw predictions of the classifier⁹. Then, I calculate the corresponding reliability
3253 curve, and take the sum of the squared residuals between it and the response of the
3254 perfectly calibrated classifier.

3255 Figure 8.27 shows the reliability diagrams for the original (blue) and calibrated
3256 (yellow) probability predictions of the classifier for the III momentum range, $0.3 \leq p <$
3257 $0.8 \text{ GeV}/c$. The original response of the classifier is given by $y_{pred} = \sigma(y_{raw}; -2, 0)$,
3258 which is the transformation applied by `scikit-learn` to produce the probability estimate.
3259 Notice how the calibrated prediction matches the ideal response much better than the
3260 original, across all the probability range.

3261 One can also compare the responses of the uncalibrated and calibrated classifiers

⁹In `scikit-learn` these correspond to the outputs of the `decision_function` method.

8.3. ECal time-of-flight

3262 broken down by true particle type, as shown in Fig. 8.28. It can be seen that the
3263 distributions for both muons (blue) and charged pions (red) smoothen after calibration,
3264 but still the separating power of the classifier remains unchanged.

3265 At this point, having the trained classifiers and the probability calibration parameters,
3266 I am able to assess the performance of the classification strategy in a physics-relevant
3267 case.

3268 8.2.6 Performance

3269 8.3 ECal time-of-flight

3270 Looking at Fig. 8.19, it is clear that for momentum values in the range $1.0 - 3.0 \text{ GeV}/c$
3271 it is not possible to separate pions and protons using a $\langle dE/dx \rangle$ measurement in the
3272 HPgTPC. However, in the previous section I assumed that protons at those energies
3273 could be identified by other means, and therefore were not an issue for the muon and
3274 pion discrimination.

3275 Some detectors, like ALICE [111] or the ILD concept [112], complement the PID
3276 capabilities of their gaseous trackers with time-of-flight measurements. The use of
3277 fast timing silicon sensors, with hit time resolutions under 100 ps, would allow for the
3278 identification of charged hadrons via a ToF measurement up to $5.0 \text{ GeV}/c$. In the case
3279 of ND-GAr, one could think of using the inner layers of the ECal, the ones consisting of
3280 high-granularity tiles, to obtain a ToF-based PID, with some inputs from the TPC.

3281 Measuring the momentum and the velocity of a charged particle allows for a
3282 determination of the mass through the relativistic momentum formula:

$$m = \frac{p}{\beta} \sqrt{1 - \beta^2}. \quad (8.19)$$

3283 In our case, the momentum is measured in the TPC, using the curvature and the dip
3284 angle of the helix inside the magnetic field. The velocity of the particle can be written

Chapter 8. Particle ID in GArSoft

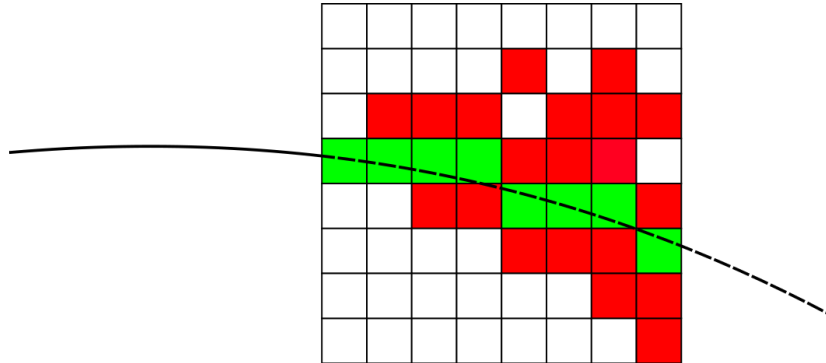


Figure 8.29: Schematic of the hit selection used for the ToF measurement. The grid represents the layers of the inner ECal, with coloured squares indicating the tiles with hits. Green squares indicate the selected hits.

3285 as:

$$\beta = \frac{\ell_{track}}{c\tau}, \quad (8.20)$$

3286 where ℓ_{track} is the length of the track, and τ the arrival time to the ECal.

3287 In GArSoft, the track length is computed at the Kalman filter stage. It is simply the
 3288 sum of the line segments along the track, either in the forward or backward fit. In this
 3289 case, because we are only interested in the particles that make it to the ECal, I choose
 3290 the fit direction based on the results of the track-cluster associations.

3291 Additionally, because the last 30 cm of the TPC radius are uninstrumented¹⁰, I need
 3292 to correct for the length of the tracks. Using the track fit parameters to propagate the
 3293 helix to its entry point in the ECal, one can write the total track length as:

$$\ell_{track} = \ell + \left| \frac{\phi_{EP} - \phi}{R^{-1}} \right| \sqrt{1 + \tan^2 \lambda}, \quad (8.21)$$

3294 where ϕ_{EP} is the angle of rotation at the entry point to the calorimeter, and ℓ , ϕ , R and
 3295 λ are the track length, angle of rotation, radius of curvature and dip angle at the last
 3296 point in the fit, respectively.

3297 To test the idea of performing a ToF measurement with the inner ECal, I generated
 3298 two data samples. Each consists of 10000 single particle events, either charged pions or

¹⁰Note to self: check this number.

8.3. ECal time-of-flight

3299 protons. Their momenta are uniformly distributed in the range $0.5 - 5.0 \text{ GeV}/c$, and
3300 their directions are isotropic. I process each sample using different values of the time
3301 resolution, from $\Delta\tau = 0$, the perfect time resolution case for comparison, to the current
3302 nominal value of $\Delta\tau = 0.7 \text{ ns}$, and the worse scenario of $\Delta\tau = 1.0 \text{ ns}$.

3303 8.3.1 Arrival time estimations

3304 In the simulation, the limited time resolution of the ECal is taken into account by
3305 applying a Gaussian smearing to the true hit times. Other effects, like the digitisation
3306 of the signals, are not taken into account and fall beyond the scope of this study. After
3307 the track-cluster, one ends up with a collection of ECal hits associated to each particle.
3308 From these, the arrival time of the particle to the ECal can be extracted.

3309 The simplest possibilities are to either take the time of the earliest hit or the hit
3310 closest to the entry point. Because these two coincide, in general, I focused only in
3311 the earliest hit time. However, this needs to be corrected, to account for the distance
3312 travelled from the entry point to the position of the hit:

$$\tau_{earliest} = \tau_{hit} - \frac{d_{EP-hit}}{c}, \quad (8.22)$$

3313 where τ_{hit} is the time of the earliest hit, and d_{EP-hit} is the distance between that hit
3314 and the entry point of the particle to the ECal. This is computed as the arc length
3315 between the entry point and the point of the extrapolated helix up to the layer of the
3316 hit. This way of correcting the time assumes c for the propagation of the particle, which
3317 may lead to biased estimates.

3318 I also tried to estimate the arrival times using information from the rest of the hits.
3319 In order to do this, as a simplifying assumption, I approximate the hadronic shower
3320 considering only its MIP component. For each layer, I keep only the hit in the tile closest
3321 to the point of the extrapolated track up to that layer. Figure 8.29 shows an example of
3322 how this hit selection works. The dashed line represents the extrapolated track, while
3323 the coloured squares are the tiles containing hits. Green indicates the tiles closer to the

Chapter 8. Particle ID in GArSoft

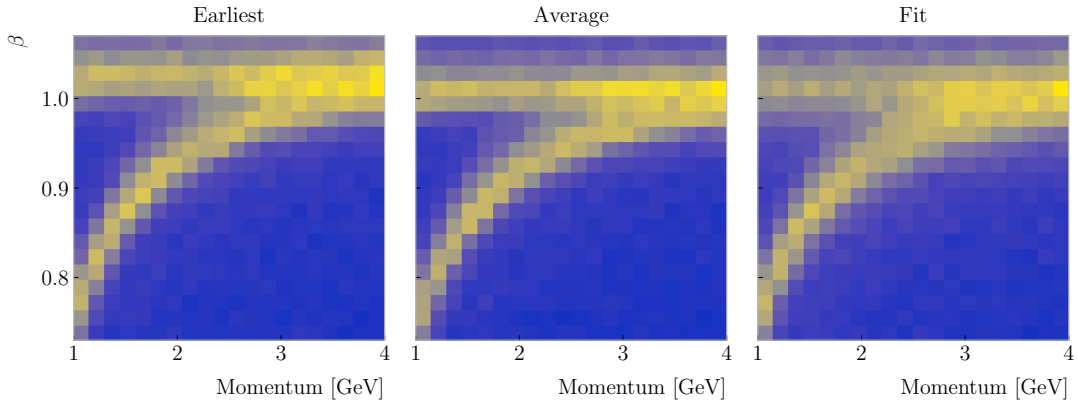


Figure 8.30: Particle velocity versus momentum measured with different ECal arrival time estimations. From left to right: earliest hit time, average hit time, and fitted hit time. In all cases the time resolution is $\Delta\tau = 0.1$ ns.

3324 track in each layer (in the sketch they correspond to the grid columns).

3325 Now, I can use these collections of hits to estimate the arrival times. A possibility
 3326 is to take the average of the times of the selected hits, denoted $\tau_{average}$. For that to
 3327 work, one needs to correct these times, in a similar way as in Eq. (8.22), before taking
 3328 the average. However, as before, this correction assumes that the particle travels at the
 3329 speed of light inside the ECal. Another option is to perform a linear fit to the hit times
 3330 and the distances to the entry point. In that case, the arrival time would be the fitted
 3331 value of the intercept, τ_{fit} . This method would not assume a speed of light propagation.

3332 Figure 8.30 shows the velocity estimations as a function of the particle momentum,
 3333 for the earliest hit time (left panel), average hit time (middle panel), and fitted hit time
 3334 (right panel). The two bands correspond to the π^\pm and the p particles. $\Delta\tau = 0.1$ ns.
 3335 Notice how, for the earliest hit time method, the velocities are significantly biased
 3336 towards larger values. For the multi-hit methods, the τ_{fit} estimate appears to produce a
 3337 larger variance than when using the $\tau_{average}$ method.

3338 8.3.2 Proton and pion separation

3339 Once we have the velocities of the particles, one can estimate their masses through
 3340 Eq. (8.19). The resulting mass spectra are shown in Fig. 8.31. I computed the masses

8.3. ECal time-of-flight

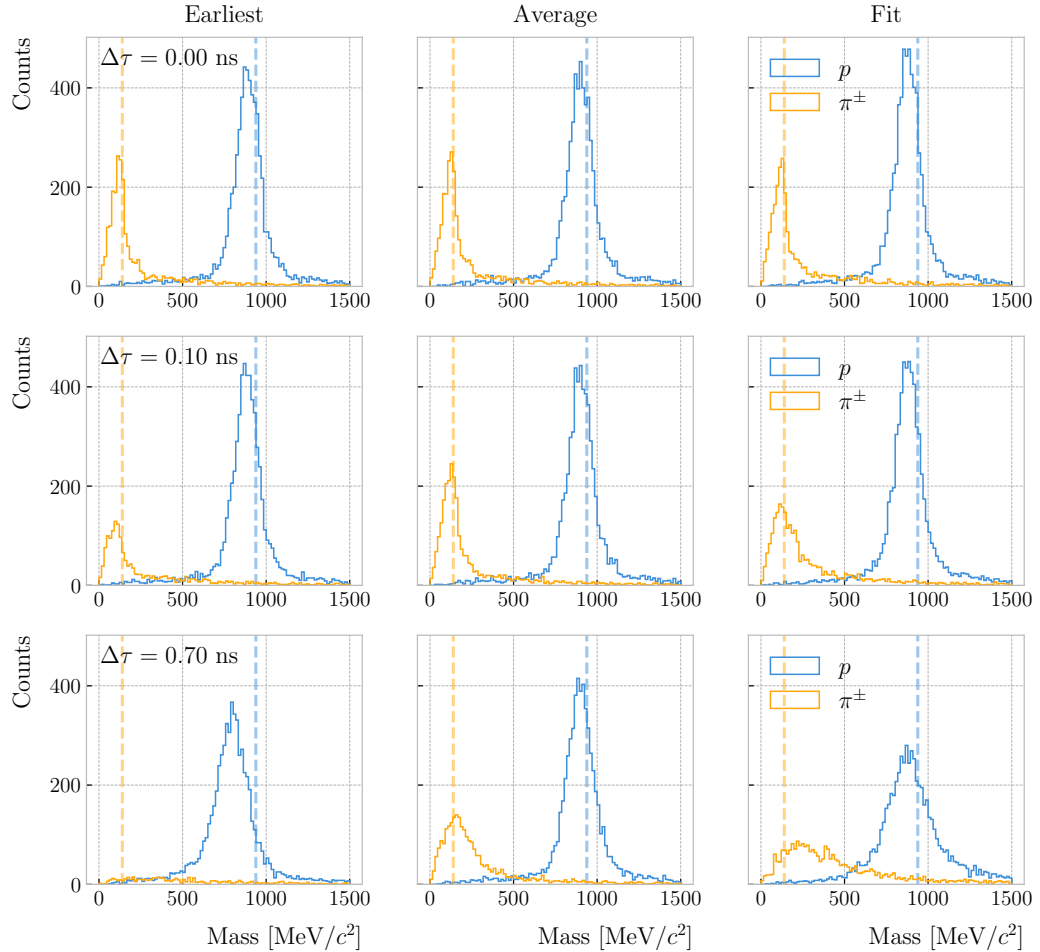


Figure 8.31: Mass spectra for p (blue) and π^\pm (yellow) particles, using different ECal time resolution values (from top to bottom, in ascending order), and arrival time estimates. From left to right: earliest hit time, average hit time, and fitted hit time. The dashed lines indicate the true masses of the particles.

for the three arrival time estimates discussed above, and three different values of the time resolution: $\Delta\tau = 0.00$ (perfect time resolution), $\Delta\tau = 0.10$ ns, and $\Delta\tau = 0.70$ ns. Although in all cases we have the same number of events, it appears as if the entries in the histograms decrease as the time resolution increases. Sometimes, the particles get unphysical values of $\beta > 1$, and in turn they do not contribute to the mass spectra. This is more likely to happen for higher values of $\Delta\tau$.

As noted before, the average hit time method produces the most robust estimates when increasing $\Delta\tau$. Intuitively this makes sense, as by taking the mean one averages

Chapter 8. Particle ID in GArSoft

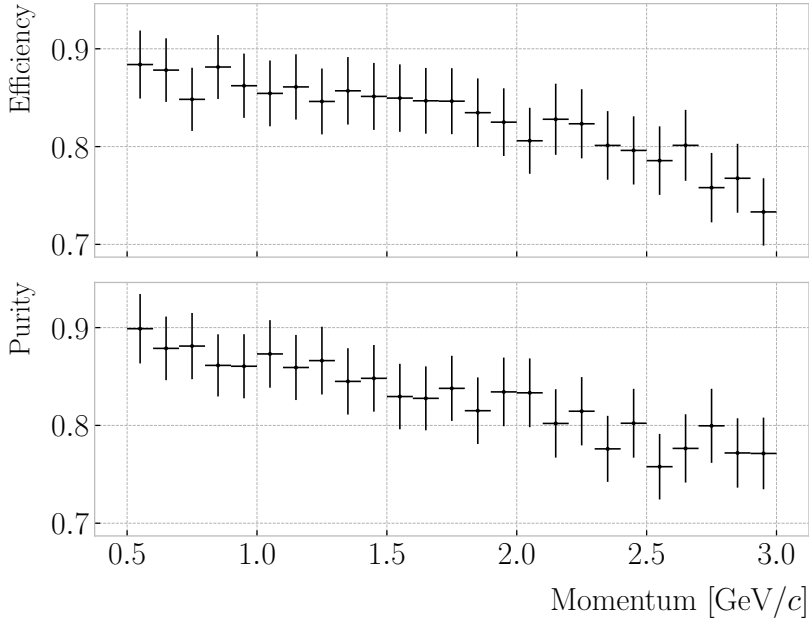


Figure 8.32: Efficiency (top panel) and purity (bottom panel) for the proton selection as a function of the momentum, for $\Delta\tau = 0.10$ ns.

3349 out the effect of the Gaussian smearing. Going forward, I will use this arrival time
 3350 estimator, as it appears to be the best performing one.

3351 It is possible to use the velocity estimations to select a sample of protons. In this
 3352 case, I do so by dividing the relevant momentum range in bins of 0.1 GeV/c . For each
 3353 momentum bin, I compute the expected velocity for the protons via the inverse of Eq.
 3354 (8.19), and then take the fractional residuals of the measured velocities. Using that
 3355 distribution, I choose the cut that maximises the F_1 -score of the proton selection.

3356 The results can be seen in Fig. 8.32, for the case $\Delta\tau = 0.10$ ns. As expected from
 3357 Fig. 8.30, the performance of the selection degrades rapidly with increasing momentum.
 3358 However, the purity is still around 75% at 3.0 GeV/c . This is likely to be sufficient, as
 3359 we do not expect protons or charged pions with higher energies from the beam neutrino
 3360 interactions.

3361 Figure 8.33

8.4. Charged pion decay in flight

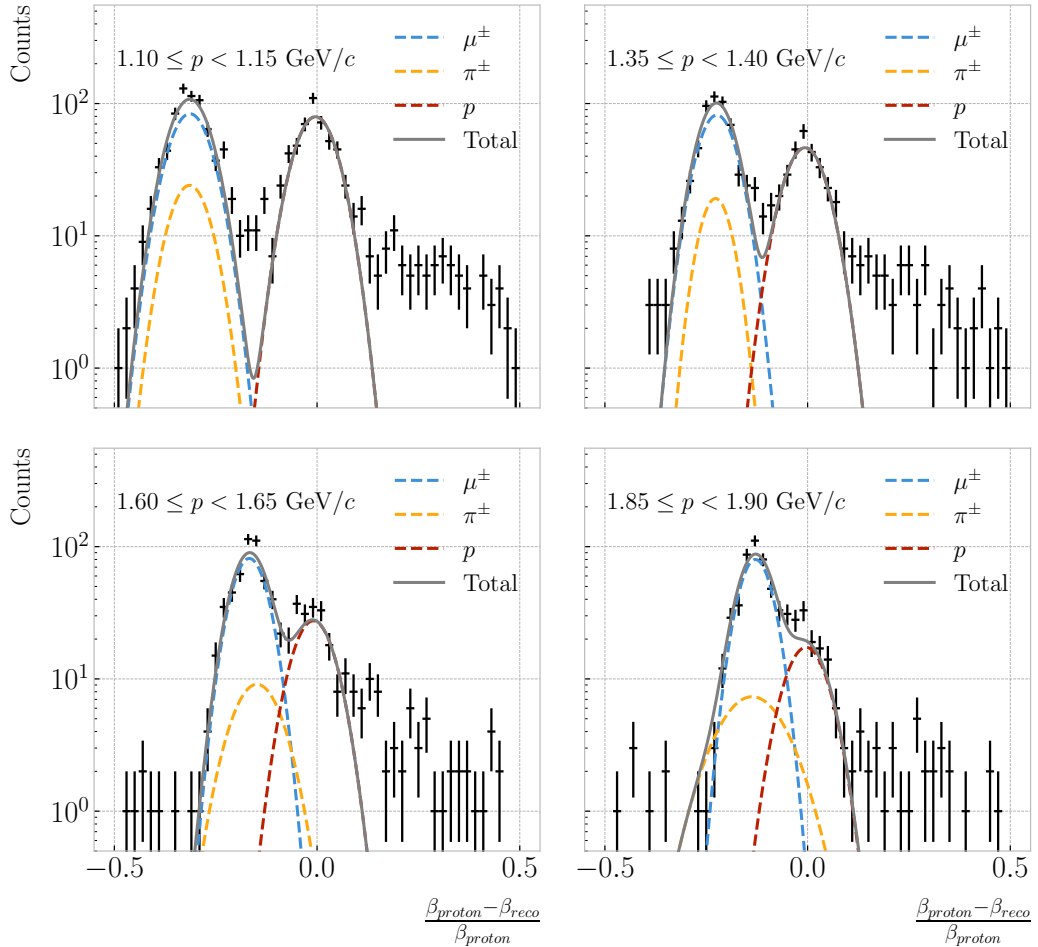


Figure 8.33: Distributions of the velocities measured by ToF with the inner ECal, for different momentum bins, in a FHC neutrino interaction sample. The Gaussian fits are performed around the maxima for each particle species.

3362 8.4 Charged pion decay in flight

3363 As discussed previously, in GArSoft the TPC tracks are formed after a pattern recognition
3364 algorithm and a Kalman filter are applied to the TPC clusters. These two steps can
3365 find discontinuities in the track candidates (e.g. due to a particle decay) when these
3366 so-called breakpoints are large enough. However, for some, more subtle, cases they may
3367 miss them and form a single reconstructed track. It has been noted in the literature
3368 that Kalman filters offer, as a by-product, additional information to form test statistics
3369 to identify these breakpoints [113, 114].

3370 Considering the mean life of the charged pion, $\tau = (2.6033 \pm 0.0005) \times 10^{-8} \text{ s}$, one

Chapter 8. Particle ID in GArSoft

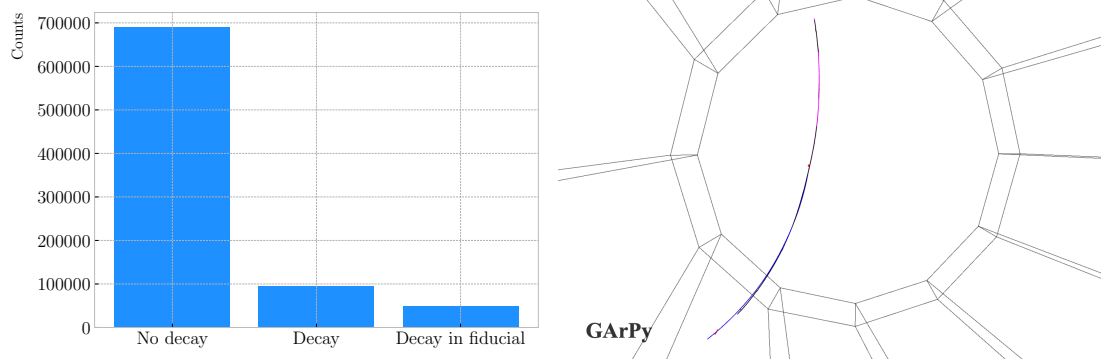


Figure 8.34: Left panel: number of non-decaying, decaying and decaying in the fiducial volume pions for a MC sample of 100000, $p = 500 \text{ MeV}/c$ isotropic positively charged pions inside the TPC. Right panel: event display for a positive pion decaying inside the fiducial volume, with a single reconstructed track for the pion and muon system.

3371 can estimate that about 12% of the pions with momentum $p \sim \mathcal{O}(500 \text{ MeV}/c)$ (roughly
 3372 the peak of the pion momentum distribution in ν_μ CC interactions off argon) decay
 3373 inside the TPC. Figure 8.34 (left panel) shows the amount of charged pions decaying in
 3374 the full TPC and fiducial volumes from an isotropic, monoenergetic sample of 100000
 3375 negatively charged pions with $p = 500 \text{ MeV}/c$. We see that about 10% of those decayed,
 3376 with more than half of them decaying inside the TPC fiducial volume.

3377 Figure 8.34 (right panel) shows an example event display of a charged pion (magenta
 3378 line) decays in flight inside the TPC, but because the angle of the muon (blue line) is
 3379 small both were reconstructed as one single track (black line). In this case, the composite
 3380 track reaches the ECal, where it undergoes a muon-like interaction, thus being classified
 3381 as a muon.

3382 A way to understand what decaying pion tracks were totally or partially reconstructed
 3383 together with the daughter muon is looking at the relative energy contributions to the
 3384 reconstructed track. In order to select a sample of such events, I require that a minimum
 3385 50% of the total energy comes from the pion and at least 20% from the muon.

3386 8.4.1 Track breakpoints

3387 To identify potential decays we can use the information we obtain from the Kalman
 3388 filter at each step of the fitted track. The simplest test we can think about is computing

8.4. Charged pion decay in flight

3389 the χ^2 of the mismatch between all the parameters in the forward and the backward fits:

$$\chi_k^{2 (FB)} = (\hat{x}_k^B - \hat{x}_k^F)^T [V^{(\hat{x}_k, B)} + V^{(\hat{x}_k, F)}]^{-1} (\hat{x}_k^B - \hat{x}_k^F), \quad (8.23)$$

3390 where \hat{x}_k^F , \hat{x}_k^B are the Kalman filter state vector estimates at step k in the forward and
3391 backward fits and $V^{(\hat{x}_k, F)}$, $V^{(\hat{x}_k, B)}$ the covariance matrices of \hat{x}_k^F and \hat{x}_k^B respectively.
3392 Using the values of the χ^2 at measurement k for the forward and backward fits we can
3393 compute another χ^2 value that characterises the overall track fit:

$$\chi_{track}^2 = \chi_k^{2 (F)} + \chi_k^{2 (B)} + \chi_k^{2 (FB)}, \quad (8.24)$$

3394 which remains approximately constant for all k .

3395 An alternative approach proposed in the context of the NOMAD experiment was
3396 using a fit with a more elaborate breakpoint hypothesis, so we can perform a comparison
3397 of the χ^2 with and without breakpoints. This can be achieved by using some alternative
3398 parametrisation with extra parameters, which allows some of the track parameters to
3399 be discontinuous at certain points. A decay changes the momentum magnitude and
3400 direction, so we can use the new state vector:

$$\alpha = (y, z, 1/R_F, 1/R_B, \phi_F, \phi_B, \tan\lambda_F, \tan\lambda_B)^T. \quad (8.25)$$

3401 As we already have the estimates from the standard Kalman filter and their
3402 covariance matrices at each point, we do not need to repeat the Kalman fit for the new
3403 parametrisation. Instead, I can compute the values of α at each point k that minimise
3404 the χ^2 resulting from comparing them to $\{\hat{x}_k^B, \hat{x}_k^F\}$. Introducing the two 5×8 matrices:

$$H^F = \begin{pmatrix} 1 & 0 & 0 & 0 & 0 & 0 & 0 & 0 \\ 0 & 1 & 0 & 0 & 0 & 0 & 0 & 0 \\ 0 & 0 & 1 & 0 & 0 & 0 & 0 & 0 \\ 0 & 0 & 0 & 0 & 1 & 0 & 0 & 0 \\ 0 & 0 & 0 & 0 & 0 & 0 & 1 & 0 \end{pmatrix}, H^B = \begin{pmatrix} 1 & 0 & 0 & 0 & 0 & 0 & 0 & 0 \\ 0 & 1 & 0 & 0 & 0 & 0 & 0 & 0 \\ 0 & 0 & 0 & 1 & 0 & 0 & 0 & 0 \\ 0 & 0 & 0 & 0 & 0 & 1 & 0 & 0 \\ 0 & 0 & 0 & 0 & 0 & 0 & 0 & 1 \end{pmatrix}, \quad (8.26)$$

Chapter 8. Particle ID in GArSoft

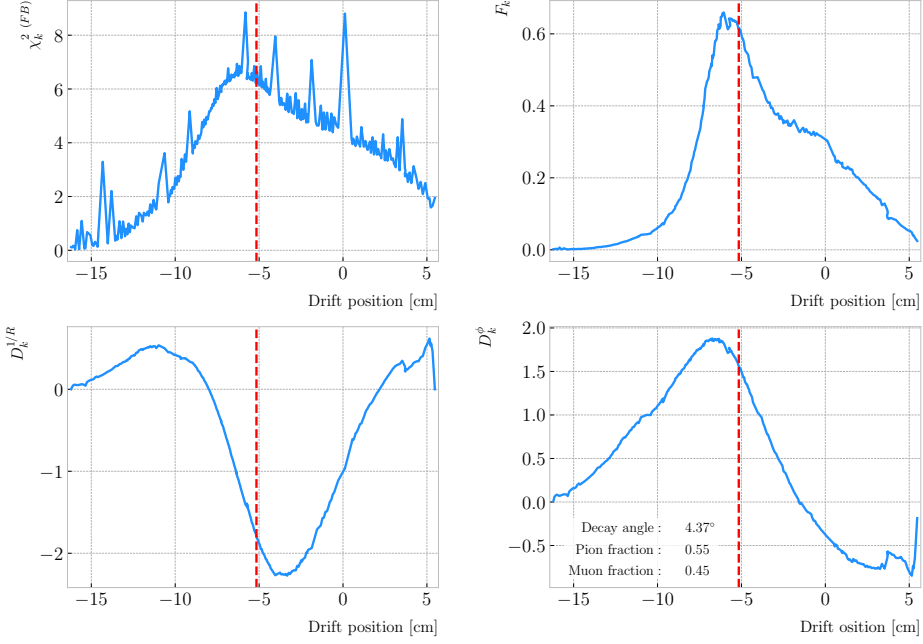


Figure 8.35: Values of $\chi_k^{2(FB)}$ (top left panel), F_k (top right panel), $D_k^{1/R}$ (bottom left panel) and D_k^ϕ (bottom right panel) versus position along the drift direction for a reconstructed track in a positive pion decay event. The vertical red dashed line indicates the true location of the decay point.

3405 we can write this as:

$$\begin{aligned}\chi_k^{2(FB)}(\alpha) &= (\hat{x}_k^F - H^F \alpha)^T \left[V^{(\hat{x}_k, F)} \right]^{-1} (\hat{x}_k^F - H^F \alpha) \\ &\quad + (\hat{x}_k^B - H^B \alpha)^T \left[V^{(\hat{x}_k, B)} \right]^{-1} (\hat{x}_k^B - H^B \alpha).\end{aligned}\tag{8.27}$$

3406 The minimum of $\chi_k^{2(FB)}(\alpha)$ is found when the measured new state vector takes the

3407 value:

$$\hat{\alpha}_k = V^{(\hat{\alpha}_k)} H^T (V^{(\hat{x}_k)})^{-1} \hat{X},\tag{8.28}$$

3408 where $\hat{X} = \{\hat{x}_k^B, \hat{x}_k^F\}$, $V^{(\hat{x}_k)}$ is the block diagonal matrix formed by $V^{(\hat{x}_k, F)}$ and $V^{(\hat{x}_k, B)}$

3409 and $V^{(\hat{\alpha}_k)}$ is the covariance matrix of $\hat{\alpha}_k$, given by:

$$V^{(\hat{\alpha}_k)} = \left(H^T (V^{(\hat{x}_k)})^{-1} H \right)^{-1}.\tag{8.29}$$

3410 From these new fit estimates we can compute the F statistic, which tells us whether

8.4. Charged pion decay in flight

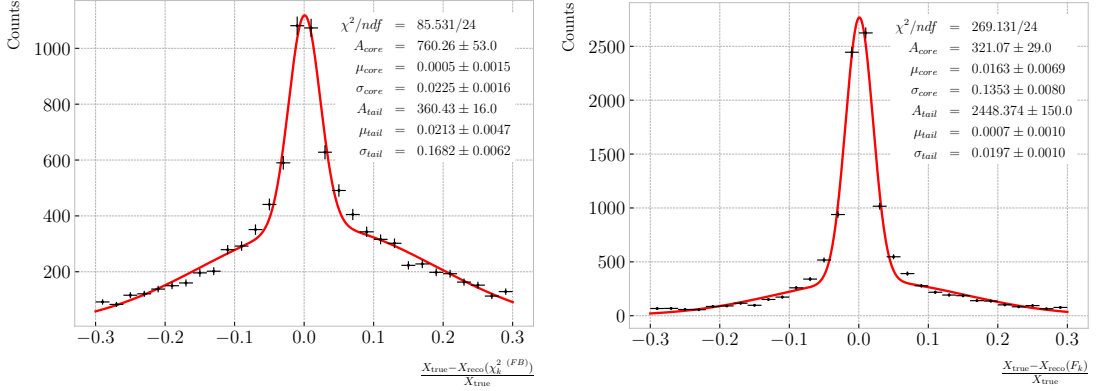


Figure 8.36: Fractional residual distributions of the true and reconstructed decay position along the drift coordinate, using the position of the maximum of $\chi_k^2 \text{ (FB)}$ (left panel) and F_k (right panel) as estimates of the decay position. Also shown are double Gaussian fits to these points (red lines).

3411 the model with breakpoint provides a statistically significant better fit:

$$F_k = \left(\frac{\chi_{\text{track},k}^2 - \chi_{\text{full},k}^2}{8 - 5} \right) / \left(\frac{\chi_{\text{full},k}^2}{N - 8} \right). \quad (8.30)$$

3412 One can also compute the signed difference of the duplicated variables divided by

3413 their standard deviation at each point. These represent how significant the discontinuity

3414 in each variable is. For any variable η we can write it as:

$$D_k^\eta = \frac{\hat{\eta}_k^B - \hat{\eta}_k^F}{\sqrt{\text{Var}[\hat{\eta}_k^F] + \text{Var}[\hat{\eta}_k^B] - 2\text{Cov}[\hat{\eta}_k^F, \hat{\eta}_k^B]}}. \quad (8.31)$$

3415 In our case, the relevant ones to look at are $D_k^{1/R}$ and D_k^ϕ .

3416 Figure 8.35 shows the values of $\chi_k^2 \text{ (FB)}$, F_k , $D_k^{1/R}$ and D_k^ϕ as functions of the position

3417 along the drift direction, for an example reconstructed track with 55.5% of the energy

3418 coming from the charged pion and 45.5% from the daughter muon. The true position of

3419 the decay is indicated (dashed red lines). Notice how $\chi_k^2 \text{ (FB)}$ and F_k , $D_k^{1/R}$ reach their

3420 maxima near the decay point. In the former case this indicates a large forward-backward

3421 difference in the track fit. In the later it represents that the extended state vector

3422 improves the fit particularly around that point.

Chapter 8. Particle ID in GArSoft

3423 I can estimate the decay position finding resolution by computing the difference
 3424 between the X position of the maxima of $\chi_k^2(FB)$ and F_k and the X position of the
 3425 true decay. Figure 8.36 represent the the fractional residual distributions for both
 3426 cases, from the sample of tracks containing pion decays. Fitting a double Gaussian to
 3427 the distributions (red lines) I find a resolution of $(3.31 \pm 0.15)\%$ and $(6.94 \pm 0.31)\%$
 3428 respectively.

3429 In principle, the F -statistic should follow a Fisher distribution with $(8 - 5)$ and
 3430 $(N - 8)$ degrees of freedom under the null hypothesis. In most of our cases $N \sim \mathcal{O}(100)$,
 3431 so the probability density functions will look very similar. In this case, it is safe to take
 3432 the limit $N \rightarrow \infty$ in the Fisher PDF:

$$\begin{aligned}\tilde{f}(x; a - b) &= \lim_{N \rightarrow \infty} f(x; a - b, N - a) \\ &= \frac{2^{-\frac{a-b}{2}}}{\Gamma(\frac{a-b}{2})} (a - b)^{\frac{a-b}{2}} x^{\frac{a-b}{2}-1} e^{-\frac{a-b}{2}x}.\end{aligned}\tag{8.32}$$

3433 In our case $a - b = 8 - 5 = 3$, so we would obtain a p-value of 0.05 at $x = 2.60$.

3434 Figure 8.37 contains the distributions of the maxima of $\chi_k^2(FB)$, F_k and D_k^ϕ and the
 3435 minima of $D_k^{1/R}$ for a sample of non-decaying pion tracks (blue) and another sample of
 3436 reconstructed tracks containing part of the pion and the daughter muon from a decay
 3437 inside the fiducial volume (red). Notice that, even though the values of $F_k^{(max)}$ for the
 3438 decay sample are typically larger than for the non-decaying one, just a small fraction of
 3439 the events go beyond the aforementioned value of $F = 2.60$. Therefore, from a practical
 3440 point of view, it is not the most efficient variable to use for selecting the decay events.

3441 However, looking at the $D_k^{1/R \text{ (min)}}$ distribution we can see there is a big difference
 3442 between non-decaying and decaying events in this variable. One can use a combination
 3443 of these four variables to distinguish between the pion decay events (signal) and the
 3444 non-decaying pions (background).

3445 An approach to this classification could be using a boosted decision tree (BDT). One
 3446 of the advantages of BDTs is that they are easy to interpret and identify the relative
 3447 importance of the different input variables. Training a BDT with 400 estimators and a

8.4. Charged pion decay in flight

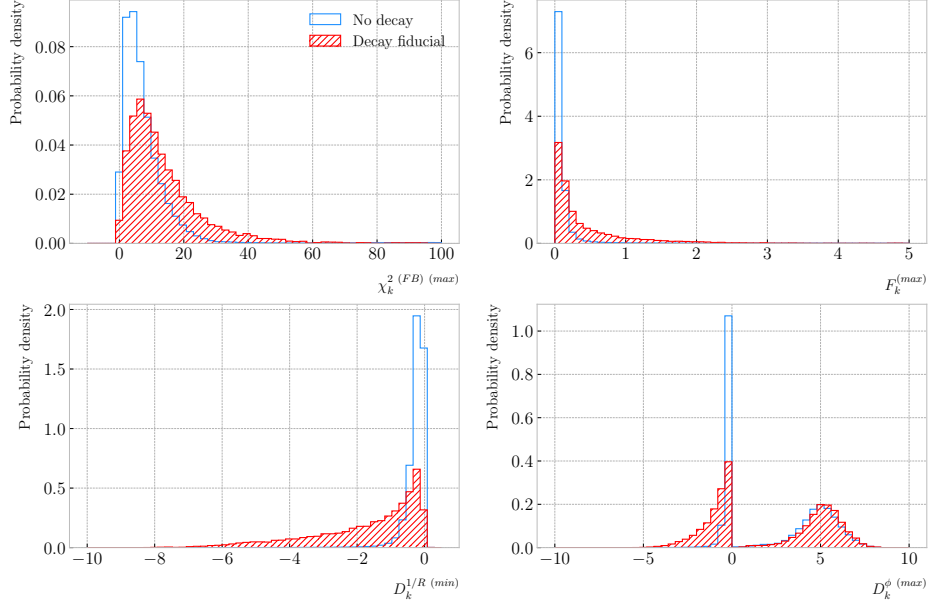


Figure 8.37: Distributions of the extreme values of $\chi_k^2(FB)$ (top left panel), F_k (top right panel), $D_k^{1/R}$ (bottom left panel) and D_k^ϕ (bottom right panel) for non-decaying reconstructed pion tracks (blue) and tracks which include the decay inside the fiducial volume (red).

maximum depth of 4 I can obtain an efficient classification without overtraining. Figure 8.38 (left panel) shows the distribution of probabilities predicted by the BDT for a test sample. The signal efficiency as a function of background acceptance, the so-called ROC curve, is shown in Fig. 8.38 (right panel). With a relative importance of 0.83, the most important variable turned out to be $D_k^{1/R}$ (min).

One thing we can check is how the resolution to the decay and the signal efficiency in the classification changes with the true decay angle. Using an equal-frequency binning for the decay angles, we can repeat the previous steps for each bin.

Figure 8.39 (left panel) shows the dependence on the decay angle of the decay finding resolution. We can see that for the $\chi_k^2(FB)$ maximum location method the resolution consistently lies between 12 to 16%. However, the $F_k^{(max)}$ approach gives a significantly better resolution for high angle values, reaching the 4 – 6% range for decay angles $\geq 4^\circ$.

For the classification dependence on the angle, I use the same classifier I trained before but evaluating the test sample for each individual angular bin. I compute the

Chapter 8. Particle ID in GArSoft

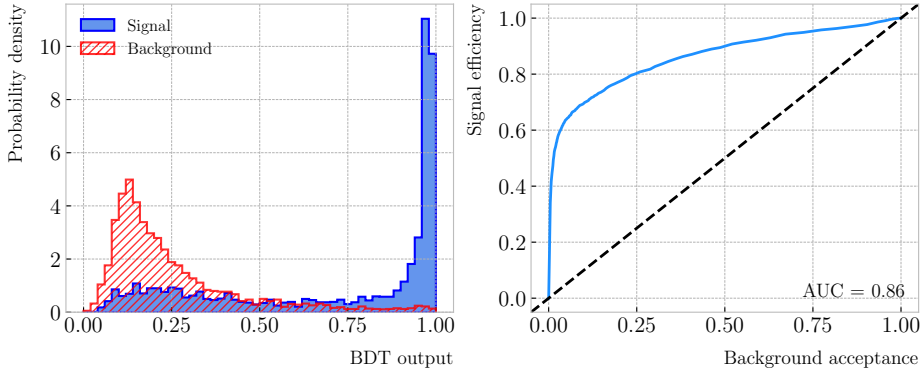


Figure 8.38: Left panel: distributions of the predicted probabilities assigned by the BDT classifier to a test sample of decaying pion+muon tracks (blue) and non-decaying pion tracks (red). Left: signal efficiency versus background acceptance (ROC curve) obtained from the BDT for the test sample.

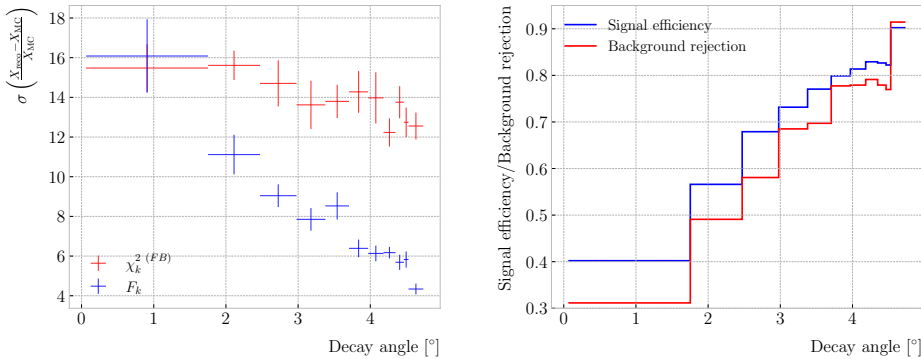


Figure 8.39: Left panel: dependence of the decay position finding resolution on the true value of the decay angle for the $\chi_k^2(FB)$ (red) and F_k (blue) methods. Right panel: signal efficiency (blue line) and background rejection (red line) from the BDT classifier versus true decay angle.

3462 signal efficiency in each bin for a fixed value of the background rejection, in this case
 3463 90%. Similarly, for the background rejection estimation I use a fixed signal efficiency
 3464 value of 90%. Figure 8.39 (right panel) represents the change in signal efficiency (blue)
 3465 and background rejection (red) with the value of the true decay angles.

8.5. Neutral particle identification

3466 8.5 Neutral particle identification

3467 8.5.1 ECal clustering

3468 Another important reconstruction item is the clustering algorithm of ECal hits in
3469 GArSoft. The default module features a NN algorithm that treats all hits in the same
3470 way, independently of the layer each hit comes from. However, the current ECal design
3471 of ND-GAr has two very different types of scintillator layers. The inner layers are made
3472 out of tiles, which provide excellent angular and timing resolutions. On the other hand,
3473 the outer layers are cross scintillator strips. That way, an algorithm that treats hits
3474 from both kinds of layers differently may be able to improve the current performance.

3475 Inspired by the reconstruction of T2K's ND280 downstream ECal [115], the idea
3476 was to put together a clustering module that first builds clusters for the different ECal
3477 views (tiles, strips segmented in the X direction and strips segmented in Y direction),
3478 and then tries to match them together to form the final clusters.

3479 Working on a module-by-module basis, the algorithm first separates the hits depending
3480 on the layer type they come from. Then, it performs a NN clustering for the 3 sets of
3481 hits separately. For the tile hits it clusters together all the hits which are in nearest-
3482 neighbouring tiles and nearest-neighbouring layers, for strip hits it looks at nearest-
3483 neighbouring strips and next-to-nearest-neighbouring layers (as the layers with strips
3484 along the two directions are alternated). For strip clusters an additional cut in the
3485 direction along the strip length is needed.

3486 After this first clustering I then apply a recursive re-clustering for each collection
3487 of strip clusters based on a PCA method. In each case, we loop over the clusters with
3488 $N_{hits} \geq 2$, computing the centre of mass and three principal components. Propagating
3489 these axes up to the layers of the rest of the clusters, we check if the propagated point
3490 and the centre of mass of the second cluster are within next-to-nearest-neighbouring
3491 strips. An additional cut in the direction along the strip length is also needed. Moreover,
3492 I require that the two closest hits across the two clusters are at most in next-to-nearest-
3493 neighbouring strips. I merge the clusters if these three conditions are satisfied. The

Chapter 8. Particle ID in GArSoft

3494 re-clustering is repeated until no more cluster pairs pass the cuts.

3495 The clusters in each strip view are combined if their centres of mass are close enough
3496 and they point in the same direction. An alternative approach for the strip cluster
3497 merging could be to compute the overlap between the ellipsoids defined by the principal
3498 axes of the clusters, and then merge the pair if the overlap exceeds some threshold.
3499 Further study is needed to understand if this change would have an impact in the overall
3500 clustering performance.

3501 To merge the tile clusters to the combined strip clusters I propagate the principal
3502 axis of the strip cluster towards the inner layers, up to the centre of mass layer of the
3503 tile cluster. I merge the clusters if the distance between the propagated point and the
3504 centre of mass is below a certain cut.

3505 The last step is to check if clusters in neighbouring modules should be merged
3506 together, both across two barrel modules, across end cap modules and between barrel
3507 end cap modules. I check the distance between the two closest hits in the pair of clusters
3508 and merge them if it passes this and an additional direction cut.

3509 Figure ?? presents an example of the clustering steps relevant for strip layer hits, from
3510 the input hits (top left panel) to the NN clustering (top right panel) and re-clustering
3511 (bottom left panel) for each strip view and the final merging strip clusters (bottom
3512 right panel). It shows the hits from a single ECal barrel module in a ν_μ CC interaction
3513 event with a neutral pion and a proton in the final state. The two clusters on the left
3514 correspond to the photon pair from the π^0 decay and the one on the upper right corner
3515 is associated to the proton.

3516 This algorithm has a total number of eight free parameters that need to be optimised.
3517 I used a sample of 1000 ν_μ CC interactions in order to obtain the optimal configuration of
3518 clustering parameters. This sample was generated up to the default ECal hit clustering
3519 level, so then I could run the new clustering algorithm each time with a different
3520 configuration of parameters. As the number of parameters is relatively large, I only
3521 performed a coarse-grained scan of the parameter space. Sampling each of the eight
3522 parameters at three different points each I obtain 6561 different configurations. These

8.5. Neutral particle identification

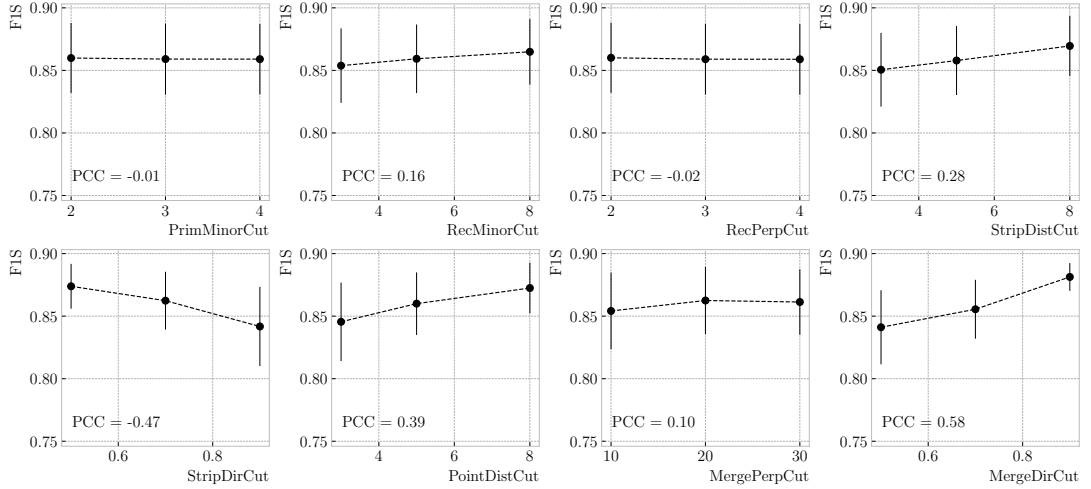


Figure 8.40: Mean values of the F_1 -score marginal distributions for the different free parameters of the new clustering algorithm, with the error bars representing one standard deviation around the mean. The F_1 -score values were computed for the 6561 possible parameter configurations using 1000 ν_μ CC interaction events.

Table 8.5: Summary of parameters and sampled values used in the optimisation of the clustering algorithm.

Name	Units	Sampled values	Description
PrimMinorCut	strips	2, 3, 4	Distance along strip length in NN clustering
RecMinorCut	strips	3, 5, 8	Distance between propagated point and CM along strip length in re-clustering
RecPerpCut	strips	2, 3, 4	Closest hit pair distance in re-clustering
StripDistCut	strips	3, 5, 8	Distance between CMs in strip cluster merging
StripDirCut	cos	0.5, 0.7, 0.9	Main axes direction cut in strip cluster merging
PointDistCut	tiles	3, 5, 8	Distance between propagated point and CM in strip-tile matching
MergePerpCut	cm	10, 20, 30	Closest hit pair distance in module merging
MergeDirCut	cos	0.5, 0.7, 0.9	Main axes direction cut in module merging

parameters, together with the used values, are summarised in Tab. 8.5.

In order to measure the performance of the clustering, I use a binary classification approach. For each formed cluster, I identify the Geant4 Track ID of the matching MC particle and the energy fraction of each hit. Then, I assign to each cluster the Track ID with the highest total energy fraction. For each of the different Track IDs associated to the clusters, I select the cluster with the highest energy (only from the hits with the same Track ID). I identify such a cluster as the main cluster for that Track ID. I count

Chapter 8. Particle ID in GArSoft

as true positives (TPs) the hits with the correct Track ID in each main cluster. False positives (FPs) are the hits with the incorrect Track ID for the cluster they are in, not only main clusters. The false negatives (FNs) are the hits with the correct Track ID in clusters other than the main.

Figure 8.40 shows the computed F_1 -score values for the different cuts. In each case, the central value represents the mean of the F_1 -score distribution for the specified value of the corresponding variable and the vertical error bar represents one standard deviation around the mean. Also shown are the Pearson correlation coefficients of these central values. We can see that five of the variables have a sizeable effect on the F_1 -score, with an absolute difference between the last and first values as big as 4%.

The working configuration is obtained as follows. I first select all configurations with purity $\geq 90\%$. Among those, I choose the combinations that yield the maximum F_1 -score. If more than one configuration remains I select the one with the highest sensitivity. Doing so, I end up with a parameter configuration with an efficiency of 88% and a 90% purity. Compared with the default algorithm, which gives an efficiency of 76% and a purity of 91% for the same sample, I have managed to improve the efficiency by a factor of 1.16.

8.5.2 π^0 reconstruction

One of the potential applications of the new ECal hit clustering is the reconstruction of neutral particles, in particular pions. Neutral pions decay promptly after being produced, through the $\pi^0 \rightarrow \gamma\gamma$ channel ($98.823 \pm 0.034\%$) of the time. The photon pair does not leave any traces in the HPgTPC (unless one or both of them converts into an electron-positron pair), but each of them will produce an electromagnetic shower in the ECal.

To test the potential impact of the new algorithm in π^0 reconstruction, I generated a MC sample of single, isotropic neutral pions inside the HPgTPC. All pions were generated with a momentum $p = 500$ MeV and their initial positions were uniformly sampled inside a $2 \times 2 \times 2$ m box aligned with the centre of the TPC. I ran both the

8.5. Neutral particle identification

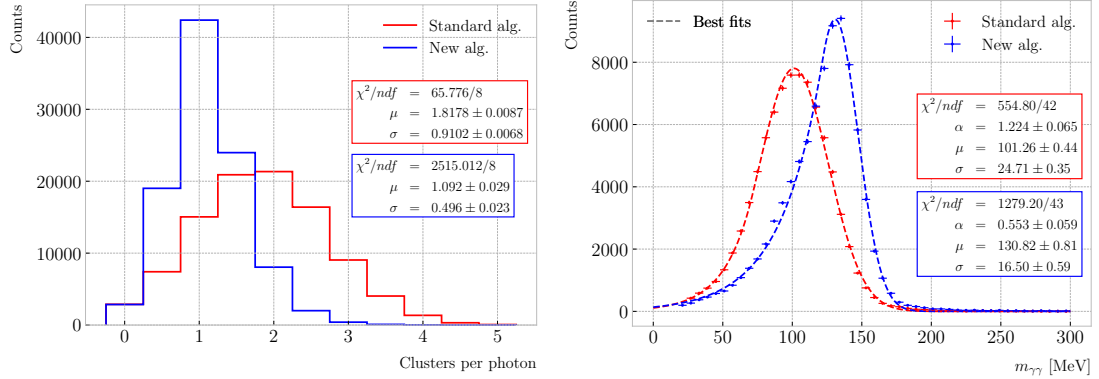


Figure 8.41: Left panel: distributions of the number of ECal clusters per photon from π^0 decays for the standard (red) and new (blue) clustering algorithms. Right panel: reconstructed invariant mass distributions for photon pairs from single π^0 events using the standard (red) and new (blue) ECal clustering algorithms.

3558 default and the new clustering algorithms, using for the latter the optimised configuration
3559 discussed above.

3560 The first thing to notice is that the number of clusters produced per photon has
3561 decreased. Figure 8.41 (left panel) shows these distributions for the default (red) and
3562 new (blue) algorithms. Using a simple Gaussian fit, we see that the mean number of
3563 ECal clusters per photon went from 1.82 ± 0.01 to 1.09 ± 0.03 . This effectively means that
3564 with the new algorithm the ECal activity of one true particle is typically reconstructed
3565 as a single object. From the reconstruction point of view this can be an advantage. As
3566 now most of the photon energy ends up in a single ECal cluster, I can simply use cluster
3567 pairs to identify the π^0 decay.

3568 In general, one calculates the invariant mass of the photon pair as:

$$m_{\gamma\gamma} = \sqrt{2E_1E_2(1 - \cos \theta)}, \quad (8.33)$$

3569 where E_i are the energies of the photons and θ the opening angle between them. In this
3570 case I can use the energies deposited in the ECal and their incident directions. This
3571 quantity is computed for all possible pairs of clusters, using their position together with
3572 the true decay point. In a more realistic scenario, e.g. ν_μ CC interaction, one could use
3573 the position of the reconstructed primary vertex instead. I also tried to use the principal

Chapter 8. Particle ID in GArSoft

3574 direction of the clusters, but that approach gave considerably worse results. For each
3575 event I only keep the pair with an invariant mass closer to the true π^0 mass value.

3576 Figure 8.41 (right panel) shows the invariant mass distributions for the photon pairs
3577 we get using the default (red) and the new (blue) ECal clustering algorithms. For the fit
3578 I used a modified version of the Crystal Ball function [116], obtained by taking the limit
3579 where the parameter controlling the power-law tail goes to infinity:

$$f(x; N, \mu, \sigma, \alpha) = N \cdot \begin{cases} e^{\frac{\alpha(2x-2\mu+\alpha\sigma)}{2\sigma}}; & x \leq \mu - \alpha\sigma, \\ e^{-\frac{(x-\mu)^2}{2\sigma^2}}; & x > \mu - \alpha\sigma. \end{cases} \quad (8.34)$$

3580 Comparing the fitted mean and standard deviation values for the Gaussian cores, we
3581 see that the distribution for the new algorithm is a 67% narrower and also peaks much
3582 closer to the true m_{π^0} value, going from 101.3 ± 0.4 MeV to 130.8 ± 0.6 MeV.

³⁵⁸³ Chapter 9

³⁵⁸⁴ Event selection in ND-GAr

³⁵⁸⁵ 9.1 CAFs and CAFAna

³⁵⁸⁶ 9.2 Event selection

³⁵⁸⁷ 9.2.1 ν_μ CC selection

³⁵⁸⁸ 9.2.2 Charged pion multiplicity

3589 Chapter 10

3590 Conclusions

₃₅₉₁ Appendix A

₃₅₉₂ An appendix

3593 Bibliography

- 3594 [1] DUNE collaboration, *Deep Underground Neutrino Experiment (DUNE), Far*
3595 *Detector Technical Design Report, Volume I Introduction to DUNE, JINST* **15**
3596 (2020) T08008 [2002.02967]. 15, 51, 52, 53, 56, 57, 58, 64, 65, 66, 73, 74
- 3597 [2] DUNE collaboration, *Deep Underground Neutrino Experiment (DUNE), Far*
3598 *Detector Technical Design Report, Volume IV: Far Detector Single-phase*
3599 *Technology, JINST* **15** (2020) T08010 [2002.03010]. 15, 61
- 3600 [3] J.N. Bahcall, A.M. Serenelli and S. Basu, *New solar opacities, abundances,*
3601 *helioseismology, and neutrino fluxes, Astrophys. J. Lett.* **621** (2005) L85
3602 [[astro-ph/0412440](#)]. 21, 121, 123
- 3603 [4] R. Garani and S. Palomares-Ruiz, *Dark matter in the Sun: scattering off electrons*
3604 *vs nucleons, JCAP* **05** (2017) 007 [[1702.02768](#)]. 21, 119, 120, 122, 123, 124, 147
- 3605 [5] M. Honda, M. Sajjad Athar, T. Kajita, K. Kasahara and S. Midorikawa,
3606 *Atmospheric neutrino flux calculation using the NRLMSISE-00 atmospheric model,*
3607 *Phys. Rev. D* **92** (2015) 023004 [[1502.03916](#)]. 22, 127, 128
- 3608 [6] M. Colom i Bernadich and C. Pérez de los Heros, *Limits on Kaluza-Klein dark*
3609 *matter annihilation in the Sun from recent IceCube results, Eur. Phys. J. C,* **80** 2
3610 (2020) 129 **80** (2019) [[1912.04585](#)]. 22, 132
- 3611 [7] ANTARES collaboration, *Search for Dark Matter in the Sun with the ANTARES*
3612 *Neutrino Telescope in the CMSSM and mUED frameworks, Nucl. Instrum. Meth.*
3613 *A* **725** (2013) 76 [[1204.5290](#)]. 22, 132

BIBLIOGRAPHY

- 3614 [8] N. Deutschmann, T. Flacke and J.S. Kim, *Current LHC Constraints on Minimal*
3615 *Universal Extra Dimensions*, *Phys. Lett. B* **771** (2017) 515 [[1702.00410](#)]. 22, 132,
3616 133
- 3617 [9] ICECUBE collaboration, *Search for GeV-scale dark matter annihilation in the Sun*
3618 *with IceCube DeepCore*, *Phys. Rev. D* **105** (2022) 062004 [[2111.09970](#)]. 24, 144,
3619 145
- 3620 [10] C.-S. Chen, F.-F. Lee, G.-L. Lin and Y.-H. Lin, *Probing Dark Matter*
3621 *Self-Interaction in the Sun with IceCube-PINGU*, *JCAP* **10** (2014) 049
3622 [[1408.5471](#)]. 24, 144, 145
- 3623 [11] N.F. Bell, M.J. Dolan and S. Robles, *Searching for dark matter in the Sun using*
3624 *Hyper-Kamiokande*, *JCAP* **11** (2021) 004 [[2107.04216](#)]. 24, 144, 145
- 3625 [12] E. Behnke et al., *Final Results of the PICASSO Dark Matter Search Experiment*,
3626 *Astropart. Phys.* **90** (2017) 85 [[1611.01499](#)]. 24, 144, 145
- 3627 [13] PICO collaboration, *Dark Matter Search Results from the Complete Exposure of*
3628 *the PICO-60 C₃F₈ Bubble Chamber*, *Phys. Rev. D* **100** (2019) 022001
3629 [[1902.04031](#)]. 24, 144, 145
- 3630 [14] DARKSIDE collaboration, *Constraints on Sub-GeV Dark-Matter–Electron*
3631 *Scattering from the DarkSide-50 Experiment*, *Phys. Rev. Lett.* **121** (2018) 111303
3632 [[1802.06998](#)]. 24, 148, 149
- 3633 [15] XENON collaboration, *Light Dark Matter Search with Ionization Signals in*
3634 *XENON1T*, *Phys. Rev. Lett.* **123** (2019) 251801 [[1907.11485](#)]. 24, 148, 149
- 3635 [16] P.F. de Salas, D.V. Forero, S. Gariazzo, P. Martínez-Miravé, O. Mena,
3636 C.A. Ternes et al., *2020 global reassessment of the neutrino oscillation picture*,
3637 *JHEP* **02** (2021) 071 [[2006.11237](#)]. 31, 48, 53
- 3638 [17] W. Pauli, *Dear radioactive ladies and gentlemen*, *Phys. Today* **31N9** (1978) 27. 37

BIBLIOGRAPHY

- 3639 [18] F. Reines and C.L. Cowan, *Detection of the free neutrino*, *Phys. Rev.* **92** (1953)
3640 830. 37
- 3641 [19] S.L. Glashow, *Partial-symmetries of weak interactions*, . 38
- 3642 [20] S. Weinberg, *A model of leptons*, . 38
- 3643 [21] A. Salam, *Weak and Electromagnetic Interactions*, *Conf. Proc. C* **680519** (1968)
3644 367. 38
- 3645 [22] A. Pich, *The Standard Model of Electroweak Interactions*, in *2010 European
3646 School of High Energy Physics*, pp. 1–50, 1, 2012 [[1201.0537](#)]. 38
- 3647 [23] ALEPH, DELPHI, L3, OPAL, SLD, LEP ELECTROWEAK WORKING GROUP,
3648 SLD ELECTROWEAK GROUP, SLD HEAVY FLAVOUR GROUP collaboration,
3649 *Precision electroweak measurements on the Z resonance*, *Phys. Rept.* **427** (2006)
3650 257 [[hep-ex/0509008](#)]. 41
- 3651 [24] SUPER-KAMIOKANDE collaboration, *Evidence for oscillation of atmospheric
3652 neutrinos*, *Phys. Rev. Lett.* **81** (1998) 1562 [[hep-ex/9807003](#)]. 44
- 3653 [25] B. Pontecorvo, *Inverse beta processes and nonconservation of lepton charge*, *Zh.
3654 Eksp. Teor. Fiz.* **34** (1957) 247. 44
- 3655 [26] Z. Maki, M. Nakagawa and S. Sakata, *Remarks on the unified model of elementary
3656 particles*, *Prog. Theor. Phys.* **28** (1962) 870. 44
- 3657 [27] L. Wolfenstein, *Neutrino Oscillations in Matter*, *Phys. Rev. D* **17** (1978) 2369. 46
- 3658 [28] B.T. Cleveland, T. Daily, R. Davis, Jr., J.R. Distel, K. Lande, C.K. Lee et al.,
3659 *Measurement of the solar electron neutrino flux with the Homestake chlorine
3660 detector*, *Astrophys. J.* **496** (1998) 505. 47
- 3661 [29] F. Kaether, W. Hampel, G. Heusser, J. Kiko and T. Kirsten, *Reanalysis of the
3662 GALLEX solar neutrino flux and source experiments*, *Phys. Lett. B* **685** (2010) 47
3663 [[1001.2731](#)]. 47

BIBLIOGRAPHY

- 3664 [30] SAGE collaboration, *Measurement of the solar neutrino capture rate with gallium*
3665 *III: Results for the 2002–2007 data-taking period*, *Phys. Rev. C* **80** (2009)
3666 015807 [0901.2200]. 47
- 3667 [31] G. Bellini et al., *Precision measurement of the ^7Be solar neutrino interaction rate*
3668 *in Borexino*, *Phys. Rev. Lett.* **107** (2011) 141302 [1104.1816]. 47
- 3669 [32] SUPER-KAMIOKANDE collaboration, *Solar neutrino measurements in*
3670 *super-Kamiokande-I*, *Phys. Rev. D* **73** (2006) 112001 [[hep-ex/0508053](#)]. 47
- 3671 [33] SNO collaboration, *Combined Analysis of all Three Phases of Solar Neutrino*
3672 *Data from the Sudbury Neutrino Observatory*, *Phys. Rev. C* **88** (2013) 025501
3673 [1109.0763]. 47
- 3674 [34] SUPER-KAMIOKANDE collaboration, *Atmospheric neutrino oscillation analysis*
3675 *with external constraints in Super-Kamiokande I-IV*, *Phys. Rev. D* **97** (2018)
3676 072001 [1710.09126]. 47
- 3677 [35] ICECUBE collaboration, *Measurement of Atmospheric Neutrino Oscillations at*
3678 *6–56 GeV with IceCube DeepCore*, *Phys. Rev. Lett.* **120** (2018) 071801
3679 [1707.07081]. 47
- 3680 [36] KAMLAND collaboration, *Reactor On-Off Antineutrino Measurement with*
3681 *KamLAND*, *Phys. Rev. D* **88** (2013) 033001 [1303.4667]. 47
- 3682 [37] RENO collaboration, *Measurement of Reactor Antineutrino Oscillation Amplitude*
3683 *and Frequency at RENO*, *Phys. Rev. Lett.* **121** (2018) 201801 [1806.00248]. 47
- 3684 [38] DAYA BAY collaboration, *Measurement of the Electron Antineutrino Oscillation*
3685 *with 1958 Days of Operation at Daya Bay*, *Phys. Rev. Lett.* **121** (2018) 241805
3686 [1809.02261]. 47
- 3687 [39] K.J. Kelly, P.A.N. Machado, S.J. Parke, Y.F. Perez-Gonzalez and R.Z. Funchal,
3688 *Neutrino mass ordering in light of recent data*, *Phys. Rev. D* **103** (2021) 013004.
3689 47

BIBLIOGRAPHY

- 3690 [40] P. Dunne, “Latest Neutrino Oscillation Results from T2K.” Jul, 2020. 47
- 3691 [41] MINOS collaboration, *Combined analysis of ν_μ disappearance and $\nu_\mu \rightarrow \nu_e$ appearance in MINOS using accelerator and atmospheric neutrinos*, *Phys. Rev. Lett.* **112** (2014) 191801 [[1403.0867](#)]. 47
- 3692 [42] OPERA collaboration, *Final Results of the OPERA Experiment on ν_τ Appearance in the CNGS Neutrino Beam*, *Phys. Rev. Lett.* **120** (2018) 211801
- 3693 [1804.04912]. 47
- 3694 [43] K2K collaboration, *Measurement of Neutrino Oscillation by the K2K Experiment*, *Phys. Rev. D* **74** (2006) 072003 [[hep-ex/0606032](#)]. 47
- 3695 [44] DUNE collaboration, *Long-baseline neutrino oscillation physics potential of the DUNE experiment*, *Eur. Phys. J. C* **80** (2020) 978 [[2006.16043](#)]. 47
- 3696 [45] HYPER-KAMIOKANDE collaboration, *Physics potential of Hyper-Kamiokande for neutrino oscillation measurements*, *PoS NuFact2019* (2019) 040. 47
- 3697 [46] SUPERNEMO collaboration, *Probing New Physics Models of Neutrinoless Double Beta Decay with SuperNEMO*, *Eur. Phys. J. C* **70** (2010) 927 [[1005.1241](#)]. 49
- 3698 [47] SNO+ collaboration, *Current Status and Future Prospects of the SNO+ Experiment*, *Adv. High Energy Phys.* **2016** (2016) 6194250 [[1508.05759](#)]. 49
- 3699 [48] NEXT collaboration, *Sensitivity of a tonne-scale NEXT detector for neutrinoless double beta decay searches*, *JHEP* **2021** (2021) 164 [[2005.06467](#)]. 49
- 3700 [49] DUNE collaboration, *Snowmass Neutrino Frontier: DUNE Physics Summary*, [2203.06100](#). 53, 54
- 3701 [50] DUNE collaboration, *Deep Underground Neutrino Experiment (DUNE), Far Detector Technical Design Report, Volume II: DUNE Physics*, [2002.03005](#). 53, 55,
- 3702 [69, 71, 127, 136, 140]

BIBLIOGRAPHY

- 3714 [51] SUPER-KAMIOKANDE collaboration, *Search for Proton Decay via $p \rightarrow e^+ \pi_0$ and*
- 3715 $p \rightarrow \mu^+ \pi_0$ in a Large Water Cherenkov Detector, *Phys. Rev. Lett.* **102** (2009)
- 3716 141801 [0903.0676]. 54
- 3717 [52] S. Raby, *Grand Unified Theories*, in *2nd World Summit: Physics Beyond the*
- 3718 *Standard Model*, 8, 2006 [[hep-ph/0608183](#)]. 54
- 3719 [53] KAMIOKANDE-II collaboration, *Observation of a Neutrino Burst from the*
- 3720 *Supernova SN 1987a*, *Phys. Rev. Lett.* **58** (1987) 1490. 55
- 3721 [54] R.M. Bionta et al., *Observation of a Neutrino Burst in Coincidence with*
- 3722 *Supernova SN 1987a in the Large Magellanic Cloud*, *Phys. Rev. Lett.* **58** (1987)
- 3723 1494. 55
- 3724 [55] DUNE collaboration, *The DUNE Far Detector Vertical Drift Technology,*
- 3725 *Technical Design Report*, 2312.03130. 59, 60
- 3726 [56] DUNE collaboration, *Deep Underground Neutrino Experiment (DUNE) Near*
- 3727 *Detector Conceptual Design Report, Instruments* **5** (2021) 31 [2103.13910]. 63,
- 3728 64, 67, 71, 151
- 3729 [57] J. Strait, E. McCluskey, T. Lundin, J. Willhite, T. Hamernik, V. Papadimitriou
- 3730 et al., *Long-baseline neutrino facility (lbnf) and deep underground neutrino*
- 3731 *experiment (dune) conceptual design report volume 3: Long-baseline neutrino*
- 3732 *facility for dune june 24, 2015*, 1601.05823. 68
- 3733 [58] C. Green, J. Kowalkowski, M. Paterno, M. Fischler, L. Garren and Q. Lu, *The*
- 3734 *Art Framework*, *J. Phys. Conf. Ser.* **396** (2012) 022020. 75
- 3735 [59] DUNE DAQ, “dtp-firmware.”
- 3736 <https://gitlab.cern.ch/dune-daq/readout/dtp-firmware>, 2020. 83
- 3737 [60] DUNE DAQ, “dtp-simulation.”
- 3738 <https://gitlab.cern.ch/dune-daq/readout/dtp-simulation>, 2020. 86

BIBLIOGRAPHY

- 3739 [61] DUNE DAQ, “dtpemulator.”
3740 https://github.com/DUNE-DAQ/dtpemulator/tree/fmlopez/filter_ana,
3741 2022. 86
- 3742 [62] J. McClellan and T. Parks, *A personal history of the Parks-McClellan algorithm*,
3743 *IEEE Signal Processing Magazine* **22** (2005) 82. 87
- 3744 [63] G. Turin, *An introduction to matched filters*, *IEEE Transactions on Information*
3745 *Theory* **6** (1960) 311. 90
- 3746 [64] J.W. Goodman, *Statistical Optics*, Wiley (1985). 92
- 3747 [65] B. Dwork, *Detection of a pulse superimposed on fluctuation noise*, *Proceedings of*
3748 *the IRE* **38** (1950) 771. 93
- 3749 [66] L. Wainstein and V. Zubakov, *Extraction of Signals from Noise*, Prentice-Hall
3750 (1962). 93
- 3751 [67] E.D. Church, *Larsoft: A software package for liquid argon time projection drift*
3752 *chambers*, **1311.6774**. 96, 97
- 3753 [68] S.V. Stehman, *Selecting and interpreting measures of thematic classification*
3754 *accuracy*, *Remote Sensing of Environment* **62** (1997) 77. 110
- 3755 [69] A.A. Taha and A. Hanbury, *Metrics for evaluating 3d medical image*
3756 *segmentation: analysis, selection, and tool*, *BMC Medical Imaging* **15** (2015) . 111
- 3757 [70] J. Silk, K.A. Olive and M. Srednicki, *The Photino, the Sun and High-Energy*
3758 *Neutrinos*, *Phys. Rev. Lett.* **55** (1985) 257. 117
- 3759 [71] M. Srednicki, K.A. Olive and J. Silk, *High-Energy Neutrinos from the Sun and*
3760 *Cold Dark Matter*, *Nucl. Phys. B* **279** (1987) 804. 117
- 3761 [72] J.S. Hagelin, K.W. Ng and K.A. Olive, *A High-energy Neutrino Signature From*
3762 *Supersymmetric Relics*, *Phys. Lett. B* **180** (1986) 375. 117

BIBLIOGRAPHY

- 3763 [73] T.K. Gaisser, G. Steigman and S. Tilav, *Limits on Cold Dark Matter Candidates*
3764 *from Deep Underground Detectors*, *Phys. Rev. D* **34** (1986) 2206. 117
- 3765 [74] N. Bernal, J. Martín-Albo and S. Palomares-Ruiz, *A novel way of constraining*
3766 *WIMPs annihilations in the Sun: MeV neutrinos*, *JCAP* **08** (2013) 011
3767 [1208.0834]. 117, 118, 119, 125
- 3768 [75] C. Rott, J. Siegal-Gaskins and J.F. Beacom, *New Sensitivity to Solar WIMP*
3769 *Annihilation using Low-Energy Neutrinos*, *Phys. Rev. D* **88** (2013) 055005
3770 [1208.0827]. 117, 124
- 3771 [76] C. Rott, S. In, J. Kumar and D. Yavlali, *Dark Matter Searches for Monoenergetic*
3772 *Neutrinos Arising from Stopped Meson Decay in the Sun*, *JCAP* **11** (2015) 039
3773 [1510.00170]. 117
- 3774 [77] DUNE collaboration, *Searching for solar KDAR with DUNE*, *JCAP* **10** (2021)
3775 065 [2107.09109]. 117
- 3776 [78] G. Busoni, A. De Simone and W.-C. Huang, *On the Minimum Dark Matter Mass*
3777 *Testable by Neutrinos from the Sun*, *JCAP* **07** (2013) 010 [1305.1817]. 118
- 3778 [79] V.A. Bednyakov and F. Simkovic, *Nuclear spin structure in dark matter search:*
3779 *The Zero momentum transfer limit*, *Phys. Part. Nucl.* **36** (2005) 131
3780 [hep-ph/0406218]. 119
- 3781 [80] A. Gould, *WIMP Distribution in and Evaporation From the Sun*, *Astrophys. J.*
3782 **321** (1987) 560. 120
- 3783 [81] J.N. Bahcall, M.H. Pinsonneault and S. Basu, *Solar models: Current epoch and*
3784 *time dependences, neutrinos, and helioseismological properties*, *Astrophys. J.* **555**
3785 (2001) 990 [astro-ph/0010346]. 122
- 3786 [82] T. Golan, J.T. Sobczyk and J. Zmuda, *NuWro: the Wroclaw Monte Carlo*
3787 *Generator of Neutrino Interactions*, *Nucl. Phys. B Proc. Suppl.* **229-232** (2012)
3788 499. 126

BIBLIOGRAPHY

- 3789 [83] G. Cowan, K. Cranmer, E. Gross and O. Vitells, *Asymptotic formulae for
3790 likelihood-based tests of new physics*, *Eur. Phys. J. C* **71** (2011) 1554 [[1007.1727](#)].
3791 127
- 3792 [84] T. Kaluza, *Zum Unitätsproblem der Physik, Sitzungsber. Preuss. Akad. Wiss.
3793 Berlin (Math. Phys.)* **1921** (1921) 966 [[1803.08616](#)]. 129
- 3794 [85] O. Klein, *Quantum Theory and Five-Dimensional Theory of Relativity. (In
3795 German and English)*, *Z. Phys.* **37** (1926) 895. 129
- 3796 [86] T. Appelquist, H.-C. Cheng and B.A. Dobrescu, *Bounds on universal extra
3797 dimensions*, *Phys. Rev. D* **64** (2001) 035002 [[hep-ph/0012100](#)]. 129
- 3798 [87] N. Arkani-Hamed, S. Dimopoulos and G.R. Dvali, *The Hierarchy problem and new
3799 dimensions at a millimeter*, *Phys. Lett. B* **429** (1998) 263 [[hep-ph/9803315](#)]. 129
- 3800 [88] L. Randall and R. Sundrum, *A Large mass hierarchy from a small extra
3801 dimension*, *Phys. Rev. Lett.* **83** (1999) 3370 [[hep-ph/9905221](#)]. 129
- 3802 [89] G. Servant and T.M.P. Tait, *Is the lightest Kaluza-Klein particle a viable dark
3803 matter candidate?*, *Nucl. Phys. B* **650** (2003) 391 [[hep-ph/0206071](#)]. 129
- 3804 [90] H.-C. Cheng, K.T. Matchev and M. Schmaltz, *Radiative corrections to
3805 Kaluza-Klein masses*, *Phys. Rev. D* **66** (2002) 036005 [[hep-ph/0204342](#)]. 131
- 3806 [91] M. Blennow, J. Edsjö and T. Ohlsson, *Neutrinos from WIMP annihilations using
3807 a full three-flavor Monte Carlo*, *JCAP* **01** (2008) 021 [[0709.3898](#)]. 131, 134
- 3808 [92] J. Edsjö, J. Elevant and C. Niblaeus, *WimpSim Neutrino Monte Carlo*. 131, 134
- 3809 [93] U. Haisch and A. Weiler, *Bound on minimal universal extra dimensions from
3810 anti-B → X(s)gamma*, *Phys. Rev. D* **76** (2007) 034014 [[hep-ph/0703064](#)]. 133
- 3811 [94] A. Freitas and U. Haisch, *Anti-B → X(s) gamma in two universal extra
3812 dimensions*, *Phys. Rev. D* **77** (2008) 093008 [[0801.4346](#)]. 133

BIBLIOGRAPHY

- 3813 [95] C. Rott, D. Jeong, J. Kumar and D. Yaylali, *Neutrino Topology Reconstruction at*
3814 *DUNE and Applications to Searches for Dark Matter Annihilation in the Sun,*
3815 *JCAP* **07** (2019) 006 [[1903.04175](#)]. 136
- 3816 [96] F. Pedregosa, G. Varoquaux, A. Gramfort, V. Michel, B. Thirion, O. Grisel et al.,
3817 *Scikit-learn: Machine learning in Python, Journal of Machine Learning Research*
3818 **12** (2011) 2825. 142
- 3819 [97] J. Kopp, V. Niro, T. Schwetz and J. Zupan, *DAMA/LIBRA and leptонically*
3820 *interacting Dark Matter, Phys. Rev. D* **80** (2009) 083502 [[0907.3159](#)]. 146
- 3821 [98] PARTICLE DATA GROUP collaboration, *Review of Particle Physics, PTEP* **2020**
3822 (2020) 083C01. 147
- 3823 [99] M. Beltran, D. Hooper, E.W. Kolb and Z.C. Krusberg, *Deducing the nature of*
3824 *dark matter from direct and indirect detection experiments in the absence of*
3825 *collider signatures of new physics, Phys. Rev. D* **80** (2009) 043509 [[0808.3384](#)].
3826 147
- 3827 [100] PLANCK collaboration, *Planck 2018 results. VI. Cosmological parameters, Astron.*
3828 *Astrophys.* **641** (2020) A6 [[1807.06209](#)]. 148
- 3829 [101] H. Bethe, *Zur theorie des durchgangs schneller korpuskularstrahlen durch materie,*
3830 *Annalen der Physik* **397** (1930) 325. 152
- 3831 [102] E. Fermi, *The ionization loss of energy in gases and in condensed materials,*
3832 *Physical Review* **57** (1940) 485. 153
- 3833 [103] R. Sternheimer, M. Berger and S. Seltzer, *Density effect for the ionization loss of*
3834 *charged particles in various substances, Atomic Data and Nuclear Data Tables* **30**
3835 (1984) 261. 153
- 3836 [104] W.W.M. Allison and J.H. Cobb, *Relativistic Charged Particle Identification by*
3837 *Energy Loss, Ann. Rev. Nucl. Part. Sci.* **30** (1980) 253. 153

BIBLIOGRAPHY

- 3838 [105] W. Blum, L. Rolandi and W. Riegler, *Particle detection with drift chambers*,
3839 Particle Acceleration and Detection (2008), 10.1007/978-3-540-76684-1. 154
- 3840 [106] ALICE TPC collaboration, *Particle identification of the ALICE TPC via dE/dx*,
3841 *Nucl. Instrum. Meth. A* **706** (2013) 55. 154
- 3842 [107] L. Landau, *On the energy loss of fast particles by ionization*, *J. Phys. (USSR)* **8**
3843 (1944) 201. 157
- 3844 [108] W. Ulmer and E. Matsinos, *Theoretical methods for the calculation of Bragg
3845 curves and 3D distributions of proton beams*, *The European Physical Journal
3846 Special Topics* **190** (2010) 1. 158
- 3847 [109] E. Aprile, A.E. Bolotnikov, A.L. Bolozdynya and T. Doke, *Noble Gas Detectors*,
3848 Wiley (Oct., 2008), 10.1002/9783527610020. 160
- 3849 [110] D.S. Wilks, *Statistical Methods in the Atmospheric Sciences*, Academic Press. 197
- 3850 [111] ALICE collaboration, *Production of pions, kaons and protons in pp collisions at
3851 $\sqrt{s} = 900 \text{ gev with alice at the lhc}$* , **1101.4110**. 199
- 3852 [112] U. Einhaus, *Charged hadron identification with de/dx and time-of-flight at future
3853 higgs factories*, **2110.15115**. 199
- 3854 [113] R. Frühwirth, *Application of filter methods to the reconstruction of tracks and
3855 vertices in events of experimental high energy physics*, Ph.D. thesis, Technischen
3856 Universität Wien, 1988. 205
- 3857 [114] P. Astier, A. Cardini, R.D. Cousins, A. Letessier-Selvon, B.A. Popov and
3858 T. Vinogradova, *Kalman filter track fits and track breakpoint analysis*, *Nuclear
3859 Instruments and Methods in Physics Research Section A: Accelerators,
3860 Spectrometers, Detectors and Associated Equipment* **450** (2000) 138. 205
- 3861 [115] T2K UK collaboration, *The Electromagnetic Calorimeter for the T2K Near
3862 Detector ND280*, *JINST* **8** (2013) P10019 [1308.3445]. 213

BIBLIOGRAPHY

- 3863 [116] J.E. Gaiser, *Charmonium Spectroscopy From Radiative Decays of the J/ψ and ψ' ,*
3864 Ph.D. thesis, Stanford University, 1982. 218